

# **Ice-nucleating particles in the free troposphere: long-term observation and first measurements at cirrus formation temperatures using the novel Portable Ice Nucleation Experiment PINEair**

Zur Erlangung des akademischen Grades eines  
DOKTORS DER NATURWISSENSCHAFTEN (Dr. rer. nat.)  
von der KIT-Fakultät für Physik des  
Karlsruher Instituts für Technologie (KIT)

angenommene

DISSERTATION

von

**M.Sc. Pia Bogert**

Tag der mündlichen Prüfung: 05.07.2024

Referent: Prof. Dr. Thomas Leisner

Korreferent: Prof. Dr. Joachim Curtius



## Abstract

Ice formation induced by ice-nucleating particles (INPs) greatly influences the formation, life cycles, and climatic impact of tropospheric clouds, as well as their ability to form precipitation. However, knowledge about the abundance of INPs especially in the free troposphere (FT) is still missing. Therefore, this thesis aimed at observing INPs at the Sonnblick Observatory (SBO, 3106 m a.s.l.) which is frequently located in the FT. The comprehensive measurements were conducted over long term to investigate the seasonal variation, at high time resolution to obtain information on the diurnal and shorter-term variability, and in a wide temperature range to cover mixed-phase cloud (MPC) and cirrus cloud conditions. INPs that impact the ice formation in cirrus clouds were measured with the novel instrument PINEair (Portable Ice Nucleation Experiment airborne), which was developed as part of this PhD thesis.

The new aircraft-based INP instrument PINEair was developed especially for use on the HALO (High Altitude and Long Range) research aircraft. It is the first aircraft-based instrument that can perform automated in-situ measurements of INPs to temperatures of  $-65^{\circ}\text{C}$ . PINEair simulates cloud-like conditions by expansion cooling. It consists of three expansion chambers operated in a cycling mode to achieve measurements with higher time and spatial resolution in a fast-flying jet aircraft. Laboratory measurements with a prototype of PINEair have successfully shown that the newly developed instrument can measure the INP concentration in a wide temperature range relevant for MPC and cirrus clouds. The distinction between homogeneous and heterogeneous freezing at cirrus conditions was demonstrated for ground-based conditions with ambient air sampling and for lower pressure ( $p = 250\text{ mbar}$ ) conditions during aircraft flights which were simulated in a series of laboratory experiments. For this purpose, a new expansion procedure was developed where the pressure in the chambers can step-wise be reduced at the beginning of the expansion. This allows the calculation of the peak ice saturation ratio ( $S_{ice,p}$ ) in the chamber assuming ice-saturated conditions before expansion start and an adiabatic temperature decrease.

As part of this PhD thesis, a mobile prototype of PINEair was engineered, built, and tested during a field campaign at the SBO in the Austrian Alps. Measurements were performed quasi continuously during the time period from May 8 - 22, 2023, at both MPC ( $T = -22.7^{\circ}\text{C}$  and  $T = -27.5^{\circ}\text{C}$ ) and cirrus ( $T = -47.8^{\circ}\text{C}$ ) temperatures. At a temperature of  $-47.8^{\circ}\text{C}$  and  $S_{ice,p} = 1.49 - 1.52$ , a median INP concentration of  $1.1\text{ std L}^{-1}$  was measured, and a maximum concentration of about  $90\text{ std L}^{-1}$ . Higher  $S_{ice,p}$  conditions in the chamber resulted in higher INP concentrations, which is consistent with the literature. During a case study with increased aerosol concentrations and particle mass concentrations, also

increased INP concentrations up to  $84 \text{ std L}^{-1}$  were measured at  $-47.8^\circ\text{C}$  and  $S_{ice,p} = 1.52 - 1.55$ .

Another major part of this PhD thesis were long-term INP measurements in the MPC temperature range at the SBO. Due to its location, the site receives both air masses from the FT and the boundary layer (BL). The measurements were performed with the freezing experiment INSEKT (Ice Nucleation Spectrometer of the Karlsruhe Institute of Technology) from August 2019 to August 2022 with a time resolution of one week. To date, this is the longest, continuous INP measurement series. In addition, a 14-month INP time series with a high time resolution of 6 min was performed with PINE, starting in August 2021. Both data sets show a recurrent seasonal sinusoidal trend with the highest INP concentrations in spring/summer and the lowest in winter. From April to September, a daily cycle in the INP concentration is observed with a maximum around noon and a minimum at midnight. In contrast, from October to February, no daily cycle was observed and the INP concentrations were consistently low. The seasonal and diurnal variations of the INP concentration are likely caused by the influence of air masses from the BL, as the concentrations of the tracers (aerosol particles with a diameter larger than 90 nm and  $^{214}\text{Polonium}$  concentration) show the same trends. A heat analysis of the filters prior to INP analysis with INSEKT showed reduced INP activity, especially at higher temperatures above  $-13^\circ\text{C}$  for all seasons, indicating that biogenic compounds contributed to the INP abundance. Strong sudden increases in the INP concentration are caused by episodically occurring dust events, which were observed by enhanced and correlated concentrations of both the INP number concentration and the aerosol mass concentration. A comparison of the measured INP concentration during a dust event in March 2022 to the parameterization of DeMott et al. (2015) showed a good agreement, the temperature dependence and 98.5% of the data within a factor of 10 were predicted correctly. The median INP concentration of the whole measurement period was slightly higher during clear-sky periods than during cloudy periods, which could be caused by processes such as wet-removal or pre-activation of INPs. Moreover, the INP concentration was found to be correlated with the aerosol concentration, size, and mass, especially at lower nucleation temperatures. However, the observed variation of the INP concentration was not correlated with meteorological parameters. From this study, it can be concluded that the INP concentration at SBO is mainly influenced by different sources including free tropospheric aerosols, long-range transported dust, and local or regional aerosol sources transported from the BL to the station.

# Contents

<b>1</b>	<b>Introduction</b>	<b>1</b>
<b>2</b>	<b>Theoretical Background</b>	<b>7</b>
2.1	Atmospheric Aerosol Particles . . . . .	7
2.2	Ice Formation in the Atmosphere . . . . .	9
2.2.1	Cirrus Clouds . . . . .	10
2.2.2	Mixed-Phase Clouds . . . . .	13
2.3	State of the Art of Ice-Nucleating Particles . . . . .	15
<b>3</b>	<b>Experimental Methods</b>	<b>21</b>
3.1	Online: Cloud Expansion Chamber PINE . . . . .	21
3.2	Offline: Freezing Experiment INSEKT . . . . .	25
3.3	Expansion Chamber AIDA . . . . .	28
3.4	Aerosol Chamber APC . . . . .	30
3.5	Generation and Injection of Aerosols . . . . .	30
<b>4</b>	<b>Development and Application of the New Aircraft-Based Expansion Chamber PINEair</b>	<b>33</b>
4.1	Introduction . . . . .	33
4.2	General Information . . . . .	35
4.2.1	Setup of PINEair . . . . .	35
4.2.2	Working Principle . . . . .	37
4.2.3	Different Versions of PINEair . . . . .	42
4.3	Validation Experiments with the PINEair Prototype I . . . . .	44
4.3.1	Overview of Campaign . . . . .	44
4.3.2	Results and Discussion . . . . .	45
4.4	Validation Experiments with the PINEair Prototype II . . . . .	50
4.4.1	Measurements at Cirrus Temperatures . . . . .	51
4.4.2	Data Evaluation at Cirrus Temperatures . . . . .	57
4.5	First Field Campaign with the PINEair Prototype II . . . . .	66
4.5.1	Overview of Campaign . . . . .	67
4.5.2	Results and Discussion . . . . .	70

4.6	Summary . . . . .	86
<b>5</b>	<b>Long-Term INP Measurements at the Sonnblick Observatory</b>	<b>89</b>
5.1	Introduction . . . . .	89
5.2	Overview of Campaign . . . . .	90
5.2.1	Field Location . . . . .	91
5.2.2	Overview of Conducted INP Measurements . . . . .	93
5.2.3	Sampling Setup . . . . .	95
5.2.4	Air Mass Origin . . . . .	96
5.3	Results . . . . .	97
5.3.1	INP Temperature Spectra . . . . .	97
5.3.2	Seasonal Variation . . . . .	99
5.3.3	Diurnal Variation . . . . .	100
5.3.4	Heat Treatment . . . . .	101
5.4	Discussion . . . . .	104
5.4.1	Aerosol Types . . . . .	104
5.4.2	Boundary Layer Influence . . . . .	104
5.4.3	Saharan Dust Influence . . . . .	107
5.4.4	Cloud Influence . . . . .	110
5.4.5	Relation to Aerosol Properties and Meteorological Conditions . . . . .	111
5.4.6	Comparison between INSEKT and PINE . . . . .	113
5.5	Dust Event in March 2022 . . . . .	116
5.5.1	Measurements . . . . .	116
5.5.2	Comparison to Existing INP Parameterizations . . . . .	117
5.5.3	Comparison to Helmos Station . . . . .	121
5.6	Summary . . . . .	123
<b>6</b>	<b>Summary and Outlook</b>	<b>127</b>
<b>A</b>	<b>List of Abbreviations and Symbols</b>	<b>133</b>
<b>B</b>	<b>Bibliography</b>	<b>137</b>
<b>C</b>	<b>List of Figures</b>	<b>163</b>
<b>D</b>	<b>List of Tables</b>	<b>167</b>

# 1. Introduction

Atmospheric aerosol particles can exert an important influence on the global climate system by directly changing the Earth's energy budget via interactions with solar and terrestrial radiation (e.g., Boucher et al., 2013; Bellouin et al., 2020; Forster et al., 2021) and indirectly by contributing to cloud formation (e.g., Boucher et al., 2013; Mülmenstädt and Feingold, 2018; Forster et al., 2021). However, according to the latest report of the Intergovernmental Panel on Climate Change (IPCC, Forster et al., 2021) aerosol-cloud interactions are still poorly understood. The largest uncertainties are related to clouds containing ice crystals, as their formation, radiative properties, and lifetime in the atmosphere are still not sufficiently understood (Forster et al., 2021). A basic understanding of atmospheric ice formation is crucial for a more accurate representation of the ice phase in cloud and climate models (e.g., Boucher et al., 2013; Storelvmo, 2017; Murray and Liu, 2022; Knopf and Alpert, 2023).

Cirrus clouds form at temperatures below  $-38^{\circ}\text{C}$  and consist only of ice crystals, while mixed-phase clouds (MPCs), which consist of supercooled liquid water droplets and ice crystals, can only form at temperatures between  $0^{\circ}\text{C}$  and  $-38^{\circ}\text{C}$  in the atmosphere. Ice formation starts by the spontaneous freezing of supercooled droplets or diluted solution droplets via homogeneous nucleation when the temperature is below about  $-38^{\circ}\text{C}$ . Ice-nucleating particles (INPs) initiate heterogeneous ice formation at higher temperatures and lower supersaturations with respect to ice (e.g., Pruppacher and Klett, 1997; Cantrell and Heymsfield, 2005; Vali et al., 2015; Kanji et al., 2017; Knopf et al., 2018; Knopf and Alpert, 2023). Depending on the temperature ( $T$ ) and the saturation ratio with respect to ice ( $S_{ice}$ ), heterogeneous ice formation occurs by one of the four different modes deposition nucleation, immersion freezing, condensation freezing, or contact freezing (e.g., Pruppacher and Klett, 1997; Cantrell and Heymsfield, 2005; Hoose and Möhler, 2012; Murray et al., 2012; Vali et al., 2015) (Figure 1.1).

INPs are a rare subset of atmospheric aerosol particles, which makes their identification and quantification a challenge (DeMott et al., 2011; Cziczo et al., 2017). This is further complicated by their strong dependence on temperature, and the strong variation of their abundance with location and season (e.g., Mason, 1972; Pruppacher and Klett, 1997; DeMott et al., 2010; Kanji et al., 2017). Although INPs have been studied for many decades (e.g., Dufour, 1862), there are still large uncertainties about their sources, concentrations, and seasonal variability, and it is still not yet known in detail which aerosol types markedly contribute to the INP population (Kanji et al., 2017). Atmospheric aerosol species that are known to act as INP are e.g. mineral dust particles (e.g., Pratt et al., 2009; Cziczo et al., 2013; Ladino Moreno et al., 2013; Vergara-Temprado et al., 2017), biological particles like bacteria, fungal

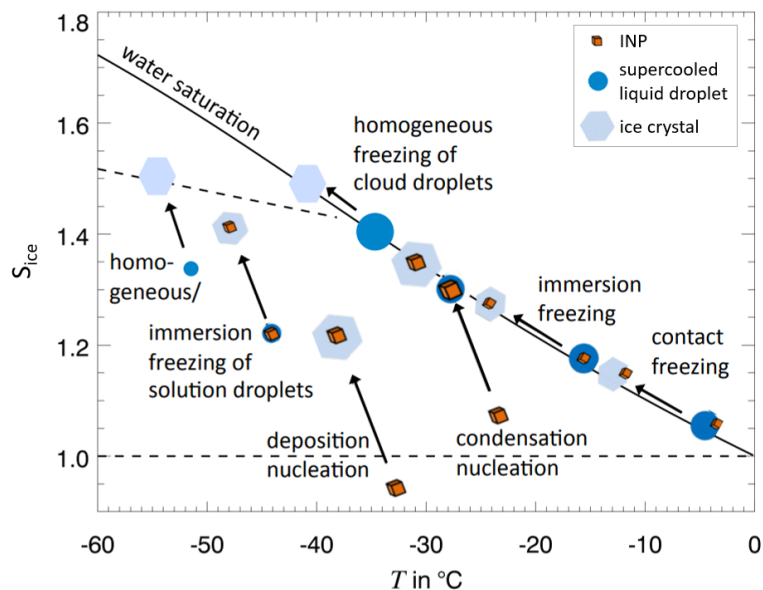


Figure 1.1.: Schematic representation of the different nucleation modes for heterogeneous ice formation and their temperature ( $T$ ) and saturation ratio with respect to ice ( $S_{ice}$ ) where they occur. Figure adapted from Hoose and Möhler (2012).

spores, pollen, lichens (e.g., Alpert et al., 2011; Hiranuma et al., 2014; Mason et al., 2015; Wex et al., 2015), volcanic ash particles (Kanji et al., 2017), sea spray aerosol (e.g., Burrows et al., 2013; Wilson et al., 2015; Vergara-Temprado et al., 2017; McCluskey et al., 2018), soil dust particles (e.g., Conen et al., 2011; Steinke et al., 2016; Suski et al., 2018) or metal particles (Cziczo et al., 2009; Cziczo et al., 2013). Comprehensive measurements and experiments are needed to identify whether a particular aerosol type can act as an effective INP (Murray et al., 2012). Nowadays there are three common techniques available (Figure 1.2): droplet freezing experiments (e.g., Hill et al., 2013), continuous flow diffusion chambers (CFDCs) (e.g., Rogers, 1988), and cloud expansion chambers (e.g., Möhler et al., 2006; Möhler et al., 2021). The first is referred to as an offline technique, as the aerosols are first collected on e.g. filters and thereafter analyzed in the laboratory. The other two techniques are online methods, as the information about the ice nucleation ability of the aerosols is obtained in real time.

Although INPs are rare, they still have a strong influence on the climate on Earth (e.g., Kanji et al., 2017; Burrows et al., 2022), as they contribute to the formation of ice crystals in the atmosphere through heterogeneous nucleation. As soon as a cloud includes ice crystals, its radiation properties change by altering the interaction between the incoming short-wave radiation and the outgoing long-wave radiation, which influences the radiation balance (e.g., Boucher et al., 2013; Storelvmo, 2017; Forster et al., 2021). For example, as soon as the first ice crystals have formed in a MPC due to the presence of INPs, a phase change from liquid to ice can rapidly occur within the whole cloud (e.g., Korolev and Field, 2008; Korolev et al., 2017). This in turn affects the radiative properties of the cloud and therefore the climate

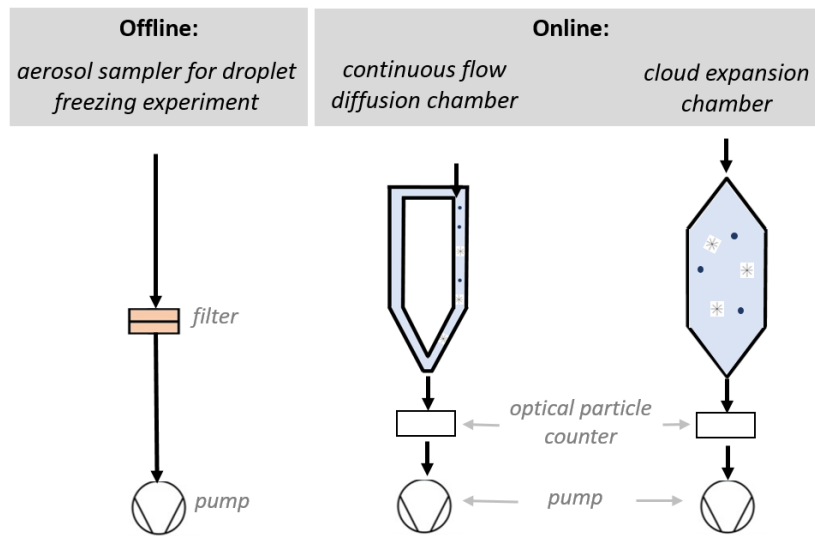


Figure 1.2.: Schematic representation of different INP instruments.

(e.g., Storelvmo et al., 2011; Storelvmo et al., 2015; Vergara-Temprado et al., 2018b). In the case of cirrus clouds, the microphysical properties, such as the size and number of ice crystals, are altered depending on the temperature and supersaturation conditions during their formation, and whether they are formed by homogeneous freezing of solute aerosols or by heterogeneous ice formation due to the presence of INPs. This has a great impact on the radiation properties of the cirrus cloud (Storelvmo, 2017). In addition, most precipitation in clouds is produced by the ice phase (Lau and Wu, 2003; Lohmann and Feichter, 2005), especially over land (Mülmenstädt et al., 2015; Field and Heymsfield, 2015; Heymsfield et al., 2020), therefore, ice formation in the atmosphere plays a key role in the global water cycle. Despite their importance, INPs are still inadequately represented in models (Murray et al., 2021; Burrows et al., 2022), as there are still many uncertainties regarding their vertical distribution, concentrations, and seasonal variations. This is due to missing knowledge about INP emission sources and transport processes in the atmosphere, which requires more measurements of INPs in ambient air. In recent years, most INP measurements have been conducted at ground-based stations in the MPC temperature range for shorter periods (Kanji et al., 2017). However, there is especially a lack of INP field data in the free troposphere (e.g., Lacher et al., 2018a), and at cirrus conditions (e.g., Wolf et al., 2020). Moreover, long-term measurements to investigate seasonal variations of the INP concentration are sparse (e.g., Bras et al., 2022). Thus, the focus of this PhD thesis is put on three aspects: A three-year long-term study of INP concentrations at MPC conditions at a high-altitude station to investigate seasonal and diurnal variations; the development of a new aircraft-based INP instrument, capable of measuring in the MPC and cirrus cloud regime, which will be used in future studies onboard the HALO (High Altitude and Long Range) aircraft; and ambient measurements of INPs at cirrus conditions using the newly developed instrument.

### **Development of a new aircraft-based INP instrument for measurements in the free troposphere:**

Most INP measurements were performed at ground-based stations in the boundary layer (BL) (Kanji et al., 2017), while there are only a handful of measurements conducted in the free troposphere (FT) (e.g., Lacher et al., 2018a and references therein; Brunner et al., 2022). Therefore, there is a lack of knowledge about the concentration and composition of INPs in the FT (Wolf et al., 2020). Studies indicated that more measurements are needed to be able to answer open questions about the INP concentrations at cloud level, and their influence on cloud formation and properties (e.g., Coluzza et al., 2017). INP measurements in the FT were conducted either at mountain sites like, for example, the Jungfraujoch station in Switzerland (e.g., Conen et al., 2015; Boose et al., 2016b; Lacher et al., 2018a; Lacher et al., 2018b; Brunner et al., 2022), by tethered balloons (e.g., Creamean et al., 2018; Porter et al., 2020), by unmanned aerial vehicles (UAV) (e.g., Schrod et al., 2017; Jimenez-Sanchez et al., 2018; Bieber et al., 2020) or by aircraft-based measurements (e.g., Flyger et al., 1973; DeMott et al., 2016; Price et al., 2018; Levin et al., 2019; Sanchez-Marroquin et al., 2020, Varble et al., 2021). In particular, aircraft-based measurements are needed to investigate INPs at higher altitudes in the atmosphere. Available aircraft-based INP instruments include an aerosol filter sampling and offline analysis method (e.g., Grawe et al., 2023) and a CFDC from the Colorado State University (Rogers et al., 2001b), which allow INP measurements only in the MPC temperature range. To date, there is no aircraft-based instrument that can measure the INP concentration at temperatures lower than  $-40^{\circ}\text{C}$  and supersaturations relevant for cirrus cloud formation. As part of this PhD thesis, a new aircraft-based instrument called PINEair (Portable Ice Nucleation Experiment airborne) was developed, which can be used to investigate the INP concentration in the temperature range between  $0^{\circ}\text{C}$  and  $-65^{\circ}\text{C}$  in freezing modes relevant for MPC and cirrus clouds.

### **Measurements of the INP concentration at cirrus cloud conditions:**

Cirrus clouds have an average global land cover of 22.8% (Heymsfield et al., 2017) and thus have a significant influence on the Earth's radiative budget, but the effect of INPs on cirrus clouds and thus the influence on the climate is highly uncertain (e.g., Kärcher, 2017; Kanji et al., 2017; Krämer et al., 2020). This is caused by the fact that a comprehensive understanding of cirrus formation is limited due to the lack of INP field data in this temperature range (e.g., DeMott et al., 2003b; Richardson et al., 2007; Kanji et al., 2017; Wolf et al., 2020). The current knowledge is based on laboratory measurements, e.g. by using the AIDA (Aerosol Interaction and Dynamics in the Atmosphere) chamber (e.g., Wagner et al., 2021) or CFDCs (e.g., Mahrt et al., 2020). Only a few mobile instruments are capable of measuring the INP concentration at cirrus conditions. Previous measurements were made with a CFDC at the mountain stations Storm Peak Laboratory in western Colorado (DeMott et al., 2003b; Richardson et al., 2007) and the Puy de Dôme Observatory in France (Wolf et al., 2020). Since more INP measurements at cirrus cloud conditions are needed, the new INP instrument PINEair was developed not only to be used on research aircraft but also as a mobile instrument for operation at research stations, to detect INPs at MPC and cirrus cloud conditions. As part of this PhD thesis, INP measurements at cirrus conditions ( $T \sim -48^{\circ}\text{C}$ )

---

were performed with a prototype version of PINEair at the high-altitude station Sonnblick Observatory (3106m a.s.l.) in Austria.

**Long-term measurements of the INP concentration at a high-altitude station:**

Many INP studies are limited to shorter measurement periods, and only a few studies focused on analyzing INP seasonal trends and variability (Brunner et al., 2022). For example, Conen et al. (2015), Wex et al. (2019), Tobo et al. (2020), Schrod et al. (2020), Schneider et al. (2021a), Brunner et al. (2022) have found a seasonal dependence of the INP concentration at different locations around the globe, with the highest concentrations measured in spring and summer. However, except Brunner et al. (2022), the studies are based on offline filter sampling measurements, with low time resolutions from about 24h to 2 weeks. This does not provide information about the diurnal variability of the INP concentration. In particular, long-term measurements with a high time resolution are needed, since INP concentrations can vary significantly on short time scales. Such measurements can be used to derive parameterizations for the formulation and prediction of INP concentrations in weather and climate models (Burrows et al., 2022; Bras et al., 2022). A long-term measurement series was performed at the Sonnblick Observatory in Austria as part of this doctoral thesis, which provides a continuous data set of three years of INP measurements performed with an offline aerosol filter sampling method and additionally, a 14-month measurement series conducted with a mobile expansion chamber. The station is an ideal location, as it is located in the lower FT and is only sometimes influenced by air masses from the BL.

The structure of this thesis is given as follows:

**Chapter 2 Theoretical Background:** This chapter provides detailed information about the aerosol particles in the atmosphere, the primary ice formation for the cirrus clouds and MPCs, and the current state of knowledge about INPs.

**Chapter 3 Experimental Methods:** This chapter includes a description of the setup and working principle of the instruments used in this doctoral thesis, as well as a description of the aerosols used for the laboratory experiments.

**Chapter 4 Development and Application of the New Aircraft-Based Expansion Chamber PINEair:** This chapter describes the structure and working principle of the newly developed PINEair instrument. It presents the first results of the laboratory measurements for testing and characterization purposes, and the first measurements at ambient air conditions at Campus North at KIT (Karlsruhe Institute of Technology) and the Sonnblick Observatory in Austria.

**Chapter 5 Long-Term INP Measurements at the Sonnblick Observatory:** This chapter discusses the long-term measurements of the INP concentration at the Sonnblick Observatory in terms of seasonal and

diurnal variations. First, an overview of the results is given, then they are interpreted and finally, a case study of a strong dust event in March 2022 is described in more detail.

**Chapter 6 Summary and Outlook:** This chapter summarizes the findings and results of this PhD thesis and gives an outlook for future experiments.

## 2. Theoretical Background

A major target of this PhD thesis are INPs, a minor number fraction of atmospheric aerosol particles that induce the nucleation of the ice phase and by that impact atmospheric clouds, precipitation, and the climate system. Section 2.1 provides an introduction to the types, properties, and impacts of atmospheric aerosols, and section 2.2 describes the basics of ice formation in atmospheric clouds. Section 2.3 summarizes the current knowledge about the types, abundance, and impact of atmospheric INPs.

### 2.1. Atmospheric Aerosol Particles

Aerosol particles are defined as solid or liquid particles suspended in air (Whytlaw-Gray et al., 1923). There are a variety of natural and anthropogenic sources with different emission rates, therefore their concentration and composition vary strongly in the atmosphere (e.g., Seinfeld and Pandis, 2012). They can be transported over very long distances far away from their emission source (e.g., Jaenicke, 1982; Abdalmogith and Harrison, 2005), and during transport they can be modified by e.g. coagulation. Finally, they can be removed from the atmosphere via processes like settling, turbulent deposition, or precipitation. Basically, a distinction can be made between primary aerosols, which are emitted directly into the atmosphere, and secondary aerosols, which are formed through chemical reactions in the atmosphere (Seinfeld and Pandis, 2012).

Primary aerosols from natural sources are, for example, biological particles such as pollen, spores, and bacteria (e.g., Despres et al., 2012), volcanic ash from volcanic eruptions (e.g., Tomasi and Lupi, 2017), sea salt aerosol from oceans (e.g., Schulz et al., 2004) or dust particles from deserts (e.g., Tegen and Schepanski, 2009). Primary aerosols can also be emitted into the atmosphere by anthropogenic sources, such as soot or sulfate particles from industrial processes, transportation, biomass burning, or deforestation (Lighty et al., 2000).

Secondary aerosols or aerosol components are formed from natural and anthropogenic precursor gases, which undergo chemical reactions in the atmosphere to form less volatile trace gases. These secondary components can either condense to existing aerosol particles or form new particles by nucleation processes. Natural precursors for secondary aerosol formation can be various monoterpenes such as alpha-pinene, which mainly originate from forests (McVay et al., 2016). Anthropogenic secondary aerosol components include, for example, nitrates or sulphates, which are produced by biomass burning or fuel combustion (Smith et al., 2011). Another important atmospheric secondary aerosol is sulfuric acid, which is a main player in atmospheric new particle formation and subsequent particle growth (e.g., Kulmala,

2003; Boy et al., 2005). Sulfuric acid aerosol particles are formed from the gas precursor sulfur dioxide ( $SO_2$ ) (Roedel and Wagner, 2011), which can be emitted into the atmosphere by both natural sources (e.g., volcanic eruptions) and anthropogenic sources (e.g., industrial burning).

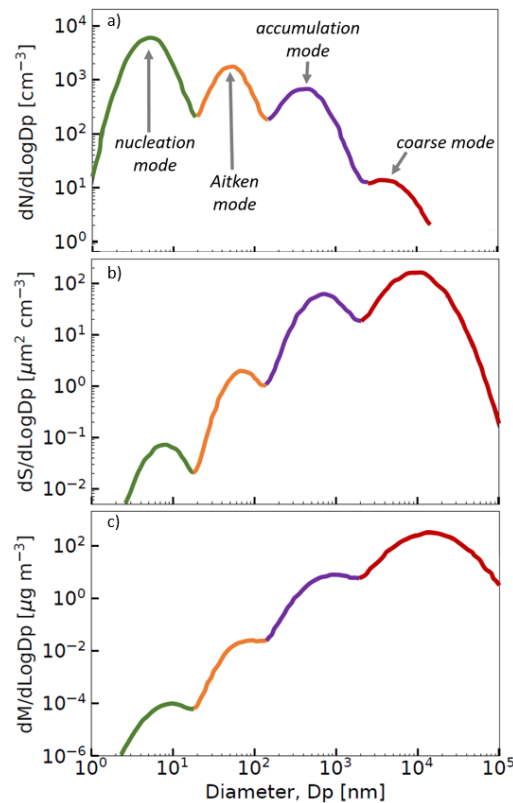


Figure 2.1.: Particle number (panel a), surface (panel b), and mass (panel c) size distribution as a function of the diameter of the aerosol particles  $D_p$  for the four different modes: nucleation mode, Aitken mode, accumulation mode, and coarse mode. Figure adapted from Seinfeld and Pandis (2012).

Due to the different aerosol sources, they can reach diameters  $D_p$  between  $< 10\text{ nm}$  and  $10000\text{ nm}$ . The aerosol size distribution is usually described by a multimodal distribution (Whitby, 1978), which consists of the following modes: nucleation mode ( $D_p < 10\text{ nm}$ ), Aitken mode ( $D_p = 10\text{ nm}$  to  $100\text{ nm}$ ), accumulation mode ( $D_p = 100\text{ nm}$  to  $1000\text{ nm}$ ) and coarse mode ( $D_p = 1000\text{ nm}$  to  $10000\text{ nm}$ ) (Seinfeld and Pandis, 2012; Lohmann et al., 2016). The nucleation mode consists of the smallest particles, which are freshly nucleated aerosol particles. They grow very quickly in size, and thus into the next mode, which is called Aitken mode and includes e.g. soot and sulfuric acid particles. The next larger aerosol particles are categorized in the accumulation mode, which contains e.g. ammonium sulfate particles. The largest aerosols are classified as coarse mode, such as mineral dust or sea salt. Particles larger than  $D_p > 10000\text{ nm}$  are commonly referred to as giant particles, such as pollen, for example. Figure 2.1 shows a schematic of the particle number (panel a), the surface (panel b), and the mass size distribution (panel

c) for the different modes. Particles of the nucleation mode and the Aitken mode usually dominate the number size distribution (panel a) and can be up to several orders of magnitude more frequent compared to larger particles of the other modes, as they stay longer in the atmosphere due to their smaller diameter, and therefore, it takes longer for them to settle out. In contrast, the surface (panel b) and mass (panel c) size distribution is mainly dominated by the particles with larger diameters, namely the accumulation mode and the coarse mode, although they can be significantly smaller in number.

It is important to investigate the abundance of the aerosol particles in the atmosphere in more detail, as they not only have a major impact on air quality (e.g., Silva et al., 2013) but can also influence the weather and climate (e.g., Boucher et al., 2013) in both direct and indirect ways. They have a direct effect by scattering and absorbing the radiation, which is also called aerosol-radiation interaction. Additionally, aerosol particles have an indirect effect on the weather and climate by contributing to cloud formation, and can thus significantly influence their radiative properties (aerosol-cloud interaction). According to the latest report of the IPCC (Forster et al., 2021), the net aerosol effective radiative forcing is negative (Figure 2.2), which results from a combination of the aerosol-radiation interaction and the aerosol-cloud interaction. This is supported by a broad agreement between both observation-based and model-based studies. However, considerable uncertainties remain between the interaction of aerosol effects on MPCs and cirrus clouds, they are indicated in Figure 2.2 by the black bars. This is mainly due to the fact that the formation of clouds consisting of ice is still not fully understood.

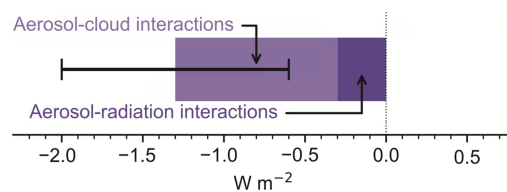


Figure 2.2.: Total aerosol effective radiative forcing from the latest report of the IPCC (Forster et al., 2021).

A rare but important subset of aerosols is called ice-nucleating particles (INPs), which can serve as seeds for the primary formation of ice crystals in clouds (Pruppacher and Klett, 2010). Section 2.2 provides more detailed information about the ice formation in the atmosphere and further information on INPs can be found in section 2.3.

## 2.2. Ice Formation in the Atmosphere

At temperatures below the freezing point ( $< 0^{\circ}\text{C}$ ), a distinction is made between MPCs (coexistence of supercooled water droplets and ice crystals) and cirrus clouds (only ice crystals) (Figure 2.3). Primary ice formation in the atmosphere can occur either by homogeneous freezing at temperatures below  $-38^{\circ}\text{C}$  from the liquid phase or by heterogeneous nucleation from the gas or liquid phase with the help of an INP

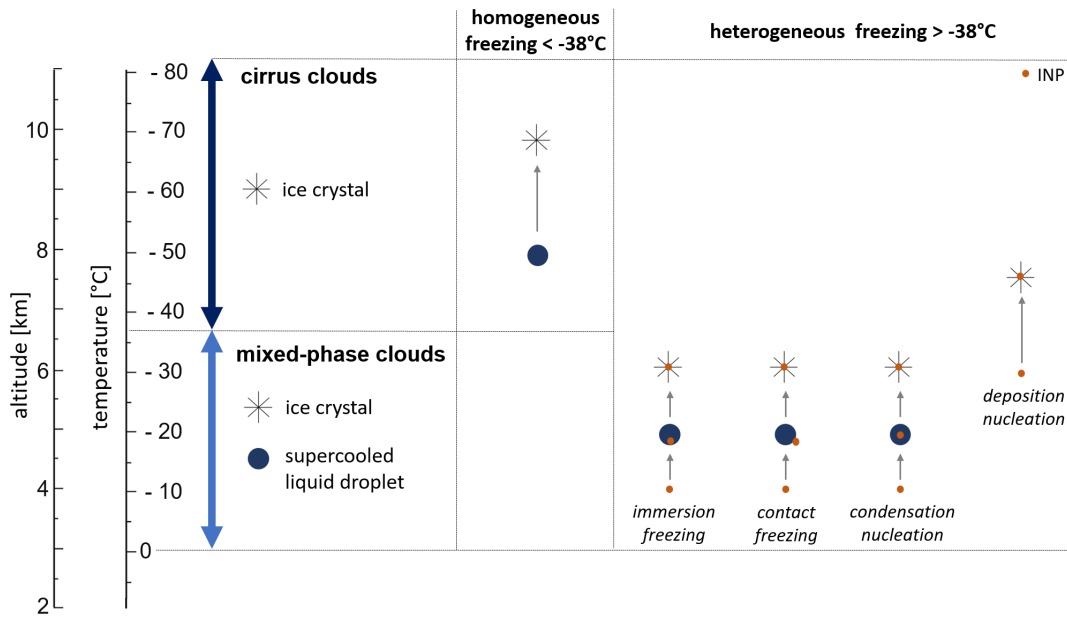


Figure 2.3.: Classification of clouds in the atmosphere depending on the phase of the particles. The middle and right columns illustrate the ice nucleation path of primary ice formation in cirrus clouds and MPCs.

(Pruppacher and Klett, 2010). In the following, the two types of clouds are described in more detail under the following aspects: general information, their effect on the weather and climate, and the different ice formation modes.

### 2.2.1. Cirrus Clouds

Cirrus clouds form at temperatures below  $-38^{\circ}\text{C}$ , the median cloud top varies from 14km in the tropics to 8km at the poles (Sassen et al., 2008), and they have an average global land cover of 22.8 % (Heymsfield et al., 2017). They play an important role in the Earth’s radiative budget, as they can have a warming effect by absorbing and re-emitting the longwave radiation of the Earth, as well as a cooling effect by scattering the incoming solar radiation back to space (Lohmann et al., 2016). Cirrus clouds remain one of the components that are least understood and quantified in the Earth’s radiative budget (e.g., Stevens and Bony, 2013; Bauer et al., 2015; Bickel et al., 2020), as their net radiative effect depends, among other aspects, on factors such as the microphysical properties like number concentration, size, and morphology of the ice crystals (Wolf et al., 2023). The microphysical properties of a cirrus cloud are dependent on the ice formation mechanism, the ice crystals can form either by homogeneous freezing or, if an INP is present, by heterogeneous freezing (Pruppacher and Klett 1997) (Figure 2.3).

In the case of homogeneous freezing, ice crystals only form at high relative humidities ( $S_{ice} > 1.42$ ) through pure water or diluted solution droplets (Koop et al., 2000). A small ice germ is formed by the random collision of multiple water molecules. However, the formation of this small ice germ is initially

kinetically inhibited, as energy has to be generated first to form the interface between the new ice phase and the surrounding liquid phase. This surface energy is greater than the energy gain from the transition of the starting phase to the new ice phase, resulting in a nucleation barrier. The energy that has to be expended to overcome this energy barrier can be derived from the Gibbs free energy ( $\Delta G$ , equation 2.1).

$$\Delta G = \underbrace{-Nk_B T \ln(S_{ice})}_{(1)} + \underbrace{\sigma A}_{(2)} \quad (2.1)$$

$\Delta G$  consists of two terms: (1) the volume term, which is associated with the energy gain from the transition from the starting phase to the new stable phase, and (2) the surface term, which describes the energy required to form the interface between the new phase and the starting phase (Salby, 2012) (Figure 2.4). The volume term depends on the number of molecules in the ice germ  $N$ , the Boltzmann constant  $k_B$ , the temperature  $T$ , and the ice saturation ratio  $S_{ice}$ . The surface term is dependent on the interface energy  $\sigma$  and the germ surface  $A$  ( $A = 4 * \pi * r^2$ ).

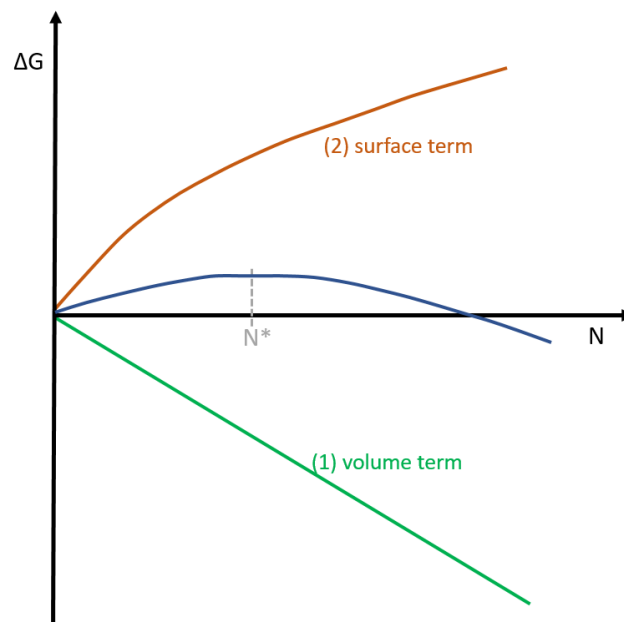


Figure 2.4.: Schematic of the Gibbs free energy  $\Delta G$  as a function of the number of molecules of the ice germ  $N$ . The orange line shows the contribution of the surface term, the green line of the volume term and the blue line shows the resulting trend of  $\Delta G$ .  $N^*$  indicates the critical size of the new ice germ.

As soon as supersaturation with respect to ice is present in the atmosphere,  $S_{ice} > 1$ , the nucleation process can start. Initially, however, the nucleation process is not stable as the surface term dominates until a critical size  $N^*$  of the germ is reached. As soon as  $N^*$  is reached, the volume term is more dominant and the energy gain is greater than the surface term, meaning that the new ice germ is in a stable phase. Now, the ice germ can continue to grow as an ice crystal as long as there is a sufficiently high  $S_{ice}$ . The

higher the supersaturation, the lower the  $N^*$ , and therefore the higher the probability of the formation of a stable ice germ.

Laboratory studies have shown that heterogeneous ice nucleation can already occur at lower  $S_{ice}$  (e.g., Hoose and Möhler, 2012), as the existing INP already provides a surface for the formation of the new ice germ, which reduces the energy barrier (Vali et al., 2015). The heterogeneous ice nucleation in the atmosphere can occur through various pathways, such as immersion freezing, condensation freezing, contact freezing, and deposition nucleation, depending on the temperature and  $S_{ice}$  (e.g., Hoose and Möhler, 2012). At temperatures lower than  $-38^\circ\text{C}$ , the ice crystals can form heterogeneously by deposition nucleation, the other three freezing modes are only relevant for temperatures in MPCs and are therefore explained in more detail in section 2.2.2. The deposition nucleation is the only freezing pathway in which the liquid phase is assumed to not occur. For this, water sub-saturated conditions are required, then the water vapor is deposited directly on the INP to form a critical germ, which can then further grow to form an ice crystal (Vali et al., 2015). Another heterogeneous freezing mechanism which is called pore condensation and freezing may be important for the primary ice formation in cirrus clouds as well (e.g., Marcolli, 2014; Wagner et al., 2015). Here, the water vapor first condenses in the pores of atmospheric aerosol particles at  $S_{ice}$  conditions below liquid water saturation (sub-saturated conditions), and then it freezes at temperatures lower than  $-38^\circ\text{C}$ . It is known that heterogeneous freezing plays a key role at cirrus cloud conditions (Cziczo et al., 2013), but it is still not fully understood whether deposition nucleation or pore condensation and freezing is more relevant (David et al., 2019). In recent years, it has also been discussed that deposition nucleation could occur by pore condensation freezing (Marcolli, 2020).

In general, primary ice formation at cirrus cloud conditions can occur through both homogeneous and heterogeneous freezing in the atmosphere based on the present aerosol population, as shown by field measurements by DeMott et al. (2003b), and later by Cziczo et al. (2013). This was already investigated by numerous theoretical and modeling studies (Haag et al., 2003; Kärcher and Lohmann, 2003; Kärcher and Spichtinger, 2009; Spichtinger and Cziczo, 2010). If sufficient INPs are present in the atmosphere, the ice crystals can form by heterogeneous freezing, during this process, a sufficient amount of water vapor may be removed from the gas-phase which means that the high supersaturation required for homogeneous ice formation might not be reached (e.g., DeMott et al., 1997; Barahona and Nenes, 2009; Krämer et al., 2016). This suppression of the homogeneous ice nucleation can strongly change the microphysical properties of a cirrus cloud (Storelvmo, 2017). If the heterogeneous ice nucleation is predominant, the cirrus cloud consists of fewer but larger ice crystals, therefore the cloud would be optically thinner (Figure 2.5a) (Lohmann and Gasparini, 2017). In cases with a major contribution of homogeneous freezing, the opposite would be true, the cirrus cloud tends to be composed of more and smaller ice crystals, resulting in an optically thicker cloud (Figure 2.5b). Thus, the two cirrus ice formation

mechanisms lead to large differences in the ice crystal size distribution, and therefore the optical properties of the cloud, the sedimentation velocities of the ice crystals, and the cloud lifetime. Despite years of research, the question of which of the two cirrus formation mechanisms dominates in the atmosphere cannot be answered (Storelvmo, 2017).

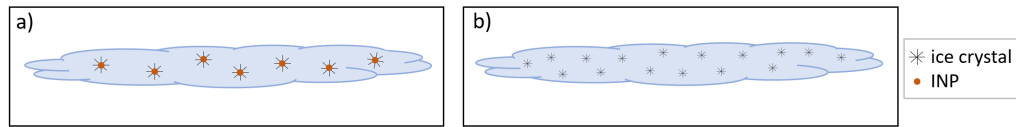


Figure 2.5.: a) Cirrus cloud, which is predominantly formed by heterogeneous ice nucleation, consists of a few large ice crystals. b) In comparison, if homogeneous freezing dominates the ice crystal formation in a cirrus cloud, it consists of many, small ice crystals.

### 2.2.2. Mixed-Phase Clouds

MPCs form in the temperature range between  $0^{\circ}\text{C}$  and  $-38^{\circ}\text{C}$ , they can consist of both ice crystals and supercooled liquid droplets (Figure 2.3). The latter are thermodynamically unstable, therefore, the transition to a more stable state, in this case to ice, can happen promptly (Murray and Sivakumar, 2010). However, they can also remain in this unstable state for hours to days (e.g., Morrison et al., 2012; Kalesse-Los et al., 2016; Pinsky et al., 2018). MPCs have a major influence on the formation of precipitation, especially over continents (e.g., Mülmenstädt et al., 2015; Field and Heymsfield, 2015), as well as the Earth's radiation budget (e.g., Lohmann et al., 2016; Forster et al., 2021). In this temperature range, the ice crystals can only form in the presence of INPs (e.g., Vali et al., 2015). Depending on the temperature and  $S_{ice}$ , the ice formation in MPCs can occur by four different freezing pathways, which are briefly explained in the following (e.g., Pruppacher and Klett, 1997; Cantrell and Heymsfield, 2005; Hoose and Möhler, 2012; Murray et al., 2012; Vali et al., 2015). For immersion freezing, the freezing of a supercooled liquid water droplet is triggered by an INP, which is already immersed in the liquid water droplet before the freezing temperature is reached. During contact freezing, a supercooled liquid water droplet collides with an INP, which initiates the freezing. Condensation nucleation describes the process when water vapor begins to condense on an INP, immediately followed by the freezing of the condensing water and further growth of the resulting ice crystal. Deposition nucleation occurs in the same way as described for cirrus cloud conditions. It is assumed that immersion freezing is the most important heterogeneous freezing pathway for MPCs (Ansmann et al., 2008; de Boer et al., 2011), which has been observed in a large number of studies (Murray et al., 2012). The role of contact freezing in the atmosphere is highly uncertain, as it is limited by the collision rate of particles with supercooled liquid droplets. However, the frequency and efficiency of such collisions in real clouds remain poorly understood (e.g., Ladino Moreno et al., 2013; Nagare et al., 2016). Deposition nucleation is also considered less important for MPC conditions, as lidar measurements have shown that liquid cloud droplets are present before the ice crystals

form by one of the heterogeneous freezing mechanisms (Ansmann et al., 2008; de Boer et al., 2011).

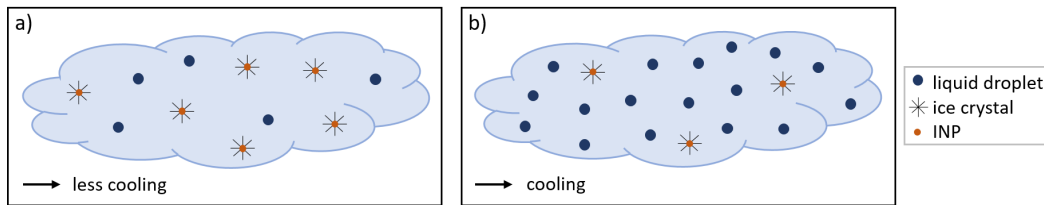


Figure 2.6.: Schematic illustration of the distribution of the liquid and ice phase in MPCs and the effect on the climate when a) many INPs are present or b) fewer INPs are present in the atmosphere.

The presence of INPs can greatly alter the distribution of the liquid and ice phase in MPCs, which in turn affects the radiative properties of the cloud and therefore the climate (e.g., Storelvmo et al., 2011; Storelvmo et al., 2015; Vergara-Temprado et al., 2018b). Liquid droplets are small (about  $10\ \mu\text{m}$ ) and can be assumed to be spherical, whereas ice crystals are about an order of magnitude larger and are usually non-spherical. If there are many INPs in the atmosphere, more ice crystals can nucleate (Figure 2.6a). Once ice has formed in MPCs, a transformation from liquid to ice can occur in the entire MPC temperature range due to the Wegener-Bergeron-Findeisen process (e.g., Korolev, 2007; Korolev and Field, 2008; Storelvmo and Tan, 2015), as the saturation vapor pressure of ice is lower compared to liquid (Murphy and Koop, 2005). This cloud glaciation would reduce the optical thickness of the cloud, as it consists of far fewer particles of larger sizes, and consequently reduce the lifetime and likely produce more precipitation, which in turn would lead to a lower cooling effect (e.g., Storelvmo et al., 2015; Vergara-Temprado et al., 2018b). On the other hand, if there are fewer INPs present, the lifetime of the liquid cloud is extended, and therefore it has a stronger cooling effect on the climate (Figure 2.6b).

Measurements of ice crystal concentration in natural clouds at temperatures above the homogeneous freezing are often orders of magnitude larger than the INP concentration (e.g., Pruppacher and Klett, 1997; Hobbs and Rangno, 1998; Cantrell and Heymsfield, 2005; DeMott et al., 2016). This is because the ice crystals can form not only through the primary ice formation with the help of an INP but also through secondary ice production (SIP) processes (e.g., Cantrell and Heymsfield, 2005; Field et al., 2017). During SIP processes, new ice crystals of preexisting ice are formed without the presence of INPs. Based on a large number of laboratory and field measurements, six different SIP mechanisms have been identified (Korolev and Leisner, 2020), the Hallett-Mossop process was considered for many years to be the main source of secondary ice in clouds (Korolev et al., 2022). This process is also called rime-splintering, and it is active at relatively high temperatures ranging from  $-3\ ^\circ\text{C}$  to  $-8\ ^\circ\text{C}$  (Mossop and Hallett, 1974).

### 2.3. State of the Art of Ice-Nucleating Particles

INPs are a minor subset of aerosol particles in the atmosphere (Rogers, 1993), typical INP concentrations ranging from  $10^{-4} \text{ cm}^{-3}$  to  $10^{-1} \text{ cm}^{-3}$  (e.g., Mason, 1972; Pruppacher and Klett, 1997; Eidhammer et al., 2009; DeMott et al., 2010). Calculations by e.g., DeMott et al. (2010) and Wilson et al. (2015) have shown that the total INP concentration is strongly dependent on the location and the season and is therefore exposed to considerable seasonal and spatial variations. For example, extreme INP concentrations of up to  $1 \text{ cm}^{-3}$  can be reached in desert dust plumes (DeMott et al., 2003a). In addition, the INP concentration is strongly dependent on the temperature, observations have shown that the INP concentration increases with decreasing temperature (e.g., Mason, 1972; Pruppacher and Klett, 1997). Kanji et al. (2017) summarized the INP measurements for a variety of field data from different locations around the world and presented them as a function of  $T$  (Figure 2.7). Here, they made the general observation that there is roughly an exponential increase in the INP concentrations with decreasing temperature, which has already been observed in earlier studies (aufm Kampe and Weickmann, 1951; DeMott et al., 2016).

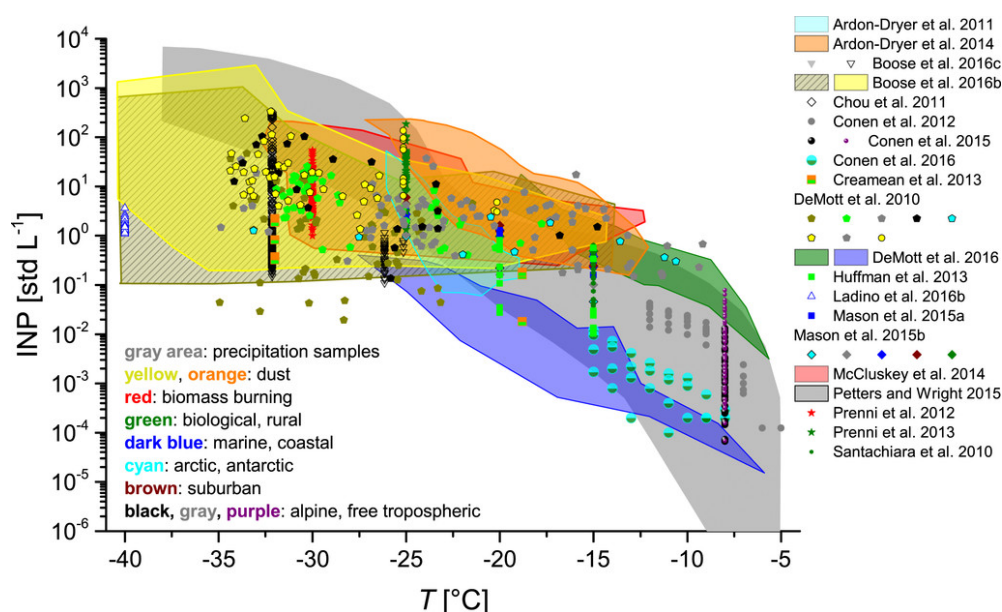


Figure 2.7.: INP concentration versus temperature  $T$  from different field measurements conducted globally. Shaded areas show the air mass type or the sampling location. Figure adapted from Kanji et al. (2017).

INPs have a size ranging from a few nanometers to hundreds of micrometers and their origin can be natural or anthropogenic (Knopf et al., 2018). Despite years of research, it is still not known in detail which properties are required for an aerosol particle to act as an INP (Kanji et al., 2017). Comprehensive measurements and experiments are needed to identify whether a particular aerosol type can act as an effective INP (Murray et al., 2012). However, it is well-known that the surface of the aerosols plays an important role, larger particles are assumed to be more efficient INPs (Connolly et al., 2009). Ice nucle-

ation likely occurs at certain locations, e.g., at lattice mismatches, cracks, or chemical contaminations (e.g., Xue et al., 2019) on the surface of the INP, which reduces the free energy of germ formation (Prupacher and Klett, 2010). As this is a surface-specific characteristic, the probability of the occurrence of such ice-active sites increases with the total available surface area of the aerosol, and thus the probability that the aerosol can act as an INP (e.g., Archuleta et al., 2005; Kanji and Abbatt, 2009; Welti et al., 2009).

Aerosol types that are known to be effective INPs are mineral dust particles and biological particles, which are explained in the following in more detail. Afterwards, the relevance of ice nucleation in the atmosphere is briefly described for a few other selected aerosol types, Figure 2.8 shows an overview.

Mineral dust aerosols consist mainly of eroded crustal rock lifted into the atmosphere by wind and turbulence, therefore their concentrations vary greatly on a spatial and temporal scale. They are not only important on a regional scale, but can also be transported over long distances and distributed globally over large areas (Prospero, 1999; Knippertz and Stuut, 2014; Kok et al., 2023). Thus, they can influence the formation of ice crystals in the atmosphere even far away from their source. Mineral dust particles have a particularly high ice nucleation ability and can already act as INP at high temperatures of  $T < -15^{\circ}\text{C}$  (e.g., Hoose and Möhler, 2012; Murray et al., 2012; Ladino Moreno et al., 2013). Simulations using global climate models have shown that in the temperature range between  $0^{\circ}\text{C}$  and  $-38^{\circ}\text{C}$ , mineral dust particles account for approximately 77% of the active INPs (Hoose et al., 2010). Another model study by Vergara-Temprado et al. (2017) indicates that desert dust dominates the contribution to the INP population over much of the world. Even under cirrus temperature conditions, the investigation of ice residuals showed that dust is one of the most important INP types in the atmosphere (DeMott et al., 2003a; Pratt et al., 2009; Cziczo et al., 2013; Creamean et al., 2013). There are a variety of different minerals in dust particles such as kaolinite, illite, quartz, and feldspar. However, it is not known exactly which properties a dust particle needs to have a high ice nucleating activity, so it varies by several orders of magnitude (e.g., Yakobi-Hancock et al., 2013; Freedman, 2015; Schill et al., 2015). But e.g., Atkinson et al. (2013), Harrison et al. (2016), and Kiselev et al. (2016) have shown in their studies that feldspar particles are one of the most active atmospherically relevant INP minerals. Furthermore, Archuleta et al. (2005), Kanji and Abbatt (2009), and Welti et al. (2009) have found that the ice nucleating activity increases with increasing size of the dust particle (i.e., larger surface area).

Biological particles are e.g., bacteria, fungal spores, pollen, lichens, or marine exudates, which are emitted by biogenic sources such as oceans, vegetation, soils, lakes, and living organisms (Despres et al., 2012). Similar to other aerosol particles, the ice nucleation ability of bio-aerosols depends on the type of the particles. The contribution of biological INPs is often derived indirectly by exposing the samples to heat, and then quantifying the loss of INP activity (Hill et al., 2016). A lot of measurements have shown that many types of bio-aerosols have a high ice nucleation ability in the MPC temperature range, for example, pollen, fungi, or bacteria (e.g., Alpert et al., 2011; Prenni et al., 2013; Hiranuma et al., 2014; Mason et al., 2015; Wex et al., 2015). For example, Pratt et al. (2009), studied ice crystal residuals during

aircraft-based measurements, and they found that 33 % of the particles from the investigated cloud were biological particles, for mineral dust it was 50 %. Although the emission rates of bio-aerosols are orders of magnitude lower than those of dust particles (Despres et al., 2012), some species can already act as INPs at much higher temperatures. For example, various fungi particles have already shown a high ice nucleation ability at temperatures between  $-5^{\circ}\text{C}$  and  $-10^{\circ}\text{C}$ . Furthermore, biological components can be attached to other particles, such as dust, and thus increase the ice nucleation ability at higher temperatures (e.g., Conen et al., 2011; Tobo et al., 2014; O’Sullivan et al., 2014; Augustin-Bauditz et al., 2016; Ladino et al., 2016). Recently, laboratory experiments have shown that even small fragments of biological particles, such as bacteria, fungal spores, and pollen can act as INPs (Pummer et al., 2012; Augustin et al., 2013; Suski et al., 2018).

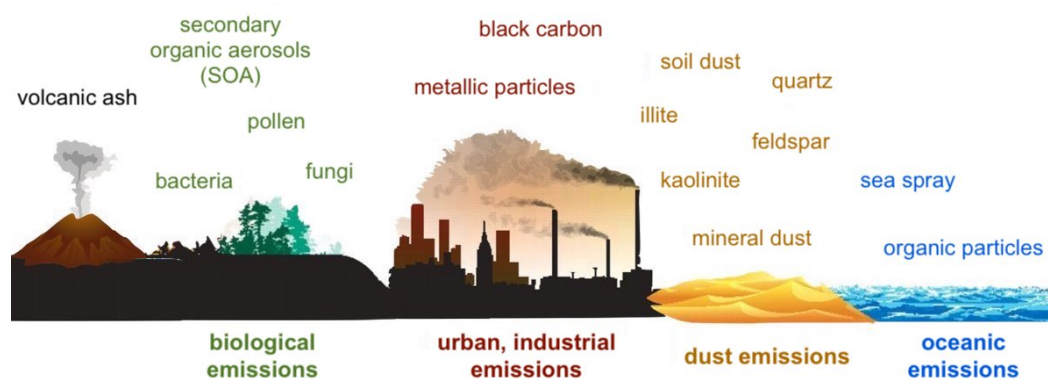


Figure 2.8.: Overview of a few selected aerosol types that can serve as INP. Figure adapted from DeMott et al. (2010) with changes.

Other aerosol types that can serve as INPs are, for example, volcanic ash particles, which could be important INPs at lower temperatures, especially in the absence of other effective INPs (Kanji et al., 2017; Umo et al., 2021). However, volcanic eruptions are very episodic events (Durant et al., 2010) and their aerosol concentrations in the atmosphere are highly variable. Organic particles emitted by marine environments are less effective INPs than dust (DeMott et al., 2016), but they are still important for ice formation, especially in regions in the troposphere where dust is not present. The studies about the ice nucleation ability of secondary organic aerosols (SOA) show partly inconsistent results, some studies observe no heterogeneous freezing under cirrus conditions (e.g., Ladino et al., 2014; Wagner et al., 2017), and others were able to show the opposite (Ignatius et al., 2016; Wolf et al., 2020). However, it should be noted that there are many different SOA systems in the atmosphere, such as alpha-pinene, naphthalene, and longifolene. Sea spray aerosol is a particularly important INP source in marine regions remote from continental aerosol sources, as observed in a variety of measurements (e.g., Burrows et al., 2013; Wilson et al., 2015; Vergara-Temprado et al., 2017; McCluskey et al., 2018). Nevertheless, the ice nucleation activity is two or more orders of magnitude lower than that of mineral dust (DeMott et al., 2016;

Vergara-Temprado et al., 2018b). Soil dust particles emitted from grazed or agricultural lands are also considered effective INPs, comparable to bio-aerosols and feldspar particles (Steinke et al., 2016; Kanji et al., 2017). It is assumed that the high ice nucleation ability is due to internal mixing with biogenic compounds in the particles (O'Sullivan et al., 2014; Tobo et al., 2014). Numerous laboratory studies observed that soil particles with biogenic compounds are more active INPs than inorganic desert dust (e.g., Conen et al., 2011; Steinke et al., 2016; Suski et al., 2018). Metallic particles can also contribute to the formation of ice crystals at cirrus conditions, this was observed by studying ice residues (Cziczo et al., 2009; Cziczo et al., 2013). The efficiency of metal particles to form ice in the atmosphere varies depending on the chemical composition of the particles, e.g. metal oxides (aluminum oxide and iron oxide) can nucleate ice well due to deposition nucleation. Another aerosol from anthropogenic emissions is black carbon, which has only a minor contribution to the ice formation in the MPC temperature range (e.g., Vergara-Temprado et al., 2018a; Kanji et al., 2020; Schill et al., 2020). However, at cirrus temperatures, certain types of black carbon have been found to act as INPs in laboratory studies (e.g., Ullrich et al., 2017; Mahrt et al., 2018). In general, it is very difficult to identify and quantify INPs due to their rarity (DeMott et al., 2011). It is still uncertain which types of aerosol particles dominate the INP population in different atmospheric environments and different temperature regimes in the atmosphere (Kanji et al., 2017).

Over the past decades, a considerable amount of field INP data has been collected, some of them were summarized in the study by Kanji et al. (2017) by presenting the measured INP concentrations as a function of temperature (Figure 2.7). However, these are not long-term measurements due to the lack of automated INP instruments, which have only been developed in recent years (e.g., Bi et al., 2019; Brunner and Kanji, 2021; Möhler et al., 2021). The data in Figure 2.7 were sorted according to their sampling location and air mass type and marked with the corresponding colors. Figure 2.7 shows a wide spread of the measured INP concentration over several orders of magnitude for each individual temperature in the range between  $-5^{\circ}\text{C}$  and  $-40^{\circ}\text{C}$ , regardless of the air mass or the particle composition of the samples. The overview of these INP measurements covers the entire MPC temperature range, but not the cirrus temperature range, as there are only a few measurements of the INP concentration in this regime (Kanji et al., 2017). Additionally, most of the existing INP measurements have been made at ground-based stations (Kanji et al., 2017), with most stations located in the BL. To obtain a better overview of the presence of the INP concentration in all atmospheric layers relevant for cloud formation, measurements at different altitudes and in particular in the FT are also required. Therefore, as part of this PhD thesis, a novel instrument was developed for aircraft-based measurements to investigate the INP concentration in the FT (see chapter 4). Furthermore, this instrument is capable of performing measurements in the whole temperature range down to  $-65^{\circ}\text{C}$ , thus providing important information about the INPs in the whole relevant temperature range for MPC and cirrus clouds. Burrows et al. (2022) highlighted in their study that the scientific understanding of the influence of INPs, and thus their implementation in models,

could be significantly maximized if there were more observational data in the atmosphere with a longer measurement period and greater spatial coverage. To contribute to the long-term measurements of the INP concentration, in order to obtain more information about their diurnal and seasonal variations at a constant location, within this PhD thesis a long-term study was conducted to measure the INP concentration at a high-altitude station (Sonnblick Observatory, 3106 m a.s.l.), which is located in the lower FT (see chapter 5).



### **3. Experimental Methods**

In this work, mobile instruments were used to measure the INP concentration of the ambient air. For that, the online cloud expansion chamber PINE (Portable Ice Nucleation Experiment), the newly developed instrument PINEair, and the offline droplet freezing experiment INSEKT (Ice Nucleation Spectrometer of the Karlsruhe Institute of Technology) were used. To test and validate the new instrument PINEair, additional laboratory measurements were performed with the expansion chamber AIDA and the aerosol chamber APC (Aerosol Preparation and Characterization). This chapter includes a brief description of the setup and working principle of the instruments, as well as a description of the aerosols used for the laboratory validation experiments. A detailed description of the newly developed aircraft-based INP instrument PINEair can be found in chapter 4.

#### **3.1. Online: Cloud Expansion Chamber PINE**

PINE is an online instrument to measure the INP concentration in real-time by first sampling ambient or laboratory-generated aerosols into a cold chamber, and then inducing cloud droplet and ice formation in this air by a rapid decrease in pressure and thus temperature, similar to cloud formation conditions in air parcels rising in the atmosphere. The instrument was developed according to the working principle of the big cloud chamber AIDA, and it is described in detail by Möhler et al. (2021). PINE is mobile, has a high time resolution of approximately 6 min, and can be used for measurements in the laboratory as well as in the field to measure, for example, the short-term variations of the INP concentration. PINE works fully automatic and can be controlled remotely if needed, which makes it suitable for measurements at remote locations over longer periods.

The first version of PINE was developed at the KIT in collaboration with the University of Leeds, and successfully tested in a cold room in January 2016. The first mobile prototype versions "PINE-1A" and "PINE-1B" with their own cooling systems and a chamber volume of about 7 L were developed and characterized during a series of laboratory experiments (Möhler et al., 2021). These versions were further improved, especially with regard to the cooling system as a combination of a vacuum-isolated vessel and a Stirling cooler, resulting in the next versions of PINE, with model numbers "PINEc", "PINE-04-0X", and "PINE-05-0X". They have a chamber volume of 10 L and they are commercially available from Bilfinger Nuclear & Energy Transition GmbH, Würzburg, Germany (Figure 3.1a).

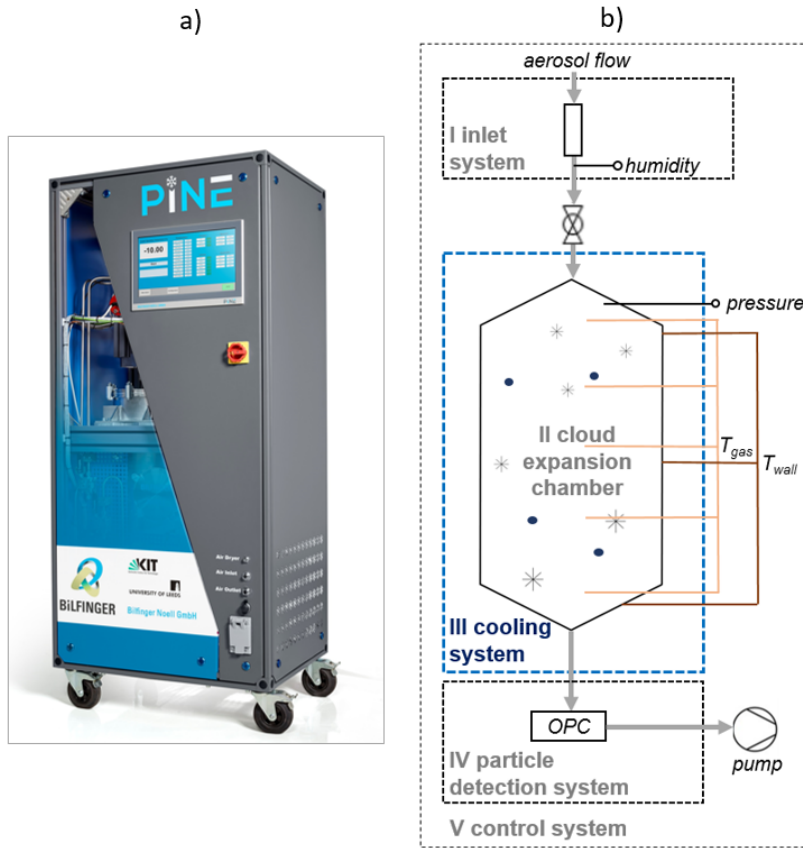


Figure 3.1.: a) Photo of the commercial version of PINE, which is available from Bilfinger Nuclear & Energy Transition GmbH. b) Schematic drawing of the setup of PINE, composed of five major parts: inlet system (I), cloud expansion chamber (II), cooling system (III), particle detection system (IV), and control system (V).

## Setup

PINE is composed of five major parts (Figure 3.1b): an inlet system (I), a cloud expansion chamber (II), a cooling system (III), a particle detection system (IV) and a control system (V). All parts are briefly explained in the following. Since most of the measurements presented in this work were performed with the version "PINE-04-0X", the term PINE in the following always refers to this PINE version.

First, the ambient air flows through the inlet system (part I), which mainly consists of a dual membrane dryer system (Perma Pure, MD-700-24S). It is important to dry the humid ambient air to prevent frost formation on the cold chamber walls and with that an increasing ice background due to frost artifacts. The dew point temperature of the sampled air is measured before it enters the expansion chamber with a dew point sensor (Vaisala, DMT143) located downstream of the dryer system.

The core of PINE is the expansion chamber (part II), where the aerosols are activated to liquid supercooled water droplets or ice crystals. This activation is achieved by a controlled pressure and related temperature decrease, similar to cloud formation occurring in air parcels rising in the atmosphere. The gas temperature  $T_{gas}$  in the expansion chamber is monitored by five temperature sensors, which are ver-

tically distributed inside the chamber (Möhler et al., 2021). The wall temperature  $T_{wall}$  is monitored at three different levels and the pressure in the chamber is measured with a pressure sensor (Thyracont, VSC43MV), which has an uncertainty of  $\pm 0.3\%$ .

The cooling system (part III) of PINE consists of a Stirling cooler (Thales, LPT9310) to operate the expansion chamber between  $0^{\circ}\text{C}$  and a minimum temperature of  $-65^{\circ}\text{C}$ . This allows INP measurements in both the MPC and the lower cirrus cloud temperature range. For thermal insulation, the expansion chamber is located in an evacuated stainless steel vessel, allowing cooling rates of  $0.6^{\circ}\text{C}$  per minute.

An optical particle counter (OPC) (Palas GmbH, fidas-pine) located in the pump tube downstream of the expansion chamber measures all particles that leave the chamber (part IV). The OPC measures the light scattered by single particles in a side-ward scattering direction, where a-spherical particles like ice crystals scatter more light than spherical particles like droplets of the same volume. Therefore, ice crystals can be distinguished from supercooled liquid water droplets due to their larger optical size (Järvinen et al., 2014). Furthermore, the ice crystals formed inside the chamber, also grow to a larger geometric size on the way to the OPC. The OPC detects particles in the entire aerosol flow and is therefore sensitive to low particle number concentrations.

PINE is controlled with a Labview program (part V), which was developed in-house. This allows pre-setting and control of operational parameters such as temperature, pressure, dew point temperature, and flow rates, and records of all important data including detected single particle sizes and number concentrations.

### Working Principle

PINE is operated in a cycled mode with sequences of runs and operations. A run consists of the following three modes: "a) flush", "b) expansion" and "c) refill" (Figure 3.2).

After cooling the expansion chamber to the selected temperature, the measurement cycle starts with the first run. In the flush mode, the valve at the inlet of the expansion chamber is open, allowing the ambient air with the aerosols to flow through the chamber (Figure 3.2a), while the measured  $T_{gas}$  (red dotted line) and pressure  $p$  (black line) inside the chamber remain constant. To replace most of the air inside the chamber with the sampled air at the start of a new measurement cycle, the flush mode typically takes between 4-5 min with a flow between  $1\text{ L min}^{-1}$  and  $2\text{ L min}^{-1}$ . The expansion mode starts by closing the valve in front of the expansion chamber (Figure 3.2b), while the sample flow is bypassed. A controlled pump rate to the chamber with a constant flow between  $2\text{ L min}^{-1}$  and  $5\text{ L min}^{-1}$ , results in a constant pressure decrease rate inside the chamber to a pre-set minimum pressure, which is typically 85 % of the starting pressure. The expansion leads to a decrease in temperature, and consequently to an increase of the relative humidity. As soon as ice or water saturation is exceeded, the aerosol particles in the chamber are activated to form ice crystals and/or liquid supercooled water droplets, depending on the temperature and the type of aerosols. All particles are detected at the outlet of the expansion chamber with the OPC

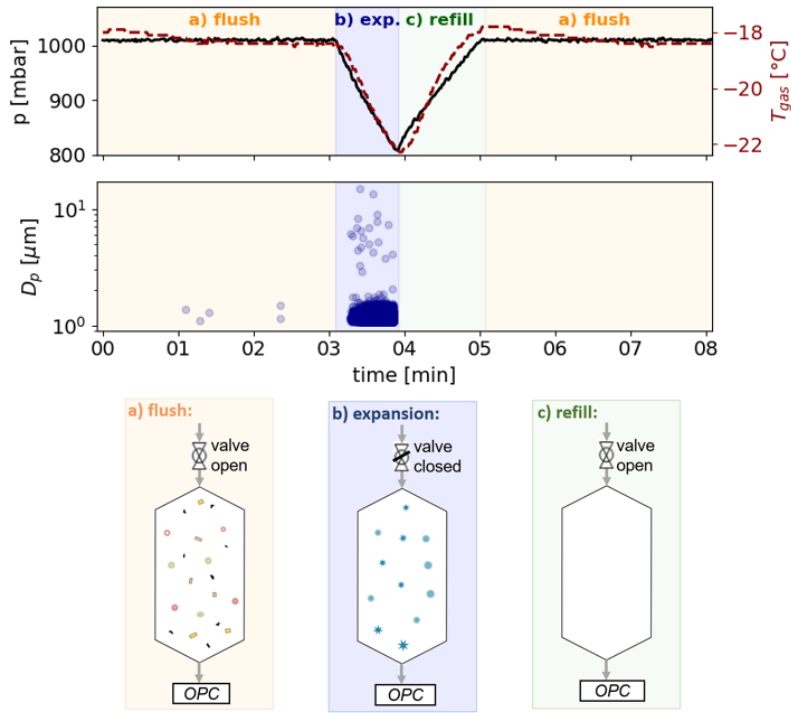


Figure 3.2.: The upper two panels show a typical measurement cycle of a run with PINE, which consists of the three modes "a) flush", "b) expansion" and "c) refill". In the top panel, the pressure  $p$  in the chamber is shown in black, and the measured gas temperature  $T_{gas}$  in red. The bottom panel shows the detected particles with the OPC, where  $D_p$  corresponds to the particle diameter. A schematic illustration of the different modes is shown in the lowest Figure.

and the number of ice crystals corresponds to the number of INPs. The INP concentration  $n_{INP}$  can be calculated using the following equation:

$$n_{INP} = \frac{\Delta N_{ice}}{\Delta V_{exp}} = \frac{\Delta N_{ice}}{\Delta f_{exp} \cdot \Delta t_{exp}} \quad (3.1)$$

Here,  $\Delta N_{ice}$  corresponds to the total number of ice crystals detected during an expansion and  $\Delta V_{exp}$  is the analyzed volume of air, which can be calculated from the flow  $\Delta f_{exp}$  and the duration  $\Delta t_{exp}$  of the expansion. The uncertainty for the measured INP concentration is estimated to  $\pm 20\%$  (Möhler et al., 2021). For the nucleation temperature of the measured INP concentration, an uncertainty of  $\pm 1^\circ\text{C}$  is assumed, which results from the inhomogeneous temperature distribution inside the chamber. In the last mode (refill mode, Figure 3.2c), the valve at the inlet of the expansion chamber is opened again and the chamber is refilled with dry, filtered air to ambient pressure. Then, a new run can start with the same series of flush, expansion, and refill modes. A full run takes about 4 min to 6 min, depending on the settings for the duration of the flush mode, the expansion flow rate, and the end pressure of the expansion.

During longer operation of PINE at low temperatures, frost can form in the chamber if the wall temperature is lower than the dew point temperature of the sampled air. For this reason, background tests are

performed regularly, typically once a day. Therefore the sample flow is passed through a HEPA filter (Whatman, WHA2609T), avoiding new aerosols from the ambient air to flow into the chamber, and a cycle of flush, expansion and refill is started. As soon as no ice particles are detected by the OPC after approximately 2 – 3 runs, this is evidence that no frost has formed on the chamber wall and the detected ice crystals do not originate from frost artifacts from the chamber wall.

The PINE measurements can either be performed at a constant temperature, or with temperature scans. A program with an arbitrary sequence of temperatures with a defined time specification can be programmed, which then runs automatically (as an example see Figure 3.3).

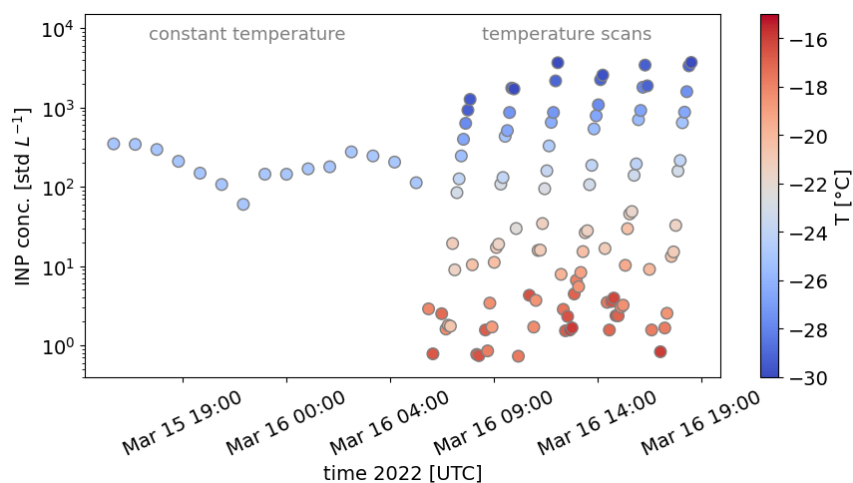


Figure 3.3.: Example of PINE measurements performed at a constant temperature  $T = -23^{\circ}\text{C}$  (on the left, data is averaged for 1 h) and temperature scans from  $-15^{\circ}\text{C}$  to  $-30^{\circ}\text{C}$  (on the right, raw data with a time resolution of 6 min). The INP concentration as a function of time is shown and the different colors indicate the measurement temperature.

### 3.2. Offline: Freezing Experiment INSEKT

INSEKT is an offline INP instrument to investigate the ice nucleation activity of atmospheric or lab-generated aerosols in a wide temperature range from about  $0^{\circ}\text{C}$  to  $-25.5^{\circ}\text{C}$ . For this, aerosols are collected first on filters and examined later offline with INSEKT in immersion freezing mode. INSEKT is based on the Ice Spectrometer (IS) of the Colorado State University (Hill et al., 2016). A detailed description of the working principle as well as the setup of INSEKT can be found in Schneider et al. (2021a).

#### Experimental Setup

The setup for collecting the aerosol particles mainly consists of a filter holder for the nuclepore filter (Whatman, nuclepore track-etched polycarbonate membrane) and a pump to maintain the aerosol sample flow through the filter (Figure 3.4a). A critical orifice is used to achieve a constant sample flow. For

the measurements presented in this work, nuclepore filters with a diameter of 47 mm and a pore diameter of  $0.2\ \mu\text{m}$  were used.

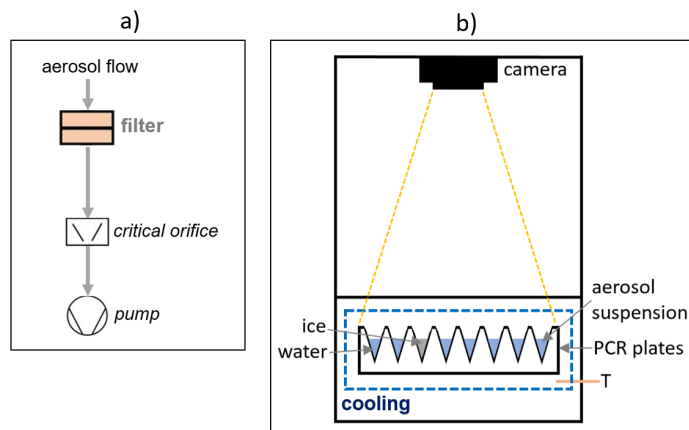


Figure 3.4.: Schematic drawings of the setup for aerosol sampling on filters (a) and the freezing experiment INSEKT (b).

The investigation of the ice nucleation activity of the collected aerosol particles is performed offline in the INSEKT laboratory (Figure 3.4b). The instrument consists of two cooled aluminum blocks that can hold two 96 well PCR plates containing the aerosol suspensions (see next paragraph) to be analyzed. The aluminum blocks are cooled with an ethanol thermostat (LAUDA, Proline 890) at a constant rate controlled with a Labview program. The temperature of the blocks is measured with several temperature sensors located close to the aerosol suspensions in the PCR plates. The temperature uncertainty of INSEKT is about  $\pm 0.3\ \text{K}$  (Schiebel, 2017). A camera located about 82 cm above the PCR plates detects the brightness change that occurs when the water in a dwell freezes. All important information like the cooling rate, the temperature, and the brightness changes are recorded and processed with a Labview software.

### Working Principle

First, the aerosol particles from ambient air or a laboratory experiment are collected on a pre-cleaned filter. For pre-cleaning the filters, a 10%  $\text{H}_2\text{O}_2$  solution is used, and then they are rinsed with deionized water. The sampling duration typically ranges from about one hour at high aerosol or INP concentrations to several days or a week at low concentrations. Accessibility to the sampling site or the occurrence and duration of specific events that impact the abundance and types of INPs may influence the choice of sampling intervals. In the laboratory, a sampling time of about 30 min can already be sufficient. After a certain time, the aerosol-loaded filters are ideally changed in a flowbox to prevent contamination. Afterwards, they are stored in petridishes, wrapped in aluminum foil, frozen, and if possible they are transported frozen to KIT until they are analyzed with INSEKT.

For the analysis, the aerosol-loaded filters are put into a small tube filled with 8 mL of nanopure water. Next, the aerosols are washed off the filters by placing the tubes on a rotator for about 20 min. Subsequently, the aerosol suspension is diluted with 10– and 100–fold volumes of nanopure water, which was passed through a 0.1  $\mu\text{m}$  syringe filter. The different dilutions provide information about the ice nucleation activity of the sampled aerosols over a wider temperature range. Small volumes of 50  $\mu\text{L}$  of the aerosol suspensions are pipetted into two 96 well PCR plates which are then inserted into the aluminum blocks of the INSEKT setup (see paragraph "Experimental Setup"). Some of the wells are filled with the nanopure water used to create the suspension (without aerosols) to serve as a freezing reference (background measurement). The actual experiment starts by cooling the PCR plates with a constant cooling rate of usually  $0.33\text{ }^{\circ}\text{C min}^{-1}$ . If the water in the wells freezes its brightness decreases, which is detected by the camera. The Labview program stores the temperature at the time of the freezing event. Based on that, the INP concentration  $n_{INP,INSEKT}$  per standard liter of the sampled air is calculated in  $0.5\text{ }^{\circ}\text{C}$  steps according to the equations from Vali (1971):

$$n_{INP,INSEKT} = -\frac{\eta}{V_{dwell}} \frac{V_{wash}}{V_{air}} \ln \left( \frac{N_u(T)}{N_{all} - \left( N_{f,bgr} \frac{N_{all}}{N_{bgr}} \right)} \right) \quad (3.2)$$

Here  $\eta$  is the dilution,  $V_{dwell}$  the volume of the suspension in one dwell,  $V_{wash}$  is the volume of water used to suspend the aerosol particles and  $V_{air}$  corresponds to the volume of the sampled air.  $N_u$  stands for the number of unfrozen samples,  $N_{all}$  means the number of all samples,  $N_{bgr}$  is the number of all samples used for the background measurement and  $N_{f,bgr}$  is the number of the frozen samples.

Throughout the whole analysis with INSEKT, careful and clean work is needed to prevent contamination. Therefore, cleaned tweezers and disinfected latex gloves are used (Barry et al., 2021), and all filter preparation and handling procedures are performed in a clean flow box. To check the cleanliness of the handling, blank filters are taken regularly during a measurement campaign, and for this purpose, no air is sampled through the filters. The blank filters are analyzed in the same way with INSEKT as described above to determine the background spectra, which can then be subtracted from the measured INP concentration if required.

To obtain information about the content of heat-sensitive INPs (e.g., Hill et al., 2016; Wilson et al., 2015; O’Sullivan et al., 2018), the aerosol samples can be additionally analyzed with a heat treatment, to denature proteinaceous INPs. For this, the aerosol suspensions are boiled at a temperature of about  $100\text{ }^{\circ}\text{C}$  for about 20 min and then analyzed in the same way with INSEKT as the unheated suspensions to investigate any changes in the INP content of the aerosol filter samples. The amount of heat-sensitive INPs is obtained from the INP concentration difference before and after the heat treatment.

### 3.3. Expansion Chamber AIDA

The simulation chamber AIDA is used to study cloud formation under atmospherically relevant conditions by simulating cloud-forming conditions in a rising air parcel. It is not only suitable for the investigation of aerosol-cloud interactions or ice nucleation processes at different temperatures but also for testing and characterizing newly developed instruments for ice nucleation research or INP measurements. A detailed description of AIDA can be found in e.g. Möhler et al. (2003), Möhler et al. (2006), and Wagner et al. (2006). In this work, AIDA was used to test the novel PINEair instrument, for instance by serving as a reservoir for a constant aerosol source or by simulating atmospheric pressure conditions that are representative for measurements with PINEair during research aircraft flights.

#### Setup

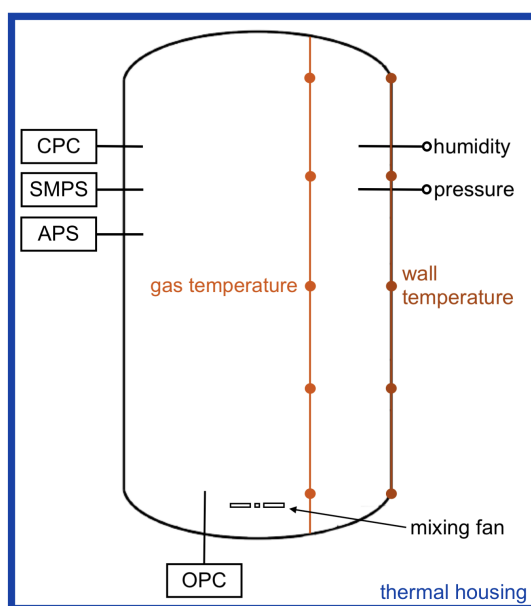


Figure 3.5.: Schematic drawing of the setup of the expansion chamber AIDA, including the most important instruments used in this study.

AIDA consists of a cylindrical aluminum vessel with a diameter of 4 m, a height of 7 m, a volume of  $84\text{ m}^3$ , and is located inside a thermal housing (Möhler et al., 2003). The air temperature in the housing can be controlled between  $60^\circ\text{C}$  and  $-90^\circ\text{C}$ , using either large refrigeration systems or the evaporation of liquid nitrogen. A mixing fan, located in the bottom part of the cylindrical chamber about 1 m above the floor, ensures a homogeneous temperature and aerosol distribution. The expansion system consists of two adjustable, mechanical pumps and allows the evacuation of the chamber from atmospheric pressure

to a minimum pressure of 0.01 mbar. The controlled expansion can be used to simulate the rise of an air parcel. A Labview program is used to control and monitor the entire experiment. The AIDA chamber is equipped with a variety of measuring instruments that monitor the conditions inside the chamber during the experiments and the formation of the simulated cloud. Like the measurements of the temperature, pressure, humidity, the aerosol properties such as number concentration (CPC: Condensation Particle Counter (TSI, 3010)) and size distribution (SMPS: Scanning Mobility Particle Sizer (TSI, 3071) and APS: Aerodynamic Particle Sizer (TSI, 3221)) (Figure 3.5). Since AIDA was used in this work only for testing purposes of the newly developed PINEair instrument, the comprehensive instrumentation is not discussed in more detail here, more information can be found in e.g. Möhler et al. (2003). The size and number concentration of liquid supercooled water droplets and ice crystals are measured with two welas systems (Weißlichtaerosolspektrometer, Palas GmbH welas2300 and welas2500) located at vertical sampling tubes below the chamber.

#### **Working Principle**

At the beginning of an expansion experiment for ice nucleation study, the AIDA chamber is cooled to a specific temperature below 0°C, and almost ice-saturated conditions are maintained by a thin layer of ice on the cold chamber walls. Subsequently, the aerosols to be investigated are injected into the AIDA chamber and their number concentration and size distribution are analyzed with a CPC, SMPS, and APS. The generation and the injection of aerosols into the AIDA chamber are described in more detail in section 3.5. Mobile instruments such as PINE or INSEKT can sample the aerosols from the AIDA chamber to study their ice nucleation ability.

The actual AIDA cloud formation experiment starts with the expansion by taking the air out of the AIDA chamber through the pumping system. Due to the pressure drop, an expansion occurs and the gas temperature also decreases, which causes the relative humidity with respect to water and ice to increase. During the expansion, the wall temperature remains constant due to the high heat capacity of the aluminum walls. This creates a heat flux from the wall to the gas which reduces the cooling rate and therefore an increasing deviation from the adiabatic temperature profile. As soon as a critical supersaturation is reached, the droplet or ice crystal formation starts, which is observable with the welas instruments. The INP concentration is then calculated from the number of ice crystals detected in a specific time interval. The expansion ends when reaching a pre-defined final pressure (usually approximately 800 mbar at a start pressure of 1000 mbar).

To simulate the atmospheric conditions of an aircraft measurement campaign, the start pressure in AIDA can be reduced to an arbitrarily low pressure value, like for example 250 mbar. Starting from this initial pressure, the AIDA experiment is performed in the same way as described above.

### 3.4. Aerosol Chamber APC

The APC chamber is a 3.7 m<sup>3</sup>- sized stainless steel vessel (Möhler et al., 2008), which is used in this work as a constant aerosol source for testing the newly developed PINEair instrument. The chamber can only be operated at ambient temperatures, and it can be evacuated to a minimum pressure of approximately 1 mbar. The aerosol number concentration is measured with a CPC (TSI, 3772), and the aerosol size distribution with a SMPS (TSI, 3071) and an APS (TSI, 3221). The air in the APC chamber consists of synthetic air, which is particle-free and very dry. However, for testing the aerosols for their ice nucleation ability, the sample air with the aerosols from the APC chamber already has to have a certain starting humidity to achieve sufficiently high saturation for the formation of ice crystals in the PINEair instrument during expansion. To increase the humidity of the air in the APC chamber, it is evacuated to approximately 930 mbar, and then slowly filled with the humid air from the laboratory through a HEPA filter (Whatman, WHA2609T) until atmospheric pressure is reached. The humidity of the air in the APC chamber is measured with the dew point sensor at PINEair for the measurements discussed in this work. After filling the APC chamber with humid and particle-free air, the aerosols to be investigated are injected. A homogeneous distribution of the aerosols within the chamber is achieved with a mixing fan.

### 3.5. Generation and Injection of Aerosols

Table 3.1 gives an overview of which types of aerosol particles were used in this work for the laboratory experiments with the AIDA and the APC chamber. In the following, the generation of the aerosol particles and their injection into the respective chamber is briefly explained.

Table 3.1.: Overview of the used aerosols, their generation and purpose for testing the new PINEair instrument.

aerosols	generation	purpose
ATD	sold commercially	heterogeneous freezing (MPC and cirrus temperature range)
SDSA01	purchased	heterogeneous freezing (MPC and cirrus temperature range)
sulfuric acid ( $H_2SO_4$ )	home-built sulfuric acid generator	homogeneous freezing (cirrus temperature range)
ammonium sulfate	dispersion of ammonium sulfate solution with ultrasonic nebulizer	homogeneous freezing (cirrus temperature range)

To test the new instrument PINEair for the detection of INPs in the immersion freezing and deposition nucleation modes, two different dust samples, ATD (Arizona Test Dust) and SDSA01 (Soil Dust South Africa), were used. Both are known to be ice-active in the MPC regime, as well as in the lower cirrus temperature range. ATD contains natural dust particles and it is often used as a reference aerosol as it is

sold commercially in large amounts by Powder Technology Inc. SDSA01 samples are collected directly from the soil surface and originate from a desert region in South Africa (Succulent Karoo biome near Soebatsfontein). The injection of the dust samples into the AIDA or APC chamber is performed by using a rotating brush generator (RBG 1000, Palas GmbH). For this purpose, the dust sample is first filled into a piston, which is inserted into the instrument and slowly moved upwards. Inside the instrument is a rotating brush that picks up the aerosols from the piston and passes them into an air stream which passes the aerosol particles directly into the appropriate chamber.

Sulfuric acid and ammonium sulfate aerosols were used to test PINEair for detecting homogeneous freezing of soluble aerosol particles. The sulfuric acid particles are generated with a home-built sulfuric acid generator. To do this, concentrated sulfuric acid is filled into a small glass container and heated to over 100°C by a heating element. Thus, sulfuric acid vapor is produced, which is passed by a flow of synthetic air into a tube system, where it cools to room temperature. As a result of cooling, the sulfuric acid vapor nucleates to liquid sulfuric acid droplets (phase changes from gaseous to liquid), which are then passed through another tubing system into the appropriate chamber. For the generation of ammonium sulfate particles, an ammonium sulfate solution consisting of 0.1 wt% - 1 wt% ammonium sulfate and ultra-pure water is first prepared. The solution is dispersed with an ultrasonic nebulizer (GA 2400, SinapTec) to form droplets, which are subsequently dried with a dryer. Finally, the solid ammonium sulfate particles are injected into the corresponding chamber.



## 4. Development and Application of the New Aircraft-Based Expansion Chamber PINEair

The PINEair instrument developed as part of this PhD thesis is designed to measure INP concentrations onboard the German research aircraft HALO to a minimum temperature of  $-65^{\circ}\text{C}$ . At present, there is no aircraft-based instrument available that can measure INPs at temperatures lower than  $-40^{\circ}\text{C}$ . Section 4.1 gives a short introduction to existing aircraft-based methods measuring the INP concentration in the FT. Section 4.2 describes in detail the setup and working principle of the newly developed instrument. The following sections present the first measurements with PINEair and demonstrate its performance to successfully measure the INP concentration in both the MPC and the cirrus temperature range. Section 4.3 includes an overview of the laboratory measurements at AIDA and the APC chamber, section 4.4 describes the results from test measurements by sampling ambient air at the institute on Campus North of KIT. Section 4.5 presents and discusses the results from the first field campaign with PINEair at the Sonnblick Observatory in Austria.

### 4.1. Introduction

To date, most INP measurements have been performed in the BL at ground-based stations in the MPC temperature regime (Kanji et al., 2017, see section 2.3). These measurements provide important information on the nature and sources of INPs, as well as their role for primary ice formation in MPCs. However, further measurements on the spatial and temporal distribution of INPs are needed to assess their influence on cloud ice formation. INP concentration data from the FT are sparse, as they are much more difficult to obtain, but they are needed to address some of the open questions like the vertical distribution of the INP concentration or the influence of INPs on cirrus cloud formation (e.g., Coluzza et al., 2017). Measurements in the FT can either be performed with research aircraft or at stations which are located in the FT due to their altitude. INP measurements in the FT in the MPC temperature range were conducted at high-altitude stations like the Jungfrauoch (JFJ) station (3580 m a.s.l.) in Switzerland (Boose et al., 2016b; Lacher et al., 2018a; Lacher et al., 2018b; Brunner et al., 2022), the Sonnblick Observatory (3106 m a.s.l.) in Austria (Bogert et al., 2024 submitted to the journal BAMS, see chapter 5), the Izaña Atmospheric Observatory (2373 m a.s.l.) on Tenerife (Boose et al., 2016a), the Pico Mountain Observatory (2225 m a.s.l.) at the Azores Islands (China et al., 2017) and the Whistler Mountain air chemistry Observatory (2182 m a.s.l.) in Canada (Mason et al., 2016). At cirrus temperatures down to  $-60^{\circ}\text{C}$  only a few INP measurements have been performed in the FT, like the study by DeMott et al. (2003a) and

Richardson et al. (2007) with a CFDC at the Storm Peak Laboratory on Mt. Werner (3200 m a.s.l.) in western Colorado.

Another possibility to investigate the INP concentration in the lower FT is, for example, by using tethered balloons, which, compared to the stationary stations, also allow for sampling the aerosols at different heights (e.g., Creamean et al., 2018; Porter et al., 2020). However, the payload weight is often limited to a few kilograms, limiting the sample equipment. The same applies to small unmanned aerial vehicles (UAVs), which can e.g. be equipped with a sampling system for the collection of aerosol particles (Schrod et al., 2017; Jimenez-Sanchez et al., 2018; Bieber et al., 2020). Both, tethered balloons and UAVs can only be operated in the lower troposphere to a maximum height of a few kilometers. INPs at higher altitudes can be measured with aircraft-based methods. To date, this is achieved either with offline methods using filter sampling systems onboard the aircraft or with an online CFDC instrument. Both methods are briefly described in the following paragraphs.

The method of aerosol sampling onboard a research aircraft and the subsequent offline analysis of the sampled aerosol particles for their INP content has been used in a number of campaigns, e.g., Bigg (1967), Flyger et al. (1973), DeMott et al. (2016), Price et al. (2018), Levin et al. (2019), Sanchez-Marroquin et al. (2020), Varble et al. (2021), Knopf et al. (2023). Recently, a new automated High-volume flow aERosol particle filter sAmpler (HERA) was developed specifically for aircraft applications (Grawe et al., 2023). Here, the filters can be changed automatically during the flight, thus no operator is needed on board. The advantage of aerosol particle filter sampling, compared to online instruments, is that their design is comparatively small and light. With the filter sampling method, the INP concentration can be analyzed in the temperature range between 0°C and -30°C or down to -37°C, when nanoliter-sized droplets are used (Grawe et al., 2023).

The only online aircraft-based INP instrument is the CFDC described by Rogers et al. (2001b), which is a re-built of the laboratory instrument of the CSU (Colorado State University) CFDC (Rogers, 1988; Rogers, 1994). The aircraft-based instrument can be operated in the temperature range between -10°C and -40°C, and has been used in numerous aircraft measurement campaigns, e.g. Rogers et al. (2001a), DeMott et al. (2003a), Prenni et al. (2007), Levin et al. (2019), Barry et al. (2021). Online methods have the advantage of a higher time resolution compared to offline methods based on aerosol filter samples.

However, at present, there is no aircraft-based INP instrument that can measure the INP concentration in the FT at temperatures below -40°C. Information about the INP concentration in this temperature range is required to improve the knowledge about ice crystal formation processes in cirrus clouds, e.g., whether heterogeneous or homogeneous freezing is more dominant for the formation of cirrus clouds (Storelvmo, 2017). This information is crucial because it can significantly change the prediction of the microphysical properties of a cloud and thus the radiation balance (Boucher et al., 2013). Previous findings on homogeneous or heterogeneous freezing in cirrus clouds were derived from direct measurements of ice particle size and ice particle number concentration from cloud combination probes (e.g., Krämer et al., 2009;

Groß et al., 2023) or ice residual measurements with aircraft-based single particle mass spectrometers (Cziczo et al., 2004; Cziczo et al., 2013). PINEair was developed as an aircraft-based instrument for online INP measurements in the FT at low cirrus formation temperatures. It is well suited for aircraft measurements due to its high time resolution, automated measurement, and wide temperature range for both MPC and cirrus measurements.

## 4.2. General Information

The following section provides general information about the newly developed INP instrument PINEair. Section 4.2.1 first describes the setup of PINEair, and section 4.2.2 presents the working principle. Finally, section 4.2.3 provides an overview of the development of the three different versions of PINEair and their differences.

### 4.2.1. Setup of PINEair

PINEair is based on the PINE instrument (Möhler et al., 2021) and was specially designed to measure the INP concentration in the FT onboard research aircraft. It can perform measurements in the temperature range from 0°C to –65°C in the MPC and cirrus temperature range. During the development of PINEair, different versions were built, which are cooled by different methods, for more information see section 4.2.3. One major goal for the development of PINEair was a high time resolution, to also achieve a high spatial resolution in a fast-flying jet aircraft. To increase the time resolution of PINEair compared to PINE, it consists of three expansion chambers, each with a chamber volume of 3 L. This triples the time resolution of the INP measurements to approximately 2.5 min – 5 min, depending on the measurement temperature, which is described in more detail in section 4.2.2. PINE consists of only one expansion chamber with a larger volume of 10 L (section 3.1), with a time resolution of about 6 min.

The overall setup of PINEair is similar to PINE and is briefly explained in the following (Figure 4.1). The inlet of PINEair is equipped with a membrane dryer system (Perma Pure, MD-700-24S), which consists of several drying tubes. The drying tubes reduce the humidity of the sampled air and thus prevent ice or frost formation on the cold chamber walls. The humidity of the sampled air is measured with a dew point sensor (Vaisala, DMT143). Similar to PINE, PINEair has the option of conducting a background test for which the flow is guided over a HEPA filter (Whatman, WHA2609T), to check for artifacts e.g. due to frost on the cold chamber wall. A valve is located at the inlet of each chamber which is used to switch between the flush, expansion, and refill modes of a run (more information about the different modes can be found in section 4.2.2). PINEair consists of three small expansion chambers, each of them has its own inlet, outlet, and OPC (Palas GmbH, fidas-pine), which detects the particles at the outlet of the respective chamber (Figure 4.2). Based on their optical size, aerosol particles, droplets, and ice crystals can be distinguished from each other. The gas and the wall temperature are measured individually in

#### 4. Development and Application of the New Aircraft-Based Expansion Chamber PINEair

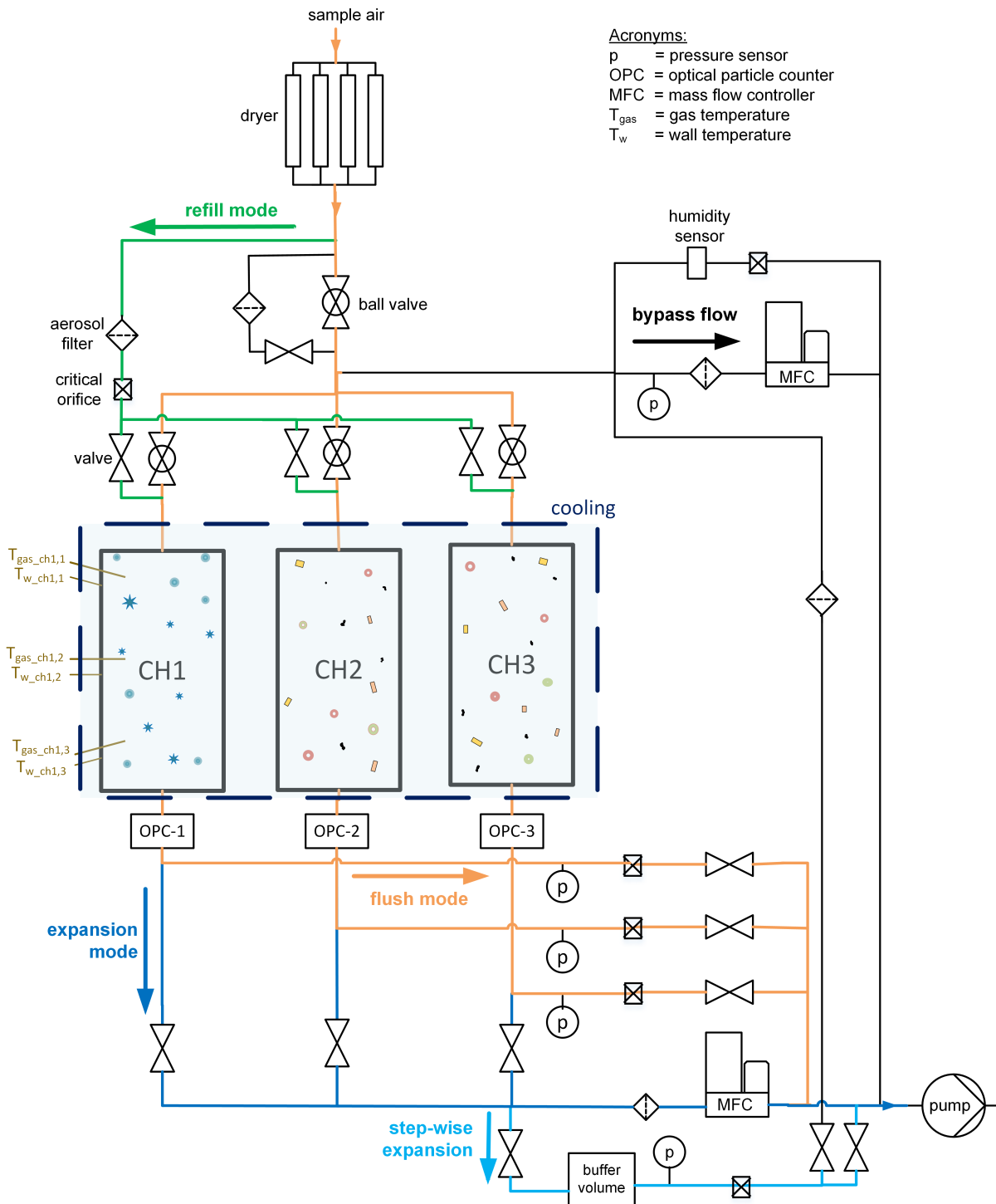


Figure 4.1.: Schematic setup of PINEair with the three chambers (CH1, CH2, CH3) including the main components of the instrument. The different colors show the flow of the sampling gas for the different run modes: flush (orange), expansion (dark blue) or step-wise expansion (light blue), refill (green), and bypass (black).

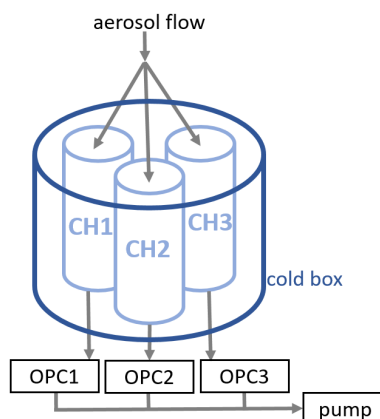


Figure 4.2.: Simplified schematic drawing of PINEair's three chambers, which are cooled and each has its own inlet, outlet, and OPC. The gray arrows show the orientation of the aerosol flow.

each chamber with three temperature sensors, which are distributed vertically: one sensor at the top near the inlet, one in the middle, and one near the outlet of the chamber. All of them were calibrated with two reference sensors in an ethanol bath in the temperature range from  $20^{\circ}\text{C}$  to  $-60^{\circ}\text{C}$ . The calibration result is considered in the analysis of the data. The pressure of each expansion chamber is measured with a pressure sensor (Thyracont, VSC43MV). Compared to PINE, PINEair has an additional small vessel with a volume of 2L, which is used as a buffer volume for a step-wise expansion (Figure 4.1 bottom right). The principle of a step-wise expansion is new for the PINEair instrument and it is used to achieve an almost adiabatic temperature decrease during the expansion in order to calculate the peak supersaturation with respect to ice inside the chamber. It is especially used for the measurements at cirrus conditions, and the procedure is explained in more detail in section 4.2.2. A Labview program was developed to control PINEair, to set the conditions for the measurements, and to store all operation parameters such as temperature, pressure, and flow. PINEair can perform INP measurements fully automatically over a longer period of time and if needed, it can be controlled remotely.

#### 4.2.2. Working Principle

The working principle of PINEair is similar to the one of PINE (compare to section 3.1). The instrument is also operated with a series of runs. Each run consists of the three modes "flush", "expansion" and "refill". Since PINEair consists of three chambers, a complete run (flush, expansion, refill) is performed consecutively by each chamber, which is called a run cycle. As soon as a run cycle has finished, the second run cycle begins and the sequence of three runs per chamber starts again from the beginning. The advantage of PINEair is the fact that expansions can be performed sequentially with the three chambers, therefore measurements with a higher time resolution are possible, while the flush time for each chamber is still long enough to exchange the aerosol content.

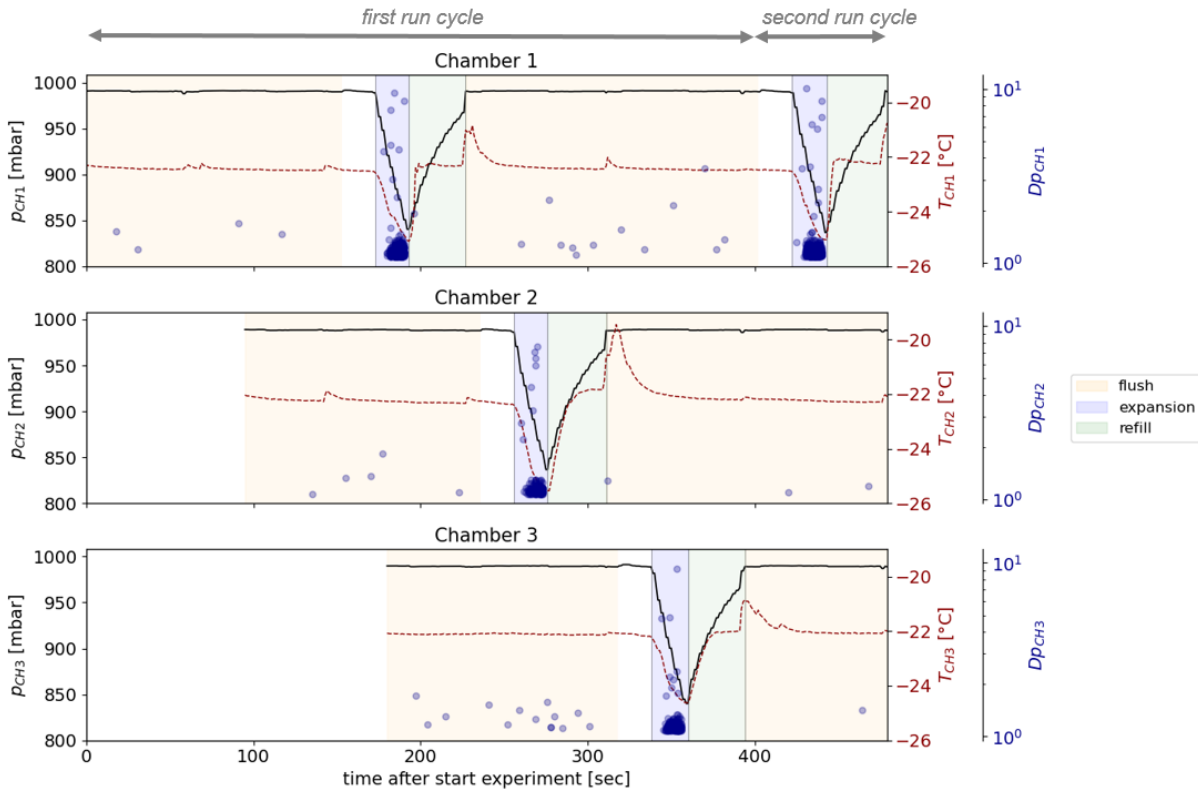


Figure 4.3.: Sequence of a complete run cycle in PINEair with the different modes: flush (orange shading), expansion (blue shading), and refill (green shading). The white shading shows the waiting time before the start of the expansion. The upper, middle, and lower panel show data of chamber 1, 2, and 3, respectively. The black thick line shows the measured pressure  $p$  in the respective chamber, and the red dashed line represents the measured gas temperature  $T$  of the lowest thermocouple. Blue circles correspond to the particles measured with the OPC, where the optical particle diameters  $D_p$  are shown. As soon as each chamber has completed a full run, a new run cycle can begin with chamber 1.

Figure 4.3 shows a complete run cycle at MPC temperature conditions, the black line represents the chamber pressure  $p$ , the red dotted line the temperature  $T$  of the lowest thermocouple, and the blue circles the optical diameter  $D_p$  of the detected particles. The upper, middle, and lower panels show data of chamber 1, 2, and 3, respectively. As soon as the cooling system reaches the desired temperature, the first run cycle begins. At the beginning, all chambers are in the flush mode, all three valves at the inlet of the respective chambers are open and the aerosols are sampled into the chambers from the ambient air or an aerosol reservoir. For the measurements described in this work, a flow of  $1.3 \text{ L min}^{-1}$  was used during the flush mode of each chamber, which is controlled with a critical orifice. To reduce the inhomogeneous vertical temperature distribution within the chamber, a "waiting time" is used for the PINEair measurements before the start of an expansion. During this process, all valves at the inlet and outlet of the expansion chamber are closed for a predefined time, so the temperature and relative humidity conditions can reach equilibrium and become more homogeneous inside the chamber. The waiting time is relevant for the entire temperature range (MPC and cirrus) and is explained in more detail in

section 4.4.1. Next, chamber 1 starts with the expansion, while chamber 2 and chamber 3 remain in the flush mode. In contrast to PINE, two different types of expansion can be performed depending on the measurement temperature. This involves a (continuous) expansion, mostly used at the higher temperatures at MPC conditions, and a step-wise expansion with the buffer volume, preferentially used at cirrus temperature conditions. The expansion type can be set independently for the three chambers, and they are both described in more detail below.

For all measurements in the temperature range PINEair can be operated, the number of heterogeneously formed ice crystals corresponds to the number of INPs, and the INP number concentration is calculated using the same equation as for PINE (equation 3.1, section 3.1). The uncertainty for the measured INP concentration is estimated to  $\pm 20\%$ , similar to PINE. For measurements at MPC temperatures, the detection limit of the INP concentration for one expansion is  $1 \text{ L}^{-1}$ , at cirrus temperatures it is  $0.7 \text{ L}^{-1}$ .

The expansion of chamber 1 is finished as soon as the previously set time is reached. Next, chamber 1 is refilled with filtered, dry air until the ambient pressure is reached (refill mode). Afterwards, chamber 1 switches to the flush mode by opening the valve in front of the inlet and sampling new aerosols into the chamber. In the meantime, chamber 2 and chamber 3 remain in the flush mode. As soon as chamber 2 and chamber 3 have also finished a complete run, the first run cycle is over. The second run cycle begins by chamber 1 starts again with a new run. The duration of one run cycle depends on the temperature range of the measurements (as the different types of expansion require different durations), the humidity of the ambient air, and the number of chambers used and it takes between approximately 2.5 min and 5 min.

#### **Measurements at MPC Conditions:**

The (continuous) expansion is performed for measurements in the MPC temperature range and is similar to the expansion with PINE. For this purpose, the valve at the inlet of one chamber is closed, and after a pre-defined waiting time, the air is pumped out of the chamber which reduces the pressure, leading to a decrease in temperature, and an increase in the relative humidity. For measurements in the MPC temperature range above approximately  $-38^\circ\text{C}$ , an expansion flow of  $1.7 \text{ L min}^{-1}$  is typically used. As soon as supersaturation with respect to ice or water is reached, ice crystals and liquid supercooled water droplets can form, which are detected at the outlet of the chamber with the OPC. In the MPC temperature range, the particles can be classified into aerosols, liquid supercooled water droplets, and ice crystals, based on their different sizes, shape, and asphericity. The minimum temperature for each (continuous) expansion corresponds to the lowest measured temperature.

#### **Measurements at Cirrus Conditions:**

The temperature decrease during the (continuous) expansion in PINEair at MPC conditions deviates from the adiabatic temperature profile, as the heat flux from the chamber walls has an influence on the gas temperature. Only the humidity of the sampled air is measured, but not the establishing relative humidity

inside the chamber during expansion. Especially for measurements in the cirrus temperature range, it is important to know the ice saturation ratio in the chamber, to be able to better distinguish between homogeneous and heterogeneous ice nucleation and to measure the INP concentration as a function of the ice saturation ratio. For this reason, a step-wise expansion with an additional buffer volume can optionally be performed with PINEair, instead of the (continuous) expansion. By that, the established relative humidity follows an almost adiabatic temperature decrease. Before the step-wise expansion starts, the pressure in the buffer volume is set to a pre-defined value below the ambient pressure  $p_{ambient}$ . For example, a step-wise expansion is started in a chamber by opening the valve between the chamber and the buffer volume, while the main valve of the chamber is closed. This causes a sudden pressure drop to a so-called balance pressure ( $p_{balance}$ ). Figure 4.4 shows the profile of  $p$  in the chamber for a step-wise expansion (black line) and a (continuous) expansion (gray dashed line).

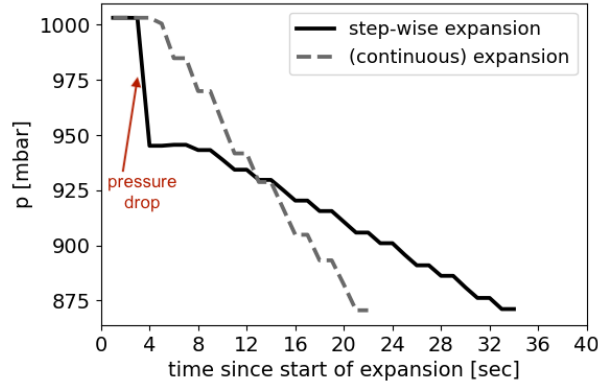


Figure 4.4.: Comparison of the pressure profile  $p$  in the chamber for a (continuous) expansion (gray dashed line) and a step-wise expansion (black thick line). The red arrow shows the pressure drop which is achieved by doing a step-wise expansion in PINEair with the use of the buffer volume.

This pressure drop is used as a parameter in the further analysis and is calculated as a percentage pressure drop ( $PPD$ ) as follows:

$$PPD = \frac{100}{p_{ambient}} \cdot (p_{ambient} - p_{balance}) \quad (4.1)$$

Depending on the difference between  $p_{ambient}$  and the reduced pressure in the buffer volume, a different  $p_{balance}$  is achieved and thus the peak ice saturation ratio in the expansion chamber can be regulated directly after the step-wise expansion.

Since the pressure in the chamber is rapidly reduced during the step-wise expansion, it can be assumed that the related temperature decrease is almost adiabatic. The dry-adiabatic temperature  $T_{ad}$  is calculated as follows:

$$T_{ad} = T_0 \cdot \left( \frac{p}{p_0} \right)^{\frac{R_d}{c_p}} \quad (4.2)$$

$T_{ad}$  is used to represent the minimum temperature for each step-wise expansion for measurements performed in the cirrus temperature range.  $T_0$  is the temperature of the lowest temperature sensor at the

start of the expansion,  $p_0$  represents the pressure at the start of the expansion, and  $p$  is the pressure measured in the chamber.  $R_d (= 287\text{J}(\text{K} \cdot \text{kg})^{-1})$  corresponds to the gas constant for dry air and  $c_p (= 1003.5\text{J}(\text{K} \cdot \text{kg})^{-1})$  refers to the specific heat capacity of dry air. At the beginning of the step-wise expansion, the relative humidity in the chamber is below water saturation, therefore, the dry adiabatic temperature can be calculated.

The peak ice saturation ratio  $S_{ice,p}$  in the chamber can be calculated as follows based on the pressure measurement and the calculated  $T_{ad}$ :

$$S_{ice,p} = \frac{p_{ice}(T_0) \cdot \frac{p}{p_0}}{p_{ice}(T_{ad})} \quad (4.3)$$

When calculating  $S_{ice,p}$ , the ratio of  $p/p_0$  has to be taken into account, as the air is constantly taken out of the chamber during the step-wise expansion assuming a constant water vapor mixing ratio inside the chamber.  $p_{ice}(T_0)$  is the saturation vapor pressure of ice at the beginning of the expansion, and  $p_{ice}(T_{ad})$  is the saturation vapor pressure of ice as a function of the adiabatic temperature and it is calculated using the equation of Murphy and Koop (2005). It is assumed that  $S_{ice} = 1$  at the beginning of the step-wise expansion since the dew point temperature of the sampled air is higher than the wall temperature of the chambers so that part of the water vapor condenses on the walls. Since  $S_{ice,p}$  cannot be measured in the chamber, this is a first-order calculation and the assumptions will be validated in the future by further laboratory measurements.

Figure 4.5 shows an example at  $T = -45^\circ\text{C}$ : the higher the pressure difference and therefore also the  $PPD$  inside the expansion chamber, the stronger the adiabatic cooling  $dT_{ad}$  (blue line) and the higher  $S_{ice,p}$  (red line).

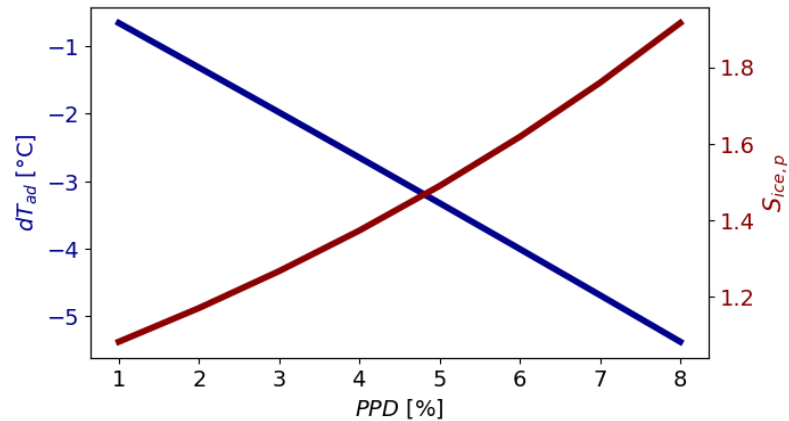


Figure 4.5.: Example for a step-wise expansion in PINEair with different  $PPDs$  at a start temperature of  $-45^\circ\text{C}$ , on the left the adiabatic temperature change  $dT_{ad}$  in blue and on the right the resulting peak ice saturation ratio  $S_{ice,p}$  in dark red. Using a higher  $PPD$  results in a stronger temperature decrease which leads to a higher relative humidity inside the chamber.

Due to the increase in the ice saturation ratio inside the chamber caused by the step-wise expansion, the aerosols can be activated to ice crystals. Immediately after the immediate pressure drop, the valve between the chamber and the buffer volume is closed again. The air from the chamber is pumped out further until a predefined time is reached, and a flow less than  $1 \text{ L min}^{-1}$  is used which is obtained via a mass flow controller (MFC). Here, the temperature which is achieved after the step-wise expansion inside the chamber should remain as constant as possible, more information and results about the test measurements can be found in section 4.4.1. The formed ice crystals are detected by the OPC at the outlet of the chamber. However, under cirrus conditions, these can either be formed homogeneously or heterogeneously. As this depends on the ice saturation ratio in the chamber, which can only be calculated (equation 4.3), the method of the analysis is described in more detail in section 4.4.2. Afterwards, the pressure in the buffer volume is regulated back to a pre-set pressure. The entire pressure regulation in the buffer volume is controlled fully automatically via the Labview program.

### 4.2.3. Different Versions of PINEair

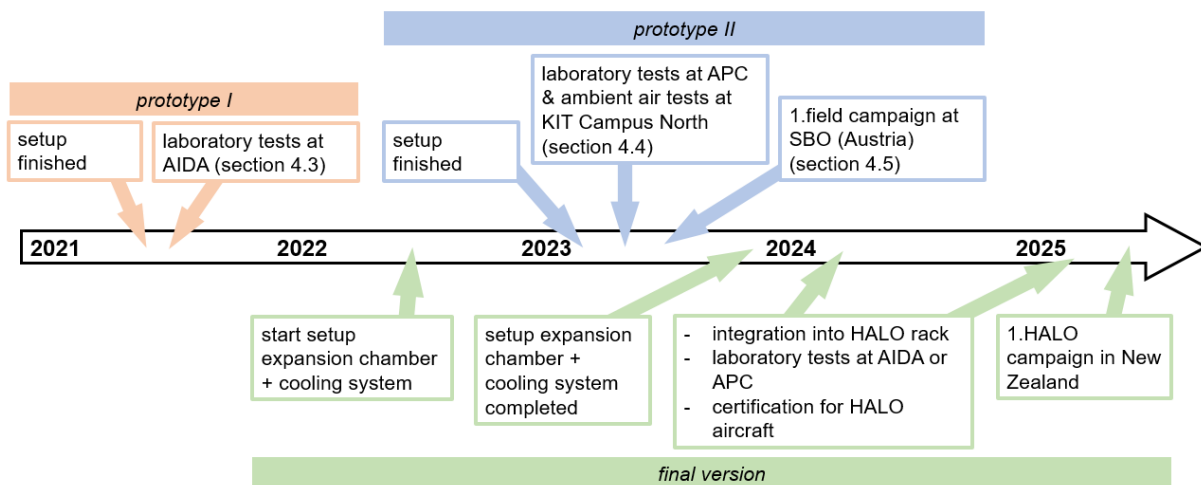


Figure 4.6.: Timeline of the most important milestones in the construction of the different PINEair versions (prototype I (red frame), prototype II (blue frame), and final version (green frame)) in the years 2021 to 2025.

Three different versions of PINEair were developed during the PhD, Figure 4.6 shows the most important milestones reached for each version. The general setup regarding the basic design such as the size of the chambers and the operation procedure was similar for the three versions, but they had different cooling systems. In the following, the differences between the versions are briefly described.

**Prototype I:** First, prototype I was built (Figure 4.7a) to test whether the principle of simulating cloud formation by an expansion also works for a smaller chamber volume as PINE and, in particular, whether

heterogeneous and homogeneous freezing in the cirrus temperature range can be distinguished since the existing PINE chambers have only been characterized for MPC temperatures. This PINEair version was set up in the thermostat housing of AIDA. As prototype I of PINEair did not have its own cooling system, it was not mobile. The intention here was to perform the first tests under well-controlled conditions, therefore it was operated at the same temperature and humidity conditions as the AIDA chamber. As the OPCs were also located in the cooled thermostat housing, *welas* systems, that can be operated in cold environments, were used to detect the particles at the outlet of each chamber, similar to AIDA. At the end of April 2021, the setup was finished and in May and June 2021, it was successfully tested during an AIDA laboratory campaign. During the campaign, the general working principle and the step-wise expansions with the buffer volume were tested, as well as the control and detection of the heterogeneous and homogeneous freezing in the cirrus temperature range (for more detailed information see section 4.3).

**Prototype II:** In contrast to prototype I, prototype II of PINEair has its own cooling system and is therefore mobile and can be used for field measurements (Figure 4.7b). An ethanol thermostat (LAUDA, PRO RP 290 E) is used for cooling so that INP measurements to temperatures of about  $-65^{\circ}\text{C}$  can be performed. For this, a novel design of double-walled chambers was applied to ensure that the ethanol coolant surrounds the entire chamber walls, thus achieving homogeneous cooling. The chamber volume of the individual chambers is also 3 L. All other components, except for the OPCs, as well as the entire electronics, were taken from prototype I. The instrument was completed at the end of January 2023. In February, March, and April 2023, the instrument was successfully tested in laboratory measurements with the APC chamber, and measurements with ambient air sampling were conducted at KIT Campus North in Karlsruhe (section 4.4). For example, systematic measurements were performed to find the most suitable settings for the operation of PINEair (section 4.4.1) and measurements at different humidity conditions of the sampled air (section 4.4.2). The first field measurement campaign was conducted in May 2023 at the Sonnblick Observatory (SBO) in Austria (section 4.5). In the future, it is planned to operate the instrument during more field measurement campaigns at various locations around the world.

**Final version:** The final version of PINEair is specifically developed for the use onboard the HALO research aircraft of DLR (Deutsches Zentrum für Luft- und Raumfahrt) (Figure 4.7c). This version is based on the same components (such as pressure sensors, valves, etc.) and the same Labview program as the prototypes I and II, but the entire instrument has to fit into a HALO rack. For cooling the chambers, a Stirling cooler is used without any liquid coolant (same principle as for the commercial PINE (PINEc)). Similar to PINEc, the three chambers are located in a vacuum chamber, which is cooled to reach temperatures down to  $-65^{\circ}\text{C}$ . The development of a liquid-free cooling system is crucial for the aircraft application of PINEair. The construction of the chambers with the cooling system was started in collaboration with Bilfinger Nuclear & Energy Transition GmbH in July 2022 and completed in De-

ember 2023. Next, the integration of the instrument into the HALO rack will take place at enviscope GmbH in Frankfurt in 2024. Afterwards, it will be tested and characterized in laboratory measurements at the chamber AIDA or the aerosol chamber APC before it is certified by enviscope GmbH for the use onboard the HALO research aircraft. The first potential measurement campaign on the HALO research aircraft might take place in New Zealand in August/September 2025.

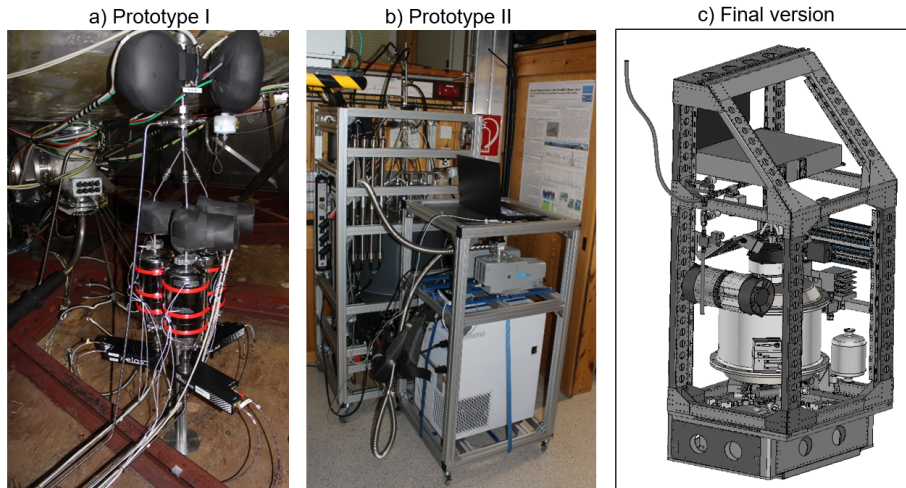


Figure 4.7.: Pictures of the different PINEair versions: a) Prototype I was located below the AIDA chamber in the thermal housing. b) Prototype II is mobile and can be cooled with an external thermostat. c) Schematic drawing of the final version of PINEair in a rack for the HALO research aircraft (data courtesy of Laurin Merkel (Goethe University Frankfurt)).

### 4.3. Validation Experiments with the PINEair Prototype I

The first validation campaign was performed with PINEair prototype I (Pictures 4.7a), which is located in the thermal housing of the AIDA chamber. Below is a brief overview of the campaign (section 4.3.1), followed by a discussion of the results (section 4.3.2).

#### 4.3.1. Overview of Campaign

The aim of the campaign at the AIDA expansion chamber was the basic testing and validation of the functions of the PINEair prototype I, as well as its control system by the Labview program. The validation campaign can be split into two parts. The first part includes the measurements at the lower cirrus temperatures which were carried out in the period from May 17 to 28, 2021, and June 15 to 18, 2021. Experiments were performed to measure the precise freezing onset temperature of supercooled water droplets, to distinguish between homogeneous and heterogeneous freezing, and to test the new instrument at aircraft-relevant conditions at reduced pressure ( $p_{start} = 250$  mbar).

The second part includes experiments about the immersion freezing of dust at MPC temperatures. Here,

the INP concentration measured with the PINEair prototype I was additionally compared to other INP instruments.

Table 4.1 provides a brief overview of the aim of each experiment, the start temperature  $T_{AIDA}$  and start pressure  $p_{AIDA}$  of the AIDA experiments, as well as the aerosol type and aerosol concentration used for the experiments. The results of the various experiments are described and discussed in more detail in section 4.3.2.

Table 4.1.: Overview of the experiments performed at the AIDA chamber to test the PINEair prototype I, with information about the purpose of each experiment, the start temperature in AIDA  $T_{AIDA}$ , the start pressure  $p_{AIDA}$ , the aerosol used, and the aerosol concentration.

Purpose	$T_{AIDA}$ [ $^{\circ}\text{C}$ ]	$p_{AIDA}$ [mbar]	aerosol (conc. [ $\# \text{cm}^{-3}$ ])
Freezing onset temperature of supercooled water droplets	$-31^{\circ}\text{C}$	ambient	ammonium sulfate (300)
Homogeneous freezing	$-45^{\circ}\text{C}$	ambient	$\text{H}_2\text{SO}_4$ (600)
Homogeneous and heterogeneous freezing	$-45^{\circ}\text{C}$	ambient	$\text{H}_2\text{SO}_4$ (600) +ATD (10)
Aircraft conditions	$-55^{\circ}\text{C}$	250	$\text{H}_2\text{SO}_4$ + SDSA01
Immersion freezing and comparison to other INP instruments	$-20^{\circ}\text{C}$	ambient	Dust

### 4.3.2. Results and Discussion

In the following, each experiment from Table 4.1 is explained in more detail, and the results are discussed.

#### Homogeneous Freezing of Water Droplets

With increasing relative humidity, ammonium sulfate aerosol particles take up water until they deliquesce and finally form almost pure liquid cloud droplets. The freezing temperature of cloud droplets is known from previous studies by e.g., Benz et al. (2005). Depending on the size of the cloud droplets, they can freeze homogeneously at temperatures between  $-35^{\circ}\text{C}$  and  $-37^{\circ}\text{C}$ . Therefore, ammonium sulfate aerosols were used as seed aerosols for cloud droplet formation, to validate the onset temperature for homogeneous freezing of supercooled water droplets measured with PINEair.

For this experiment, the AIDA chamber was cooled to  $-31^{\circ}\text{C}$  and filled with  $300\# \text{cm}^{-3}$  ammonium sulfate aerosols. The generation of the ammonium sulfate aerosols and the injection into the AIDA chamber are explained in more detail in section 3.5. The ammonium sulfate aerosols were then sampled with PINEair prototype I to validate the instrument for the correct detection of homogeneous freezing of water droplets. Now several (continuous) expansions were performed with PINEair, and the flow rate during the expansion  $flow_{exp}$  was varied between  $0.9 \text{L min}^{-1}$  and  $1.1 \text{L min}^{-1}$ .

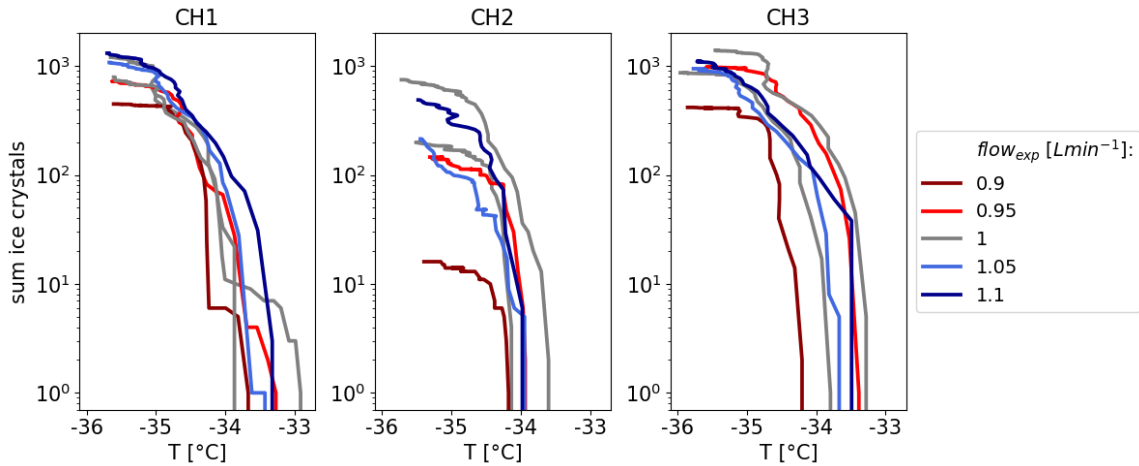


Figure 4.8.: Results of the AIDA experiment about the onset temperature of homogeneous freezing of ammonium sulfate aerosols for the respective chamber (CH1, CH2, CH3) in PINEair prototype I. The sum of ice crystals per expansion is shown as a function of the measured temperature  $T$  in PINEair. Each line corresponds to an expansion in PINEair, where the different colors show the flow rate used for the (continuous) expansion  $flow_{exp}$ .

Figure 4.8 shows the sum of the ice crystals that formed during each expansion as a function of the measured temperature  $T$  for the three expansion chambers of PINEair (CH1, CH2, CH3). The color corresponds to the respective  $flow_{exp}$ . The temperature  $T$  refers to the lowest gas temperature sensor ( $T_{gas3}$ ). The ice onset temperature varies between  $-32.91^{\circ}\text{C}$  and  $-34.20^{\circ}\text{C}$  and on average the homogeneous freezing starts at a temperature of  $-33.67^{\circ}\text{C}$ . It is noticeable that the homogeneous freezing of the ammonium sulfate aerosols in CH1 and CH3 tends to occur at higher temperatures (on average about  $0.5^{\circ}\text{C}$ ) than in comparison to CH2. The reason for the differences is probably due to the slightly different positions of the thermocouples inside the expansion chambers. No correlation to the different  $flow_{exp}$  can be observed for the variation of the ice onset temperature. For CH2, in total, a lower number of ice crystals is detected by the OPC compared to the other chambers. The reason for this might be that the sensitivity setting of the welas system of CH2 was different for larger particles.

In comparison to the literature values, which vary between  $-35^{\circ}\text{C}$  and  $-37^{\circ}\text{C}$  (e.g. Benz et al., 2005), the PINEair measurements have on average an offset of  $1.33^{\circ}\text{C}$  towards higher temperatures. This is probably related to the temperature inhomogeneities inside the chamber. During expansion, the inhomogeneity of the temperature distribution increases even further, which is mainly caused by the temperature difference between the expanded gas and the chamber walls.

### Distinction between Homogeneous and Heterogeneous Freezing

PINEair is also used to measure the INP concentration in the temperature range of cirrus cloud formation below about  $-38^{\circ}\text{C}$ . Here, ice crystals can form either by heterogeneous ice nucleation at lower ice saturation ratios due to the presence of an INP, or by the homogeneous freezing of solution droplets (for more detailed information see section 2.2.1). The following experiment is intended to demonstrate that it

is possible with PINEair to distinguish between homogeneous freezing and heterogeneous ice nucleation in the cirrus temperature range. Sulphuric acid aerosols ( $H_2SO_4$ ) were used, as it is known that these aerosol particles can only freeze homogeneously at temperatures lower than  $-38^\circ\text{C}$  (Tabazadeh et al., 1997). As an INP, the dust aerosol ATD was used, which is ice-active at low ice supersaturations (e.g., Möhler et al., 2006; Murray et al., 2012). The generation and injection of the respective aerosol into the AIDA chamber are explained in section 3.5.

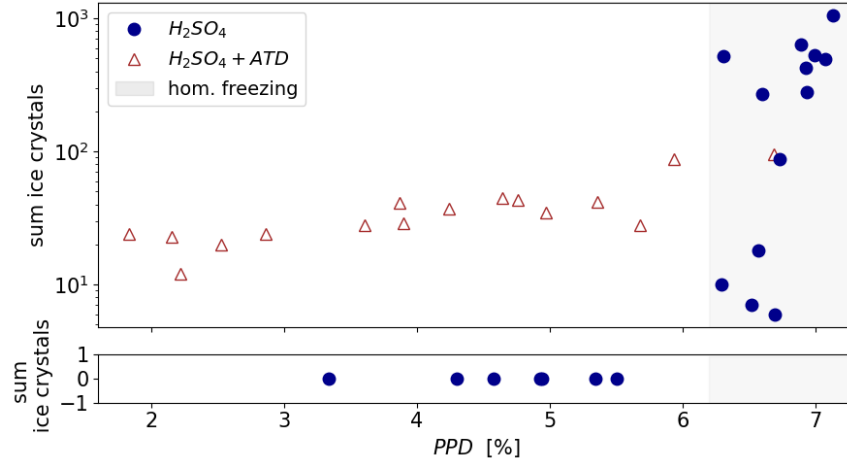


Figure 4.9.: Experiment using sulfuric acid aerosols (blue circles) and ATD dust aerosols (brown triangles) to test the distinction between heterogeneous and homogeneous ice nucleation at cirrus temperatures ( $T_{start} = -45^\circ\text{C}$ ) with PINEair. The sum of ice crystals as a function of the  $PPD$  during step-wise expansions is shown. The relative humidity conditions for homogeneous freezing are only reached at  $PPD > 6.29\%$  (gray shaded area).

At the beginning of the experiment, the AIDA chamber was cooled to a start temperature of  $-45^\circ\text{C}$ , and first, only the sulphuric acid aerosols were injected. PINEair was then sampling the aerosols and performing several step-wise expansions with different  $PPDs$  in the range from 1.83% to 7.14% to achieve different peak relative humidity conditions inside the chamber (this corresponds to  $S_{ice,p}$  of 1.13 to 1.65 using the  $T_{ad}$  calculation, see equation 4.3 in section 4.2.2). In Figure 4.9, the blue circles show the results for the sulphuric acid aerosols, the sum of the ice crystals per step-wise expansion is shown as a function of the  $PPD$ . The homogeneous ice formation only occurs at a  $PPD > 6.29\%$ , which corresponds to  $S_{ice,p} = 1.55$  by using  $T_{ad}$  for the calculation. At a lower  $PPD$ , the relative humidity in the chamber is not high enough for the sulfuric acid aerosols to freeze homogeneously.

In the second part of the experiment, ATD aerosols were additionally added to the sulfuric acid particles in the AIDA chamber, as they can act as INP enabling the ice crystals to form even at lower  $S_{ice}$  due to heterogeneous deposition nucleation. Next, several step-wise expansions were performed with PINEair again with similar  $PPDs$  as for the sulfuric acid particles, the results are shown in Figure 4.9 by the brown triangles. As expected, the heterogeneous ice nucleation of the dust particles starts already below the threshold for homogeneous freezing, which confirms that it is possible to distinguish between

homogeneous and heterogeneous freezing by using PINEair.

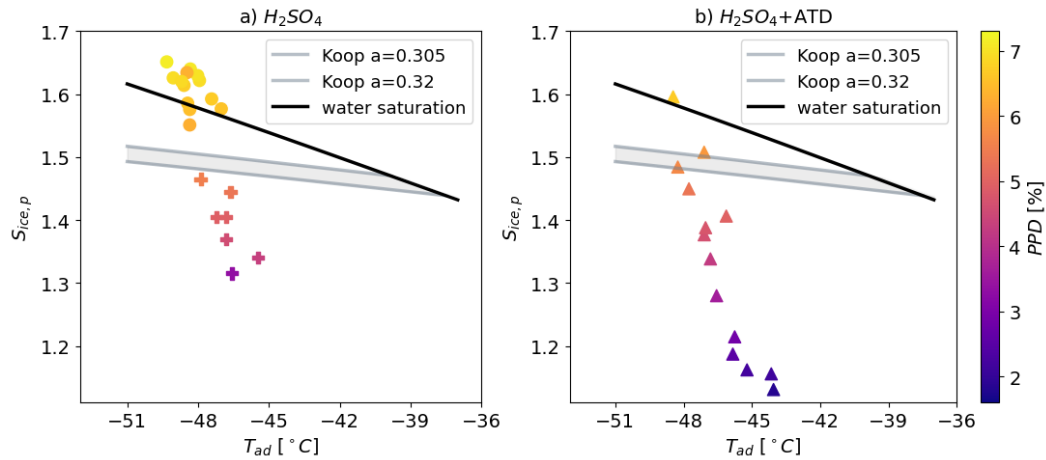


Figure 4.10.: Start of ice formation in PINEair for the different *PPDs* also shown in Figure 4.9 for the AIDA experiments with a) sulfuric acid aerosols and b) sulfuric acid aerosols + ATD. Each data point corresponds to a step-wise expansion in PINEair, the colors represent the used *PPD*. The Figure shows the calculated  $S_{ice,p}$  as a function of  $T_{ad}$ , the grey shaded area shows the onset of homogeneous freezing according to the parameterization of Koop et al. (2000) with two different  $a$  and in black the water saturation. The circles in Figure a) indicate that ice crystals formed in the chamber at these relative humidity conditions, the crosses show that no ice crystals formed during the run. In b), ice crystals formed during each run.

Figure 4.10 shows the calculated  $S_{ice,p}$  as a function of  $T_{ad}$  (equations see section 4.2.2) for all the step-wise expansions which are shown in Figure 4.9, a) all experiments with sulfuric acid aerosols and b) all experiments with sulfuric acid aerosols + ATD. The black line shows the water saturation and the gray shaded area shows the beginning of the homogeneous freezing of solution droplets according to Koop et al. (2000) ("Koop line") with two different values for the water activity  $a$ . In Figure 4.10a (only experiments with sulfuric acid aerosols), the step-wise expansions at which homogeneous ice formation has started are shown with circles, and the crosses show the step-wise expansions at which no ice has formed, as the relative humidity conditions in the chamber were too low. The result agrees well with the literature values, homogeneous freezing of the sulfuric acid aerosols only occurs above the Koop line. This confirms the assumption that the temperature decrease during the step-wise expansion is almost adiabatic and  $T_{ad}$  can be used to calculate  $S_{ice,p}$  inside the chamber. Figure 4.10b shows the experiments with sulfuric acid aerosols + ATD, where the heterogeneous ice formation occurred at every step-wise expansion, regardless of the value of the *PPD*. Compared to Figure 4.10a, this was already the case at significantly lower peak relative humidity conditions.

### Tests at Aircraft-relevant Conditions

PINEair is specially developed for the use onboard aircraft and therefore the measurement of the INP concentration in the FT. Depending on the scientific objectives of the measurement campaign, aircraft

measurements can take place at altitudes of up to 14km, where the ambient pressure is low. It is therefore an important part of the validation of PINEair to test whether the instrument also works at reduced pressure conditions.

For this type of validation experiment, the AIDA expansion chamber was cooled to  $-55^{\circ}\text{C}$  and sulfuric acid aerosols (concentration:  $1000\# \text{cm}^{-3}$ ) and SDSA01 dust aerosols (concentration:  $40 - 50\# \text{cm}^{-3}$ ) were injected into the chamber at ambient pressure as described in section 3.5. Afterwards, the pressure in the AIDA chamber was reduced slowly to 250mbar to prevent an expansion and with that the activation of the aerosol particles to form ice crystals. The aerosols were then sampled from the AIDA chamber into PINEair and several step-wise expansions with different *PPDs* were performed.

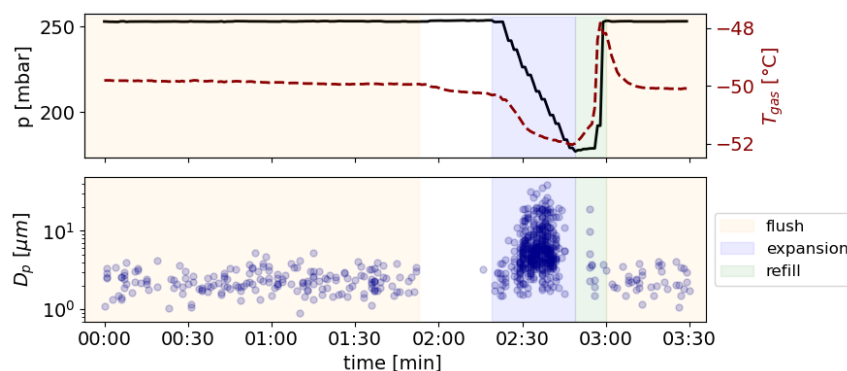


Figure 4.11.: Example measurement with sulfuric acid and SDSA01 aerosols for one run with the modes flush (orange shading), expansion (blue shading), refill (green shading) using PINEair at conditions relevant to aircraft measurements ( $p_{start} = 250\text{mbar}$  in AIDA). The upper panel shows the measured pressure  $p$  in black and the measured gas temperature  $T_{gas}$  in the red dashed line. In the lower panel, a circle corresponds to a detected particle with the OPC as a function of the optical particle diameter  $D_p$ .

Figure 4.11 shows an example measurement, in the upper panel the measured gas temperature  $T_{gas}$  (red dashed line) and the pressure  $p$  (black solid line), both decrease during the step-wise expansion. The lower panel shows the particles detected by the OPC as a function of their optical particle diameter  $D_p$ . The particles visible in the flush mode (orange shaded area) are the injected aerosols. The step-wise expansion occurs during the blue-shaded area, it can be observed that an ice cloud is formed. This confirms that PINEair is also suitable for measuring the INP concentration at a reduced start pressure and thus for the use on a research aircraft.

### Comparison to other INP Instruments in Immersion Freezing

To test the performance of the novel PINEair in comparison to other INP instruments, an immersion freezing experiment was performed at AIDA at a start temperature of  $T_{AIDA} = -20^{\circ}\text{C}$  (MPC temperature regime). For that, a dust aerosol was injected into the AIDA chamber with the RBG as described in

section 3.5. PINE-04-02 was used as a comparison instrument to measure the temperature-dependent INP concentration.

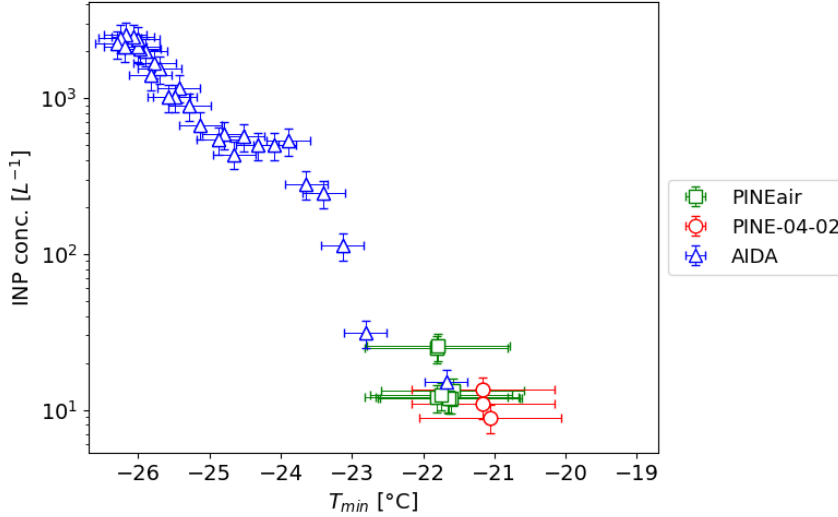


Figure 4.12.: AIDA experiment with dust aerosols at a start temperature of  $T_{AIDA} = -20^{\circ}\text{C}$ , for a comparison between the INP instruments PINEair (green diamonds), PINE-04-02 (red circles) and AIDA (blue triangles). In the case of PINEair and PINE-04-02, each data point corresponds to an expansion.

For the measurement with PINEair, several (continuous) expansions were performed with  $flow_{exp} = 1.3\text{L min}^{-1}$  and  $1.4\text{L min}^{-1}$  without using the buffer volume. Figure 4.12 shows the INP concentration as a function of the measured minimum temperature  $T_{min}$ . For the measurements with PINEair and PINE-04-02, each single data point corresponds to an expansion with the instrument. The results from PINEair (green squares) are in good agreement with the results from PINE-04-02 (red circles) and the AIDA expansion chamber (blue triangles). The measurements agree within the temperature uncertainty for the different methods.

#### 4.4. Validation Experiments with the PINEair Prototype II

After the successful tests with PINEair prototype I, the mobile PINEair prototype II was built (compare to section 4.2.3). To test the performance of the new instrument and to develop optimum operational parameters, test measurements were performed by sampling specific aerosol types from the APC chamber under laboratory conditions, and by sampling ambient air consisting of a more natural mixture of aerosol types. The way of analyzing the data depends on the cloud regime at which the measurements were conducted. For measurements in the MPC temperature range, the ice crystals can be distinguished from the supercooled liquid water droplets due to their larger optical size (Järvinen et al., 2014). Since in this temperature range the ice crystals can only form through heterogeneous nucleation (section 2.2.2), the number of ice crystals is equal to the number of INPs. In contrast, in the cirrus temperature range, the ice

crystals can form through homogeneous or heterogeneous ice nucleation (section 2.2.1), requiring the use of a different evaluation routine. For this purpose, some methodical measurements were performed at cirrus temperatures, which helped to find the optimal settings for the measurements with the new INP instrument, which are discussed in section 4.4.1. Finally, section 4.4.2 describes in more detail how the data is evaluated in this temperature range.

#### 4.4.1. Measurements at Cirrus Temperatures

Several laboratory and field measurement campaigns have already been performed with the commercial PINE instruments at temperatures in the MPC temperature range (e.g., Hiranuma et al., 2020; Vogel, 2022; Brasseur et al., 2022; Lacher et al., 2024; Ponsonby et al., 2023), but so far only very few measurements were conducted at cirrus conditions. Consequently, there is little to no experience in operating this kind of small expansion chambers at temperatures  $< -38^\circ\text{C}$ . Therefore, comprehensive test experiments were performed with the PINEair prototype II as described in the following sections. These experiments aimed at finding the optimal settings for the following three parameters: Duration of the waiting time before the start of the expansion, pump flow after the step-wise expansion, and the duration of the expansion. Experiments were done either under laboratory conditions at the APC chamber or with ambient air at the inlet at Campus North (KIT).

#### Duration of Waiting Time Before Expansion

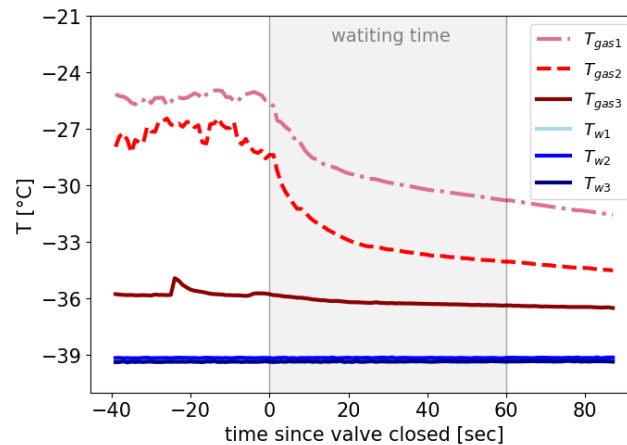


Figure 4.13.: Measured gas temperature  $T_{gas}$  and wall temperature  $T_w$  at the different positions (numbered vertically from top to bottom) in PINEair as a function of time. From  $-40\text{sec}$  to  $0\text{sec}$  the conditions during flush mode are shown. The waiting time starts from  $0\text{sec}$ , where all valves at the inlet and outlet of the expansion chamber are closed. Based on the measurements, a waiting time of  $60\text{sec}$  is recommended, which is illustrated by the gray shaded area.

During flush mode, when the air is sampled in PINEair, there is an inhomogeneous temperature distribution inside the chamber: the highest temperatures are on the top and the lowest temperatures are at

the outlet, as the air flows through the chamber from top to bottom. For example, Figure 4.13 shows a temperature measurement of one chamber of PINEair which is cooled to about  $-39^{\circ}\text{C}$ . The lines in reddish colors show the measured gas temperature  $T_{gas}$  and the lines in bluish colors show the measured wall temperature  $T_w$ . The temperature sensors are numbered as follows:  $T_1$  corresponds to the sensor at the inlet,  $T_2$  to the sensor in the middle, and  $T_3$  is the sensor close to the outlet of the chamber. In the first time range of the Figure from  $-40\text{sec}$  to  $0\text{sec}$ , the temperature deviation between the top temperature  $T_{gas1}$  at the inlet and the bottom sensor at the outlet  $T_{gas3}$  is approximately  $11^{\circ}\text{C}$ , which corresponds to the conditions when PINEair is in flush mode. This may lead to an uneven distribution of the relative humidity, ice-saturated conditions may already be achieved in some places within the chamber, while at others not. One way of counteracting the vertical temperature gradient is to include a "waiting time" before the start of an expansion, to allow the incoming sample air to be cooled down by the cold walls. During this process, all valves are closed to enable the temperature and relative humidity to be homogeneously distributed within the chamber, this is shown in Figure 4.13 starting at  $0\text{sec}$ . The air in the upper and middle parts of the chamber cools down quickly, while the temperature in the lower part changes only slightly. The longer the waiting time, the closer  $T_{gas}$  converges to  $T_w$ . However, the waiting time should not be too long, to keep aerosol losses in the chamber low and to operate the instrument at higher time resolution. Based on the results presented in Figure 4.13, a waiting time of  $60\text{sec}$  was chosen. The waiting time of  $60\text{sec}$  is used for all measurements with PINEair in the entire temperature range (MPCs and cirrus).

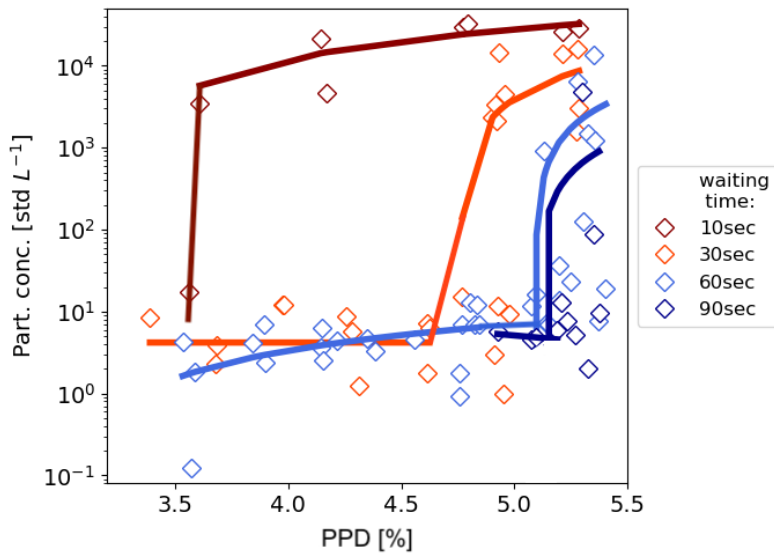


Figure 4.14.: Figure represents the particle concentration per expansion as a function of the  $PPD$ . The result of the test measurement (March 10, 2023 with ambient air sampling at the KIT Campus North,  $T = -40^{\circ}\text{C}$ ) showing the influence of the waiting time (shown in different colors) on the start of the homogeneous freezing in PINEair. The longer the waiting time, the higher the  $PPD$  has to be to achieve the relative humidity conditions for homogeneous freezing.

The onset of homogeneous freezing may also depend on the initial temperature distribution in the chamber, and by that also on the waiting time. This was investigated in a series of experiments with different waiting times (10 sec, 30 sec, 60 sec, and 90 sec). For each waiting time, a series of runs with increasing *PPD* was conducted. The start temperature in PINEair was approximately  $-40^{\circ}\text{C}$  and the measurements were performed at ambient air conditions on March 10, 2023, at Campus North (KIT). The ambient air flowing into PINEair had a dew point temperature of  $-25.07^{\circ}\text{C}$  after passing through the dryers. The result is shown in Figure 4.14, the particle concentration per step-wise expansion as a function of the different *PPDs* and in color the waiting times. At the suggested waiting time of 60 sec, homogeneous freezing occurs at a *PPD* of 5.1 % (blue line). With a waiting time of 90 sec, homogeneous freezing begins in a similar range, but at a slightly higher *PPD* (dark blue line). At a lower waiting time of 10 sec, the homogeneous freezing already starts at a *PPD* of 3.52 % (red line). From these measurements, it can be concluded, that with increasing waiting time, the homogeneous freezing onset shifts to larger *PPDs*.

### Pump Flow After Step-wise Expansion

After the initial step-wise expansion, the formed ice crystals are pumped out of the chamber with a pre-set  $flow_{exp}$  and guided through the OPC for detection. In this section, measurements are shown to find an appropriate  $flow_{exp}$ . Here, it is important that the peak relative humidity that is reached immediately after the pressure drop remains constant and is not changed by the following pumping. If the pumping process is too fast, there may be further cooling in the chamber, which could cause an increase in the relative humidity. In this case, the peak relative humidity can no longer be determined accurately, as the temperature distribution in the chamber becomes more inhomogeneous after the pressure drop of the step-wise expansion due to heat flux from the walls.

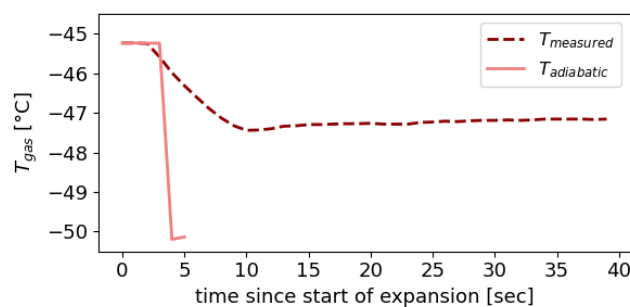


Figure 4.15.: Comparison of the lowest measured temperature (dark red dashed line) with the adiabatically calculated temperature (red thick line) during one run performed with a step-wise expansion in PINEair.

Figure 4.15 shows an example of a run with a step-wise expansion in which the lowest measured temperature ( $T_{gas}$ , dashed dark red line) is shown in comparison to the adiabatically calculated temperature (according to equation 4.2, solid red line). The adiabatic temperature decrease is only shown for the

pressure drop of the step-wise expansion, as this assumption is no longer valid for further pumping due to the heat flux from the chamber walls. Immediately after the pressure drop at 4 sec, the measured temperature and the adiabatic temperature deviate from each other by 4°C. This demonstrates that during a step-wise expansion, the temperature sensor cannot correctly detect the sharp temperature change in the chamber due to its response time.

Two different sets of experiments were conducted to investigate which  $flow_{exp}$  directly after the step-wise expansion allows a good detection and measurement of the formed ice crystals. In the first experiment, a  $PPD$  for the step-wise expansion was selected at which homogeneous relative humidity conditions are achieved. In the second experiment, a lower  $PPD$  was selected, therefore only heterogeneous relative humidity conditions were reached. Both experiments are described in more detail in the following.

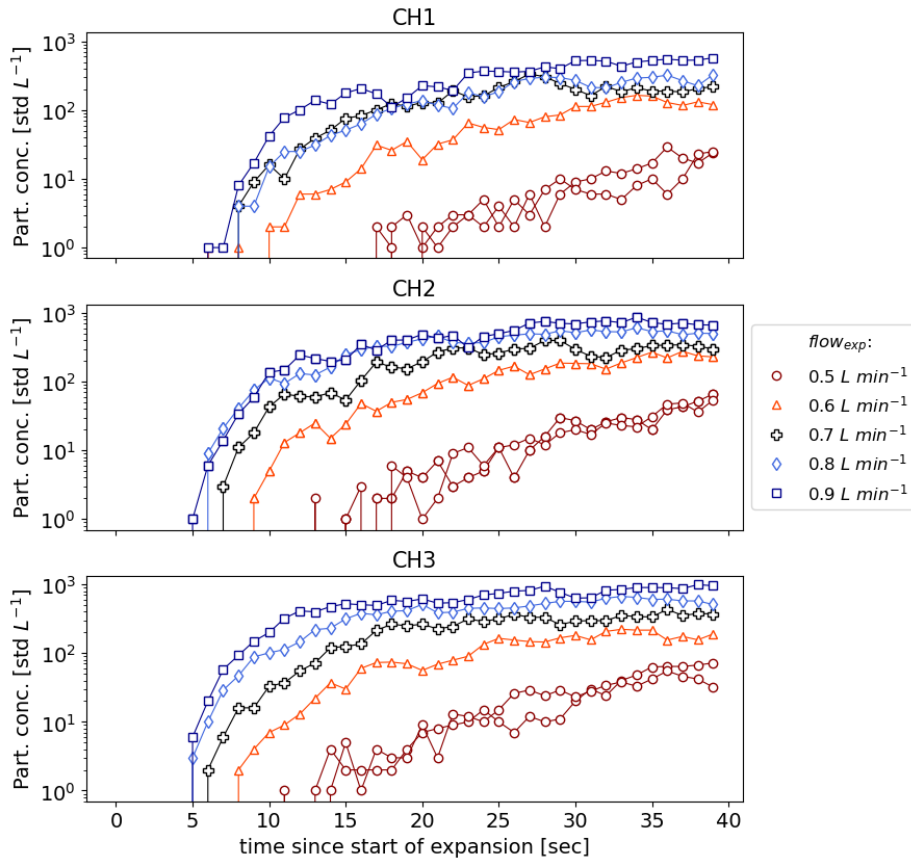


Figure 4.16.: Experiment with sulfuric acid aerosols at  $T = -45^{\circ}\text{C}$  to find a suitable setting of  $flow_{exp}$  for the measurements with PINEair. The particle concentration during each run ( $PPD = 7.19\%$ ) is shown as a function of time for the respective expansion chamber (CH1, CH2, CH3). Each curve corresponds to one run and the colors represent  $flow_{exp}$ . Based on the results, it can be concluded that  $flow_{exp}$  should be larger than  $0.7\text{L min}^{-1}$ .

For the first experiment, sulphuric acid aerosols were used, which were injected into the APC chamber as described in section 3.5. The measurements with PINEair were conducted at a starting temperature of  $-45^{\circ}\text{C}$ , and the APC chamber was at room temperature with  $T_{DP} = -30^{\circ}\text{C}$ . PINEair was then used to perform several runs with step-wise expansions with a  $PPD$  of 7.19%, which corresponds to a  $S_{ice,p}$  of 1.66, therefore homogeneous relative humidity conditions were achieved. After each complete run cycle a new  $flow_{exp}$  was used, they varied in the range between  $0.5\text{L min}^{-1}$  and  $0.9\text{L min}^{-1}$ .

Figure 4.16 shows the measured particle concentration during each run as a function of time for the three different chambers (CH1, CH2, and CH3). The different  $flow_{exp}$  after the step-wise expansion are represented in different colors and symbols. If  $flow_{exp} < 0.7\text{L min}^{-1}$ , it takes several seconds until the ice crystals are detected at the OPC. This is an indication that this  $flow_{exp}$  is too slow. In contrast, if  $flow_{exp} \geq 0.7\text{L min}^{-1}$ , the first ice crystals are detected in the OPC at approximately the same time for the different flows ( $\sim 5 - 8\text{sec}$ ) and the measured total particle concentrations are similar. It can be concluded that a higher pump flow larger than  $0.7\text{L min}^{-1}$  is more appropriate than a lower one.

However, it is important that  $flow_{exp}$  is not too high, as otherwise the peak relative humidity immediately after the step-wise expansion could be further increased due to a further drop in temperature. Therefore, in a second experiment, the results of two selected  $flow_{exp}$  of  $0.7\text{L min}^{-1}$  and  $1.5\text{L min}^{-1}$  are compared with each other. Similar to the first experiment, the second experiment was performed at the APC chamber at room temperature and PINEair was at a starting temperature of  $-45^{\circ}\text{C}$ . Several runs with step-wise expansions were conducted with a  $PPD$  of  $\sim 4.9\%$ , which corresponds to  $S_{ice,p} = 1.39 \pm 0.02$ , thus achieving heterogeneous conditions in the chamber. At first, only sulfuric acid aerosols were injected, and later dust aerosols ATD were added.

Figure 4.17 shows the results: the first column displays the measured particle concentration during the run as a function of time for chamber 1 (a1, b1) and the second column shows the results for chamber 3 (a3, b3). The data from chamber 2 are not shown due to a problem with the setting of  $flow_{exp}$ . Experiments with sulfuric acid aerosols are represented by the blue circles and the experiments with sulfuric acid aerosols+ATD by the brown triangles. The two plots in the top row show the data if  $flow_{exp} = 1.5\text{L min}^{-1}$  (a1, a3). Here, in the experiment with sulfuric acid aerosols (blue circles), a clear homogeneous ice cloud has formed in both chambers, although only heterogeneous relative humidity conditions are generated by the peak ice saturation ratio due to the used  $PPD$  for the step-wise expansion. This is an indication that the relative humidity in the chamber has increased further after the step-wise expansion, which means that  $flow_{exp} = 1.5\text{L min}^{-1}$  is too fast. The two plots in the bottom row show the result for  $flow_{exp} = 0.7\text{L min}^{-1}$  (b1, b3). A measurement with sulfuric acid aerosols was also conducted (blue circles), but no ice crystals formed. From these results it can be concluded that  $flow_{exp} = 0.7\text{L min}^{-1}$  is a good choice, it is therefore used for further measurements with PINEair at cirrus conditions.

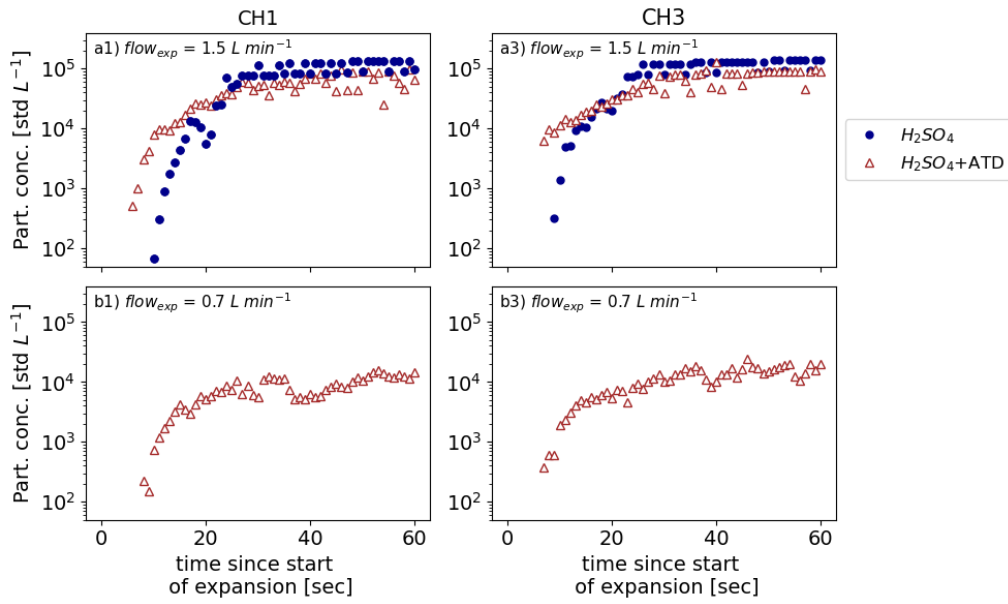


Figure 4.17.: The particle concentration during each run with  $PPD \sim 4.9\%$  is shown as a function of time for the chamber 1 (a1 and b1) and chamber 3 (a3 and b3) of PINEair ( $T = -45^\circ\text{C}$ ). Blue circles represent the result for the measurements with sulfuric acid aerosols and the brown triangles for the experiments with sulfuric acid aerosols + ATD. For the two plots in the top row (a1 and a3)  $flow_{exp} = 1.5\text{ L min}^{-1}$  was used and for the bottom row (b1 and b3) it was  $flow_{exp} = 0.7\text{ L min}^{-1}$ .

### Duration of Expansion

The duration of the expansion ( $t_{exp}$ ) is important to ensure that the ice crystals that formed after the step-wise expansion in PINEair are detected with the OPC. If  $t_{exp}$  is too long, the time resolution of the measurements is unnecessarily reduced and the increase of the gas temperature due to the influence of the chamber wall becomes larger, which may lead to an evaporation of the ice crystals. Therefore, an optimum setting for  $t_{exp}$  is when a constant particle concentration is reached.

To investigate  $t_{exp}$  in more detail, measurements were performed with PINEair at a starting temperature of  $-45^\circ\text{C}$  at the ambient air at Campus North (KIT). Several measurements with step-wise expansions at different  $PPDs$  in the range of  $4.30\%$  to  $5.66\%$  were made to achieve different relative humidity conditions in the chamber (from heterogeneous to homogeneous  $S_{ice}$  conditions). For the other settings during the expansion, the suitable settings from the two previous sections were selected accordingly (waiting time =  $60\text{ sec}$ ,  $flow_{exp} = 0.7\text{ L min}^{-1}$ ). Figure 4.18 shows the measured particle concentration during the expansion as a function of time, the different  $PPDs$  are displayed in different colors. After approximately  $90\text{ sec}$ , a constant particle concentration is achieved for all step-wise expansions where the relative humidity conditions for homogeneous freezing have been reached. Afterwards, the particle concentration slowly decreases again. From this experiment can be concluded that the total duration for the expansion should be  $t_{exp} = 90\text{ sec}$ , as otherwise, the ice crystals may evaporate.

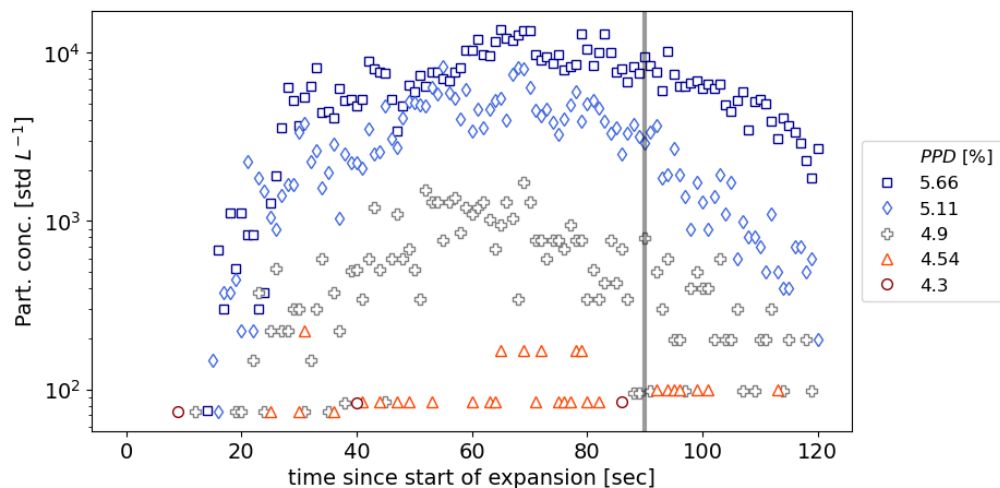


Figure 4.18.: Several measurements using PINEair for various step-wise expansions with different  $PPDs$  (different symbols and colors) to find the optimum time for  $t_{exp}$ . The particle concentration during the runs with step-wise expansions is shown as a function of time. Measurements were carried out at  $T = -45^\circ\text{C}$  at ambient air conditions at Campus North. The grey line  $t_{exp} = 90\text{sec}$  is the optimum setting.

#### 4.4.2. Data Evaluation at Cirrus Temperatures

The data evaluation of the measurements with PINEair at cirrus temperatures lower than  $-38^\circ\text{C}$  is different from that in the higher MPC temperature range, as the ice crystals can form through heterogeneous or homogeneous nucleation (section 2.2.1). Therefore, when measuring in this regime, it is important to distinguish between these two ice formation modes. A relative humidity scan with PINEair is performed to find the threshold at which the  $PPD$  during the step-wise expansion leads to homogeneous relative humidity conditions in the chamber. For this purpose, several runs with step-wise expansions are conducted starting at low  $PPDs$  up to larger  $PPDs$  to obtain information about the particle concentration in a wide relative humidity range. Next, the measured particle concentration for each run is displayed graphically as a function of the  $PPDs$ . This can be used to determine the threshold for the start of the homogeneous nucleation as soon as a sharp, sudden increase in the particle concentration occurs. A more detailed evaluation of the data measured in the cirrus temperature range is explained in the following sections: First, it is explained how the balance pressure  $p_{balance}$  is determined to calculate the  $PPD$ . Laboratory measurements at the APC chamber and measurements at ambient air conditions at Campus North are presented and discussed on how homogeneous and heterogeneous freezing can be distinguished. In the last subsection of this section, the influence of the dew point temperature on the threshold value for the start of homogeneous freezing is explained in more detail. All the measurements presented in this section were performed with the mobile PINEair prototype II.

### Determination of Balance Pressure After Step-wise Expansion

It is important to know the *PPD* of the step-wise expansion as precisely as possible, as the threshold for the *PPD* needs to be defined for the relative humidity in the chamber to reach a value for homogeneous nucleation to occur. To calculate the *PPD*,  $p_{balance}$  is required (equation 4.1 in section 4.2.2), which is shown graphically in Figure 4.19 (red line). Figure 4.19 shows a typical pressure profile of the pressure in the chamber  $p_{chamber}$  (black line) and the pressure in the buffer volume  $p_{buffer}$  (gray dashed line) during a step-wise expansion. The balance pressure  $p_{balance}$  corresponds to  $p_{chamber}$  at the time at which  $p_{chamber}$  and  $p_{buffer}$  are equal to each other (red line). Figure 4.19 also shows that  $p_{balance}$  does not match the mean value between  $p_{chamber}$  and  $p_{buffer}$ , as the two vessels have different volumes (expansion chamber: 3L, buffer volume: 2L). Therefore,  $p_{balance}$  has to be determined individually for each different *PPD*. Since PINEair is intended to be used for long-term measurements, it is important that  $p_{balance}$  is determined via an automatic evaluation routine. Two different methods were used for this, which are briefly explained in the following.

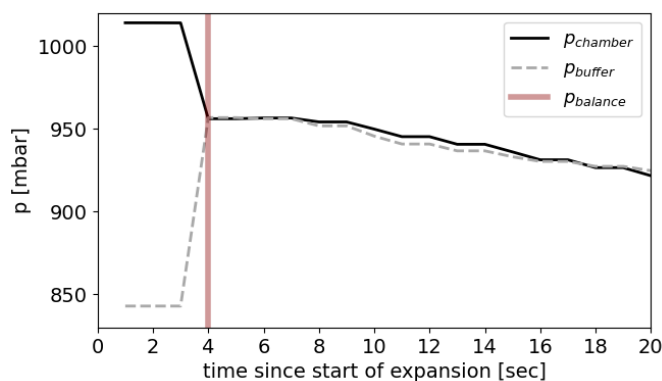


Figure 4.19.: Typical pressure profile in PINEair during a step-wise expansion, the black line shows the pressure in the expansion chamber  $p_{chamber}$ , and the gray dashed line represents the pressure in the buffer volume  $p_{buffer}$ . The red line indicates the balance pressure  $p_{balance}$ , at which  $p_{chamber}$  and  $p_{buffer}$  are in balance.

In method 1,  $p_{balance}$  is determined by using the highest pressure value 5 sec after the start of the step-wise expansion. The duration of 5 sec is based on experience. For method 2, the difference between  $p_{chamber}$  and  $p_{buffer}$  is calculated.  $p_{balance}$  corresponds to  $p_{chamber}$  at the point in time at which the difference is the smallest. During the analysis, it was found that the use of both methods does not always result in the same pressure value for  $p_{balance}$ . This is because  $p_{chamber}$  is not measured directly in the chamber, but only at the outlet of the chamber shortly after the OPC (see schematic drawing setup PINEair, Figure 4.1). As it is not known which of the two methods is the best, both methods are taken into account in the analysis to determine  $p_{balance}$  as accurately as possible. Therefore, the difference between the two  $p_{balance}$  determined from the different methods is calculated for each run with a step-wise expansion. If the difference is  $< 2$  mbar,  $p_{balance}$  is determined from the mean value of both methods. If the difference

is  $> 2$  mbar, it has to be assumed that one of the two methods gives an incorrect pressure value, which is why  $p_{balance}$  is determined manually in this case. The calculation of the standard deviations (Figure 4.20) shows that the pressure value of  $p_{balance}$  can be reliably determined using both methods and an uncertainty of  $\pm 1.42$  mbar is assumed.

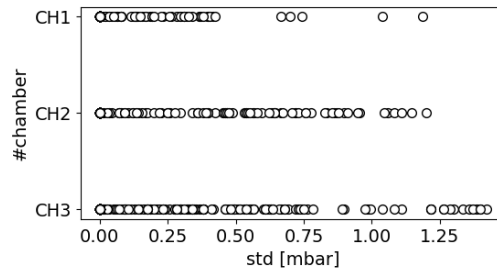


Figure 4.20.: Calculated standard deviations  $std$  for the calculation of the pressure balance the respective expansion chambers CH1, CH2, CH3 from the averaging of the two different methods for determining  $p_{balance}$ .

### Laboratory Measurements: Distinction between Homogeneous and Heterogeneous Freezing

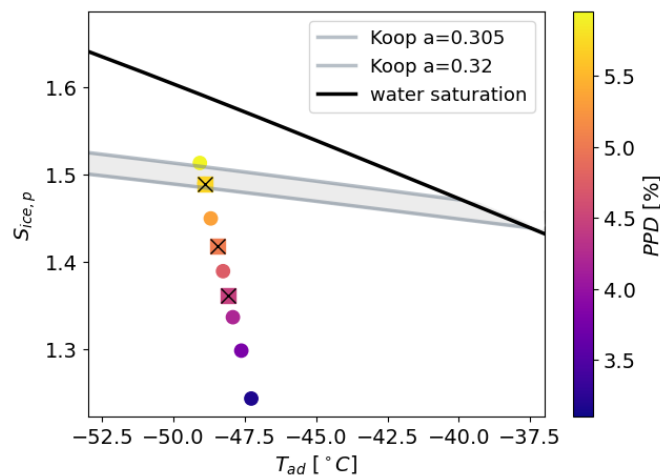


Figure 4.21.: Relative humidity scan with PINEair, the calculated  $S_{ice,p}$  is shown as a function of  $T_{ad}$ , the colors correspond to the  $PPD$  of the step-wise expansion. The black line represents the water saturation, the grey lines the beginning of homogeneous freezing according to Koop et al. (2000). For the symbols marked with a cross, the measurement results are shown in more detail in Figure 4.22.

Test measurements at cirrus conditions were performed with the PINEair prototype I at the AIDA cloud chamber to investigate the differentiation between the homogeneous and heterogeneous ice formation (section 4.3). This paragraph describes the test measurements with the PINEair prototype II, where it was also investigated whether homogeneous and heterogeneous ice formation in the cirrus temperature

range  $< -38^{\circ}\text{C}$  can be distinguished from each other. Here, the APC chamber was used at room temperature and the dewpoint temperature of the air analyzed with PINEair varied between  $-29^{\circ}\text{C}$  and  $-34^{\circ}\text{C}$ . The starting temperature of PINEair was at  $-45^{\circ}\text{C}$ , similar to the measurements with the prototype I at AIDA. Next, a relative humidity scan was performed with PINEair by making several runs with step-wise expansions in a wide range of different *PPDs*, which are illustrated in Figure 4.21. For this, the *PPD* was varied between 3.1 % and 6.2 %, which corresponds to  $S_{ice,p} = 1.24$  and  $S_{ice,p} = 1.52$  using the adiabatic temperature (equation 4.3 in section 4.2.2). According to the parameterization of Koop et al. (2000),  $S_{ice,p}$  has to be larger than 1.48 in order to achieve the relative humidity conditions for homogeneous freezing inside the chamber. Similar to the test measurements with the PINEair prototype I at the AIDA cloud chamber, first only sulfuric acid aerosols were used for a set of experiments where the *PPD* was varied. ATD dust aerosols were added at a later stage to repeat the set of experiments. The generation and injection of the respective aerosols into the APC chamber are described in more detail in section 3.5.

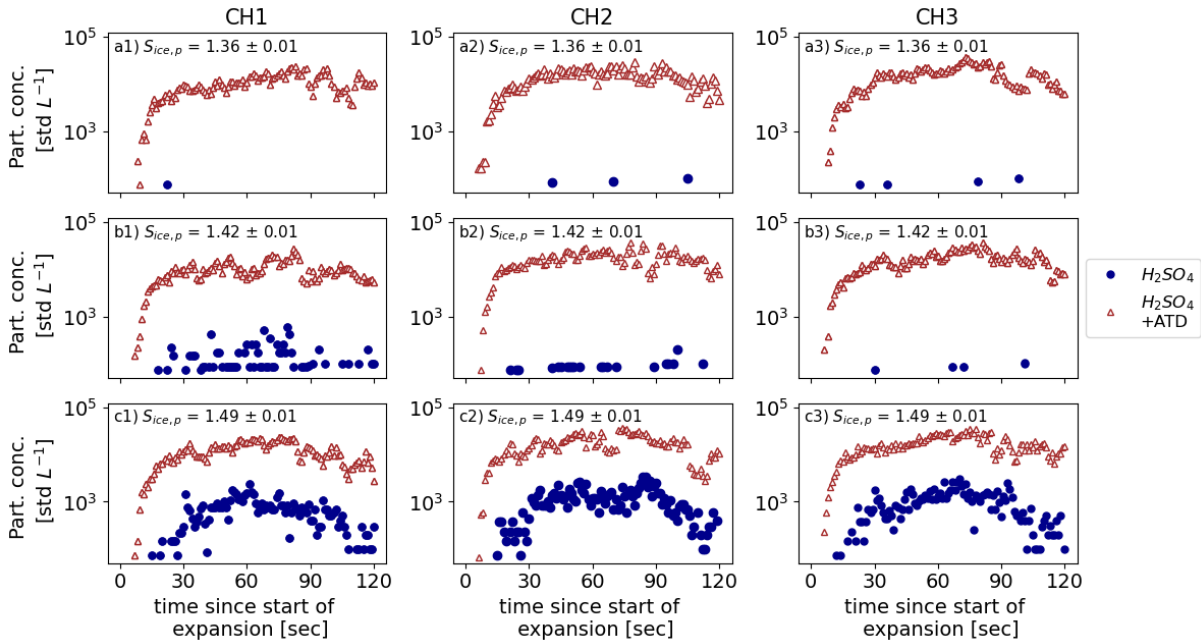


Figure 4.22.: Laboratory measurements with PINEair at the APC chamber with sulfuric acid aerosols (blue circles) and sulfuric acid aerosols+ATD (brown triangles), the particle concentration during different runs with step-wise expansions is shown as a function of time. The panels in the left column show the measurement data of chamber 1 (a1, b1, c1), the middle column of chamber 2 (a2, b2, c2), and the right column of chamber 3 (a3, b3, c3). The measurements were performed at  $T = -45^{\circ}\text{C}$ , waiting time = 60sec and  $flow_{exp} = 0.7\text{L min}^{-1}$ . For the measurements, the *PPD* was varied during the step-wise expansion: for the graphs in the first row (a1, a2, a3)  $S_{ice,p} = 1.36 \pm 0.01$ , in the middle row (b1, b2, b3)  $S_{ice,p} = 1.42 \pm 0.01$ , and in the bottom row (c1, c2, c3)  $S_{ice,p} = 1.49 \pm 0.01$ .

Figure 4.22 shows the measured ice crystal particle concentration during the run as a function of time for three selected *PPDs*, which are marked with a cross inside the square in Figure 4.21. The first column

shows the results of chamber 1 (CH1), the second of chamber 2 (CH2), and the third of chamber 3 (CH3). In the top row, the measurements were performed at a low peak relative humidity (a1, a2, a3), the results in the middle row were conducted at slightly higher peak relative humidity conditions (b1, b2, b3), and in the bottom row, the peak relative humidity inside the chamber was the highest (c1, c2, c3). The calculated  $S_{ice,p}$  are shown in each panel at the top left. In all panels, the blue circles show the experiments with only sulfuric acid aerosols, and the brown triangles show the experiments with sulfuric acid aerosols + ATD. The panels in the first row (a1,a2,a3) indicate by the blue circles (sulfuric acid aerosols) that homogeneous relative humidity conditions are not yet achieved in the chamber at this  $PPD$ , as the particle concentration is almost zero. However, if the same  $PPD$  and sulfuric acid aerosols + ATD aerosols are used (brown triangles), a significantly higher particle concentration is measured, as ATD is an efficient INP, therefore the ice crystals can already form at lower  $S_{ice,p}$ . All three chambers show the same result (top row: a1, a2, a3), which demonstrates that the three chambers of PINEair provide comparable measurements. In the middle row (b1,b2,b3), the experiments are shown with a slightly increased  $PPD$  of 5.03% to 5.11% ( $S_{ice,p} = 1.42 \pm 0.01$ ). At this peak relative humidity, homogeneous freezing already occurs, which is indicated by the higher particle concentration using sulfuric acid aerosols (blue circles). For the runs with an even higher  $PPD$  of 5.64% to 5.73% (bottom row: c1,c2,c3), an even higher peak relative humidity ( $S_{ice,p} = 1.49 \pm 0.01$ ) is achieved inside the chamber, enabling even more ice crystals to be formed homogeneously. These test measurements again demonstrate that it is possible to achieve different peak relative humidity conditions within the chamber by doing runs with step-wise expansions and adjusting the  $PPD$ .

Figure 4.23 shows the comparison of the measurements at the APC chamber with PINEair prototype II (a) with the results from the measurements at the AIDA chamber with PINEair prototype I (b) (see section 4.3.2). In both panels, the calculated  $S_{ice,p}$  is shown as a function of the adiabatic temperature, but only for the experiments with sulfuric acid aerosols. A cross means that homogeneous relative humidity conditions have not yet been reached inside the chamber and therefore no ice crystals have formed. A circle means that homogeneous ice nucleation has occurred. In comparison, it is remarkable that for the measurements at the AIDA chamber (panel b), the beginning of the homogeneous freezing agrees very well with the parameterization according to Koop et al. (2000). In contrast, the homogeneous freezing of the measurements at the APC chamber (panel a) already begins at lower  $S_{ice,p}$  and thus fits better with the parameterization of Schneider et al. (2021b). This parameterization is based on a comprehensive collection of laboratory-based homogeneous freezing experiments with aqueous sulfuric acid aerosol particles at the AIDA chamber (Schneider et al., 2021b). From the differences between the two parameterizations for the onset of homogeneous freezing (Koop et al., 2000 and Schneider et al., 2021b), it is noticeable that further research is necessary. Although the measurements were performed with two different prototypes of PINEair, this is probably not the reason for the different onsets of the homogeneous freezing, as the volume of the expansion chambers of both instruments is identical. The main difference is the hu-

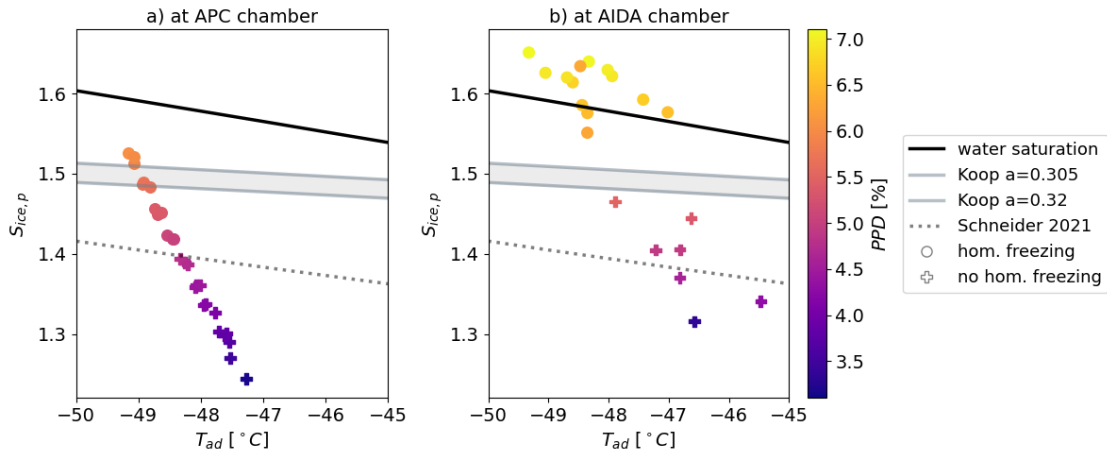


Figure 4.23.: Comparison between the measurements from a) the APC chamber and b) the AIDA chamber with sulfuric acid aerosols. The calculated  $S_{ice,p}$  as a function of  $T_{ad}$  is shown, and the color corresponds to the  $PPD$  during the step-wise expansion with PINEair. The circles indicate that homogeneous ice nucleation occurred in PINEair at this  $PPD$ , while the crosses show that no ice crystals were formed. The black line shows the water saturation, the grey line the onset of homogeneous freezing according to Koop et al. (2000) and the dashed line the parameterizations for homogeneous freezing by Schneider et al. (2021b).

midity of the sampled air, for the measurements at the AIDA chamber the relative humidity was 100%, while for the measurements at the APC chamber, the air was significantly more humid. This shows that the humidity of the sampled incoming air has an influence on the onset of the homogeneous freezing, therefore this observation is explained and discussed in more detail in the subsection "Influence of dew point temperature".

These differences show that the threshold for the start of the homogeneous freezing should not be determined based on  $S_{ice,p}$  and the comparison with existing parameterizations, since, on the one hand, it is not known which of the various parameterizations is the best and, on the other hand, the calculation of  $S_{ice,p}$  in the measurements with PINEair has uncertainties. Here, the highest uncertainty is caused due to  $S_{ice}$  at the start of the expansion, which can only be estimated. For the calculation of  $S_{ice,p}$  the assumption is made that  $S_{ice} = 1$  at the start of the expansion. However, this assumption is probably not valid for measurements at ambient air conditions. Especially when measurements are performed in the cirrus temperature range, the dew point temperature of the sampled air was  $> -27^{\circ}\text{C}$  and this means  $S_{ice} > 1$ . In addition, the waiting time before the start of the expansion also has an influence on  $S_{ice}$ , it can be assumed that the entering humidity is decreased, as the excess of water vapor deposits on the chamber walls. In the future, more detailed laboratory measurements will be done to investigate  $S_{ice}$  at the start of the expansion.

A better way to specify the conditions for reaching the homogeneous relative humidity conditions inside the chamber is to determine a threshold value for the  $PPD$  of the step-wise expansion. For this purpose, a relative humidity scan is performed with PINEair by making several consecutive runs with increasing

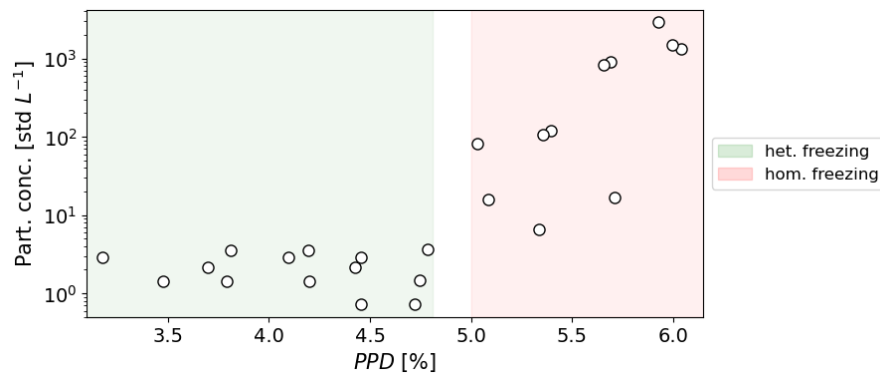


Figure 4.24.: Particle concentration for each run as a function of the  $PPD$  for the PINEair measurements using sulfuric acid aerosols in the APC chamber ( $T = -45^{\circ}\text{C}$ ). The green background shows the range of the  $PPD$  where no ice crystals have formed homogeneously. By contrast, the red background shows the range for the  $PPD$  at which homogeneous relative humidity conditions were achieved in the chamber resulting in the formation of ice crystals.

$PPDs$ . Figure 4.24 shows the measured particle concentration of each run as a function of the  $PPD$ , only measurements with sulfuric acid aerosols are shown. At approximately  $PPD = 5\%$ , a steep, sharp increase in the measured INP concentration can be seen, which indicates the start of the homogeneous freezing. This means relative humidity conditions for homogeneous freezing are achieved inside the chamber for all runs where a  $PPD$  larger than  $5\%$  was used. In the case of runs with a  $PPD$  lower than  $4.8\%$ , the relative humidity in the chamber is too low for homogeneous freezing, and only heterogeneous ice nucleation can occur with the help of an INP. Since only the measurements performed with sulfuric acid aerosols are shown in Figure 4.24, it is easier to identify the onset of homogeneous freezing.

### Field Measurements: Distinction between Homogeneous and Heterogeneous Freezing

The measurements in the laboratory (see subsection above) were performed with aerosol types of known ice nucleation activity and at constant humidity conditions at the start of the expansion. When operating PINEair for atmospheric measurements, the situation is less clear because the sampled aerosol may include a mixture of aerosols with different ice nucleation behavior, and the ambient humidity can vary. Therefore, some test measurements were performed with the PINEair prototype II by sampling ambient air at Campus North to determine the threshold of the  $PPD$  for inducing the onset of homogeneous freezing.

Figure 4.25 shows an example measurement series from April 14, 2023. The starting temperature in PINEair was  $-45^{\circ}\text{C}$  and the dewpoint temperature of the sampled air was  $-24.2^{\circ}\text{C}$ . The peak relative humidity was increased in a series of runs with step-wise expansions at increasing  $PPDs$  (relative humidity scan), as described in the previous subsections. The particle concentration measured in each run is shown in Figure 4.25 as a function of the  $PPD$ . Similar to the laboratory measurements (see subsection above), the measured particle concentration increases with increasing  $PPDs$ , and therefore, the

homogeneous freezing can as well be detected and distinguished from the heterogeneous ice nucleation. However, when measuring at ambient air conditions, a transition area can be observed (blue shaded area), e.g. in Figure 4.25 between a  $PPD$  of 4.89 % and 5 %. Here, at similar  $PPDs$ , for some runs, only heterogeneous ice nucleation occurred, whereas for other runs already homogeneous freezing happened. This transition area is strongly influenced by  $S_{ice}$  at the start of the expansion in the chamber (more detailed information in the next subsection), which fluctuates more in field measurements than in laboratory measurements. Therefore, it is important to regularly perform a relative humidity scan, especially during field measurements, in order to redefine the onset of the transition range, depending on the  $PPD$ . Then, measurements can be performed specifically in that range of  $PPDs$  where only heterogeneous humidity conditions are reached to obtain information about the existing INP concentration as a function of the different  $PPDs$ . This area is indicated by the green shaded area in Figure 4.25, here, the measured particle concentration is equal to the INP concentration. At even higher  $PPDs$ , homogeneous relative humidity conditions are achieved (red shaded area). In this area, both heterogeneous ice nucleation takes place, as this already starts at lower  $S_{ice}$  and homogeneous freezing. The unshaded areas show the  $PPDs$  where no measurements were performed, thus they cannot be categorized in any of the previously mentioned areas.

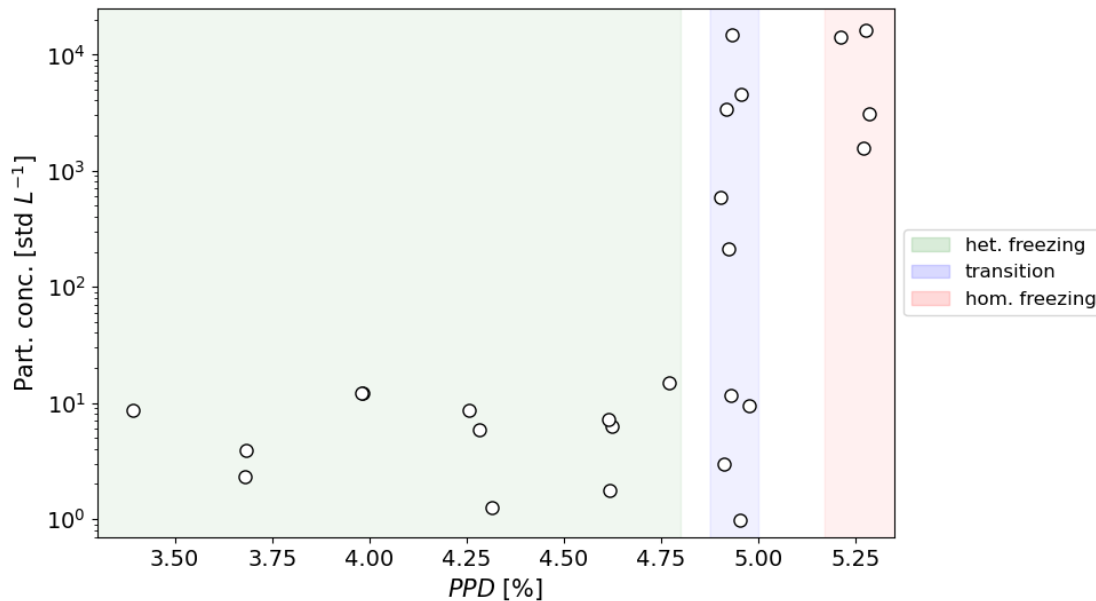


Figure 4.25.: The particle concentration of different runs as a function of  $PPD$  is shown for a typical series of measurements performed under ambient air conditions on April 14, 2023 at Campus North ( $T_{start} = -45^{\circ}\text{C}$ ,  $T_{DP} = -24.2^{\circ}\text{C}$ ). The colored shading indicates the different areas: in the green area relative humidity conditions for heterogeneous freezing are achieved, in the blue area the transition area occurs (homogeneous and heterogeneous ice nucleation possible) and in the red area and thus at the highest  $PPD$  homogeneous relative humidity conditions are achieved.

### Influence of Dewpoint Temperature

A comparison of the laboratory measurements performed at the AIDA and the APC chamber has shown that the threshold of the *PPD* for the start of the homogeneous freezing is strongly dependent on the humidity of the sampled air into PINEair (Figure 4.23). The humidity of the ambient air can vary on short time scales, e.g. by precipitation events. The humidity content of the sampled air can be reduced to some extent using the dryer of PINEair, but it cannot be reduced to a dewpoint temperature below about  $-26^{\circ}\text{C}$  or kept constant at low dewpoint temperature for longer time periods.

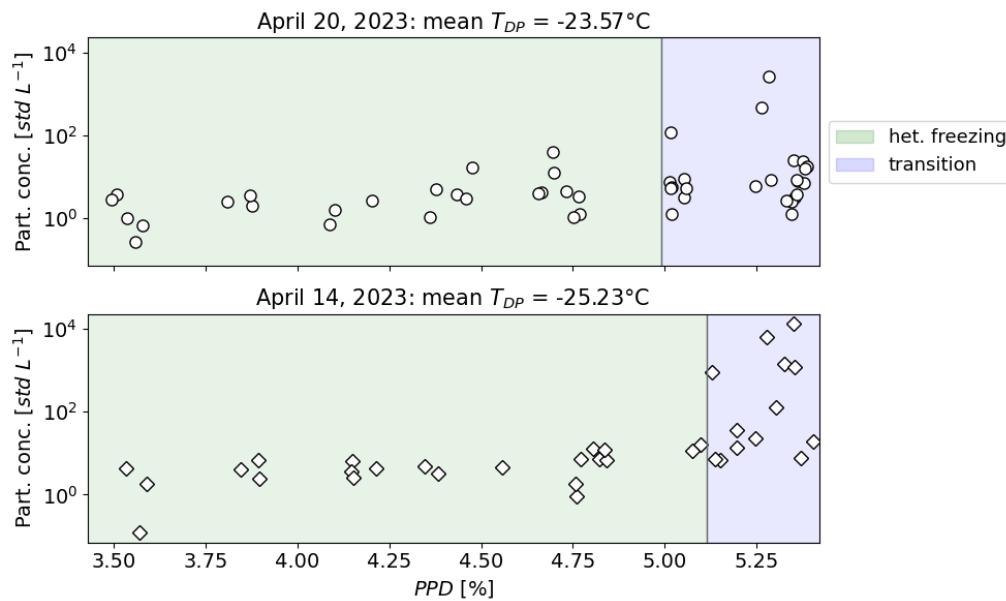


Figure 4.26.: Comparison of two measurement series performed with PINEair at ambient air conditions at Campus North, upper panel on April 20, 2023 with  $T_{DP} = -23.57^{\circ}\text{C}$  and the lower panel on April 14, 2023 with  $T_{DP} = -25.23^{\circ}\text{C}$ . The ice particle concentration as a function of the *PPD* is shown ( $T = -45^{\circ}\text{C}$ ). The green background indicates the heterogeneous freezing and the blue background represents the transition region where both heterogeneous ice nucleation and homogeneous freezing may contribute to the observed ice number concentration. If the incoming air in PINEair is more humid, the relative humidity conditions for the transition region are reached at a lower *PPD*.

Figure 4.26 shows a comparison of two measurements at different ambient conditions performed at Campus North, in each case a relative humidity scan was performed in PINEair with several runs at different *PPDs* for the step-wise expansion. The measured ice particle concentration per run is shown as a function of the *PPD* and the area where only heterogeneous freezing happens is shaded in green, while the transition area (homogeneous and heterogeneous ice nucleation) is shaded in blue. The starting temperature in PINEair was  $-45^{\circ}\text{C}$  in both cases. The upper panel shows the measurement from April 20, 2023,  $T_{DP} = -23.57^{\circ}\text{C}$ , and the transition area starts at a *PPD* of 4.99%. In comparison, the lower panel shows the measurements from April 14, 2023, where  $T_{DP} = -25.23^{\circ}\text{C}$  and the beginning of the transition area is shifted to a larger *PPD* of 5.11%. This can probably be explained by the fact that in the second example,  $S_{ice}$  at the start of the expansion is lower, and therefore a larger *PPD* with a larger

adiabatic cooling is required to achieve the same  $S_{ice}$  conditions required for homogeneous freezing.

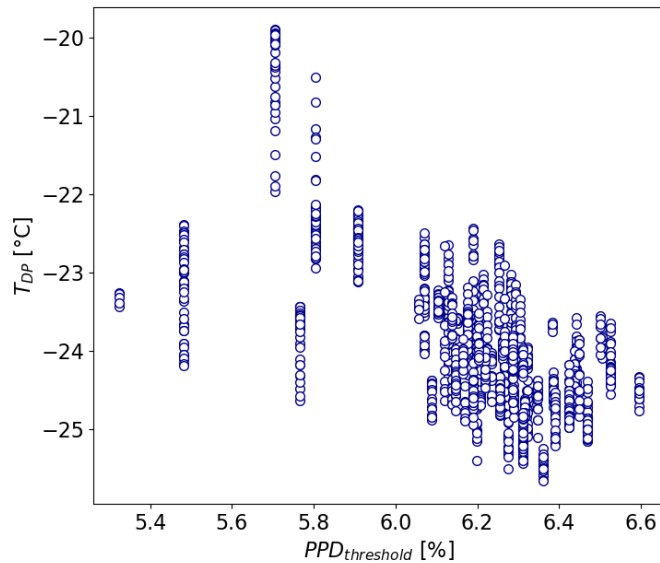


Figure 4.27.: Data from the first field measurement campaign with PINEair at the SBO:  $T_{DP}$  of the sampled air as a function of  $PPD_{threshold}$  for all runs with step-wise expansions. The higher  $T_{DP}$  is, the lower the threshold  $PPD_{threshold}$ .

Figure 4.27 shows an overview of  $T_{DP}$  of the incoming air as a function of the threshold value  $PPD_{threshold}$  at the beginning of the transition area of all measurements made during the first field measurement campaign with PINEair prototype II at the Sonnblick Observatory (more detailed information in section 4.5). The threshold  $PPD_{threshold}$  shifts significantly to lower values as soon as the incoming air is more humid. This illustrates the importance of the waiting time before the start of the expansion to achieve more homogeneous temperature and relative humidity conditions inside the chamber before start of the expansion.

The influence of the humidity of the sampled air on the start of the transition area or homogeneous freezing makes the evaluation of the data measured by PINEair in the cirrus temperature range more difficult. Particularly for long-term measurements or in places where the humidity changes considerably during the day, it is important to ensure that relative humidity scans in PINEair are carried out regularly with step-wise expansions at different  $PPDs$ .

#### 4.5. First Field Campaign with the PINEair Prototype II

For the first time, INP concentrations in the cirrus temperature range were measured at the SBO (3106 m a.s.l.) during a field campaign from May 8 to 22, 2023, using the PINEair prototype II. Section 4.5.1 first provides a general overview of the measurement campaign, information about additional instruments that were used to evaluate the INP data, and the temperature settings for the measurements with PINEair.

In section 4.5.2, the measurements with PINEair are discussed, first the INP measurements in the MPC temperature range and then the measurements in the cirrus temperature range. As part of this doctoral thesis, further extensive long-term measurements were conducted at the SBO to investigate the diurnal and seasonal variability of the INP concentration, which are described and discussed in more detail in the next chapter 5.

#### 4.5.1. Overview of Campaign



Figure 4.28.: Picture of the mountain Hoher Sonnblick in Austria during summertime. On its peak, the Sonnblick Observatory (SBO) is located.

The novel PINEair instrument is designed to measure INP concentrations during research aircraft missions in a wide temperature range from MPC to cirrus formation conditions, with special emphasis on measurements in the FT. To test the PINEair operation in the lower FT, the SBO site was selected for the first field measurement campaign (May 8 to May 22, 2023) using the PINEair prototype II. This location is well-suited for this purpose since it is a high-altitude observatory at 3106 m a.s.l. (Figure 4.28), which is mostly situated in the lower FT. Thus, the sampled aerosol and INP population has the potential to impact cirrus cloud formation when lifted further in the atmosphere. Moreover, especially in summer, there is also an influence from the BL, due to the rising warm air masses caused by convection (Holzinger et al., 2010), which increases the number concentration of natural and anthropogenic aerosols. A detailed description of the location of the SBO, as well as further information about the observatory (e.g. measuring instruments), can be found in section 5.2.

#### 4. Development and Application of the New Aircraft-Based Expansion Chamber PINEair

For the INP measurements during the campaign in May 2023, PINEair was connected to the total air inlet at the SBO station. The inlet is designed according to GAW (Global Atmospheric Watch) guidelines and has an upper cut-off size for particles with a diameter larger than  $20\ \mu\text{m}$  at a wind speed of  $20\ \text{m s}^{-1}$ . To be able to compare the measurement results of the new PINEair instrument at MPC conditions with other already established INP instruments, aerosol filter samples with a time resolution of 10 – 12 h were additionally taken on certain days and then analyzed in the laboratory using the offline freezing experiment INSEKT (see section 3.2). The aerosol sampler was connected to the same inlet as standard station instruments that measure aerosol parameters. For the interpretation of the measured INP concentration, the data from the following instruments are used (Figure 4.29): The total aerosol concentration measured with a CPC 3775 (company: TSI GmbH), the particle size distribution measured with the particle counter model TCC (company: Klotz GmbH), and the particle mass concentration measured with the SHARP (Synchronized Hybrid Ambient Real-time Particulate) Monitor 5030 (company: Thermo Scientific). The measurements of these instruments are performed at the respective ambient temperature and a time resolution of a few minutes. For the results shown in this PhD thesis, average values for 30 min time intervals were used. A detailed overview of further measurements performed at the SBO can be found in section 5.2.

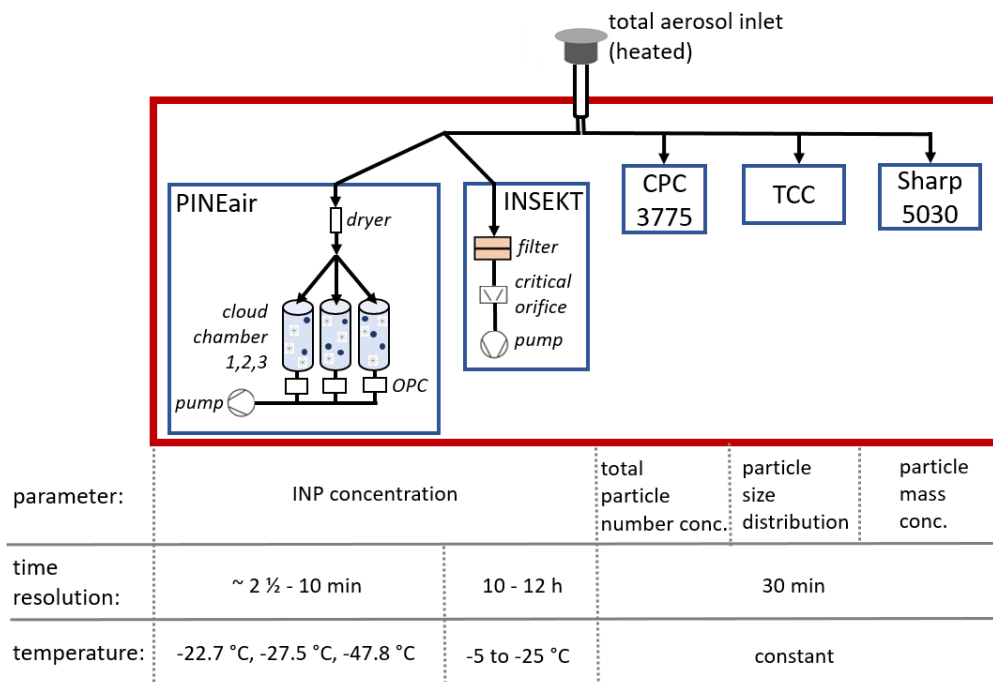


Figure 4.29.: Instrumental setup that was used during the campaign from May 8 to 22, 2023, at the SBO. Measured parameters, the time resolution, and the temperature range are listed below the scheme.

During the campaign, the temperature and targeted cloud regime in PINEair was varied. During the day, INP measurements were conducted between  $T = -49.24\ ^\circ\text{C} \pm 1\ ^\circ\text{C}$  and  $T = -46.45\ ^\circ\text{C} \pm 1\ ^\circ\text{C}$  in the

cirrus temperature range. During the night, the instrument was operated in the MPC temperature range at  $T = -27.5^\circ\text{C} \pm 1^\circ\text{C}$  and  $T = -22.7^\circ\text{C} \pm 1^\circ\text{C}$ . The start of the daytime measurement cycle varied between 4 and 8 UTC, and the end between 7 and 9 UTC.

For the measurements in the cirrus temperature range, runs with step-wise expansions were performed with PINEair at different  $PPDs$  in the range of 4.87% and 6.52% to achieve different  $S_{ice,p}$  conditions inside the chamber. For this, the temperature of the ethanol thermostat was always set to  $T_{chiller} = -48^\circ\text{C}$ . Depending on the value used for the  $PPD$ , this results in a minimum temperature between  $T = -46.45^\circ\text{C} \pm 1^\circ\text{C}$  and  $T = -49.24^\circ\text{C} \pm 1^\circ\text{C}$  after the adiabatic temperature drop due to the step-wise expansion (see equation 4.2 for the calculation of the adiabatic temperature). The dew point temperature of the sampled air varied between  $-20.5^\circ\text{C}$  and  $-25.6^\circ\text{C}$  after the drying process with the dryers from PINEair. A waiting time of 60sec and  $flow_{exp} = 0.7\text{L min}^{-1}$  was used for all measurements (see section 4.4.1 for validation of these values).

The first experiments at cirrus temperatures showed that the sampled air was too humid for longer operation over several hours. The humidity could only be reduced by reducing the sample flow through the dryers. Therefore, only two chambers instead of all three were used for most of the operations at cirrus cloud temperatures. The time resolution was thereby approximately 5 min - 10 min.

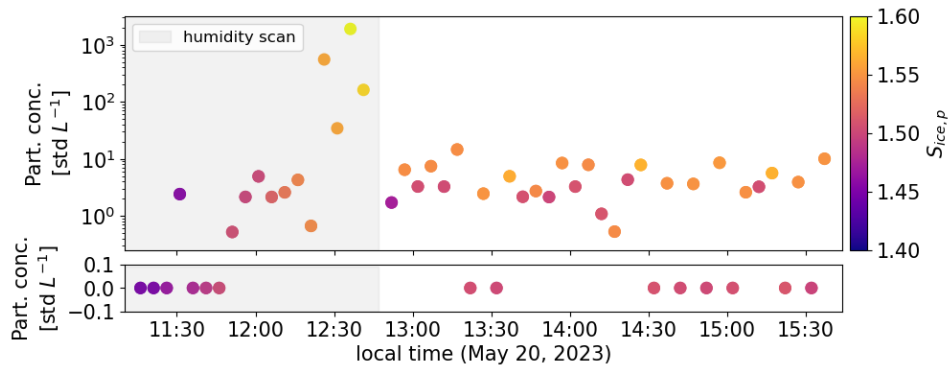


Figure 4.30.: Example measurement with PINEair at cirrus temperatures ( $T_{chiller} = -48^\circ\text{C}$ ) on May 20, 2023 at the SBO: Grey area shows the relative humidity scan, where  $PPD$  and thus  $S_{ice,p}$  (marked by the colors) is increased until homogeneous freezing conditions are reached. The area without shading shows the measurement at  $\sim$  constant  $PPD$ , where only heterogeneous saturation conditions are reached in the expansion chamber.

As already explained in more detail in section 4.4.2, the humidity of the sampled ambient air changes the threshold value of the  $PPD$ , where the peak relative humidity inside the chamber is high enough that homogeneous freezing can occur. For this reason, relative humidity scans with PINEair were performed regularly throughout the day during the INP measurements at cirrus conditions to identify the threshold value of the  $PPD$  for the onset of the homogeneous freezing. Afterwards, INP measurements were conducted for several hours at a constant  $PPD$ , which limited the peak relative humidity conditions to

conditions where only heterogeneous ice nucleation can occur in the chamber. Figure 4.30 shows an example measurement for the INP concentration from May 20, 2023, between 11:10 local time and 15:40 local time ( $T_{chiller} = -48^{\circ}\text{C}$ ), the colors correspond to  $S_{ice,p}$  inside the chamber, which is caused by the different  $PPD$  during the step-wise expansions. The gray shaded area shows the relative humidity scan; at a higher  $S_{ice,p}$ , higher particle concentrations are measured. The unshaded area shows the measurement at an approximately constant  $PPD$  (only heterogeneous freezing), here the particle concentration varied between  $0\text{std L}^{-1}$  and  $14.6\text{std L}^{-1}$  corresponding to ice crystals formed by the presence of INPs.

For the INP measurements in the MPC temperature range, (continuous) expansions without the buffer volume were performed with  $flow_{exp} = 1.7\text{L min}^{-1}$  and a waiting time of 60sec. In this analysis, the INP activation temperature corresponds to the gas temperature measured with the lowest temperature sensor  $T_{gas3}$  in the PINEair chamber. In the period from May 9 to May 16, 2023, measurements were performed with PINEair at  $-27.5^{\circ}\text{C} \pm 1^{\circ}\text{C}$ . To compare the INP concentration from the novel PINEair instrument to another INP technique, and thus to validate its results, in the second week of the campaign, from May 17 to May 22, 2023, additional, aerosol filters were taken overnight to analyze them for their INP content offline in the laboratory with the instrument INSEKT. As this INP measurement method provides information about the INP content in the temperature range between approximately  $-5^{\circ}\text{C}$  and  $-25.5^{\circ}\text{C}$ , PINEair measurements were performed in parallel at a temperature of  $-22.7^{\circ}\text{C} \pm 1^{\circ}\text{C}$  in the same period. For those experiments in the MPC temperature range, the drying of the ambient air with the dryers of PINEair was sufficient, and therefore all three expansion chambers of PINEair could be used for the measurements, resulting in a time resolution of approximately 2.5 min.

Background tests were carried out at least twice a day to ensure that there was no internally formed ice on the chamber walls of PINEair due to the incoming humid air with dew point temperatures higher than the wall temperatures. All the tests showed that no internal ice formed. They were always conducted before changing the cloud regime, which means in the morning before the start of the measurements at the cirrus temperatures and in the evening before the start of the measurements in the MPC temperature range.

#### 4.5.2. Results and Discussion

In the following, the results of the PINEair measurements in the MPC temperature range are discussed. First, a time series for comparing the INP concentration with aerosol properties, second, a comparison of PINE air with the offline freezing experiment INSEKT is presented.

Afterwards, the results of the INP measurements in the cirrus temperature range are presented. The INP concentration measured as a function of  $S_{ice,p}$  is discussed for the entire measurement period and for two selected days when changes in the aerosol population occurred. Next, a comparison is shown between the INP measured for a selected  $S_{ice,p}$  range and the aerosol measurements. Finally, results are shown for INP measurements at the SBO and other stations (Puy de Dôme (France, 1470m a.s.l), KIT Campus

North (Germany, 120 m a.s.l.), providing a broader view on the FT INP concentration in the cirrus cloud regime.

## INP Measurements at Mixed-phase Cloud Temperatures

### Comparison to Aerosol Measurements

Due to the high time resolution of 2.5 min, the measurements with PINEair can detect short-term variations in the INP concentration. To better understand the sources for the variations in the INP concentration, a comparison to the measurements of the aerosol particle properties is conducted. This approach has been used in other previous studies, such as by e.g., DeMott et al. (2010), Conen et al. (2015), Schneider et al. (2021a), and Brunner et al. (2022).

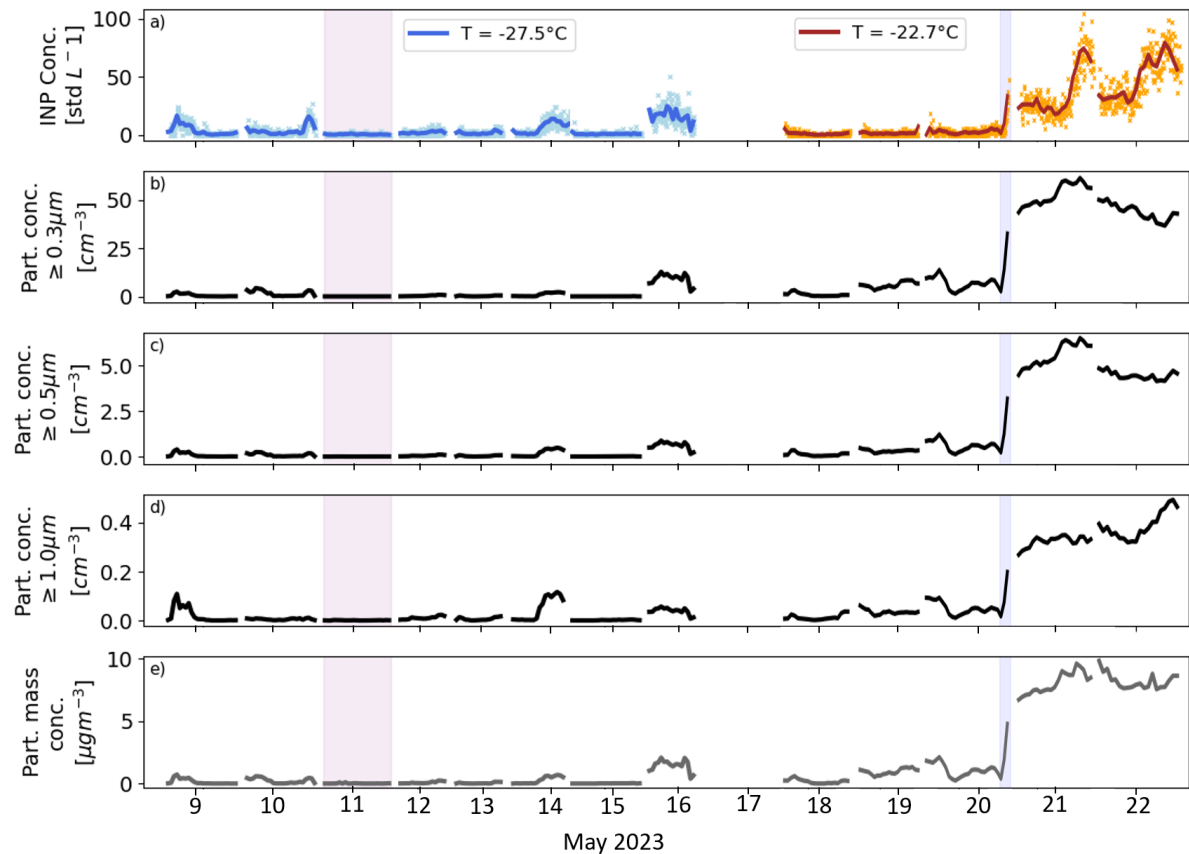


Figure 4.31.: Time series of the INP concentration measured with PINEair (panel a:  $T = -27.5^{\circ}\text{C} \pm 1^{\circ}\text{C}$  in blue,  $T = -22.7^{\circ}\text{C} \pm 1^{\circ}\text{C}$  in orange), the concentration of aerosol particles with diameters  $d$  larger than  $0.3\ \mu\text{m}$  (panel b),  $0.5\ \mu\text{m}$  (panel c),  $1.0\ \mu\text{m}$  (panel d) and the particle mass concentration (panel e) in the period from May 8 to May 22, 2023. Purple and blue shaded area show an example in which all parameters show the same trend. Crosses indicate the measurements with a time resolution of 2.5 min, solid lines show the 30 min mean values.

The INP concentration measured at  $T = -27.5^{\circ}\text{C} \pm 1^{\circ}\text{C}$  and  $T = -22.7^{\circ}\text{C} \pm 1^{\circ}\text{C}$  (Figure 4.31 panel a) is compared to the concentration of aerosol particles with diameters  $d \geq 0.3\ \mu\text{m}$  (panel b),  $\geq 0.5\ \mu\text{m}$

(panel c) and  $\geq 1.0 \mu\text{m}$  (panel d), and the particle mass concentration (panel e). In panel a, the crosses show the single data points with the highest time resolution of the PINEair measurements with 2.5 min and the thick lines in Figure 4.31 depict the 30 min mean values.

For the PINEair measurements at  $T = -27.5^\circ\text{C} \pm 1^\circ\text{C}$ , the INP concentration varied between a concentration below the limit of detection (LOD) and  $50.0 \text{ std L}^{-1}$  (Figure 4.31 blue crosses in panel a). At the higher temperature of  $T = -22.7^\circ\text{C} \pm 1^\circ\text{C}$ , on the other hand, the INP concentration varied between a concentration below LOD and  $104.3 \text{ std L}^{-1}$  (Figure 4.31 red crosses in panel a).

The time series of the INP concentration, the aerosol concentration, and the particle mass concentration show similar trends for both nucleation temperatures. For example, on the morning of May 20, 2023 (blue shaded area in Figure 4.31), a sudden increase in the particle concentration in all three sizes, as well as in the particle mass concentration, was measured. At the same time, a peak in the INP concentration from approximately  $1 \text{ std L}^{-1}$  to  $33 \text{ std L}^{-1}$  was measured. If, on the other hand, the particle concentration and the particle mass concentration remained constantly low, e.g. in the night from May 10 to May 11, 2023 (purple shaded area in Figure 4.31), the INP concentration also remained constantly low between a concentration below LOD and  $1.1 \text{ std L}^{-1}$ .

Table 4.2.: Spearman correlation coefficient  $\rho$  between INP concentration (measured with PINEair at  $T = -27.5^\circ\text{C}$ ,  $-22.7^\circ\text{C}$ ) and concentration of aerosol particles for different sizes, and particle mass concentration. All data sets are averaged to 30min mean values. For all parameters, the p-value is  $< 0.05$  and therefore the correlation is significant.

	$\rho (T = -27.5^\circ\text{C})$	$\rho (T = -22.7^\circ\text{C})$
part. conc. $\geq 0.3 \mu\text{m} [\text{cm}^{-3}]$	0.89	0.82
part. conc. $\geq 0.5 \mu\text{m} [\text{cm}^{-3}]$	0.9	0.85
part. conc. $\geq 1.0 \mu\text{m} [\text{cm}^{-3}]$	0.86	0.87
part. mass conc. $[\mu\text{m m}^{-3}]$	0.83	0.86

Indeed, there is a strong correlation between the aerosol concentration, the particle mass concentration, and the INP concentration. This is confirmed by calculating the Spearman correlation coefficient  $\rho$ . The calculated  $\rho$  for the correlation between the measured INP concentration and the respective aerosol parameters are larger than 0.8 (table 4.2). It is noticeable that  $\rho$  for the correlation is higher for the INP concentration and the larger aerosol particles ( $\geq 1.0 \mu\text{m}$ ), but only at the higher temperature of  $T = -22.7^\circ\text{C} \pm 1^\circ\text{C}$ . This indicates that larger particles may be more efficient INPs, which was also shown by e.g., Connolly et al. (2009), and Mason et al. (2016). This can also be seen, for example, in the measurement on May 22, 2023, where the trend of the INP concentration corresponds best with the trend of the concentration of aerosol particles with diameters larger than  $1.0 \mu\text{m}$ . In the study by Lacher et al. (2018b), the INP concentration was measured with the online instrument HINC (Horizontal Ice Nucleation Chamber (Lacher et al., 2017) type: CFDC) at the High Altitude Research Station Jungfraujoch (Switzerland, 3580m a.s.l.) during eight field campaigns in winter, spring, and summer between

the years 2014 - 2017. Here, a maximum  $\rho = 0.7$  was calculated for the correlation of the aerosol parameters and the INP concentration at  $T = -31^\circ\text{C}$ . Interestingly the calculated correlation coefficients are higher at the SBO, which might be related to the shorter observation period, the sampling location, or the difference in nucleation temperature.

Furthermore,  $\rho$  was calculated for the correlation of the INP concentration with meteorological parameters such as temperature, pressure, relative humidity, wind direction, and wind speed, but the correlation was found to be  $< 0.5$  and therefore not significant. This suggests that the INP population at the SBO was not directly dependent on the weather situation during the measurement period. A similar result was found in the study by Lacher et al. (2018b).

### Comparison of PINEair with INSEKT

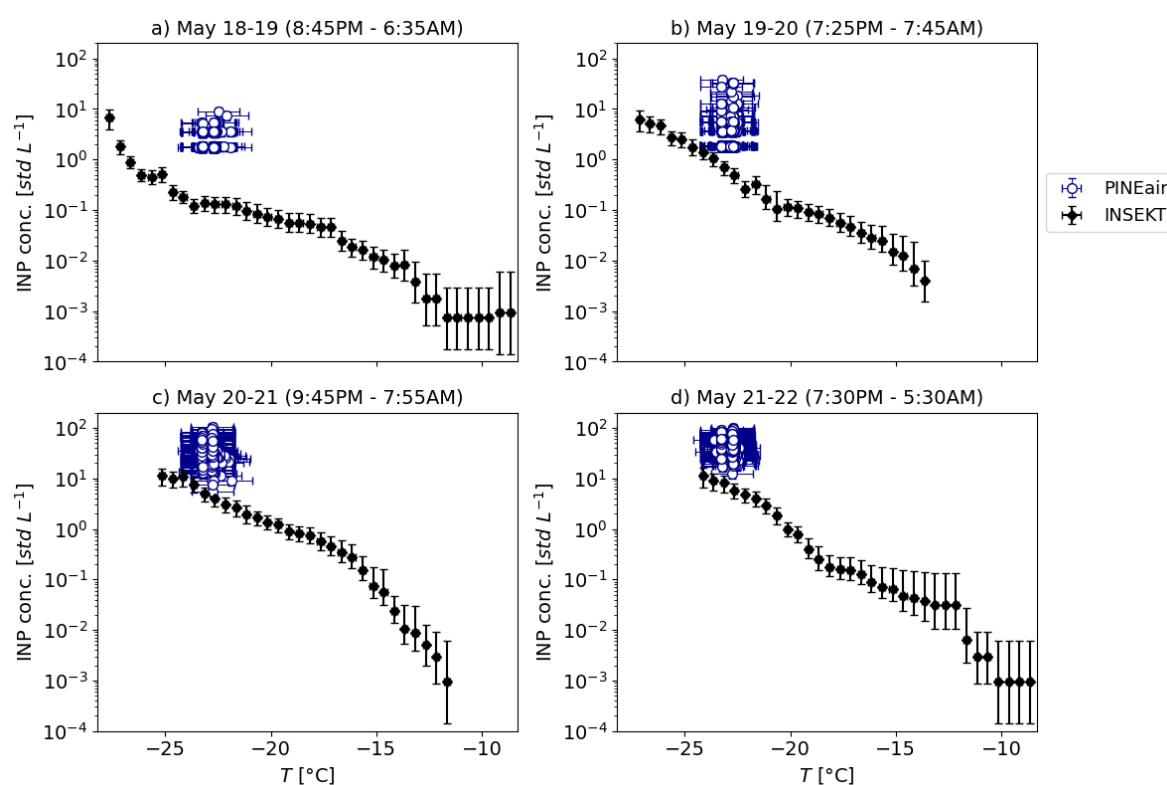


Figure 4.32.: INP temperature spectra for four different nights, where a comparison between the measurements of the online instrument PINEair (blue circles) and offline instrument INSEKT (black diamonds) is possible. Data measured by PINEair have a time resolution of 2.5 min and were taken during the same period as the filter sampling.

To evaluate the performance of the new PINEair instrument during measurement intervals at the higher temperature of  $-22.7^\circ\text{C}$ , aerosol filters were simultaneously taken for analysis with the offline freezing experiment INSEKT. Figure 4.32 shows the INP temperature spectra for the four nights where PINEair

was operated at high temperatures overlapping with the INSEKT temperature range. The aerosol filters (black diamonds) were collected for time periods of  $\sim 10 - 12$ h. The measurements with PINEair (blue circles) were performed during the same interval of the aerosol sampling, they are shown with a time resolution of 2.5 min (no averaging) from all three expansion chambers. Due to the high time resolution, it can be seen that the INP concentration varies during all four nights. For example, on the night of May 20 - 21, the INP concentration varies from  $5.5 \text{ std L}^{-1}$  to  $104.3 \text{ std L}^{-1}$  (Figure 4.32 panel c).

In all four examples, the INP concentration measured with PINEair is slightly higher compared to the measurement with INSEKT. The reason for the differences is not clear, only assumptions can be made and similar differences have also been found in other studies. For example, section 5.4.6 shows a comparison between PINE-04-02 (commercial PINE version with a chamber volume of 10L) and INSEKT, where also an underestimation of the INP concentration by INSEKT was found for some days. Possible sources of error for the measurement with PINEair could be a temperature offset. This could be caused due to the temperature inhomogeneities inside the chambers, or the response time of the temperature sensors is too slow so that the rapid temperature change during the expansion cannot be detected quickly enough. At the same time it is possible that INSEKT is underestimating the INP concentration, e.g., by an incomplete wash-off of the particles from the filter, or by a partial dissolution of the particles or ice-active structures in water.

### INP Measurements at Cirrus Temperatures

#### INP Concentration as a Function of Ice Saturation Ratio

For the PINEair measurements at cirrus conditions, several runs were performed with different *PPDs* between 4.87% and 6.52%, resulting in different  $S_{ice,p}$  inside the expansion chambers. This aims at differentiating between homogeneous and heterogeneous freezing.

The lower panel in Figure 4.33 depicts the measured ice crystal concentration as a function of  $S_{ice,p}$ , averaged over the entire period of the campaign. The measured ice crystal concentration is shown as a box plot, here, the red number corresponds to the red line and describes the median. The circles show the outliers and the top horizontal line indicates the maximum of the data set. The minimum is represented by a lower horizontal line, as the ice crystal concentration is below the LOD for all  $S_{ice,p}$  ranges and is not visible due to the logarithmic scale of the y-axis. The upper line of the box indicates the 75% quartile, which corresponds to the median of the top 50% of the data set. The bottom line of the box describes the 75% quartile and shows the median of the lowest half of the data set. For the calculation of  $S_{ice,p}$  (described in section 4.2.2), the adiabatic temperature was used, which varied between  $T_{ad} = -46.45^\circ\text{C}$  and  $-49.24^\circ\text{C}$ , depending on the *PPD* used for the step-wise expansion. In all the measurements shown in Figure 4.33, the ethanol thermostat was set to  $T_{chiller} = -48^\circ\text{C}$ , which corresponds to a start temperature inside the chambers of  $T_{gas3} \sim -44.6^\circ\text{C}$  (lowest temperature sensor). The numbers in the upper panel show the number of runs performed with PINEair in each  $S_{ice,p}$  range, as information about the statistics

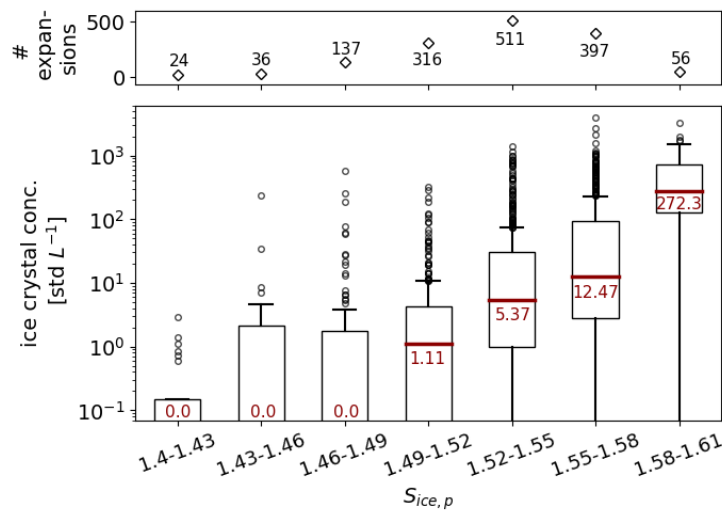


Figure 4.33.: Number of performed runs (upper panel) and ice crystal concentration (lower panel) as a function of different  $S_{ice,p}$  ranges. All measurements performed in the cirrus temperature range ( $T_{chiller} = -48^\circ\text{C}$ ) during the entire measurement period are shown; the ice crystals were formed via heterogeneous and homogeneous nucleation. The red numbers show the median of the ice crystal concentrations per  $S_{ice,p}$  range.

of the data. Based on the median of the ice crystal concentration, it can be seen that the measurements agree well with the theory (Koop et al., 2000), that more ice crystals are formed if there is a higher  $S_{ice,p}$  inside the chamber. The median ice crystal concentration varies between the LOD and  $272.3 \text{ std L}^{-1}$  depending on the different  $S_{ice,p}$  ranges. The transition between homogeneous and heterogeneous freezing is not clearly visible due to the averaging of the long time series.

Therefore, an analysis was performed where only the measurements in which the ice crystals were formed by heterogeneous ice nucleation are considered (Figure 4.34). The distinction between heterogeneous and homogeneous freezing was done in the same way as described in section 4.4.2 by determining a threshold value for the  $PPD$  during the step-wise expansion by visualizing the measured INP concentration as a function of the  $PPDs$ . The measured INP concentrations are shown in a box plot (Figure 4.34 lower panel). In general, a wide range of INP concentration can be observed for each  $S_{ice,p}$  range, for example at  $S_{ice,p} = 1.49 - 1.52$  the measured INP concentration varies between a concentration below LOD and  $90.1 \text{ std L}^{-1}$ . This is probably because the air masses came from different directions during the two-week measurement campaign, and thus the aerosol concentration present at SBO was also affected by strong fluctuations (see next subsection). When comparing the ranges  $S_{ice,p1} = 1.43 - 1.46$  and  $S_{ice,p2} = 1.55 - 1.58$ , it is noticeable that the maximum and the 75% quartile are higher for  $S_{ice,p1}$ , although  $S_{ice,p1} < S_{ice,p2}$ . The reason for this is probably that for  $S_{ice,p2}$  a fewer number of runs were performed with PINEair because homogeneous freezing has already occurred for  $S_{ice,p2}$  more often, thus the statistic is not optimal.

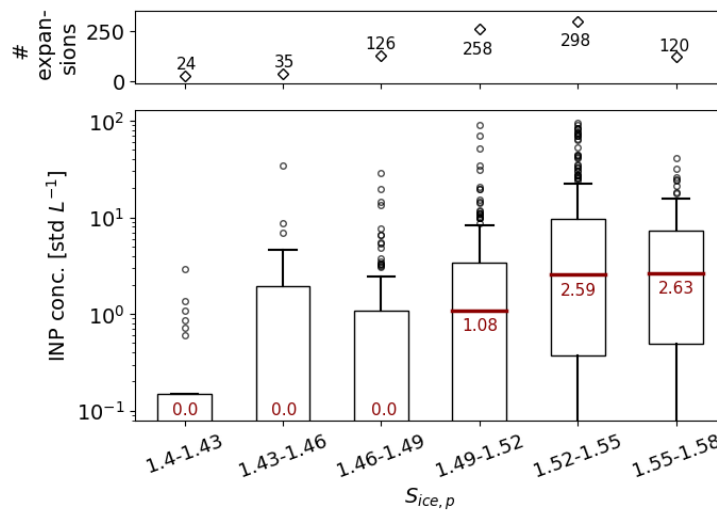


Figure 4.34.: Number of performed runs (upper panel) and INP concentration (lower panel) as a function of different  $S_{ice,p}$  ranges. Only the measurements where the ice crystals were formed by heterogeneous ice nucleation are shown ( $T_{chiller} = -48^{\circ}\text{C}$ ). The red numbers show the median of the INP concentrations per  $S_{ice,p}$  range.

To investigate the variation of the INP concentration within a day, two days were selected from the campaign in which the air masses originated from different directions. The trajectory of the air masses on May 18, 2023, originated from a north-westerly direction (Figure 4.35a), while on May 22, 2023, they originated from an easterly direction (Figure 4.35b, data courtesy GeoSphere Austria). Each trajectory shows the paths for all three hours of the specified day that the air traveled for four days before arriving at the SBO, with the color indicating the height of the air movement.

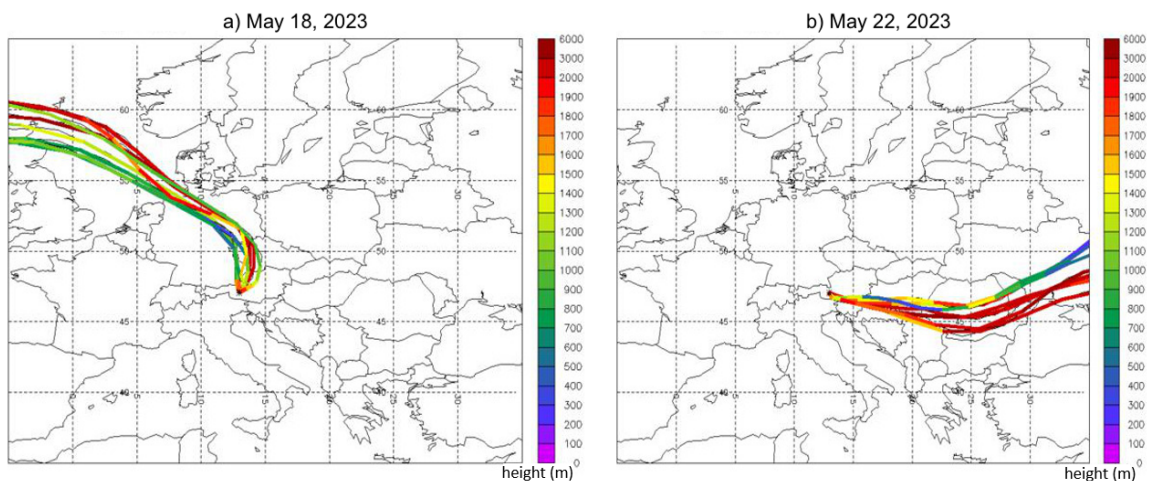


Figure 4.35.: Trajectories of the air masses that reached the SBO on May 18, 2023 (a) and May 22, 2023 (b) (data courtesy of GeoSphere Austria). The colors show the height at which the air mass moved.

Figure 4.36a) describes the measured INP concentration as a function of  $S_{ice,p}$  for May 18, 2023, while panel b) shows the measured data from May 22, 2023. The red numbers indicate the median INP concentration in the corresponding  $S_{ice,p}$  range, and the number of the performed runs is shown again in the upper panel. The same trend can be seen here as in the previous Figures (4.33 and 4.34), with increasing  $S_{ice,p}$  the median INP concentration also increases, which is true for both days. The same applies to the 75% quartile and the maximum for both data sets in the respective  $S_{ice,p}$  range. No INP measurements are shown for May 22, 2023, in the range  $S_{ice,p} = 1.55 - 1.58$  because there was only one run performed with PINEair. When comparing the INP concentrations between the two days, the median INP concentration on May 22, 2023, is higher for all  $S_{ice,p}$  ranges, which can probably be explained by the different air masses. In the next subsection, this assumption is examined and discussed in more detail.

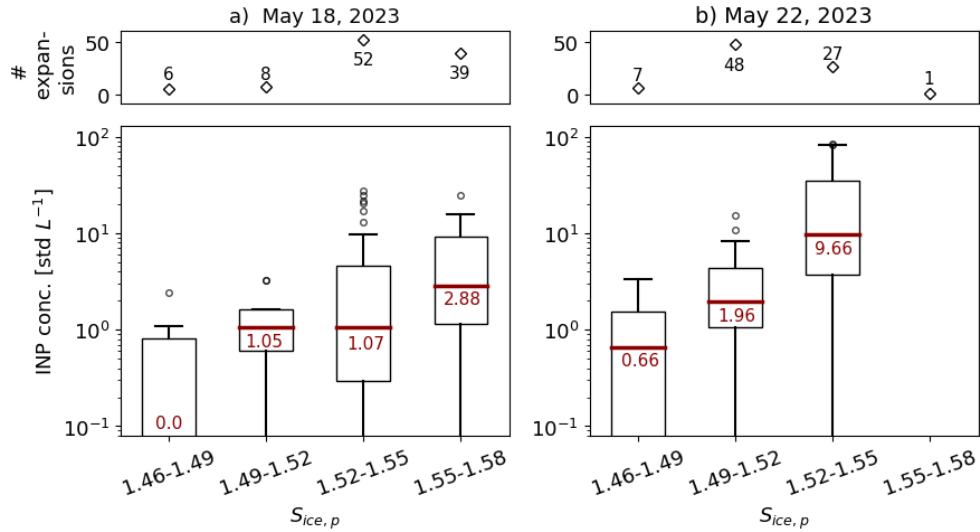


Figure 4.36.: Comparison between two days (a: May 18, 2023 and b: May 22, 2023): Number of performed runs (upper panel) and INP concentration (lower panel) as a function of different  $S_{ice,p}$  ranges. Only the measurements where the ice crystals were formed by heterogeneous ice nucleation are shown ( $T_{chiller} = -48^\circ\text{C}$ ). The red numbers show the median of the INP concentrations per  $S_{ice,p}$  range.

Figure 4.37 shows  $S_{ice,p}$  as a function of  $T_{ad}$  to compare the  $S_{ice,p}$  range where heterogeneous ice nucleation has taken place at the SBO with the parameterizations of homogeneous freezing according to Koop et al. (2000) (red line) and Schneider et al. (2021b) (red dashed line). The circles show the measurements at SBO where only heterogeneous freezing occurred ( $T_{chiller} = -48^\circ\text{C}$ ). The colored shadings show the  $S_{ice,p}$  ranges used in the previous Figures (4.33, 4.34, and 4.36). It is noticeable that the heterogeneous freezing of the measurements at SBO occur until  $S_{ice,p}$  values just below the water saturation (black line), and thus clearly above the parameterizations for homogeneous freezing according to Koop et al. (2000) and Schneider et al. (2021b).

As already discussed in section 4.4.2, the beginning of the homogeneous freezing in PINEair shifts to-

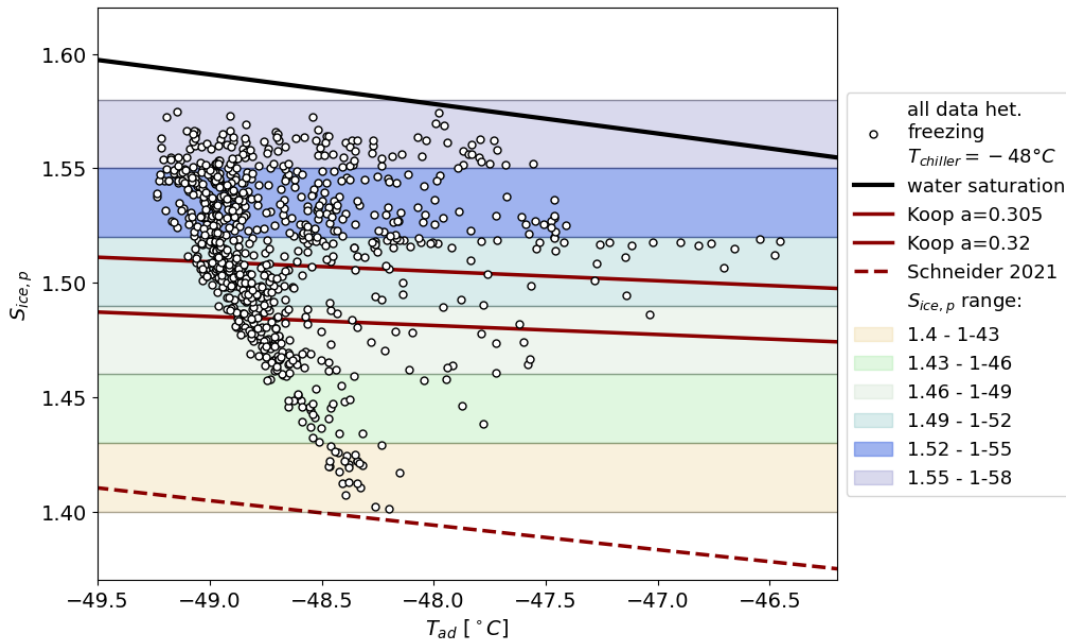


Figure 4.37.:  $S_{ice,p}$  as a function of  $T_{ad}$ , the colored shadings show the different  $S_{ice,p}$  ranges of the previous Figures. The black line represents the water saturation, and the parameterization for the onset of the homogeneous freezing is shown as a red solid line by Koop et al. (2000) and as a red dashed line by Schneider et al. (2021b). The circles show the measurements from the SBO, at  $T_{chiller} = -48^{\circ}\text{C}$  where the ice crystals in the chamber were only formed by the heterogeneous ice nucleation.

wards higher  $S_{ice,p}$  the lower the dewpoint temperature of the sampled air (Figure 4.26 in section 4.4.2). However, this cannot be the only reason for the strong shift of the SBO data towards higher  $S_{ice,p}$  values. When comparing the start of homogeneous freezing of the laboratory measurements with the APC chamber and the AIDA chamber (Figure 4.23 in section 4.4.2),  $S_{ice,p}$  shifts to lower values at a higher dew point temperature, thus in the opposite direction compared to the SBO measurements. In the comparison between the measurements at SBO and the laboratory measurements at the APC chamber, the dew point temperature of the sampled air is higher at the SBO, but the onset of homogeneous freezing still occurs at higher  $S_{ice,p}$  values.

This inconsistent shift in  $S_{ice,p}$  can have several reasons, for example, there may be sources of error in the calculation of  $S_{ice,p}$ . It can be assumed, for example, that the assumption of  $S_{ice} = 1$  inside the chamber is underestimated at the beginning of the expansion, and that it is actually significantly higher. Secondly, as already discussed in section 4.4.2, it is, in general, difficult to determine the threshold between heterogeneous and homogeneous freezing, which could lead to errors. Furthermore, the continuous operation of PINEair at low temperatures could have an influence on  $S_{ice,p}$  inside the chamber. A stable layer of ice could form on the cold chamber walls after a longer time of operation, which would not create ice artifacts due to falling ice crystals, but the ice layer could significantly influence  $S_{ice,p}$  inside the chamber. Since PINEair is a new instrument and these are the very first measurements, it is cur-

rently not possible to determine which of the possible reasons mentioned above is causing the shift in  $S_{ice,p}$ . For example, additional information about the peak relative humidity inside the chamber could be provided by a humidity sensor at the exit of the chamber, which will also be implemented in the future.

### Comparison to Aerosol Measurements

Aerosol measurements are important to obtain information on the sources and types of INPs. For this reason, the INP concentration measured in the range  $S_{ice,p} = 1.52 - 1.55$  is compared with various aerosol parameters (Figure 4.38). This  $S_{ice,p}$  range was selected because most of the measurement data about heterogeneous freezing is available in this range (Figure 4.34).

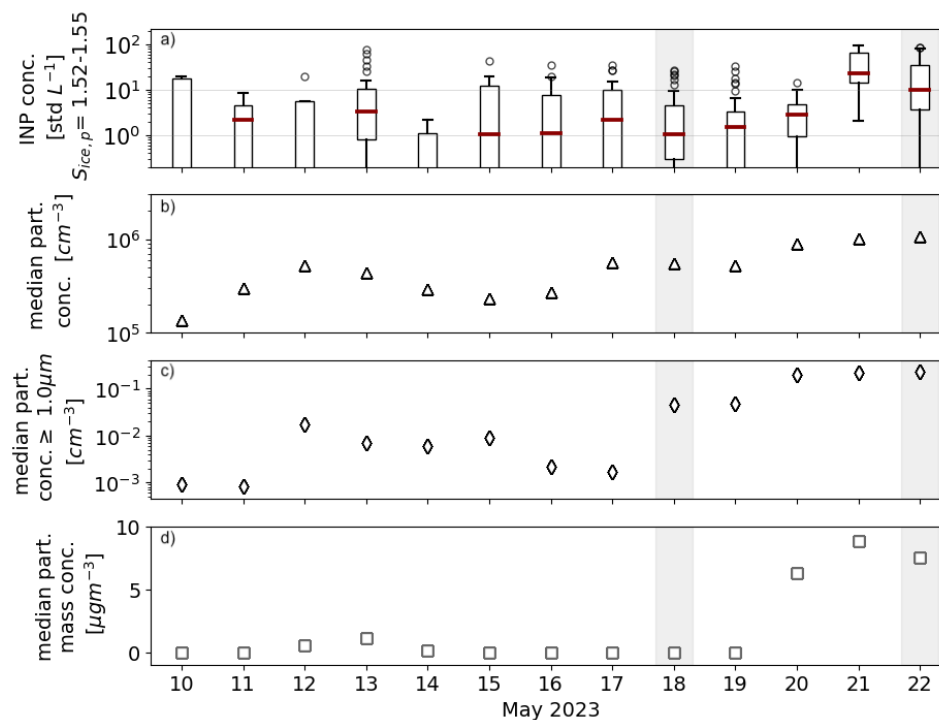


Figure 4.38.: Time series of the following parameters measured during the SBO campaign in May 2023: INP concentration with PINEair at  $S_{ice,p} = 1.52 - 1.55$  ( $T_{chiller} = -48^{\circ}\text{C}$ ) (panel a), median of the total particle concentration (panel b), median of the concentration of aerosol particles with a diameter  $d \geq 1 \mu\text{m}$  (panel c) and median of the particle mass concentration (panel d). The gray shaded areas show the two days that are shown in Figure 4.39 with a higher time resolution and are described in more detail in the text.

Panel a in Figure 4.38 shows the measured INP concentration as a box plot in the range  $S_{ice,p} = 1.52 - 1.55$ , panel b represents the median of the total particle concentration, panel c the median of the concentration of aerosol particles with a diameter  $d \geq 1 \mu\text{m}$ , and panel d presents the median of the particle mass concentration per day. The median of the respective aerosol parameters was only calculated from the data set where PINEair measured in the cirrus temperature range, which was during the daytime. Overall, the INP concentration varied during the entire measurement campaign between a concentra-

tion below LOD and  $94.8 \text{ std L}^{-1}$  at  $S_{ice,p} = 1.52 - 1.55$ . On some days, strong outliers were measured in the INP concentration, e.g. on May 13, 2023, it ranged between a concentration below LOD and  $75.8 \text{ std L}^{-1}$ . In contrast, on other days, such as May 11, 2023, the variations in the INP concentration ranged between a concentration below LOD and  $8.5 \text{ std L}^{-1}$ , which is significantly lower. In general, the course of the aerosol parameters matches that of the measured INP concentration: Towards the end of the campaign, all three aerosol parameters (total particle concentration, concentration of aerosol particles with a diameter  $d \geq 1 \mu\text{m}$  and particle mass concentration) show a maximum, the highest median INP concentrations are measured on the same days.

To find the reason for the variations in the INP concentration, the Spearman's rank correlation coefficient  $\rho$  is calculated. Table 4.3 shows  $\rho$  for the correlation of the INP concentration and the different aerosol parameters (time resolution of 5 min), such as total particle concentration, the concentration of aerosol particles with diameters  $d \geq 0.3 \mu\text{m}$ ,  $0.5 \mu\text{m}$ ,  $0.7 \mu\text{m}$ ,  $1.0 \mu\text{m}$  and the particle mass concentration. In addition, table 4.3 shows  $\rho$  for the correlation between the INP concentration and different meteorological parameters (like ambient temperature, relative humidity, pressure, and wind speed), the time resolution of the data is 30 min. There is no significant correlation ( $\rho < 0.5$ ), so it can be assumed that the variations in the INP concentration are not related to the parameters considered here. The result of  $\rho$  for the correlation between the INP concentration and the aerosol parameters differs from the measurements at the MPC temperatures, where  $\rho > 0.8$ . In the future, more long-term measurements have to be conducted to obtain a larger data set to be able to interpret this finding more precisely and to find the reason for the fluctuations in the INP concentrations at cirrus temperatures. Moreover, an analysis of the ice residuals would provide useful additional information to get details about the aerosol type of the INPs.

Table 4.3.: Spearman correlation coefficient  $\rho$  between INP concentration measured with PINEair at  $T_{chiller} = -48^\circ\text{C}$  ( $S_{ice,p} = 1.52 - 1.55$ ) and various aerosol parameters, as well as meteorological parameters. P-value  $< 0.05$  for all calculated  $\rho$ .

	$\rho$
total particle concentration [ $\text{cm}^{-3}$ ]	0.3
particle concentration $d \geq 0.3 \mu\text{m}$ [ $\text{cm}^{-3}$ ]	0.25
particle concentration $d \geq 0.5 \mu\text{m}$ [ $\text{cm}^{-3}$ ]	0.25
particle concentration $d \geq 0.7 \mu\text{m}$ [ $\text{cm}^{-3}$ ]	0.25
particle concentration $d \geq 1.0 \mu\text{m}$ [ $\text{cm}^{-3}$ ]	0.24
particle mass concentration [ $\mu\text{m m}^{-3}$ ]	0.31
ambient temperature	0.28
relative humidity	-0.25
pressure	0.34
wind speed	-0.21

Figure 4.39 shows the measurement data with a higher time resolution for the two days May 18, 2023 (a) and May 22, 2023 (b), which were already discussed in more detail in the previous section (Figure 4.36 for the INP concentration as a function of  $S_{ice,p}$ , and Figure 4.35 for the trajectories of the air masses). In the top panel the INP concentration at  $S_{ice,p} = 1.52 - 1.55$  (no averaging of the data) is shown, the second panel presents the total aerosol concentration, the third panel the concentration of aerosol particles with a diameter  $d \geq 1.0 \mu\text{m}$ , and the lowest panel represents the particle mass concentration. The time resolution of the data is approximately 10min, data gaps occur when the INP measurements were performed at another  $S_{ice,p}$  range than  $1.52 - 1.55$ , explaining the differences in the times (x-axis) for the two days. On May 22, 2023, higher INP concentrations are measured in the range  $S_{ice,p} = 1.52 - 1.55$ , it fluctuated between  $0.8 \text{ std L}^{-1}$  and  $84.0 \text{ std L}^{-1}$ . In contrast, on May 18, 2023, the INP concentrations varied between  $0.1 \text{ std L}^{-1}$  and  $27.3 \text{ std L}^{-1}$ . This is consistent with the median INP concentration as a function of  $S_{ice,p}$  between the two days (Figure 4.36). The same trend can also be observed in the aerosol parameters: the total particle concentration, the concentration of aerosol particles with a diameter  $d \geq 1.0 \mu\text{m}$  and the particle mass concentration are higher on May 22, 2023, compared to May 18, 2023, which might be due to the different origin of the air masses.

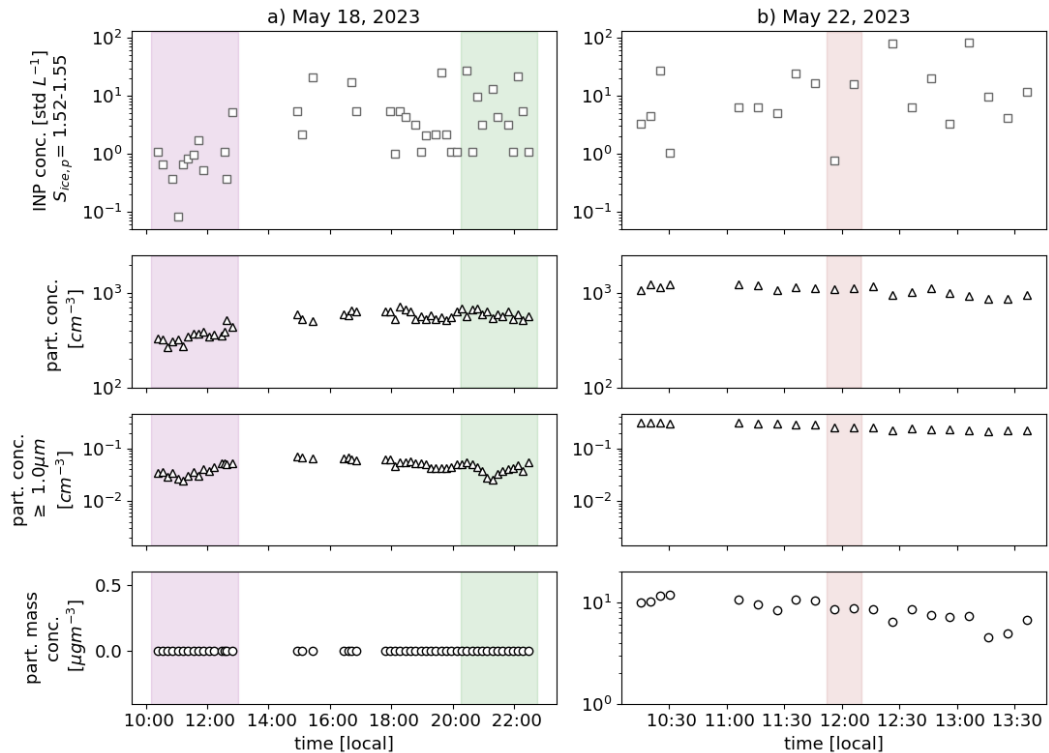


Figure 4.39.: Time series of two selected days (a) May 18, 2023 and (b) May 22, 2023 from the SBO campaign with the following parameters from top to bottom: measured INP concentration with PINEair at  $S_{ice,p} = 1.52 - 1.55$  ( $T_{chiller} = -48^\circ\text{C}$ ), median of the total particle concentration, median of the concentration of aerosol particles with  $d \geq 1 \mu\text{m}$  and median of the particle mass concentration. The colored shadings highlight examples that are explained in more detail in the text.

On May 18, 2023, between 10 am and 12:10 pm (purple shaded area in Figure 4.39a) the total aerosol concentration increases from  $266\text{cm}^{-3}$  to  $443\text{cm}^{-3}$ , the concentration of aerosol particles with a diameter larger than  $1.0\mu\text{m}$  also increases, and at the same time, an increase in the INP concentration from a concentration below LOD to  $5.2\text{std L}^{-1}$  was detected. Thus, all three parameters show a similar trend. At around 8.15 pm on May 18, 2023 (green shaded area), stronger fluctuations can be seen in the INP concentration, so-called jumps between  $1.1\text{std L}^{-1}$  and  $27.3\text{std L}^{-1}$  are measured, although the total particle concentration generally decreases and the concentration of aerosol particles with a diameter  $d \geq 1.0\mu\text{m}$  also fluctuates, but a smooth trend is still visible. Similar behavior can be observed on May 22, 2023 (e.g. brown shaded area in Figure 4.39b), the INP concentration increases from  $0.8\text{std L}^{-1}$  to  $16.1\text{std L}^{-1}$  although no similar trend can be seen in the aerosol parameters. The increases in the INP concentration are therefore likely not caused by the aerosol parameters shown here (total particle concentration, concentration of aerosol particles with a diameter  $d \geq 1.0\mu\text{m}$ , particle mass concentration). The reason for the fluctuations in the INP concentration can currently not be explained. They are probably no outliers but occur regularly. It is also unlikely that they are caused by instrument artifacts. In general, there are very few similar INP measurements in the cirrus temperature range at other stations with which the new data from SBO could be compared, and to investigate how realistic these sudden increases in the INP concentration are and whether they could already be observed at other locations in the atmosphere.

With the measurements carried out so far with the new PINEair instrument, no statement can be made about the cause of the fluctuations. In the future, further laboratory measurements will be performed to be able to interpret such fluctuations better. One way to exclude artifacts caused by the instrument itself could be the use of a well-known ice-active aerosol (such as dust (ATD or SDSA01)) and the APC chamber or AIDA chamber for a constant aerosol source. Measurements could be done with PINEair at constant settings over a longer period of several hours. As a result, the measured INP concentration should be as constant as possible.

#### Comparison to Other Measurements

Only very few INP measurements exist at ambient air conditions in the cirrus temperature range (DeMott et al., 2003b, Richardson et al., 2007, Wolf et al., 2020). In the following, the INP measurements performed in the cirrus temperature range at SBO are compared with the INP measurements of Wolf et al. (2020) at the Puy de Dôme observatory and the measurements with PINEair at Campus North, KIT in Karlsruhe.

Puy de Dôme (France, 1470 m a.s.l.):

From October 5 to 15, 2018, INP measurements with the continuous flow diffusion chamber SPIN (Spectrometer for Ice Nuclei, Garimella et al., 2016) were conducted at the Puy de Dôme Observatory in France (Wolf et al., 2020). The station is located at an altitude of 1470 m a.s.l. on a mountain chain and

is therefore influenced both by air masses from the lower FT and the BL (Farah et al., 2018). The INP measurements were performed at a temperature of  $-46^{\circ}\text{C}$  and  $S_{ice} = 1.3$ .

Figure 4.40 in the lower panel shows the measured INP concentration during the period of the measurement campaign, variations between  $\sim 0.1\text{L}^{-1}$  to  $70\text{L}^{-1}$  were observed (Wolf et al., 2020). Similar to the measurements at SBO, the INP concentration varies more strongly on some days (e.g. October 13, 2018) and less strongly on others (e.g. October 9, 2018). Wolf et al. (2020) could not find any correlation between the INP concentration and meteorological parameters such as temperature, pressure, relative humidity, wind speed, and wind direction. A positive correlation was observed between the INP concentration and the concentration of aerosol particles with diameters  $d < 0.15\ \mu\text{m}$ , while there was no correlation for the larger particles with  $d > 0.15\ \mu\text{m}$ .

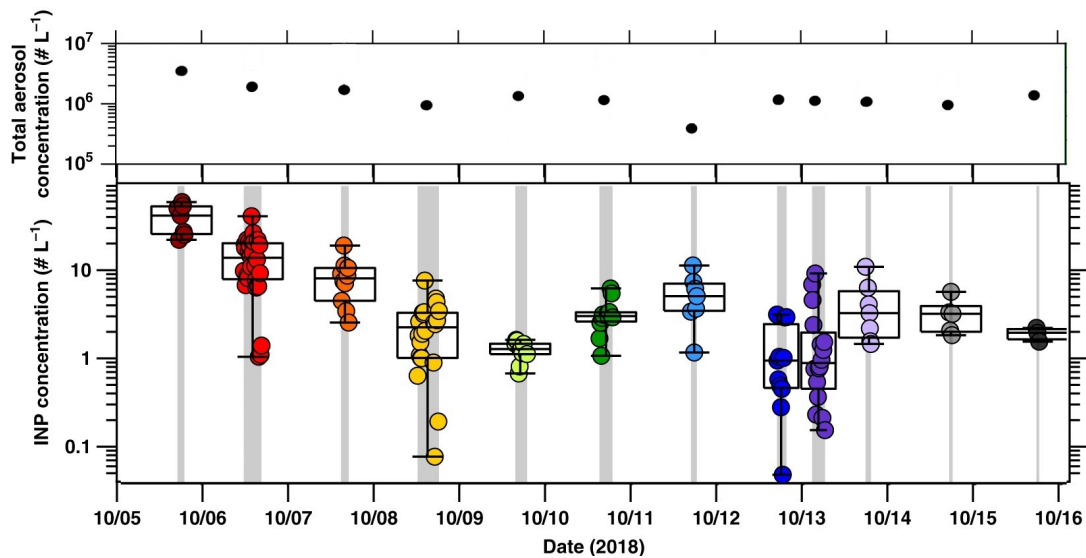


Figure 4.40.: Measurements of the total aerosol concentration (upper panel) and INP concentration (lower panel) with SPIN at the Puy de Dôme Observatory in France from October 5 to 16, 2018. Figure adapted from Wolf et al. (2020).

For the INP measurements at the SBO, no correlation was observed between the INP concentration and meteorological parameters and the concentration of aerosol particles with a diameter  $d > 0.15\ \mu\text{m}$ , which is in agreement with the measurements at the Puy de Dôme Observatory. A more detailed contrast of the measured INP concentration at the Puy de Dôme and the SBO is not worthwhile, as the measurements were carried out at different  $S_{ice}$  ranges. While at Puy de Dôme, they measured INP concentrations at  $S_{ice} = 1.3$ , at SBO the measurements were performed at the lowest  $S_{ice,p}$  range of 1.4 – 1.43. Furthermore, the measurements were performed during different seasons and both instruments are based on different measurement methods, which should first be compared more closely to each other in laboratory studies.

Campus North (Germany, 120 m a.s.l.):

On several days in April 2023 (April 14, 20, 21, 26) daytime INP measurements were performed with PINEair at Campus North, KIT. The site is located at an altitude of 120 m a.s.l. directly next to a forest, close to a road, and approximately 10 km from the city of Karlsruhe. The ethanol thermostat was constantly set to  $T_{chiller} = -48^\circ\text{C}$  for all measurements (the same as for the measurements at SBO), several runs with different  $PPDs$  were performed resulting in an adiabatic temperature between  $T_{ad} = -47.13^\circ\text{C}$  and  $T_{ad} = -48.68^\circ\text{C}$ . The other settings for the measurements with PINEair were identical to the measurements at SBO, the waiting time before the start of the expansion was 60 sec and  $flow_{exp} = 0.7\text{L min}^{-1}$ .

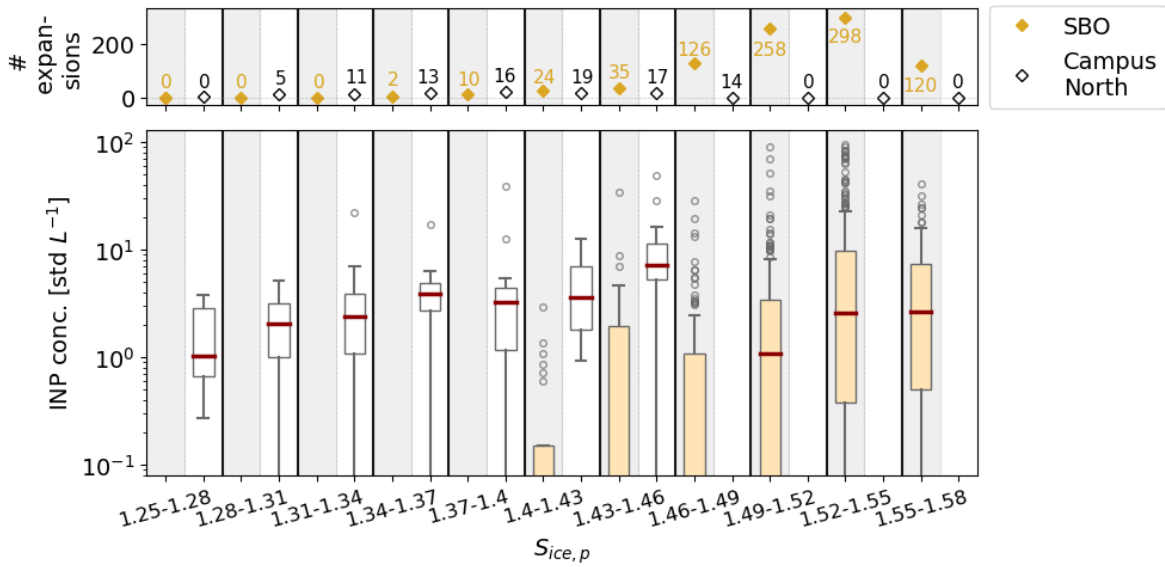


Figure 4.41.: Comparison of the measurements performed with PINEair ( $T_{chiller} = -48^\circ\text{C}$ ) at Campus North (April 2023, unfilled markers) and SBO (May 2023, orange markers). The upper panel represents the number of runs and the lower panel shows the measured INP concentration as a function of the  $S_{ice,p}$  ranges.

The lower panel in Figure 4.41 shows the measured INP concentration at Campus North (white box plot) and SBO (orange box plot) as a function of  $S_{ice,p}$ , only the data where heterogeneous ice nucleation occurred are shown. The upper panel in Figure 4.41 again shows the number of runs in the respective  $S_{ice,p}$  range for the two measurement time series at Campus North (white marker) and SBO (orange marker). Although there is no information about the particle concentration at Campus North at the time of the measurements, it can be assumed that it is significantly higher compared to the SBO, as the aerosol population is different between the two locations due to the different heights. While the SBO is remote and is mainly influenced by air masses from the lower FT and only occasionally by air masses from the BL, Campus North might be influenced by biological aerosols from the nearby forest, as well as urban and anthropogenic aerosols due to its proximity to the city. This is also reflected in the measured INP

concentration, in the  $S_{ice,p}$  ranges where measurements are available for both locations, the median INP concentration is significantly higher at Campus North. For example, at a peak ice saturation ratio of 1.43 – 1.46, the median INP concentration at Campus North is 7.2 std  $L^{-1}$ , while at the SBO the concentration is below the LOD.

It is noticeable that there are stronger outliers at SBO than at Campus North. The reason for this could be the shorter duration of measurements at Campus North, where data was collected over four days, compared to approximately 14 days at the SBO.

Furthermore, the  $S_{ice,p}$  for the observation of heterogeneous ice nucleation differs between the two stations (see Figure 4.42a). At Campus North (black diamonds), INP measurements can be made until  $S_{ice,p} = 1.43 - 1.46$ , at higher  $S_{ice,p}$  conditions homogeneous freezing already begins. In contrast, when measuring at SBO, INP measurements can be performed in the heterogeneous range down to  $S_{ice,p}$  values just below the water saturation. This difference cannot be explained by different dew point temperatures of the sampled air, as it is very similar for both measurement periods and varies between  $-20.5^{\circ}\text{C}$  and  $-25.6^{\circ}\text{C}$  (see Figure 4.42b). A difference between the two time series is the duration for which PINEair was operated at temperatures  $< 0^{\circ}\text{C}$ , which could have an influence on  $S_{ice}$  at the start of the expansion and therefore on the calculation of  $S_{ice,p}$ . At Campus North, it was only for several hours, while at the SBO station, PINEair was operated continuously for approximately seven days. However, this assumption has to be investigated by further laboratory measurements first. Ideally, a CFDC could be used as a reference INP instrument to obtain more accurate information about the INP concentration at different  $S_{ice,p}$ .

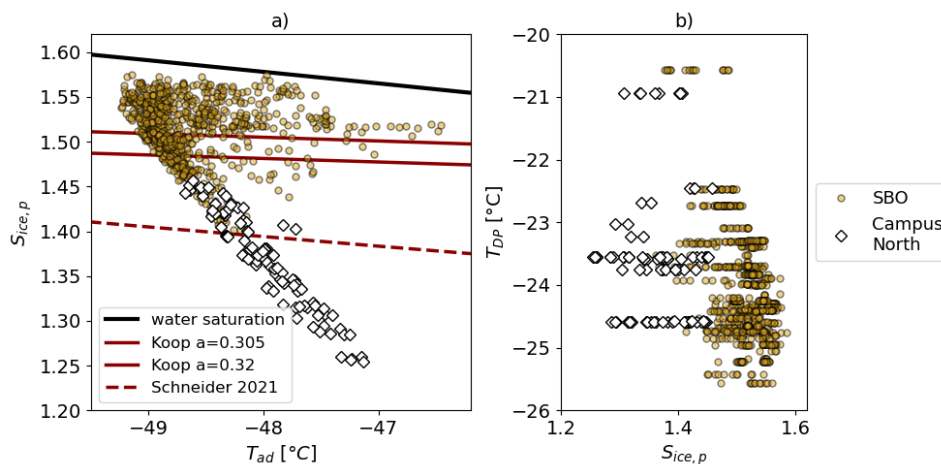


Figure 4.42.: a)  $S_{ice,p}$  as a function of  $T_{ad}$ , the black line represents the water saturation, and the parameterization for the onset of the homogeneous freezing is shown as red thick line by Koop et al. (2000) and as red dashed line by Schneider et al. (2021b). b) The dewpoint temperature as a function of  $S_{ice,p}$  is shown. In both plots the orange circles indicate the INP measurements at SBO and the unfilled diamonds represent the measurements at Campus North, only the data points where the ice crystals were formed heterogeneously are shown ( $T_{chiller} = -48^{\circ}\text{C}$ ).

#### 4.6. Summary

To get a better understanding about the abundance of the INP concentration in the atmosphere and therefore improve their implementation in weather and climate models, measurements at ground-based stations need to be complemented by aircraft measurements in air layers where clouds containing ice are formed (Coluzza et al., 2017). Currently, no aircraft-based instrument exists which is capable of measuring the INP concentration at temperatures  $< -40^{\circ}\text{C}$ , limiting the understanding and formulation of the contribution of heterogeneous freezing to the formation of cirrus clouds.

As part of this doctoral thesis, the new instrument PINEair was developed for application on aircraft, capable of measuring INP concentrations at conditions relevant for MPC and cirrus clouds. PINEair is based on the design of the mobile expansion chamber PINE (Möhler et al., 2021), with modifications for an improved time resolution of the measurements, and a more precise establishment of supersaturation and temperature. To improve the time resolution, which is especially relevant for aircraft-based measurements, PINEair consists of three expansion chambers (3L each) operating in an alternating cycle of flushing particles through the chamber, expanding the chamber and thus creating temperature and supersaturations relevant for cloud formation, and refilling the chamber to ambient pressure conditions. To better quantify the INP activation conditions regarding temperature and supersaturations, which is especially important for the differentiation between homogeneous and heterogeneous freezing in the cirrus temperature range, PINEair can be operated with a step-wise expansion, optionally to the continuous expansion of the commercial PINE. For this, a buffer volume is used to create an immediate pressure drop, leading to an almost adiabatic temperature decrease. This allows to calculate the adiabatic temperature decrease and peak relative humidity inside the chamber. As PINEair is designed to work continuously, and automatically and can be controlled remotely, it can be operated for long-term measurements with minimal user input.

The final version of PINEair is designed specifically for the use on the HALO research aircraft and is expected to be part of the measurement campaign "HALO-South" in New Zealand in September 2025, where the INP concentration over the clean, pristine Southern Ocean will be investigated. To test the functionality of the new instrumental design, a prototype I of PINEair was first built and placed in the thermal housing of the AIDA chamber. Successful experiments were performed at a start pressure of 250mbar and a start temperature of  $-50^{\circ}\text{C}$  to mimic aircraft-relevant conditions. Here, the formation of ice crystals by homogeneous and heterogeneous ice nucleation was observed. A comparison between PINEair and other INP instruments such as AIDA and PINE in the MPC temperature range showed good agreement. Furthermore, the onset temperature of homogeneous freezing of supercooled water droplets was investigated using ammonium sulfate aerosols, which occur at temperatures between  $-35^{\circ}\text{C}$  and  $-37^{\circ}\text{C}$  (e.g., Benz et al., 2005). The PINEair measurements with (continuous) expansions on homogeneous water droplet freezing showed on average an offset of  $1.33^{\circ}\text{C}$  towards higher temperatures, which could possibly be caused by temperature inhomogeneities inside the chambers, which needs to be inves-

tigated by further laboratory measurements.

Successful experiments for the differentiation of homogeneous and heterogeneous freezing at cirrus cloud conditions were performed, by measuring sulfuric acid aerosols for homogeneous nucleation and ATD as INP at a start temperature of  $-45^{\circ}\text{C}$ . For this purpose, by systematically changing the *PPD* during a series of runs with step-wise expansions, different  $S_{ice,p}$  were achieved inside the chamber until a sufficiently high  $S_{ice,p}$  was reached that the homogeneous freezing could occur.

Subsequently, the PINEair prototype I was redesigned as prototype II by adding an ethanol thermostat to independently cool the instrument. By that, the instrument is becoming mobile and therefore also suitable for field measurements. Especially for the INP measurements at cirrus conditions and the use of the buffer volume for the step-wise expansions, the performance of the new instrument was tested and the optimal operational parameters were identified. For example, the duration of the waiting time, which is introduced before the start of the expansion when no flow is guided over the chamber, to equilibrate the temperature inside the chambers, should be 60 sec. To ensure that the ice crystals formed during the step-wise expansion, are transported to the OPC and are finally detected, the pump flow directly after the step-wise expansion  $flow_{exp}$  should be larger than  $0.7\text{L min}^{-1}$ .

During the laboratory measurements at the APC chamber and the first test measurements at ambient air conditions, it was demonstrated that the  $S_{ice,p}$  onset of homogeneous freezing can be well detected with PINEair by doing a series of runs with step-wise expansions at increasing *PPDs* (relative humidity scan). However, there is a transition area where, at similar values for the *PPD*, sometimes only heterogeneous humidity conditions are achieved and sometimes already homogeneous humidity conditions. Furthermore, it was observed that  $T_{DP}$  of the sampled ambient air has an influence at the onset of the homogeneous freezing. The limit value of the *PPD*, where  $S_{ice,p}$  inside the chamber is high enough for the homogeneous freezing to occur, shifts to lower values if  $T_{DP}$  of the sampled air is higher. Therefore, especially during the long-term operation of PINEair, regular relative humidity scans should be performed when measuring cirrus-relevant INPs in order to redefine the start of the homogeneous freezing.

To test the PINEair prototype II, a field campaign was performed from May 8-22, 2023, at the Sonnblick Observatory (3106 m a.s.l.) in Austria. The SBO is a well-suited observatory to study aerosol-cloud interactions, as it is located in the lower FT, but may also be influenced by air mass injections from the BL, resulting in the presence of aerosols from long-range transport, such as dust particles, as well as regional aerosols.

PINEair proved its suitability as an instrument for long-term operation, as it measured almost continuously for the duration of the campaign. Different operations were tested: During the night, (continuous) expansions were performed with PINEair in the MPC temperature range ( $T = -22.7^{\circ}\text{C}$  and  $-27.5^{\circ}\text{C}$ ) with a time resolution of 2.5 min. A comparison between the INP measurements and the aerosol parameters (concentration of aerosol particles with diameters  $d \geq 0.3\mu\text{m}$ ,  $0.5\mu\text{m}$ ,  $0.7\mu\text{m}$ ,  $1.0\mu\text{m}$  and the particle mass concentration) showed a strong dependence, which is supported by a positive Spear-

man correlation coefficient  $\rho > 0.8$  for all parameters. No clear correlation between the meteorological parameters (temperature, pressure, relative humidity, wind direction, and wind speed) and the INP concentration was found ( $\rho < 0.5$ ). This is in agreement with the study by Lacher et al. (2018b) at the Jungfraujoch station in Switzerland. Four time periods of PINEair measurements at  $T = -22.7^\circ\text{C}$  were used to compare the PINEair data with the aerosol filters for the analysis with the offline freezing experiment INSEKT. Here, slightly higher INP concentrations were measured with PINEair. Possible reasons for this could be, for example, the temperature inhomogeneities in the chamber, or a too slow response time of the temperature sensors during expansion. In the future, laboratory measurements using an INP sample with a well-known ice onset, for example, Snomax<sup>®</sup>, will be performed to investigate the accuracy of the temperature measurement in PINEair during a (continuous) expansion. Furthermore, longer-term comparison measurements with other INP instruments will be performed.

For the first time in the Alpine region, PINEair measured cirrus-relevant INP concentrations during the daytime hours of the campaign at the SBO station. First measurements at a temperature of approximately  $-47.8^\circ\text{C}$  and  $S_{ice,p}$  in the range of 1.49 and 1.52 resulted in INP concentrations up to 90 std  $\text{L}^{-1}$ . Runs with step-wise expansions with a *PPD* in the range of 4.87% and 6.52% were made, resulting in different  $S_{ice,p}$  between 1.4 and 1.61. Here, higher median INP concentrations were measured at higher  $S_{ice,p}$ . The threshold value for the *PPD* at which homogeneous freezing for the sampled ambient air at SBO starts differs compared to the threshold observed during measurements at Campus North, although the dew point temperatures were very similar. Possible reasons for this could be the operation of PINEair over a longer period of time at temperatures  $< 0^\circ\text{C}$ , which could have an influence of  $S_{ice}$  at the start of the expansion.

A case study between two selected days has shown that during increased aerosol concentrations, and particle mass concentrations, also increased INP concentrations are measured. When analyzing the whole time period, no relation between the INP concentration and the aerosol parameters (concentration of all aerosol particles and concentration of aerosol particles with diameters  $d \geq 0.3 \mu\text{m}$ ,  $0.5 \mu\text{m}$ ,  $0.7 \mu\text{m}$ ,  $1.0 \mu\text{m}$  and the particle mass concentration) was found ( $\rho < 0.5$ ). The same applies to  $\rho$  for the correlation between the INP concentration and meteorological parameters (ambient temperature, relative humidity, pressure, wind speed), which is in agreement with the study by Wolf et al. (2020) at the Puy de Dôme Observatory in France.

The mobile prototype of PINEair, and the final aircraft-based PINEair instrument, which is specifically designed for use onboard the HALO research aircraft, will allow comprehensive and online INP measurements in the free troposphere, both in the MPC and cirrus temperature ranges. The laboratory measurements, as well as the first field campaign, have demonstrated that the design of the instrument is suitable to perform INP measurements in a wide range of temperature and ice supersaturation. Further laboratory measurements will aim at characterizing the instrument more precisely regarding the activation temperature and ice supersaturated conditions inside the chamber.

## 5. Long-Term INP Measurements at the Sonnblick Observatory

Data about long-term measurements of INP concentrations are rare, but they are important to get a better understanding of the seasonal and diurnal variations in order to improve their implementation in weather and climate models (Burrows et al., 2022; Bras et al., 2022). For this reason, as part of this PhD thesis, an INP long-term measurement series was performed at the high-altitude Sonnblick Observatory (SBO) in Austria. Section 5.1 summarises previous INP measurements investigating the seasonal and diurnal variability, and section 5.2 gives an overview of the campaign performed at SBO. Section 5.3 describes the results of the measurements at SBO, which are then discussed in section 5.4. A large dust event in March 2022 is examined in more detail in section 5.5. Finally, section 5.6 summarizes the results and conclusions.

### 5.1. Introduction

<sup>1</sup> Numerous INP measurements have already been performed in different environments by using different measurement methods (offline and online) (e.g., Kanji et al., 2017). However, long-term studies at high time resolution are rather rare, leading to missing information about the seasonal variability of the INP concentrations. Brunner et al. (2022) present a summary of studies focusing on the seasonal variability of the INP concentrations (e.g., Conen et al., 2015; Wex et al., 2019; Schneider et al., 2021a; Tobo et al., 2020; Schrod et al., 2020), which are distributed around the globe. They conclude that a seasonal dependence of the INP concentration was apparent in all studies, with the highest concentrations measured in spring and summer. Most studies have been performed using offline measurement methods, where aerosols are sampled in the field and post-analyzed in the laboratory. These measurements usually have a time resolution ranging from 24 h to 2 weeks, which does not provide any information about the diurnal variability.

In recent years, automatic online instruments were developed (e.g., Möhler et al., 2021; Brunner and Kanji, 2021; Bi et al., 2019) which directly analyze the sampled aerosols, and are thus capable of measuring the INP concentrations with a high time resolution. This is important to identify and analyze short-term variations, like for example diurnal variations or changes in the air mass origin. For example, a long-term study was conducted at the High Altitude Research Station Jungfrauoch (JFJ) (3580 m a.s.l.)

---

<sup>1</sup>A slightly modified version of some sections are part of a manuscript which was recently submitted to the journal BAMS (Bulletin of the American Meteorological Society): Pia Bogert, Larissa Lacher, Maksym Gachkivskyi, Kristina Höhler, Ingeborg Levin, Elke Ludewig, Christian Maier, Thomas Leisner and Ottmar Möhler (2024): New insight into the annual cycle of ice-nucleating particle concentrations from long-term measurements at the Sonnblick Observatory

by Brunner et al. (2022) using the online instrument HINC-Auto (automated Horizontal Ice Nucleation Chamber, Brunner and Kanji, 2021), with a time resolution of 20 min. They only observed a daily cycle in the INP concentration on days when the Jungfraujoch was influenced by air masses from the BL. Other INP studies that have observed the diurnal variability of the INP concentration are e.g., Isoni et al. (1971), Rosinski et al. (1995), Wieder et al. (2022).

To get a better overall understanding of the presence of INPs, it is important to investigate not only the diurnal and seasonal variability but also the INP distribution in the altitude, especially in the FT. Existing INP measurements have mostly been made at ground-based stations (Kanji et al., 2017), with most stations located in the BL. Measurements of the INP concentration in the FT are difficult. A number of measurements were achieved by aircraft (e.g., Eidhammer et al., 2010; Field et al., 2012) or at high mountain stations, like for example the Jungfraujoch station (3580 m a.s.l.) in Switzerland (Chou et al., 2011; Conen et al., 2015; Lacher et al., 2018a; Lacher et al., 2021) or the Storm Peak Laboratory (3200 m a.s.l.) in Colorado (e.g., DeMott et al., 2003b; Richardson et al., 2007). For more information see the details in section 4.1. The SBO (3106 m a.s.l.) in Austria is a well-suited location to study aerosol-cloud interactions at higher altitudes, as the station is located in the lower FT, but it is regularly influenced by the updraft of warm air masses by convection from the BL. Especially in the summer months, the BL can reach up to several kilometers (Stull, 1988). Through this process, which is very distinct in the mountains, air masses including aerosols and trace gases are transported from the BL into the FT (Stull, 1988).

As part of this doctoral thesis, a long-term study was conducted at the SBO to measure the INP concentration at different temperatures in the MPC temperature range to investigate the diurnal and seasonal variability. The INP measurements discussed in this thesis were performed with the method INSEKT (see section 3.2) during 3 years in the period from August 2019 to August 2022. This represents the longest constant INP measurement time series to date. In addition, the INP concentration was measured for about 14 months from August 2021 to October 2022, with the online expansion chamber PINE (see section 3.1), this measurement time series is the longest INP study with such a high time resolution ( $\sim 6$  min) to date.

### 5.2. Overview of Campaign

The following sections provide an overview of the INP measurements performed at the SBO. Section 5.2.1 first describes the station and its location. The next section 5.2.2 provides an overview of the conducted campaigns to investigate the INP concentration at SBO. Section 5.2.3 describes the sampling setup, and section 5.2.4 describes and discusses the air mass origin.

### 5.2.1. Field Location

The SBO (12.96°E, 47.05°N) is a measuring and research station in the Austrian Alps (south in the province of Salzburg, Figure 5.1) and is located on the summit of the mountain "Hoher Sonnblick" at an altitude of 3106m above sea level (Figure 4.28).



Figure 5.1.: Location of the SBO in Austria, marked by the star.

It is situated on rocks, surrounded by large glacier fields, approximately 1000m above the tree line. Figure 5.2a shows the SBO in summer, where it is surrounded by bare rocks, whereas in winter (Figure 5.2b) most of the surrounding area is snow covered. The air temperature at the SBO is affected by seasonal variations, in the period from August 2019 to mid-October 2022 (time period of the measurements discussed here), it varied between  $-25.8^{\circ}\text{C}$  and  $13.2^{\circ}\text{C}$ , on average it was  $-3.6^{\circ}\text{C}$ . During this period, the ambient pressure was on average 695.7 mbar with a maximum of 712.7 mbar and a minimum of 663.6 mbar.

Due to its altitude and location, the SBO receives air masses from both the FT and the BL, therefore the location is well-suited for measuring the sources and concentration of INPs at higher altitudes and in the FT. Aerosols at SBO may be influenced by both regional sources and long-range transport, such as the transport of Saharan dust or mineral dust. Previous measurements at SBO showed that there is a mineral dust influence for up to 30 days per year (Greilinger et al., 2018). The interaction between the air masses from the FT and the BL has an influence on the aerosol concentration. If the SBO is more influenced by the air masses from the FT, the air present at the remote site is pristine. In contrast, if the SBO is predominantly influenced by the air masses from the BL, the number concentrations of natural aerosols (e.g., particles from vegetation or soils) and anthropogenic aerosols are increased, which is more often the case in summer, due to the rising warm air masses caused by convection (Holzinger et al., 2010).

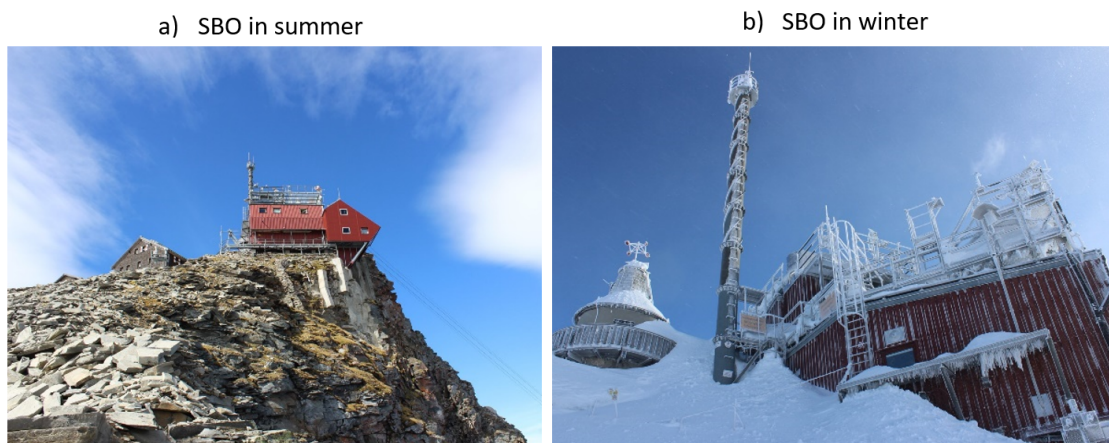


Figure 5.2.: Photo a) shows the SBO in summer, surrounded by rocks, and Photo b) shows the SBO in winter, covered with snow.



Figure 5.3.: Aerosol inlet on the rooftop of the SBO station.

The SBO is operated by Geosphere Austria, it is part of the GAW program and part of the ACTRIS (Aerosol, Clouds and Trace Gases Research Infrastructure) research infrastructure by hosting the European Center for Cloud Ambient Intercomparison (ECCINT), which is part of the Cloud In Situ (CIS) topical center of ACTRIS. The first meteorological measurements at SBO were conducted in 1886 and today the station is staffed permanently. There are a number of long-term measurements available for a variety of parameters from different areas such as meteorology, radiation, gases, aerosols, permafrost, and glaciology. The aerosol sampling is performed via a heated total air inlet designed according to GAW guidelines, with an upper cut-off size of  $20\mu\text{m}$  at a wind speed of  $20\text{m s}^{-1}$ , which is installed

on the rooftop of the station (Figure 5.3). Because aerosol properties are particularly important for the interpretation of the INP measurements, their measurements are explained in more detail in section 5.2.3.

### 5.2.2. Overview of Conducted INP Measurements

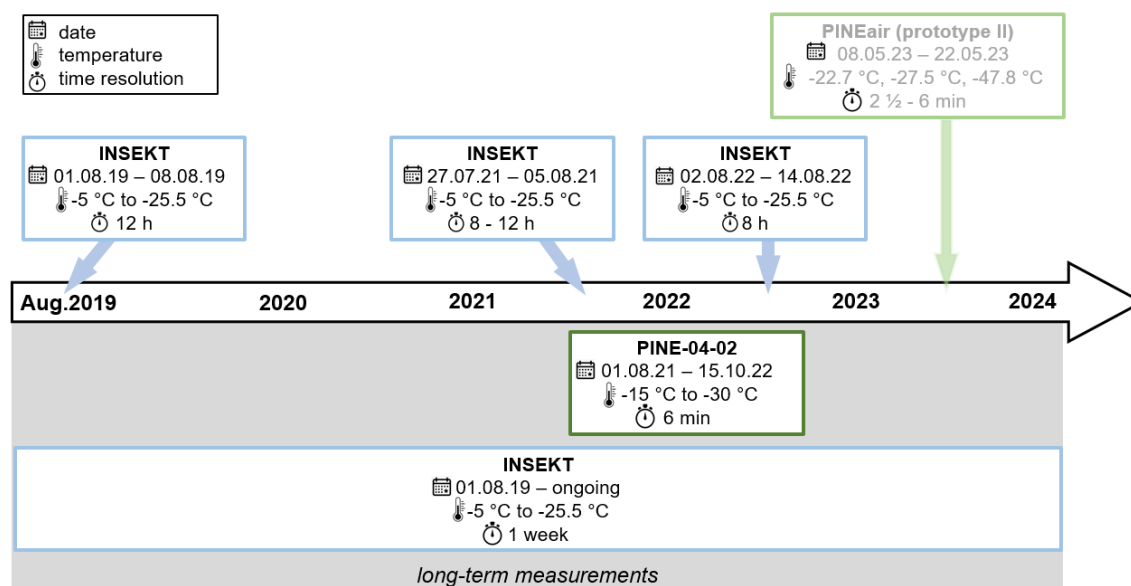


Figure 5.4.: Overview of all measurement campaigns conducted at the SBO to investigate the INP concentration using the instruments INSEKT (blue frame), PINE-04-02 (dark green frame), and PINEAir (green frame). The shorter intensive campaigns are listed above the timeline, and the long-term measurements are shown below the timeline in the gray shaded area.

The INP measurements presented in this section are the first which were conducted at the SBO. Figure 5.4 provides an overview of the time periods of the long-term measurements (gray shaded area) and the shorter intensive campaigns. The INP instruments that were used were the freezing experiment INSEKT (blue frame, more information in section 3.2), and the expansion chambers PINE (model 04-02, Bilfinger Nuclear & Energy Transition GmbH; dark green frame, more information in section 3.1) and the new instrument PINEAir prototype II (green frame, more information in section 4.2.2). The results of the measurement campaign with PINEAir have already been discussed in section 4.5. This section focuses on the measurements with INSEKT and PINE which were performed in the MPC temperature regime. In the following, the individual campaigns are described in more detail.

The INSEKT INP measurements at SBO started in August 2019. Since then, aerosol filters were taken regularly in time intervals of one week. These measurements are still ongoing (status: spring 2024). In this PhD thesis, the filters are analyzed and the results are discussed until August 2022 (in total 210 filters), providing a long-term measurement series of three years. During the intensive campaigns in August 2019, July 2021, and August 2022, day and night filters were sampled more frequently with an

8 – 12 h interval. This aims to receive information about the difference of the INP concentrations during day and night hours and to compare the results of INSEKT with the results of PINE (section 5.4.6).

A blank filter is also sampled every five weeks to check the cleanliness during the filter handling (more information see section 3.2). An analysis of the blank filters has shown that there is no substantial contribution of ice-active aerosols from the laboratory on the filters, therefore no INP concentration needs to be subtracted due to contamination.

Approximately half of all filters were additionally analyzed in the laboratory with a heat treatment to obtain information about the content of heat-sensitive INPs. A description of this procedure can be found in section 3.2. The results are described in section 5.3.4.

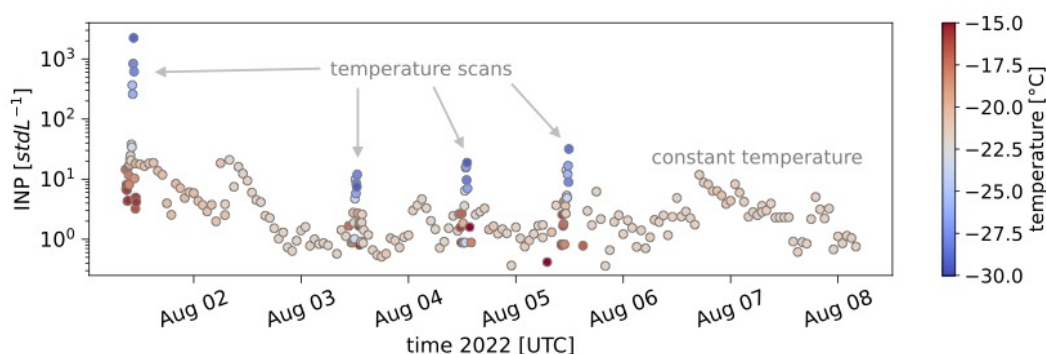


Figure 5.5.: Example of a typical series of PINE measurements at SBO for one week from August, 1 to 8, 2022. Different colors indicate the measurement temperature. During operation at an almost constant temperature of  $-23^{\circ}\text{C} \pm 2^{\circ}\text{C}$ , the data was averaged for 1 h. During temperature scans from  $-15^{\circ}\text{C}$  to  $-30^{\circ}\text{C}$ , indicated in the Figure with arrows, single run data with a time resolution of 6 min is shown.

From August 2021 to mid-October 2022, the INP concentration at the SBO was additionally measured with PINE to achieve measurements with a high time resolution of about 6 min in order to obtain additional information about shorter-term variations or diurnal cycles of the INP concentration. In general, PINE was operated at a constant temperature of  $-23^{\circ}\text{C} \pm 2^{\circ}\text{C}$ , at regular intervals or during events of elevated INP concentrations (such as dust events) temperature scans from  $-15^{\circ}\text{C}$  to  $-30^{\circ}\text{C}$  were performed. Figure 5.5 shows an example week from August 1 to 8, 2022 of the PINE measurements at SBO. For the time periods of constant temperature operation, the data was averaged for 1 h. During the four temperature scans indicated in Figure 5.5, single run data is shown. The instrument works automatically and was controlled remotely from Karlsruhe, for example, to perform temperature changes or background tests. Regular ice background tests were performed once a day. More information can be found in section 3.1.

### 5.2.3. Sampling Setup

The PINE instrument and the INSEKT aerosol sampler were connected to the heated total aerosol inlet (same as for aerosol sampling, Figure 5.3) through a y-splitter, as shown schematically in Figure 5.6.

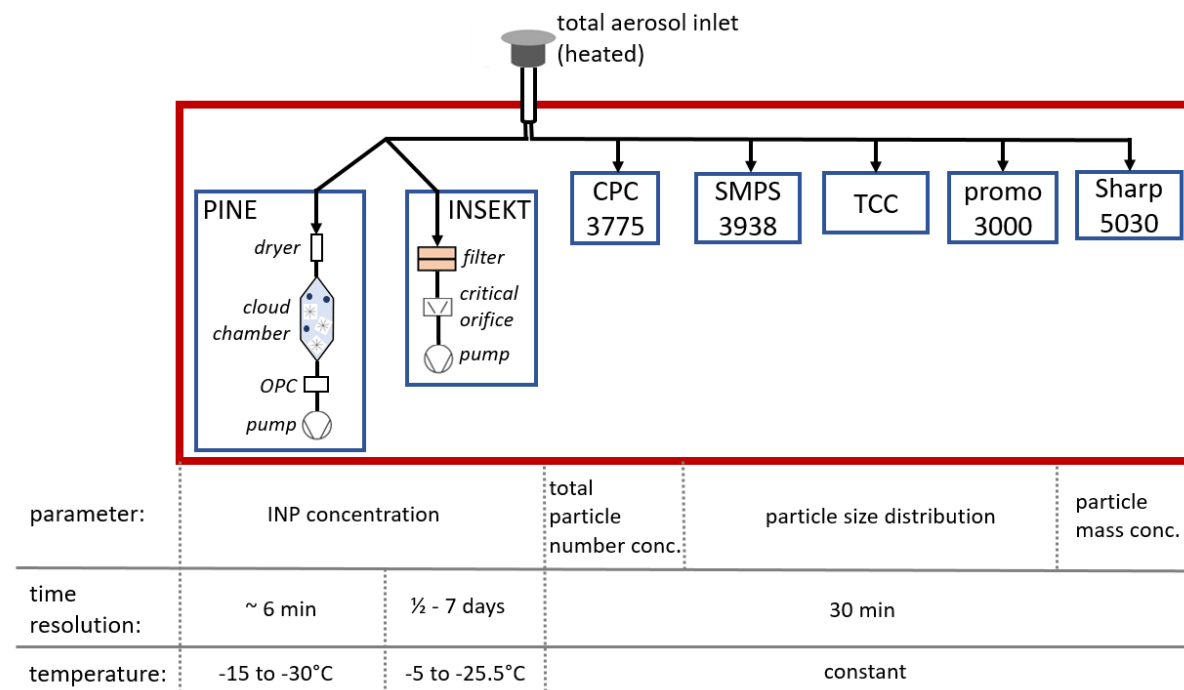


Figure 5.6.: Schematic setup of the INP and aerosol measurements at SBO. The measured parameters, the time resolution of measurements, and the measurement temperature are indicated in the lower part of the Figure.

For the discussion of the INP data in section 5.4, the data of the following aerosol parameters were used: The total particle number concentration is measured with a CPC model 3775 from TSI GmbH. For the measurement of the particle size distribution a SMPS (model 3938, TSI GmbH) is used for the smaller particle size ranges (diameter of 1 nm to 480 nm) and for the larger particles (diameter >300 nm to >5000 nm) the particle counter model TCC from Klotz GmbH, and the optical particle counter promo 3000 from Palas GmbH. The presence of dust may be indicated by the aerosol mass concentration (e.g., Schauer, 2015; Baumann-Stanzer et al., 2018; O’Sullivan et al., 2020) which is continuously measured at the SBO with a SHARP Monitor 5030 from Thermo Scientific. For the evaluation of the INP measurements with PINEair (section 4.5), the measurement data from the same instruments were used, except for the promo. All aerosol parameters are measured at the permanently staffed station continuously with a time resolution of a few minutes. However, the average values of 30 min are used for the data evaluation, and the measurements are performed at the corresponding ambient temperature. Table 5.1 shows a list of the meteorological parameters used to calculate the Spearman correlation coefficients (section 5.4.5) and the corresponding instrument.

Table 5.1.: Overview of the instruments used to measure the meteorological parameters at the SBO.

parameter	instrument
air temperature	Logotronic
air pressure	Meteolabor BM35
relative humidity	E+E 33
precipitation	Thies 5.4103.10.000
wind speed	Thies 2D inkl. heater
wind direction	Thies 2D inkl. heater

#### 5.2.4. Air Mass Origin

As mentioned above, the air masses at SBO are influenced by both, FT and BL air, in particular during the warmer months of late spring, summer, and early autumn. A tracer to identify the air mass origin is the number concentration of aerosol particles larger than 90 nm in diameter (Herrmann et al., 2015). Aerosol particles in this size range mainly originate from natural or anthropogenic surface sources, and therefore can accumulate to higher concentrations in the well-mixed BL, depending on emission rates and the residence time. The exchange of BL air with the FT is slow, and the aerosol number concentrations in the FT are typically much lower due to dilution and deposition processes during long-range transport in the FT. Therefore, increased number concentrations are a consequence of the influence of air masses from the BL, as they can only originate from vertical transport from local sources. At SBO, the aerosol concentrations with a diameter larger than 90 nm (measured with the SMPS) varied during the time period of the INP measurements between  $1.6 \text{ cm}^{-3}$  and  $1569.9 \text{ cm}^{-3}$ .

Another tracer to identify BL air is  $^{222}\text{Rn}$  ( $^{222}\text{Rn}$ ). It is a short-lived radioactive noble gas produced in soils from the decay of  $^{226}\text{Radium}$ . With its relatively well-known sources close to the ground (e.g., Nazaroff, 1992; Karstens et al., 2015) and its only sink being radioactive decay, high  $^{222}\text{Rn}$  concentrations indicate air mass origin from the BL (Griffiths et al., 2014). At SBO,  $^{222}\text{Rn}$  concentrations are not measured directly, but they can be derived from the  $^{214}\text{Polonium}$  ( $^{214}\text{Po}$ ) daughter activity, assuming radioactive equilibrium. While a correction for  $^{214}\text{Po}$  disequilibrium is typically required (Levin et al., 2002; Schmithüsen et al., 2017), at SBO, equilibrium is achieved due to the high altitude of the site. The  $^{214}\text{Po}$  concentrations are monitored by the Heidelberger University (data courtesy of Ingeborg Levin and Maksym Gachkivskyi) using the Heidelberg Radon Monitor (Levin et al., 2002; Gachkivskyi and Levin, 2022). During the time period of the INP measurements, the  $^{214}\text{Po}$  concentrations varied between  $0.03 \text{ Bq m}^{-3}$  and  $8.7 \text{ Bq m}^{-3}$ .

An attempt was made to divide the entire data set into periods in which the SBO was in the FT or was additionally influenced by air masses from the BL. For this purpose, the limit values found during measurements at the JFJ station (3580 m) were used for the tracers  $^{222}\text{Rn}$  (Griffiths et al., 2014) and number concentration of particles with  $d > 90 \text{ nm}$  (Herrmann et al., 2015). However, the use of these limits for

the SBO site has produced an inconsistent result, therefore the limits are not considered to be appropriate, which might be caused by the different heights of the stations.

Another tracer to identify the influence of BL air is the use of ceilometer measurements which are routinely performed at SBO with a CL51 from Vaisala. A ceilometer can be used to infer the top of the aerosol layer, which indicates the top of the BL. Further information about the method can be found in Lotteraner and Piringer (2016). With the additional information about the BL height, an attempt was made to determine separate limit values for both BL air mass tracers ( $^{214}\text{Po}$  concentration and particle concentration  $d > 90\text{ nm}$ ) for the SBO site. However, it was not possible to define limit values, as there were often data gaps in the data set of the ceilometer measurements as the air at the alpine location of the SBO is clean. Therefore the aerosol concentration is low and the ceilometer is often unable to detect aerosol layers that indicate the upper limit of the BL near the ground. In the future, further measurements should first be performed on-site, or other tracers have to be considered to identify the times of the influence of BL air.

### 5.3. Results

This section describes the results of the INP measurements at the SBO, first the INP temperature spectra, then the seasonal and diurnal variation of the INP concentrations. Finally, the result of the heat treatment of the aerosol filters is shown.

#### 5.3.1. INP Temperature Spectra

Figure 5.7 shows the INP temperature spectra measured with INSEKT (circles) from August 2019 to August 2022, sorted for the different seasons (spring: Mar., Apr., May; summer: Jun., Jul., Aug.; autumn: Sep., Oct., Nov.; winter: Dec., Jan., Feb.). The blue stars show the INP data measured with PINE, here only the data of constant temperature operation ( $T = -23^\circ\text{C} \pm 2^\circ\text{C}$ ) is presented and averaged to 1 h mean values. No temperature scans with PINE are shown, as they were performed at irregular times but mostly during dust events, therefore the data would not be characteristic for the different seasons. The INP concentrations steeply increase with decreasing temperature, however, they vary considerably at a constant temperature. For example, during summer at a temperature of  $-21.5^\circ\text{C}$ , the INP concentration measured with PINE varied over three orders of magnitude, from  $0.1\text{ std L}^{-1}$  to  $150\text{ std L}^{-1}$ , and the data measured with INSEKT varied between  $0.2\text{ std L}^{-1}$  and  $3\text{ std L}^{-1}$  at the same temperature. A good agreement between the results of PINE and INSEKT is only partially present, with a tendency for higher INP concentrations measured with PINE. However, PINE can detect short-term variations in the INP concentration, which is not possible with INSEKT due to the time resolution of one week. Therefore, a more detailed comparison between the two instruments is given in section 5.4.6, where a period of an intensive campaign with a higher time resolution of 8 h for the INSEKT filters is considered.

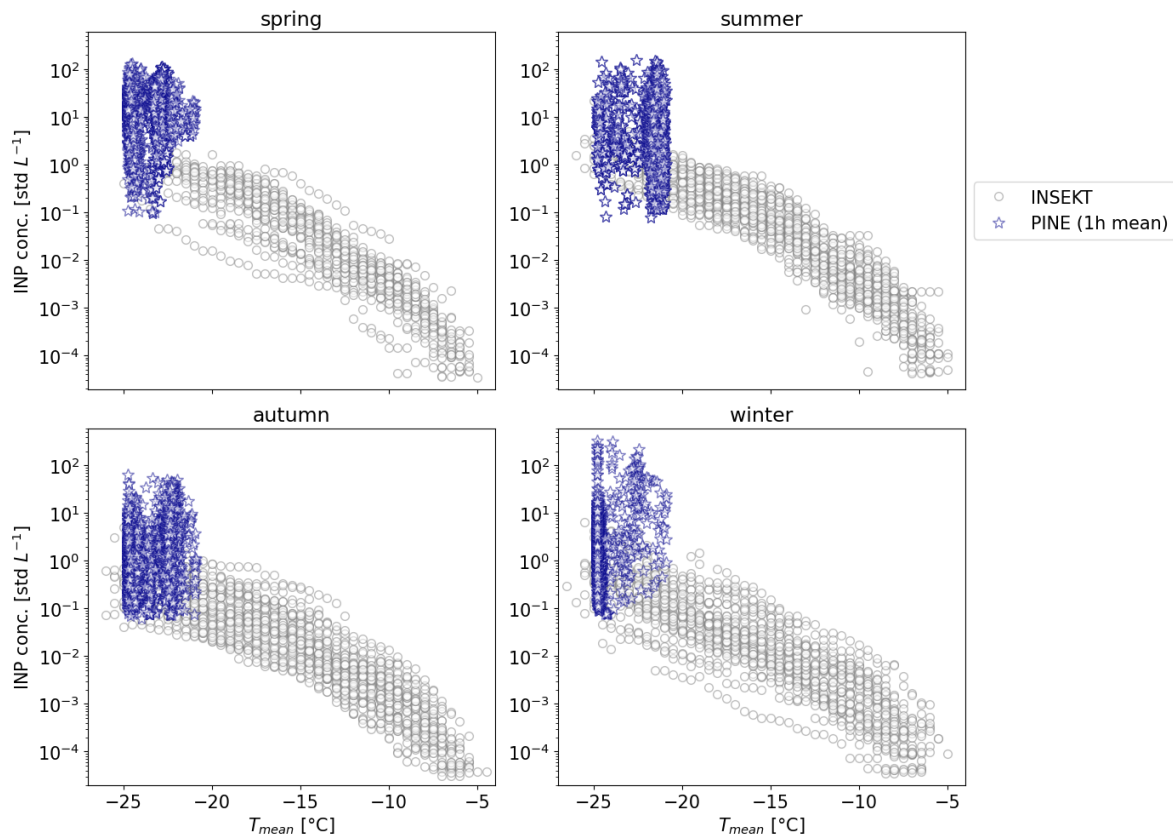


Figure 5.7.: INP temperature spectra measured with INSEKT (circles) and PINE (stars) for the different seasons from August 2019 to August 2022. The aerosol particles analysed with INSEKT were sampled for time periods of one week, PINE data are averaged to 1 h mean values.

To better compare the temperature-dependent INP concentrations measured with INSEKT during the different seasons, the mean values are shown in Figure 5.8 for the data from August 2019 to August 2022. Only the mean value is presented if there are temperature spectra obtained from at least three filters. The mean INP concentrations steeply increase with decreasing temperature from about  $0.00008 \text{ std L}^{-1}$  at  $-5^\circ\text{C}$  to about  $4 \text{ std L}^{-1}$  at  $-25.5^\circ\text{C}$ . In general, the mean INP temperature spectra have a similar trend and similar concentrations in spring and summer. The INP concentrations are significantly lower in autumn/winter, with the difference increasing with decreasing temperature. Possible reasons for the differences in INP concentrations during the seasons are analyzed and discussed in section 5.4. For the averaged INP concentration in winter, the INP temperature spectra look unusual for temperatures higher than  $-7^\circ\text{C}$ , as slightly higher INP concentrations are measured at higher temperatures. This can be explained by the fact that the INP concentrations are in general very low at this temperature and there is not a value for each filter, which makes the outliers more significant when averaging the mean values.

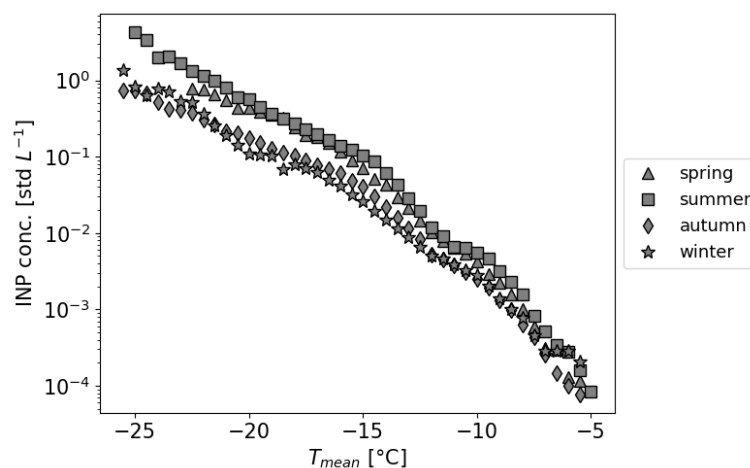


Figure 5.8.: Mean INP temperature spectra measured with INSEKT for the different seasons from August 2019 to August 2022.

### 5.3.2. Seasonal Variation

Figure 5.9 shows a time series of INP concentrations measured with INSEKT and PINE between August 2019 and August 2022 at different temperatures.

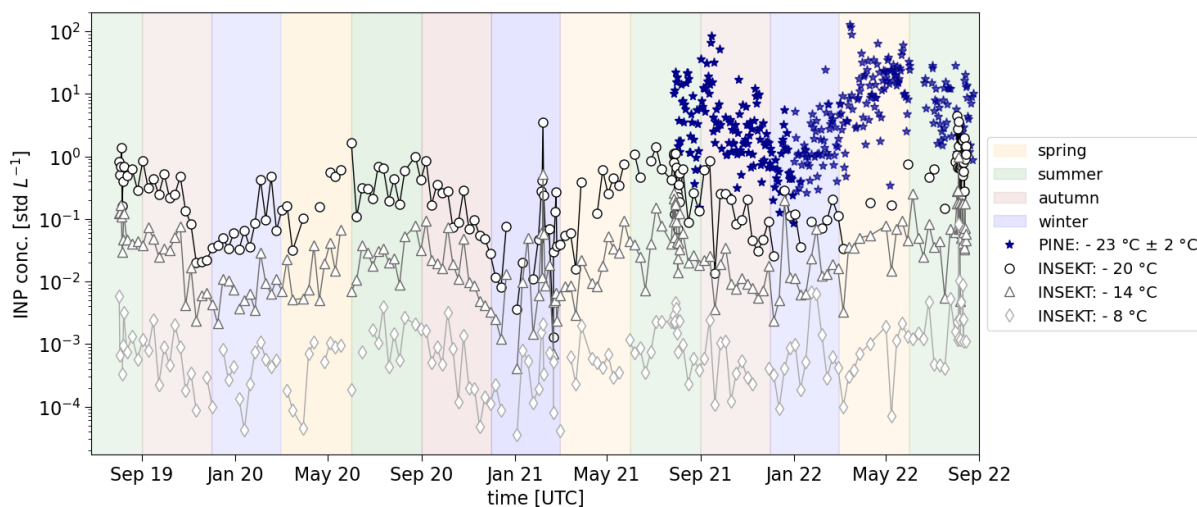


Figure 5.9.: Time series of the INP concentration measured at SBO from August 2019 to August 2022 with INSEKT and PINE. The INSEKT data is shown for the temperatures  $-20^{\circ}\text{C}$  (gray circles),  $-14^{\circ}\text{C}$  (gray triangles) and  $-8^{\circ}\text{C}$  (gray diamonds). The time resolution is 7 d for most data, or 12 h for specific time periods. The PINE data (dark blue stars), is shown for a temperature of  $-23^{\circ}\text{C} \pm 2^{\circ}\text{C}$  and averaged for 1 d. The colored background indicates the seasons with spring in yellow, summer in green, autumn in brown, and winter in blue.

There is a clear seasonal cycle in the INP concentration with lower values in autumn and winter and higher values in spring and summer. This cycle is visible in both the INSEKT data measured at temperatures of  $-20^{\circ}\text{C}$ ,  $-14^{\circ}\text{C}$ , and  $-8^{\circ}\text{C}$  and the PINE data derived at around  $-23^{\circ}\text{C}$ . The time resolution

of the INSEKT data is one week for most of the shown data. Only for shorter periods from August 1 to 8, 2019, July 27 to August 5, 2021, and August 2 to 14, 2022, aerosols were sampled at SBO for shorter time intervals of about 8 – 12 h to e.g. obtain information about the difference of the INP concentrations during day and night hours. The PINE instrument was operated at SBO from August 2021 to October 2022. Figure 5.9 only depicts the PINE INP data measured at a temperature of about  $-23^{\circ}\text{C} \pm 2^{\circ}\text{C}$ . The PINE has a maximum time resolution of about 6 min, but the data shown in Figure 5.9 is averaged for 1 d.

In addition to the seasonal difference, the INP concentration also strongly varies on shorter time scales. For example, at a temperature of  $-14^{\circ}\text{C}$ , it varies from about  $0.0004 \text{ std L}^{-1}$  to  $0.98 \text{ std L}^{-1}$ . Both the seasonal cycle and the shorter-term variations may be caused by different air mass origins, which is discussed in more detail in sections 5.4.2 and 5.4.3.

Brunner et al. (2022) also found an annual variation of INP concentrations measured at the JFJ station, (3580 m a.s.l.) from February 2020 to January 2021, with the highest concentrations in April, July, and August, and the lowest in December. These measurements were performed with the online instrument HINC-Auto at a temperature of  $-30^{\circ}\text{C}$ . Excluding the data where the JFJ was influenced by dust events, they measured a median INP concentration of  $0.5 \text{ std L}^{-1}$  in autumn and  $0.7 \text{ std L}^{-1}$  in winter. In comparison, the median INP concentration at the SBO at the same temperature is higher during both seasons, in autumn it is  $9.8 \text{ std L}^{-1}$ , and in winter  $5.6 \text{ std L}^{-1}$ . In general, the observation of a seasonal cycle with high INP concentrations in spring/summer and the lowest INP concentration in winter is also consistent with other studies in a wide temperature range between  $-13^{\circ}\text{C}$  and  $-22^{\circ}\text{C}$ , which were not performed at mountain stations, but e.g. in the Arctic (Wex et al., 2019) or in the boreal forest (Schneider et al., 2021a). The seasonal variations in the INP concentration can be caused by different sources (dust vs. local biogenic aerosols) or different transport pathways (long-range vs. convective uplift) (Brunner et al., 2022).

### 5.3.3. Diurnal Variation

Figure 5.10 shows the monthly averaged diurnal variation of the INP concentrations measured with PINE at a temperature of  $-23^{\circ}\text{C} \pm 2^{\circ}\text{C}$ . The median INP concentration is presented to avoid over-weighting of strong outliers, e.g. due to dust events. The plots show the data as a function of the local time for the different seasons from September 2021 to August 2022. Data for June 2022 are not shown, because, due to technical problems and a power failure at SBO, the PINE instrument measured only on a few days, therefore the measurement data are not representative for the whole month.

The highest INP concentrations are measured in spring, for example in May 2022, with up to  $22.9 \text{ std L}^{-1}$ . From April to September, a clear daily cycle of the INP concentration is observed with a maximum around noon and a minimum at midnight. For example, in July 2022, the INP concentration varied from  $2.4 \text{ std L}^{-1}$  to  $9.8 \text{ std L}^{-1}$ . The time at which the maximum INP concentration is reached varies between the different months. From October 2021 to February 2022, there is no diurnal variation, and

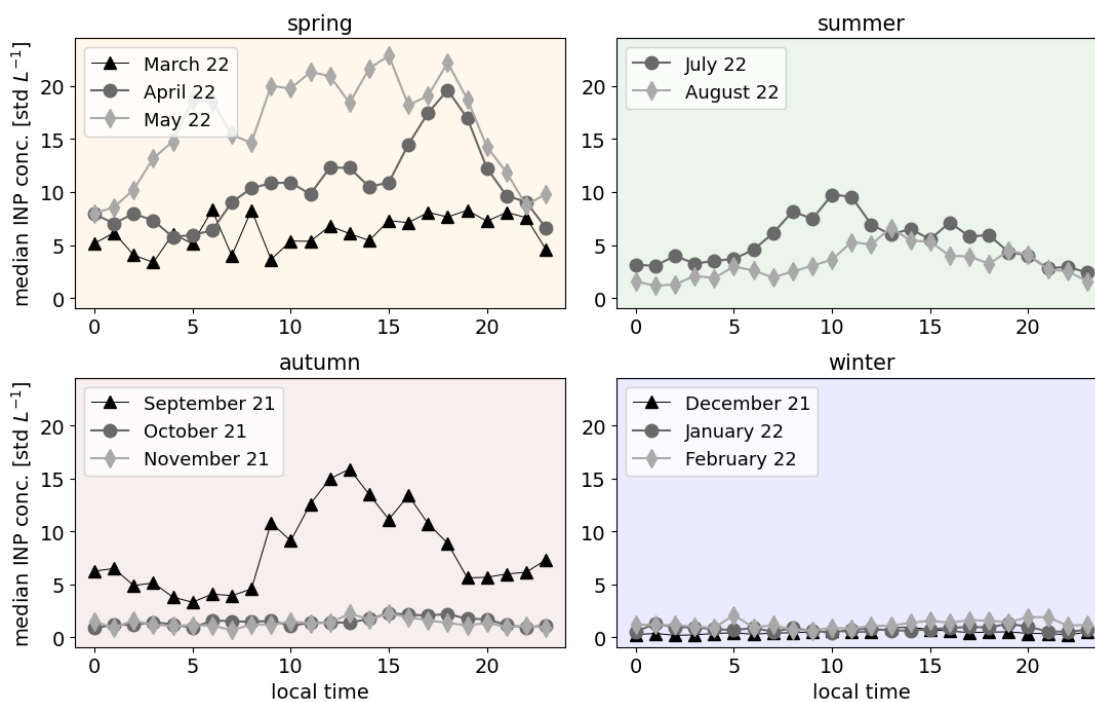


Figure 5.10.: Monthly averaged diurnal variation of the INP concentration measured with PINE at a temperature of  $-23^{\circ}\text{C} \pm 2^{\circ}\text{C}$ . The different panels show the data for the different seasons from September 2021 to August 2022.

the INP concentrations are constantly low between about  $0.2 \text{ std L}^{-1}$  and  $2.3 \text{ std L}^{-1}$ . Brunner et al. (2022) observed in their INP measurements at the JFJ station that there is only a daily cycle in the INP concentration on the days when the site is influenced by the air masses from the BL. For the SBO data set, this aspect is investigated and discussed in more detail in section 5.4.2.

#### 5.3.4. Heat Treatment

As already explained in section 3.2 the filters for the analysis with INSEKT can additionally be analyzed with a heat treatment to obtain information about heat-sensitive INPs. This was done for some filters from the long-term measurements, which have a time resolution of one week, providing information on the seasonal variations of heat-sensitive INPs. Figure 5.11 shows all INP temperature spectra for the untreated samples (grey circles) and the heat-treated samples (red circles) measured with INSEKT from August 2019 to August 2022, sorted for the different seasons. Also shown are the temperature-dependent mean INP concentrations for each season (dark grey symbols), and the mean INP concentrations after heat treatment of the aerosol particle suspensions (red symbols). After heat treatment, the INP concentrations increase with decreasing temperature, but they are significantly reduced, in particular at higher temperatures between around  $-13^{\circ}\text{C}$  and  $-6.5^{\circ}\text{C}$ .

Figure 5.12 shows that the INP temperature spectra for the heated filters are similar for the different

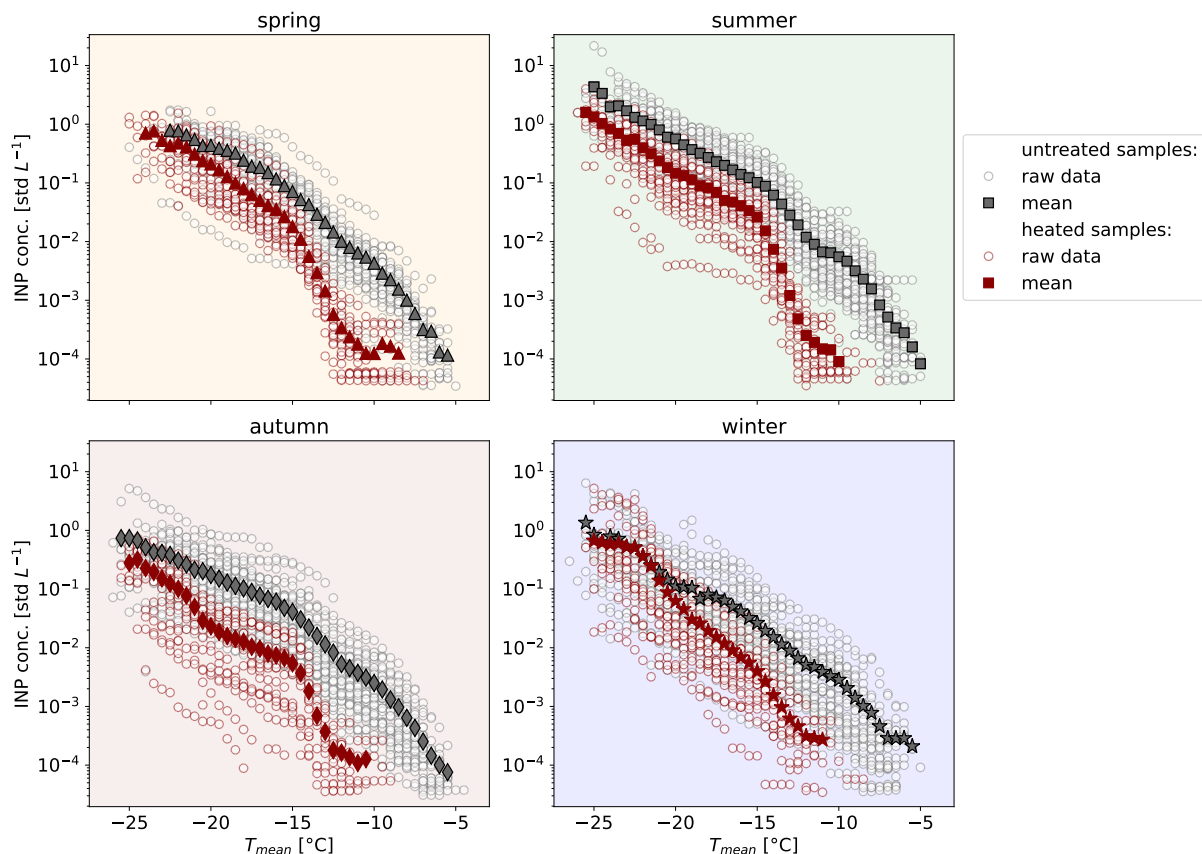


Figure 5.11.: INP temperature spectra measured with INSEKT for the different seasons. Grey circles correspond to aerosol sampled between August 2019 to August 2022 with a time resolution of one week, and red circles indicate the results for the heat-treated suspensions. Filled symbols show the respective mean values.

seasons at the higher temperatures. At lower temperatures between around  $-25.5^{\circ}\text{C}$  and  $-13^{\circ}\text{C}$ , the INP concentrations of the heat-treated samples are slightly lower in autumn and winter than in spring and summer. Overall, the decrease of the INP concentration by heat treatment is stronger at higher temperatures than at lower temperatures, indicating the presence of heat-sensitive INPs which are more active at higher temperatures and probably are related to biological aerosol particles.

To obtain information about the presence of heat-sensitive INPs between day and night, the filters from the intensive campaign on August 2-14, 2022, with a time resolution of 8 h, are additionally analyzed with the heat treatment. Figure 5.13 shows the INP concentration measured with INSEKT for the different temperatures a)  $-20^{\circ}\text{C}$ , b)  $-17^{\circ}\text{C}$ , and c)  $-14^{\circ}\text{C}$ , the untreated samples in black and the heat-treated samples in red. The gray background shows the time period of the night filters, which were sampled from 10 pm to 6 am local time. The day filters were sampled from 10 am to 6 pm local time. After the heat treatment, the INP concentrations are decreased for all three temperatures, both during the day and at night.

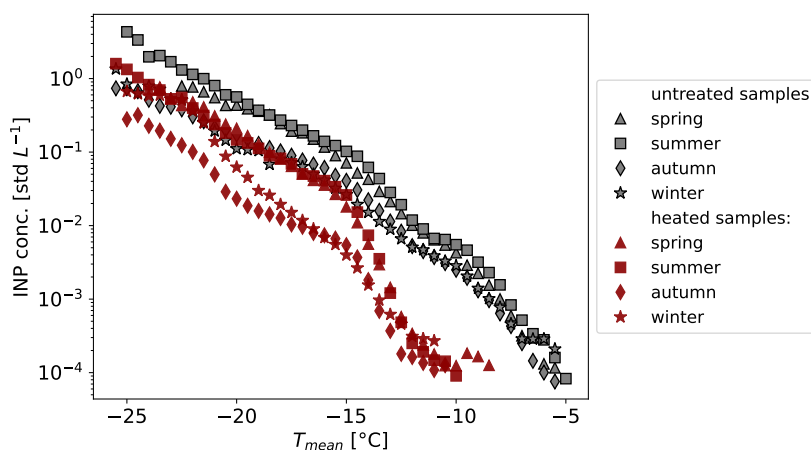


Figure 5.12.: Mean INP temperature spectra for the untreated samples (dark grey symbols) and the heat-treated samples (red symbols) measured with INSEKT for the different seasons from August 2019 to August 2022. The different symbols indicate the different seasons.

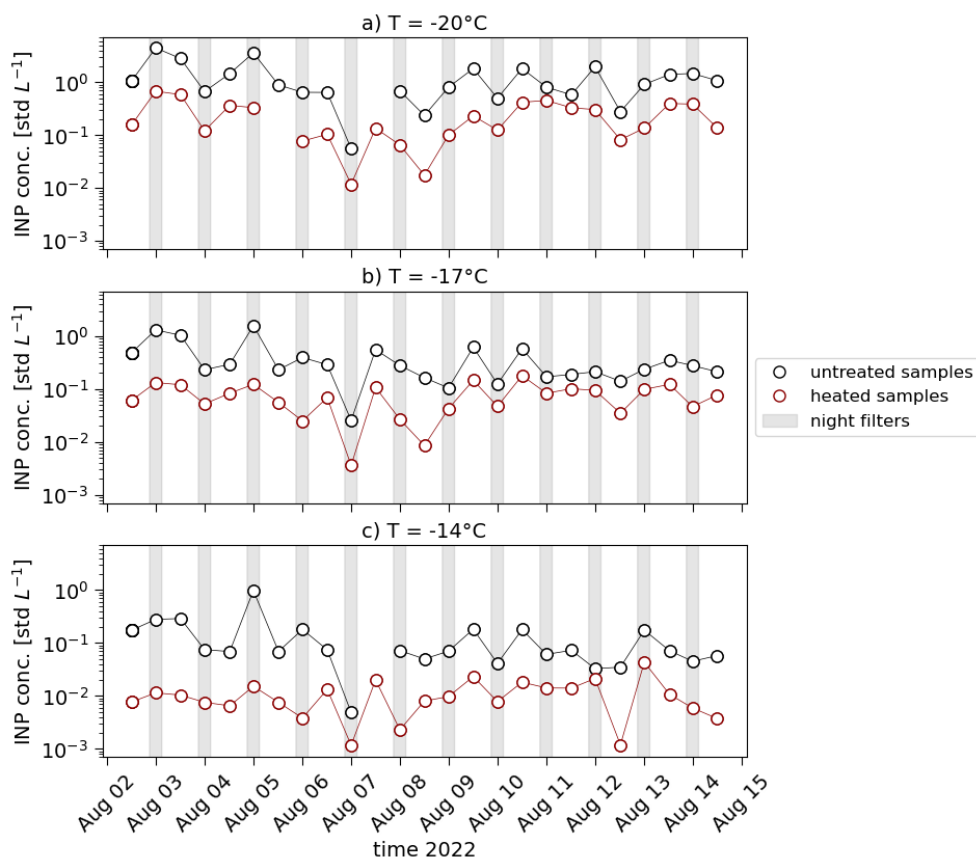


Figure 5.13.: INP concentration of the untreated day and night filters (black circles) and heat-treated suspensions (red circles) for the temperatures a)  $-20^{\circ}\text{C}$ , b)  $-17^{\circ}\text{C}$ , and c)  $-14^{\circ}\text{C}$  in the period from August 2-14, 2022. The time resolution of the data is 8h, the gray shaded area shows the period of the night filters.

## 5.4. Discussion

In this section, the INP measurements at SBO are discussed and interpreted for different aspects. First, for the potential contribution of different aerosol types. Then for the role of the air mass origin, including BL air influenced by more regional or local aerosol sources and long-range transport episodically influenced by Saharan dust sources, for the influence of clouds and other parameters. Finally, a comparison between the measurements with INSEKT and PINE is shown.

### 5.4.1. Aerosol Types

Heat treatment of the aerosol particle suspensions caused a significant reduction of the INP concentration, especially at temperatures higher than  $-13^{\circ}\text{C}$  (Figure 5.11). On average, this general INP reduction by heat treatment was observed for all seasons (Figure 5.12), which means that heat-sensitive INPs are present at the SBO throughout the whole year and at almost all tested temperatures from about  $-25.5^{\circ}\text{C}$  to  $-5^{\circ}\text{C}$ , except during winter at temperatures lower than  $-21.5^{\circ}\text{C}$ . At temperatures below about  $-13^{\circ}\text{C}$ , the heat treatment had a lower effect, but still, a significant fraction of all INPs seems to be heat-sensitive. Only during winter and at temperatures below about  $-21.5^{\circ}\text{C}$ , no significant reduction of the INP concentration by heat treatment was observed. Both the day and night filters showed a reduction in the INP concentration by the heat treatment for all three temperatures  $-20^{\circ}\text{C}$ ,  $-17^{\circ}\text{C}$ ,  $-14^{\circ}\text{C}$  (Figure 5.13), indicating that heat-sensitive INPs were present throughout the day during the intensive campaign in August 2022. It is generally assumed that heat-sensitive INPs are of biological origin (Morris et al., 2004; Hill et al., 2016), whereas heat-resistant INPs in particular at lower temperatures are considered to be mineral dust particles (Murray et al., 2012). The presence of both INP types throughout the year, in combination with the also observed seasonal and diurnal variations of the INP concentrations (section 5.3.2 and section 5.3.3) indicates that the air masses at SBO are not only influenced by the FT but also by both BL air masses and long-range transport of Saharan dust. This will be further discussed in the following two sections. The investigation of ice residuals in a future study could provide further information about the aerosol types at the SBO that can serve as INPs.

### 5.4.2. Boundary Layer Influence

Figure 5.14 shows the three-year record (August 2019 to August 2022) of INP concentrations measured with INSEKT at a temperature of  $-17^{\circ}\text{C}$  and with a time resolution of 12h to 7d (top panel), the daily averaged  $^{214}\text{Po}$  concentration (middle panel), and the daily averaged number concentration of aerosol particles with diameters larger than 90 nm (bottom panel). The different seasons are color-shaded with yellow for spring, green for summer, brown for autumn, and blue for winter. The data depicted in Figure 5.14 can all be represented by a sinusoidal function (solid lines), with a recurring annual trend of highest concentrations in summer and lowest concentrations in winter for all three parameters. As discussed in section 5.2.4, both the aerosol concentration and the  $^{214}\text{Po}$  concentration are used as tracers for

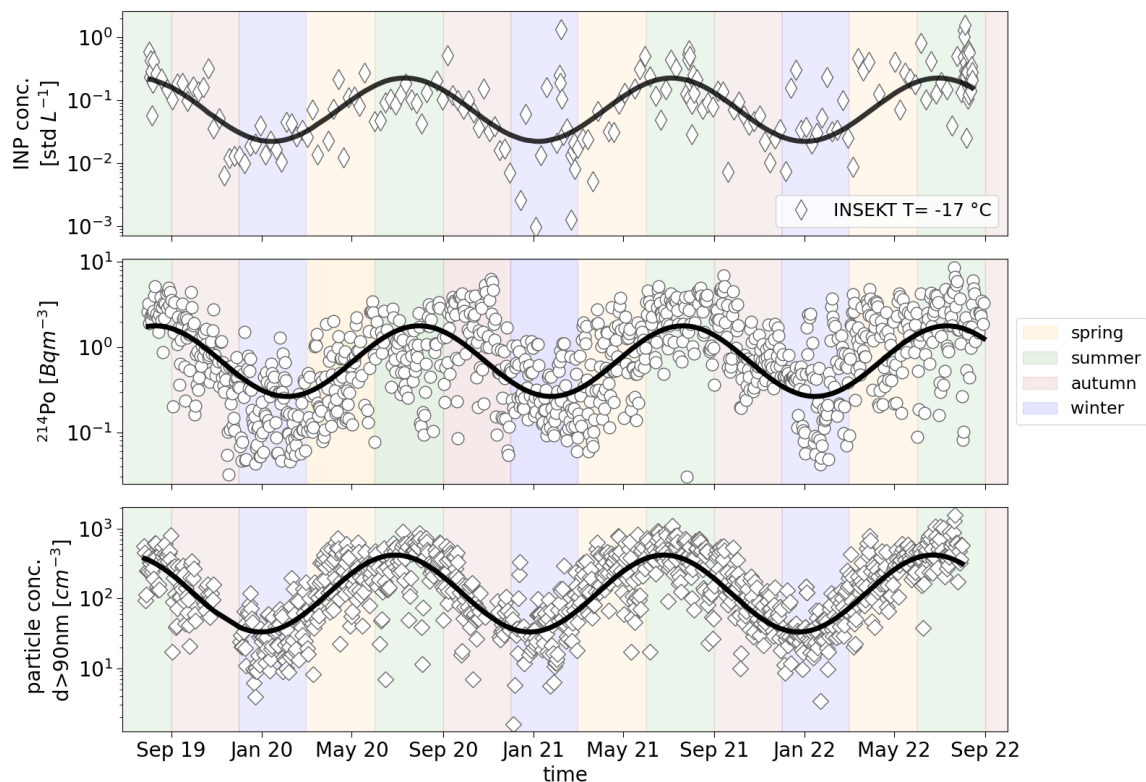


Figure 5.14.: INP concentrations measured with INSEKT at a temperature of  $-17^{\circ}\text{C}$  (upper panel), daily averaged  $^{214}\text{Po}$  concentration (middle panel), and daily averaged concentration of aerosol particles with diameters larger than 90 nm (lower panel). The lines in each panel represent sinusoidal fits to the data. The color shaded areas indicate the different seasons.

the air mass origin at SBO, and larger values indicate a larger contribution of air masses originating from the BL. It should be noted, however, that the daily averaged values shown in Figure 5.14 do not allow to quantify the relative contribution or fraction of BL and FT air to the INP concentrations measured at SBO. More information on the processes contributing to the INP concentrations may be obtained from the monthly averaged daily cycles measured with the PINE instrument at higher time resolution (Figure 5.10). From April to September, a clear diurnal cycle of INP concentrations is observed, with maximum values during the daytime and minimum values during the night. A similar diurnal variation is also shown in the aerosol concentrations (Figure 5.15) and the  $^{214}\text{Po}$  concentrations (Figure 5.16). This is probably caused by BL mixing processes during the day, also influenced by convective updraft in the complex mountain terrain around SBO. In contrast, from October to February, the INP (Figure 5.10), aerosol (Figure 5.15) and  $^{214}\text{Po}$  (Figure 5.16) concentrations are constantly low during the day, indicating that the SBO is located in the FT most of the winter time. Therefore, the INP concentrations measured at SBO during the winter months may represent the more constant and well-mixed INPs present in the lower FT.

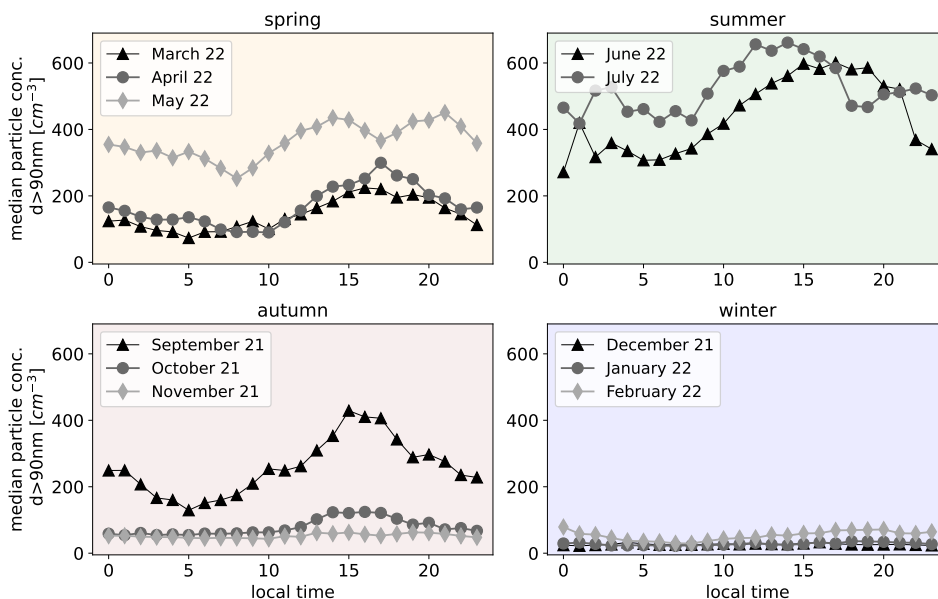


Figure 5.15.: Monthly averaged diurnal variation of the number concentration of aerosol particles with diameters larger than 90 nm. The different panels show the data for the different seasons from September 2021 to July 2022, data from August 2022 are not available.

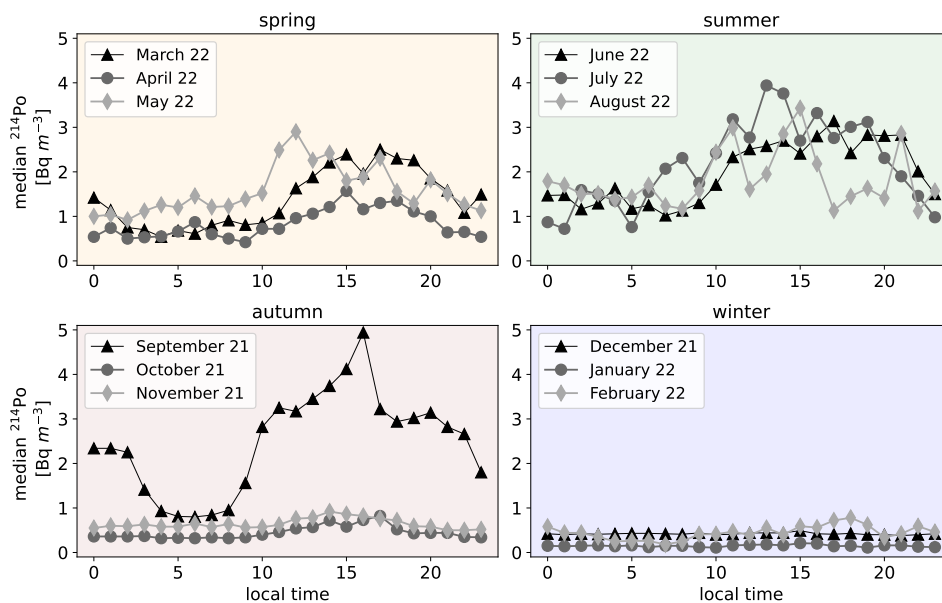


Figure 5.16.: Monthly averaged diurnal variation of the number concentration of  $^{214}\text{Po}$  concentration. The different panels show the data for the different seasons from September 2021 to August 2022.

From October 2021 to February 2022 the median INP concentration only varied between about  $0.2 \text{ std L}^{-1}$  and  $2.3 \text{ std L}^{-1}$ . It should be noted here, that also during this winter time period, a significant decrease was observed for the monthly mean INP concentration after heat treatment of the INSEKT aerosol suspensions for temperatures higher than  $-21.5^\circ\text{C}$ . From this, it can be concluded that there is a significant

contribution of heat-sensitive INPs to the overall abundance of INPs in the lower FT, at least during winter time.

The strong correlation between the INP concentration measured with PINE at a temperature of  $-23^{\circ}\text{C} \pm 2^{\circ}\text{C}$  and the BL air mass tracer of aerosol particles with diameters larger than 90nm is also underlined by a Spearman correlation analysis which resulted in a positive correlation coefficient  $\rho$  of 0.78. The correlation was calculated for all available hourly mean data between September 2021 and August 2022. Notably, the two tracers ( $^{214}\text{Po}$  and aerosol concentration) have slightly shifted minima and maxima with respect to time of about 27 days (Table 5.2). In the study of Brunner et al. (2021), performed at the High Altitude Research Station Jungfraujoch (3580 m a.s.l.) the measurements of  $^{222}\text{Rn}$  and number concentration of aerosol particles with a diameter larger than 90nm were also used, among others, to identify the air mass present at the station. Here they also pointed out that the tracers do not always show the same result. In the study at SBO, the minima, and maxima of the INP concentration are reached in the time between the minima and maxima of the two tracers, with a better agreement to the data of the number concentration of aerosol particles with  $d > 90\text{nm}$  (Table 5.2), which is also reflected by the high correlation coefficient  $\rho$ . The position of the maxima of the INP concentration is strongly influenced by the diurnal variation of the tracers, which is different for both tracers for each month (Figures 5.15 and 5.16). More research needs to be done in the future to better interpret the tracers, or additional tracers need to be considered.

parameter	Min 19/20	Max 20	Min 20/21	Max 21	Min 21/22	Max 22
INP conc. (INSEKT, $-17^{\circ}\text{C}$ )	13.01.20	12.07.20	03.01.21	04.07.21	02.01.22	26.06.22
$^{214}\text{Po}$ conc.	04.02.20	31.07.20	24.01.21	21.07.21	15.01.22	11.07.22
Particle conc. $d > 90\text{nm}$	31.12.19	29.06.20	26.12.20	26.06.21	24.12.21	23.06.22

Table 5.2.: Times for minima and maxima of the INP concentration (INSEKT,  $T = 256\text{K}$ ),  $^{214}\text{Po}$  and particle concentration of aerosol particles with  $d > 90\text{nm}$  in the period from August 2019 to August 2022. Compare with Figure 5.14.

### 5.4.3. Saharan Dust Influence

In section 5.4.2, the general diurnal and annual trends of the INP concentrations and their correlation with similar trends of the two BL air mass origin tracers were discussed. Short-term changes of the INP concentration, e.g. during February 2021 (Figure 5.9), will be discussed in more detail in this section.

The air masses at the SBO are frequently influenced by the long-range transport of mineral dust from the Saharan desert (Tsamalis et al., 2013). They can be transported in the FT over very long distances between continents (e.g., Prospero, 1999) and can thus have an influence on cloud formation. Saharan desert dust particles are known to be efficient INPs, especially at temperatures lower than about  $-15^{\circ}\text{C}$

(e.g., Hoose and Möhler, 2012; Murray et al., 2012; Kanji et al., 2017). The presence of dust may be indicated by the aerosol mass concentration (e.g., Schauer, 2015; Baumann-Stanzer et al., 2018; O’Sullivan et al., 2020), which is shown in Figure 5.17 (lower panel) for the time period from August 2021 to August 2022, together with the INP concentration measured with PINE at a temperature of  $-23^{\circ}\text{C} \pm 2^{\circ}\text{C}$  (upper panel).

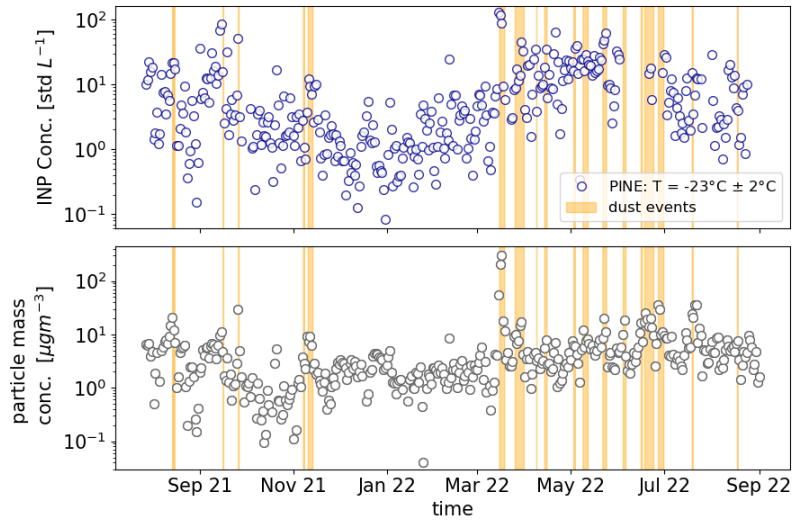


Figure 5.17.: Time series from August 2021 to August 2022 for INP concentration measured with PINE at a temperature of  $-23^{\circ}\text{C} \pm 2^{\circ}\text{C}$  (upper panel), and for the aerosol particle mass concentration (lower panel). Both data sets are averaged to 1 d. The yellow shaded time periods represent dust events identified according to the SBO dust report.

Both data sets are shown as daily averaged values. The yellow shaded areas in Figure 5.17 indicate dust events that have been classified by the SBO (dust report from the SBO data portal <https://data.sonnblick.net>). This classification is based on the following two criteria to be fulfilled: (1) the particle mass concentration has to be larger than  $5\mu\text{g m}^{-3}$  for at least 8 half-hour averages, and (2) the exponent of the single scattering albedo has to be negative. Figure 5.17 shows that for several dust events the INP concentration is larger than during time periods without dust influence. The Spearman correlation coefficient of the INP concentration and the particle mass concentration for the whole time period from August 2021 to August 2022 results in a positive correlation coefficient of 0.6.

A similar observation was also made in the study by Brunner et al. (2021) at the JFJ in the period from February 2020 to December 2020, INP measurements were performed with HINC-Auto in the immersion freezing mode at  $T = -30^{\circ}\text{C}$  and saturation ratio with respect to water  $S_w = 1.04$ . They also measured an increase in the INP concentration during each dust event, but the measured median INP concentration varied over two orders of magnitude.

Figure 5.18 illustrates an example of how strongly the INP concentration can be influenced by the presence of dust. For this, a day with dust influence (red, February 10, 2022) and without dust influence

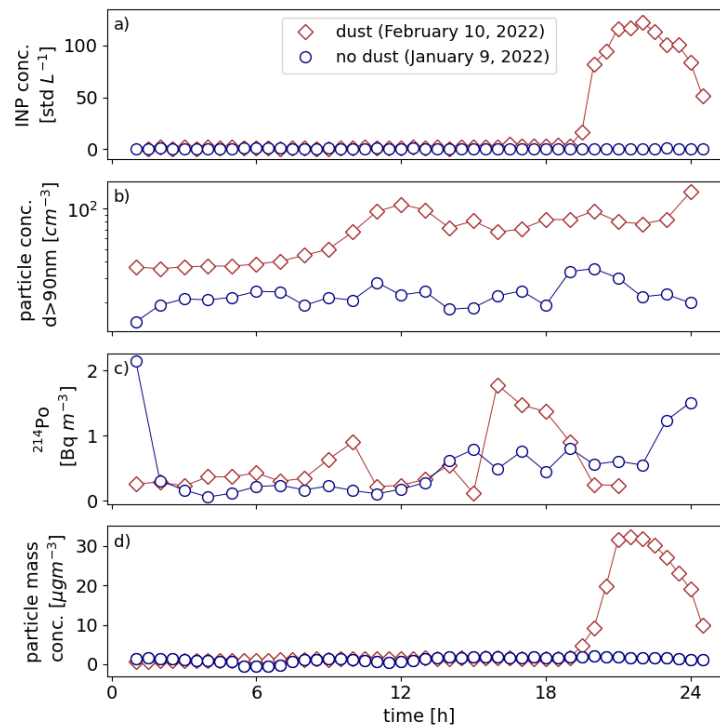


Figure 5.18.: Comparison between a dust event on February 10, 2022 (red square) and a day with no dust influence (January 9, 2022, blue circles). Panel a) shows the INP concentration measured with PINE (data averaged to 30min mean), panel b) the particle concentration of aerosol particles with  $d > 90\text{nm}$  (data averaged to 1h mean), panel c) the  $^{214}\text{Po}$  concentration (data averaged to 1h mean) and panel d) the particle mass concentration (data averaged to 30min mean) as a function of time in  $h$ .

(blue, January 9, 2022) are compared to each other. All parameters are shown as a function of time, in panel a) the INP concentration measured with PINE at  $T = -23^\circ\text{C} \pm 2^\circ\text{C}$ , and in panel d) the particle mass concentration, each data set is averaged to a time resolution of 30 min. Panel b) and c) represent the tracers for BL air (concentration of aerosol particles with  $d > 90\text{nm}$  and the  $^{214}\text{Po}$  concentration), both tracers show low concentrations on both days, therefore it can be assumed that the SBO was predominantly influenced by the air masses from the lower FT. On January 9, 2022 (lines in blue), no dust impact occurred at the SBO, the particle mass concentration is constant  $< 2.05 \mu\text{g m}^{-3}$ , and the INP concentration is  $< 1 \text{std L}^{-1}$ . In red an example day for dust influence is shown (February 10, 2022). Around 19h the particle mass concentration increased from about  $1.5 \mu\text{g m}^{-3}$  to  $32.3 \mu\text{g m}^{-3}$ , at the same time an increase in the INP concentration from  $3.7 \text{std L}^{-1}$  to  $122.5 \text{std L}^{-1}$  can be observed. The aerosol concentration is higher during the dust event compared to the day without dust influence, but the  $^{214}\text{Po}$  concentration is low for both days. It can therefore be concluded that the dust is mostly transported in the lower FT to the SBO. In section 5.5 is a more detailed description of another case study (March 2022) of the strongest dust event during the measurement period with PINE.

#### 5.4.4. Cloud Influence

Another source that may influence the INP concentration is the presence of clouds, for example, precipitation can remove aerosols through wet-removal processes (Wang et al., 2014). Furthermore, pre-activation of INPs to ice crystals can lead to a reduction in the INP concentration, for example, this was observed in a study by Stopelli et al. (2015) at temperatures higher than  $-10^{\circ}\text{C}$  at the Jungfraujoch station. To investigate this with the SBO data, the PINE measurements ( $T = -23^{\circ}\text{C} \pm 2^{\circ}\text{C}$ ) from August 2021 to October 2022 are split into "clear sky" and "cloudy" conditions, using the approach of Herrmann et al. (2015). For this purpose, first, the sky temperature  $T_{sky}$  is calculated according to the Stefan Boltzman law by using the longwave irradiance measurements (LW) on-site and the Boltzman constant ( $\sigma_{LW} = 5.67 \cdot 10^{-8} \text{ W m}^{-2} \text{ K}^{-4}$ ):

$$LW = \sigma_{LW} \cdot T_{sky}^4 \quad (5.1)$$

Afterwards,  $T_{sky}$  is compared to the ambient temperature. If  $T_{sky}$  is approximately equal (deviation  $< 5^{\circ}\text{C}$ ) to the ambient temperature, it can be assumed that cloudy conditions exist as the longwave radiation is absorbed by the cloud. In contrast, if the deviation between  $T_{sky}$  and the ambient temperature is  $> 5^{\circ}\text{C}$ , it is considered that there are clear sky conditions.

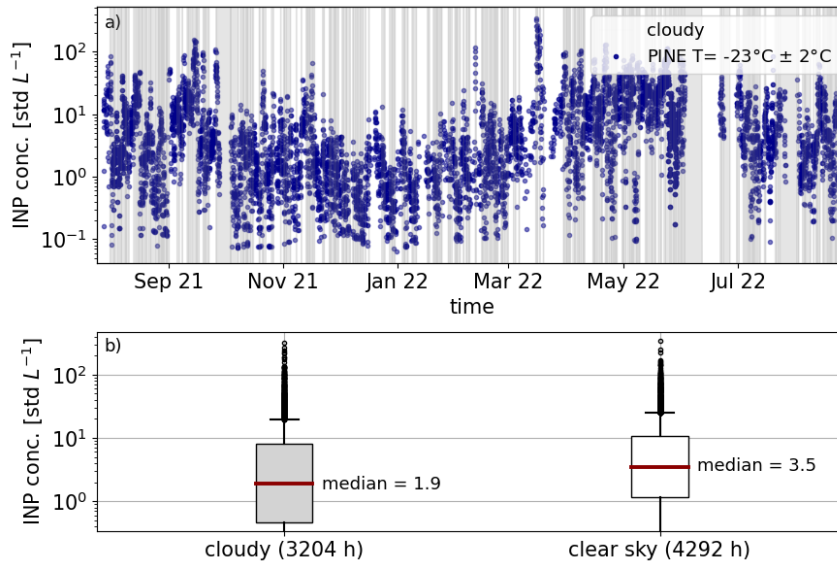


Figure 5.19.: a) INP concentration measured with PINE at  $T = -23^{\circ}\text{C} \pm 2^{\circ}\text{C}$  in the period August 2021 to October 2022. The gray shaded area indicates cloudy periods, and a white background means a clear sky. Panel b) shows the boxplots of the measured INP concentration divided into the periods cloudy (left) and clear sky (right) with the number of hours during the measurement period and the median INP concentration.

In Figure 5.19a, the cloudy periods are marked in gray, the clear-sky periods are shown in white, and panel b shows the corresponding boxplots of the two conditions. Clear-sky periods occurred with about

1000h more at the SBO in the considered measurement period of about 14 months (Figure 5.19b), and they are distributed over the whole year. Furthermore, in both cloudy and clear-sky conditions outliers up to several  $100 \text{ std L}^{-1}$  INPs are measured, as these are likely caused by dust events. There is a difference in the comparison between the median INP concentration of the cloudy ( $1.9 \text{ std L}^{-1}$ ) and clear-sky ( $3.5 \text{ std L}^{-1}$ ) periods, with a slightly higher concentration for the latter. This could be caused by the processes mentioned above, such as wet-removal or pre-activation. To quantify these two effects even more precisely, the measurements should be investigated with a higher time resolution in a further analysis and, for example, the INP concentration in the transition phases between cloudy and clear-sky periods and vice versa should be analyzed.

In contrast, no difference in the INP concentrations was found between cloudy and clear-sky periods in the study by Lacher et al. (2018b) at the High Altitude Research Station Jungfraujoch. Here, nine individual field campaigns were analyzed in winter, spring, and summer in the years 2014 to 2017 at a temperature of  $-31^\circ\text{C}$ .

#### 5.4.5. Relation to Aerosol Properties and Meteorological Conditions

To investigate other possible sources for the variations in the INP concentration in more detail, the Spearman correlation coefficient  $\rho$  is calculated for various meteorological parameters (air temperature, air pressure, relative humidity, precipitation, wind direction, wind speed) and some aerosol properties (particle concentration: total,  $d \geq 0.3 \mu\text{m}$ ,  $\geq 0.5 \mu\text{m}$ ,  $\geq 0.7 \mu\text{m}$ ,  $\geq 1.0 \mu\text{m}$ ,  $\geq 2.5 \mu\text{m}$ , particle mass concentration).

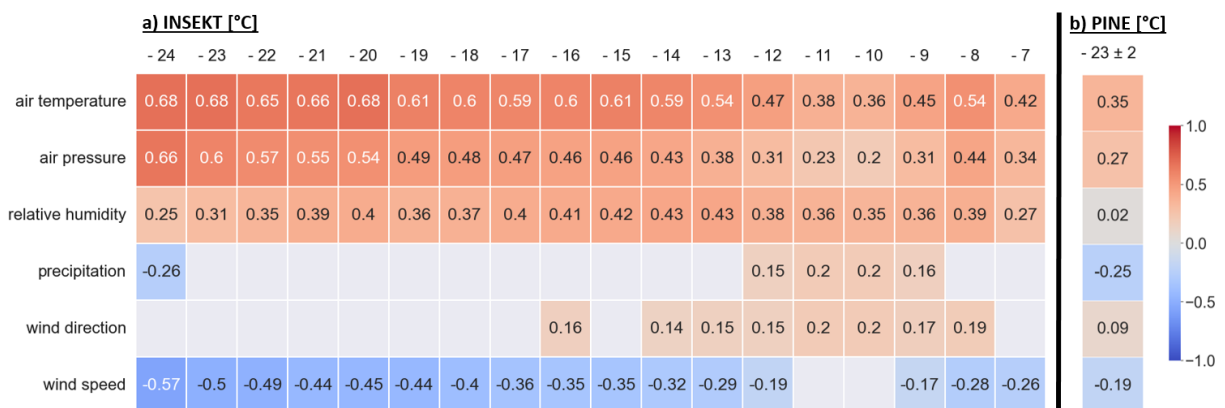


Figure 5.20.: a)  $\rho$  for the correlation between the INP concentration measured with INSEKT in the temperature range of  $-24^\circ\text{C}$  to  $-7^\circ\text{C}$  and meteorological parameters. All data sets are averaged according to the time resolution of the INSEKT data which is 8h to 7d. b)  $\rho$  for the correlation between the INP concentration measured with PINE at a temperature of  $-23^\circ\text{C} \pm 2^\circ\text{C}$  and meteorological parameters. All data sets are averaged to 30 min mean values.

Figure 5.20a shows  $\rho$  (number in the respective boxes) for the correlation for the INP concentration measured with INSEKT at the temperatures from  $-24^{\circ}\text{C}$  to  $-7^{\circ}\text{C}$  and the meteorological parameters. The meteorological data were averaged to the same time periods of the INSEKT filters, which is usually one week, except during the intensive campaigns. The colors of the boxes correspond to the calculated  $\rho$  for the correlations, red means a positive correlation and blue means a negative correlation. For boxes without a number, the p-value was not  $< 0.05$ , so the correlation is considered to be insignificant. Figure 5.20b shows  $\rho$  for the correlation for the INP concentration measured with PINE at a temperature of  $-23^{\circ}\text{C} \pm 2^{\circ}\text{C}$  and the meteorological parameters, 30 min mean values were calculated. Especially at the lower nucleation temperatures for the measurements with INSEKT, there is a positive correlation ( $\rho > 0.5$ ) between the measured INP concentration and the air temperature (Figure 5.20a first row). The same applies to  $\rho$  for the correlation between the INP concentration measured with INSEKT and the ambient pressure (Figure 5.20a second row). It is striking that this behavior is not reflected in the INP measurements with PINE, there is no positive correlation for either the air temperature or the ambient pressure (Figure 5.20b first and second row). The reason for this is probably the difference in the time resolution of the two data sets. No short-term variations can be detected with the measurements performed with INSEKT, therefore the calculation of  $\rho$  with the PINE data is considered to be more representative. This assumption is supported by the fact that the calculated  $\rho$  for the correlation from the measurement campaign with PINEair in the MPC temperature range at the SBO (May 2023, section 4.5.2) also showed no correlation ( $\rho < 0.5$ ) between the measured INP concentration and the meteorological parameters and they were also averaged to 30min mean values. Therefore, it can be concluded that none of the considered meteorological parameters can explain the variation in the INP concentration.

In the long-term study at the Jungfraujoch station by Brunner et al. (2022), they also found no correlation between the INP concentration and the ambient temperature ( $\rho = 0.149$ ). They hypothesized that the reason for this could be that the investigated ice-activation temperature ( $T = -30^{\circ}\text{C}$ ) is significantly lower than the median ambient temperature ( $T = -6.5^{\circ}\text{C}$ ) and that therefore a considerable part of the INPs could be removed from the air layers around the site when the INPs activate and the formed ice crystals sediment. For the INP measurements performed with PINE at the SBO, the investigated ice-activation temperature ( $T = -23^{\circ}\text{C}$ ) is also lower compared to the median ambient temperature ( $T = -2.8^{\circ}\text{C}$ ) during the measurement period, so this could be the same reason for a non-correlation to the ambient temperature. However, this assumption is not consistent with the observations of Schneider et al. (2021a), where a positive correlation between INP concentration and ambient temperature was found, although the INP concentration was investigated at  $T = -16^{\circ}\text{C}$  and the median ambient temperature was  $T = 5^{\circ}\text{C}$ . But the study was performed in a boreal forest environment and it is assumed that the predominant INP types are biological aerosols.

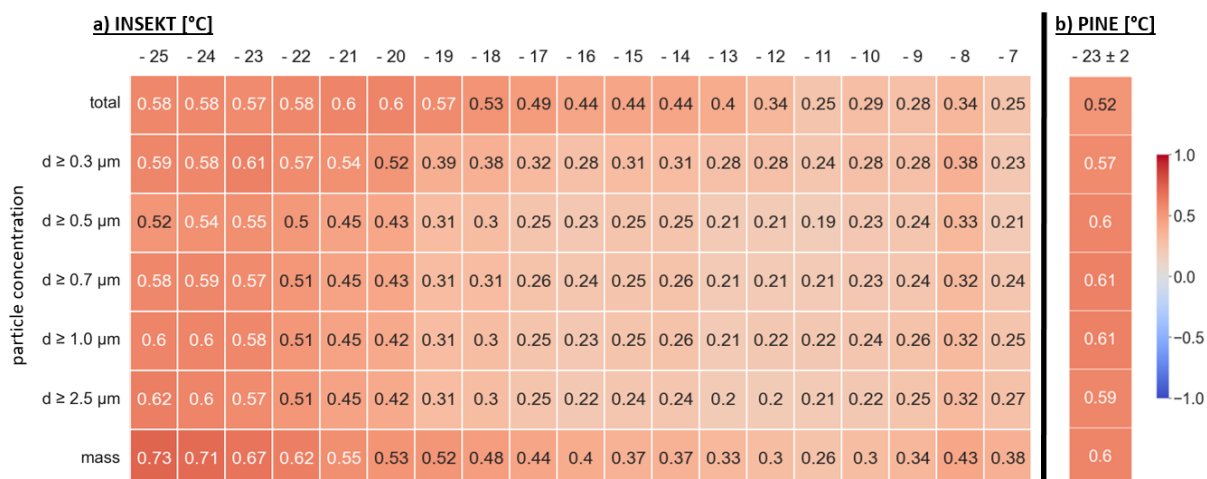


Figure 5.21.: a)  $\rho$  for the correlation between the INSEKT INP data set in the temperature range of  $-25^\circ\text{C}$  to  $-7^\circ\text{C}$  and the concentration of particles with different sizes. All data sets are averaged according to the time resolution of the INSEKT data which is 8 h to 7 d. b)  $\rho$  for the correlation between the INP concentration measured with PINE at a temperature of  $-23^\circ\text{C} \pm 2^\circ\text{C}$  and the concentration of particles with different sizes. All data sets are averaged to 30 min mean values.

Figure 5.21a displays  $\rho$  for the correlation between the INP concentration measured with INSEKT and aerosol properties regarding concentration, size, and mass. Figure 5.21b shows the same for the PINE data set. The time resolution of the measurement data from INSEKT is again 8 h to 7 d and the measurements with PINE are again averaged to 30 min mean values. A trend can be observed in the INSEKT measurements, as  $\rho$  for the correlation varies with the nucleation temperature, with higher correlation coefficients at the lower temperature range for all considered parameters. No direct explanation can currently be found for that, but it might be related to the fact that the INP measurements with INSEKT are more uncertain at higher temperatures, as the counting statistics are low and only very few INPs are collected on the filters. When comparing the PINE and INSEKT data, there are only small differences between the calculated  $\rho$ , which is probably again caused by the different time resolutions of the measurements, but both show a positive correlation ( $\rho > 0.5$ ) between the INP concentration and the here considered aerosol parameters.

#### 5.4.6. Comparison between INSEKT and PINE

As shown in Figure 5.7 (section 5.3.1), the INP concentrations measured with INSEKT and PINE are only partially in agreement with each other. The differences could be explained by the different time resolutions of both instruments (INSEKT: one week and PINE: averaged values for 1 h). Therefore, this section focuses on the comparison of the INP concentrations measured with INSEKT and PINE during the intensive campaign on August 02-14, 2022, when both day and night INP filter samples were taken with an increased time resolution of 8 h.

Figure 5.22 shows the time series of the measured INP concentration during the intensive campaign.

## 5. Long-Term INP Measurements at the Sonnblick Observatory

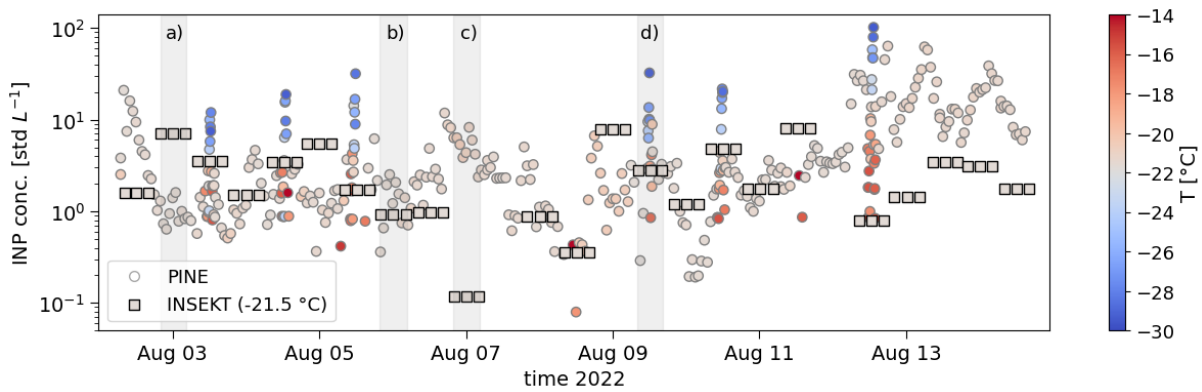


Figure 5.22.: Comparison between INSEKT (squares) and PINE (circles, color-coded for the activation temperature) INP data measured during the intensive campaign in August 2022. PINE data have a time resolution of 6 min during the temperature scans and are averaged to 1 h during operation of constant temperature of  $-21.5^{\circ}\text{C} \pm 1^{\circ}\text{C}$ . INSEKT filters were sampled for a duration of 8 h, and data shows the INP concentrations at a temperature of  $-21.5^{\circ}\text{C}$ .

The circles show the PINE data, color-coded for the activation temperature. During the temperature scans, the time resolution of the INP data is 6 min, for the operation period at a constant temperature ( $T = -21.5^{\circ}\text{C} \pm 1^{\circ}\text{C}$ ) the data is averaged to 1 h. The squares indicate the period of the filter collection for the analysis with INSEKT and show the measured INP concentration at  $T = -21.5^{\circ}\text{C}$ , thus they can be compared to the PINE measurements performed at a constant temperature. The grey shaded areas show selected time periods, which are analyzed in more detail in the following.

Figure 5.22 shows that the agreement between the INP concentration measured with PINE and INSEKT differs strongly. Sometimes they agree very well (e.g., time period of b), on some days higher INP concentrations are measured with PINE (e.g., time period c), and in some cases, they are lower (e.g., time period a). Figure 5.23 shows the INP temperature spectra from the selected days (gray shaded areas in Figure 5.22: a, b, c, and d), the PINE measurements are shown as blue stars, and the black diamonds represent the measurements with INSEKT.

During the period of the intensive campaign, the aerosol concentration of the different aerosol sizes varied strongly (Figure 5.24), which is also reflected in the strongly fluctuating INP concentration (Figure 5.22). It is well-known that larger aerosol particles are more likely to serve as INP (Connolly et al., 2009) therefore they can be decisive for the measured INP concentration. One reason for the differences between the two instruments might be the loss of larger aerosol particles. PINE has a high sampling efficiency only for particles  $< 4 \mu\text{m}$ . Larger particles are lost in the inlet system (dryers, tubings) of the instrument (Möhler et al., 2021). A similar observation was also found during the PICNIC comparison campaign between several INP instruments at the Puy de Dôme observatory (central France) in October 2018 (Lacher et al., 2024). It was concluded that the online instruments have a slight tendency to measure lower INP concentrations during some sampling intervals compared to the offline instruments.

The time intervals where INSEKT measured a lower INP concentration may be explained by the fact

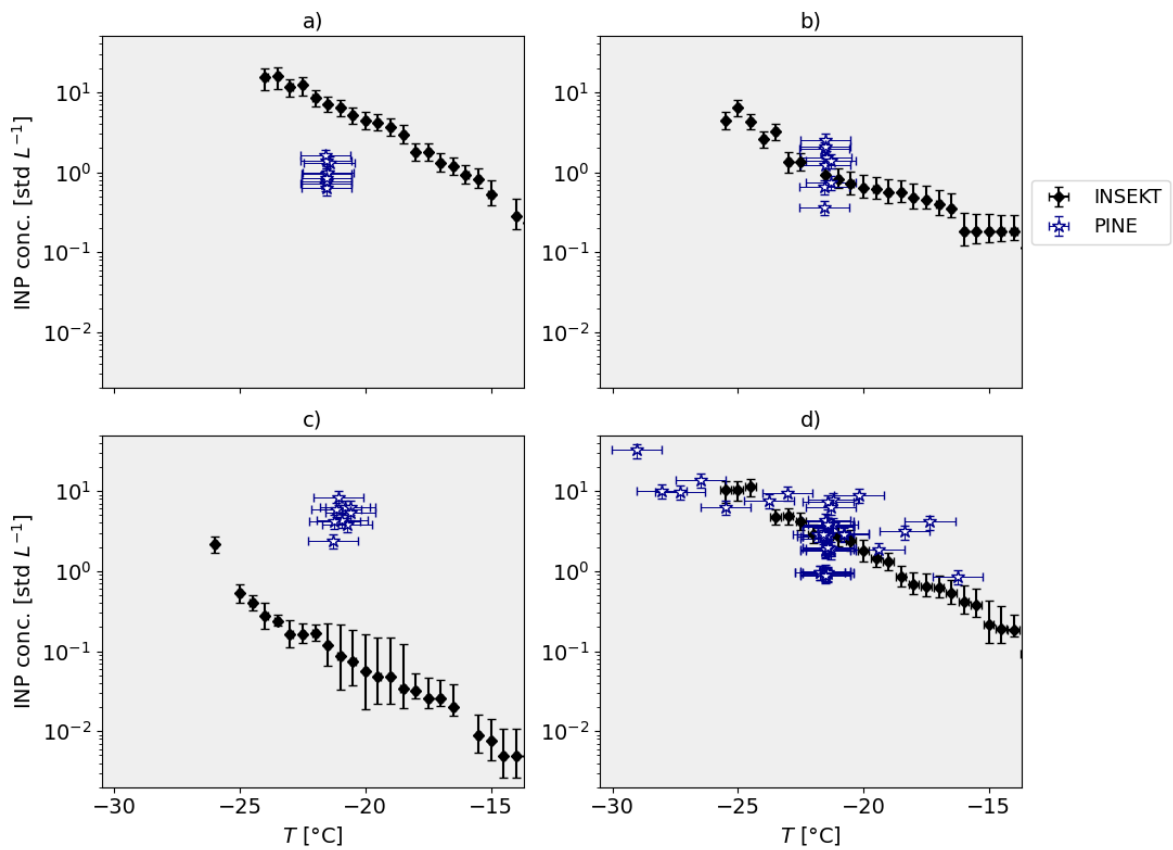


Figure 5.23.: INP temperature spectra for the data of the gray shaded areas from Figure 5.22, the black diamonds indicate the INSEKT measurements, and the blue stars show the PINE data. a) shows the data from August 2 - 3, 8 pm to 4 am, b) from August 5 - 6, 8 pm to 4 am, c) from August 6 - 7, 8 pm to 4 am, and d) from August 9, 8 am to 4 pm.

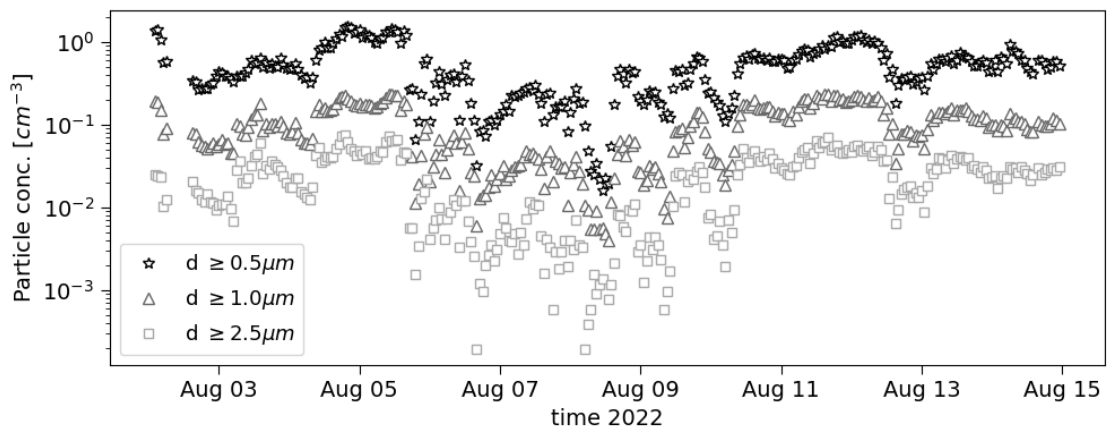


Figure 5.24.: Concentration of aerosol particles with diameters  $d \geq 0.5 \mu\text{m}$ ,  $\geq 1.0 \mu\text{m}$ ,  $\geq 2.5 \mu\text{m}$  during the intensive campaign in August 2022. Data are averaged to 1h.

that some aerosol particles can change their ice activity when immersed in water. For example, certain chemical groups could detach from the aerosol surface after water contact, thus reducing the ice nucleation activity of the particle (Harrison et al., 2016).

Another difference between both INP instruments is the method to measure the INPs. For the measurements with PINE, all aerosols in the expansion chamber are activated as ice crystals within approximately 30 sec to 40 sec, and ice nucleation can take place by immersion freezing as well as by deposition nucleation. In contrast, only the immersion freezing mode can be analyzed with the INSEKT method and the freezing process takes significantly longer, as the cooling is slower on a time scale of several minutes.

However, to decide which of the two instruments provides better performance in which situation, more measurements need to be performed in the laboratory first. Some efforts have already been made, for example, to find a suitable calibrating aerosol (Vogel, 2022), but so far without a satisfying result.

### 5.5. Dust Event in March 2022

This section includes a detailed discussion of the measurements during a Saharan dust event that occurred in March 2022. First, the measurements are presented (section 5.5.1), followed by a comparison with existing parameterizations for the INP concentration (section 5.5.2). In section 5.5.3, the measured INP concentrations at the SBO are compared with the INP concentrations at another mountain station in Greece (Helmos Observatory) that was also impacted by the dust event.

#### 5.5.1. Measurements

As already described in section 5.4.3, the INP concentration at the SBO is strongly influenced by dust events. The highest concentrations in both the INP concentration and the particle mass concentration were reached on March 15-18, 2022 during the strongest dust event in the measurement period with PINE (Figure 5.17).

Figure 5.25 depicts both parameters in this period with a higher time resolution. The INP data is shown as circles, which are color-coded for the activation temperature inside the PINE cloud chamber (Figure 5.25a). During temperature scans, the time resolution of the INP data is 6 min, for the operation period at a constant temperature the data is averaged over 1 h. The particle mass concentration is averaged over 30 min (Figure 5.25b). The grey shaded area shows the time period of the dust event classified by the SBO station (dust report from the SBO data portal <https://data.sonnblick.net>). At the lowest temperature of  $-30^{\circ}\text{C}$ , the highest INP concentrations of up to  $6718 \text{ std L}^{-1}$  are measured. During the course of the three days that were impacted by Saharan dust, the particle mass concentration and the INP concentrations are well correlated,  $\rho = 0.96$  for hourly mean data at a temperature of  $-26^{\circ}\text{C} \pm 1^{\circ}\text{C}$ .

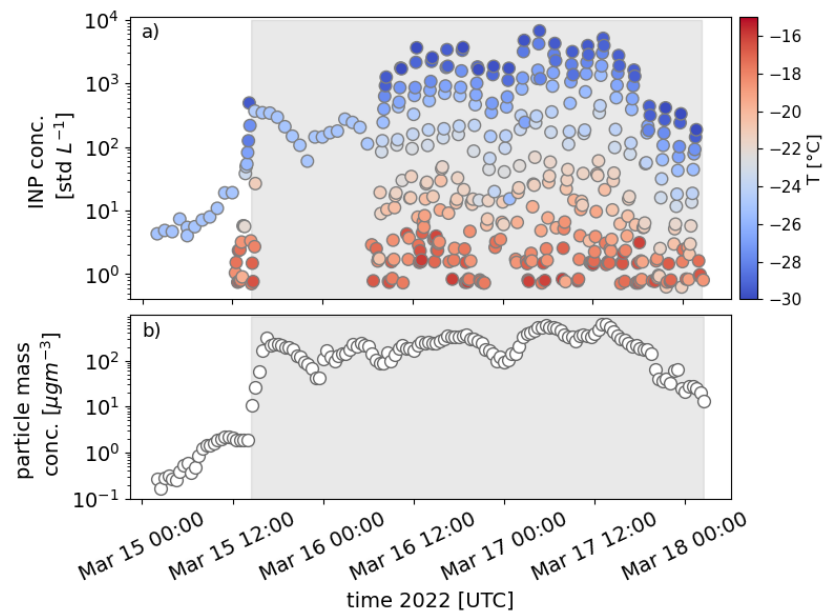


Figure 5.25.: Data from a strong dust event in March 2022. Panel a) depicts the time series of the INP concentration measured with PINE as a function of the temperature. Data at constant  $T$  is averaged to 1 h, and data during  $T$  scans are plotted for the highest time resolution of 6 min. Panel b) shows the time series of the particle mass concentration, averaged to 30 min mean.

### 5.5.2. Comparison to Existing INP Parameterizations

To accurately formulate primary ice formulation, cloud and climate models need parameterizations for the abundance of INPs as a function of aerosol parameters and temperature. Such parameterizations have been derived from previous field observations. Here the INP concentration measured with PINE at the SBO during the dust event in March 2022 is compared to those predicted by the parameterizations from DeMott et al. (2010) and DeMott et al. (2015). Only INP data from the grey-shaded time periods in Figure 5.25 are considered for the comparison, as they were classified as dust events according to the SBO station. The INP parameterization of DeMott et al. (2010) is based on nine ground-based and airborne field campaigns, it assumes to represent a globally mixed aerosol and is limited to the MPC temperature range lower than  $-15^{\circ}\text{C}$ . The INP parameterization of DeMott et al. (2015) was especially developed for mineral dust aerosols based on both field measurements and laboratory experiments. Both parameterizations predict the INP concentration as a function of the freezing temperature  $T_f$  and the concentration of aerosol particles with a diameter larger than  $0.5\ \mu\text{m}$   $n_{d>0.5\mu\text{m}}$ , the respective equations can be found in Table 5.3.

Figure 5.26 shows the comparison of the INP concentration ( $c_{\text{INP,observed}}$ ) measured with PINE during the dust event in March 2022 at SBO with the INP concentrations ( $c_{\text{INP,predicted}}$ ) calculated with the parameterizations from DeMott et al. (2010) in plot a) and DeMott et al. (2015) in plot b). The parameterization of DeMott et al. (2010) does not correctly represent the slope of the measured data, and in particular, the

## 5. Long-Term INP Measurements at the Sonnblick Observatory

Table 5.3.: Equations for the INP parameterization of DeMott et al. (2010) and DeMott et al. (2015),  $T_f$  means the freezing temperature and  $n_{d>0.5\mu m}$  the concentration of aerosol particles with a diameter larger than  $0.5\mu m$ . The temperature range defines the range for which the INP parameterization is valid.

name	parameterization	fit parameters	T range
DeMott et al., 2010	$c_{INP,predicted} = a(273.16 - T_f)^b \cdot (n_{d>0.5\mu m})^{(c(273.16 - T_f) + d)}$	a = 0.0000594, b = 3.33, c = 0.0264, d = 0.0033	-15 °C to -35 °C
DeMott et al., 2015	$c_{INP,predicted} = (cf)(n_{d>0.5\mu m})^{(a(273.16 - T_f) + b)} \cdot \exp(c(273.16 - T_f) + d)$	a = 0 b = 1.25, c = 0.46, d = -11.6, cf = 1	-21 °C to -35 °C

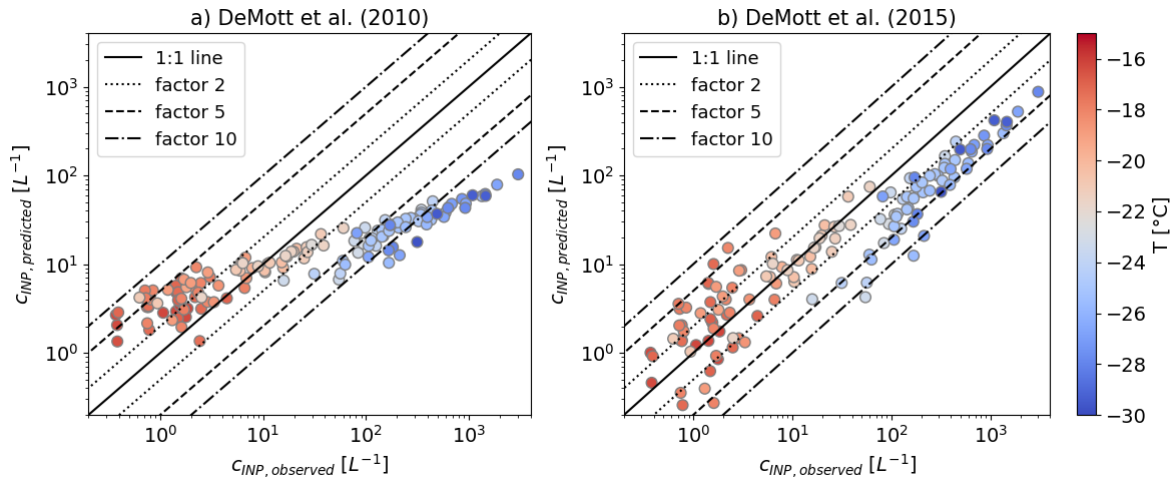


Figure 5.26.: The observed INP concentration with PINE during the dust event in March 2022 is compared against the predicted INP concentration using the two different parameterizations from a) DeMott et al. (2010) and b) DeMott et al. (2015). The dotted, dashed, and dashed-dotted lines represent a deviation from the 1:1 line (solid) of a factor of 2,5,10, respectively.

INP concentrations at the lower temperatures (blue-colored symbols) are over-predicted by up to a factor of 10. Overall, 82.1% of the data are within a factor of 10 from the 1:1 parameterization line, within a factor of 5 it is 51.7% of the data and within a factor of 2 it is 26.2%.

The parameterization from DeMott et al. (2015), which was developed on the basis of INP measurements in mineral dust dominated aerosols, provides a much better fit to the INP data measured during the dust event at the SBO. In particular, the slope of the data, caused by the different freezing temperatures, is better represented by the parameterization of DeMott et al. (2015), and 98.5% of the data is correctly predicted within a factor of 10 (91.2% within a factor of 5 and 35.8% within a factor of 2). The parameterization of DeMott et al. (2015) is described for a temperature range between  $-21\text{ °C}$  and  $-35\text{ °C}$ . For the comparison to the SBO data, it was extended to a minimum temperature of  $-15\text{ °C}$ . A trend can be

observed, with a better agreement for the higher temperatures.

Another way to formulate the INP concentration as a function of aerosol properties is the ice-active surface site density  $n_s$  (Hoose and Möhler, 2012). Here, the INP concentration is normalized to the available surface area concentration of the ambient aerosol population ( $A_{tot}$ ), and it can be calculated by  $n_s = \text{INP concentration} / A_{tot}$ . For the measurements at the SBO,  $A_{tot}$  was calculated from the data of the instruments SMPS3938 and promo3000 (see section 5.2.3). In the following, the measured  $n_s$  from the INP measurements in the period of the dust event in March 2022 (grey shaded area in Figure 5.25) at the SBO are compared with the  $n_s$  parameterizations of Niemand et al. (2012), Steinke et al. (2016), and Ullrich et al. (2017) (Figure 5.27a). All three parameterizations are based on the freezing temperature  $T_f$ , see Table 5.4.

Table 5.4.: Equations for the parameterization of  $n_s$  from Niemand et al. (2012), Steinke et al. (2016), Ullrich et al. (2017), and Boose et al. (2016b).  $T_f$  means the freezing temperature and the temperature range defines the range for which the parameterization is valid.

name	parametrization	fit parameters	T range
Niemand et al., 2012	$n_{s,predicted} = \exp(a(T_f - 273.15) + b)$	a = -0.517 b = 8.934	-12 °C to -36 °C
Steinke et al., 2016	$n_{s,predicted} = \exp(a \cdot T_f + b)$	a = -0.350 b = 110.266	-11 °C to -26 °C
Ullrich et al., 2017	$n_{s,predicted} = \exp(a \cdot T_f + b)$	a = -0.517 b = 150.577	-14 °C to -30 °C
Boose et al., 2016b (Sinai Peninsula)	$n_{s,predicted} = \exp(-a(T_f - 273.15) + b)$	a = 0.390 b = 13.22	
Boose et al., 2016b (Canary Islands)	$n_{s,predicted} = \exp(-a(T_f - 273.15) + b)$	a = 0.455 b = 10.16	
Boose et al., 2016b (Crete)	$n_{s,predicted} = \exp(-a(T_f - 273.15) + b)$	a = 0.545 b = 7.32	
Boose et al., 2016b (Peloponnese)	$n_{s,predicted} = \exp(-a(T_f - 273.15) + b)$	a = 0.535 b = 6.84	

While the parameterizations of Niemand et al. (2012) and Ullrich et al. (2017) are based on laboratory experiments with pure mineral dust aerosols, the parameterization of Steinke et al. (2016) is derived from laboratory experiments with soil dust aerosols including some fraction of soil organic matter. Figure 5.27a shows that the measured  $n_s$  are overestimated by 2 – 3 orders of magnitude by all three parameterizations in the entire temperature range from -15 °C to -30 °C. However, the temperature dependence of  $n_s$ , which is shown by the slope of the data, agrees well between the measured and calculated data.

The overestimation could be caused by incorrect aerosol measurements, especially of the larger a-spherical dust particles. The measurements were performed with a promo instrument using an optical measuring principle that may overestimate the diameter of large a-spherical particles (Järvinen et al., 2014). This potential bias will be investigated in more detail in the future by using an APS for measuring

the larger particles at the SBO, an instrument that is also used for aerosol measurements at the AIDA chamber and which was used to derive the parameterizations used here for comparison with the INP measurements at SBO. Another reason for the difference might be that the measured dust particles are less ice-active because of their large distance from the source region. A number of laboratory studies (e.g., Kanji et al., 2013; Sullivan et al., 2010) have demonstrated that the ice activity of dust particles can be reduced by coating or other aging processes in the atmosphere. This assumption should also be investigated in the future with further measurements. The INP measurements by Lacher et al. (2018a) performed with the HINC instrument at the Jungfraujoch station show exactly the same result: the measured INP concentration at  $-31\text{ }^{\circ}\text{C}$  during a dust event at Jungfraujoch is lower compared to the predicted  $n_s$  by the parameterizations of Niemand et al. (2012), Steinke et al. (2016), and Ullrich et al. (2017).

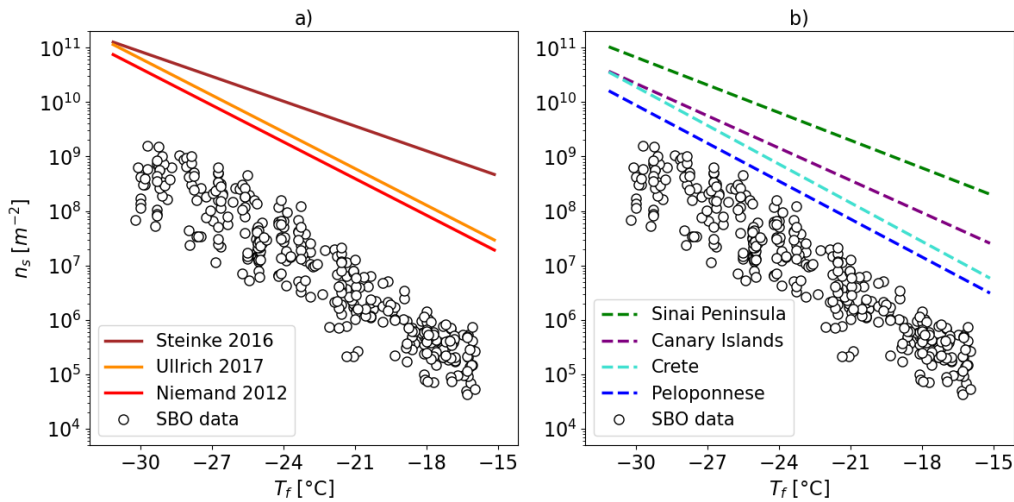


Figure 5.27.: a) Ice-active surface site density  $n_s$  as a function of the freezing temperature  $T_f$  for the INP data measured with PINE (black circles) at SBO during the dust event in March 2022, and the parameterizations from Steinke et al. (2016) (brown line), Ullrich et al. (2017) (orange line) and Niemand et al. (2012) (red line). b) The same SBO data as in a) is shown and compared to the parameterizations by Boose et al. (2016b) from the different locations Sinai Peninsula (green line), Canary Islands (purple line), Crete (turquoise line), and Peloponnese (blue line).

Figure 5.27b additionally shows a comparison of the measured  $n_s$  at the SBO with different  $n_s$  parameterizations of Boose et al. (2016b), which are also all dependent on the freezing temperature  $T_f$  (Table 5.4). In the study by Boose et al. (2016b), the dust samples were collected after airborne transport in the troposphere from the Sahara to various locations (Crete, the Peloponnese, the Canary Islands, and the Sinai Peninsula) and then analyzed for their ice activity. The parameterization for  $n_s$  is already in better agreement as compared to Niemand et al. (2012), Steinke et al. (2016), and Ullrich et al. (2017), which might be related to the fact that these dust aerosols were exposed to a longer transport distance, however, the measurements at the SBO are still slightly overestimated.

### 5.5.3. Comparison to Helmos Station

During the observation of the dust event described in section 5.5.1, another PINE instrument was in operation at the Helmos Atmospheric Aerosol and Climate Station in Greece (Vogel, 2022), which is also part of the ACTRIS network for aerosol and cloud in situ measurements. The Helmos observatory is located at mount Helmos (22.2E and 37.9N) at an altitude of 2314m above sea level.

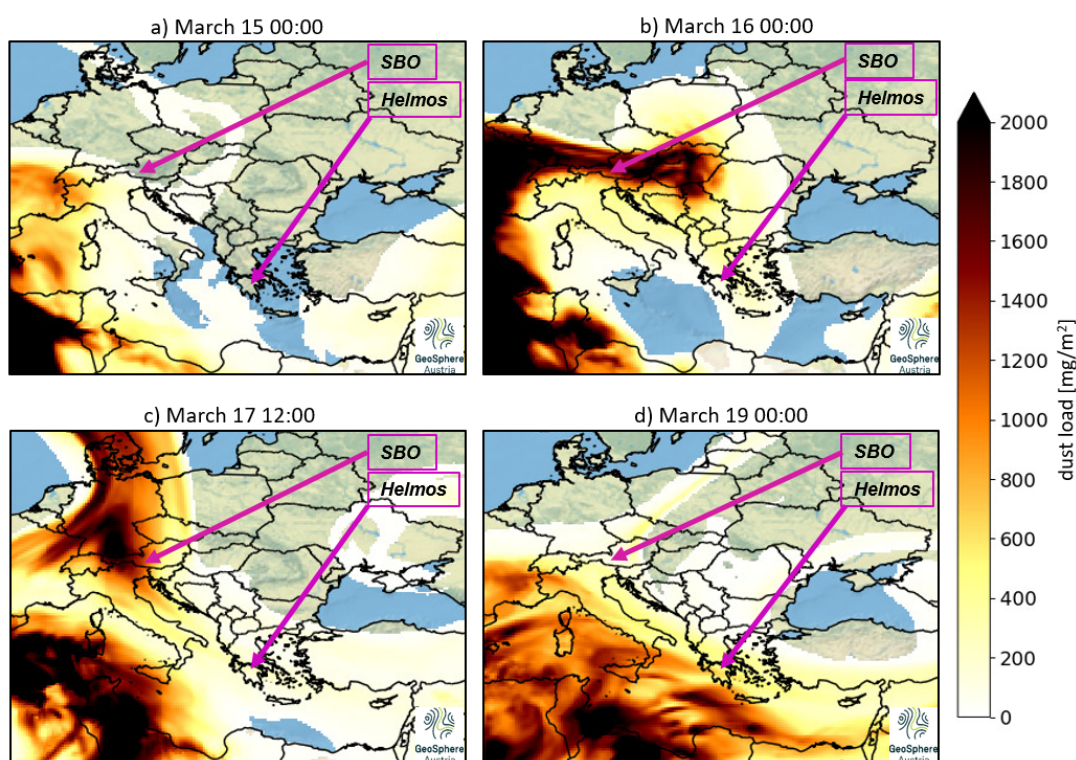


Figure 5.28.: Simulations of the dust load with the WRF/Chem model at selected times before, during, and after the dust event in March 2022. The selected times of the panels a, b, c, and d are marked in gray shaded areas in Figure 5.29. Data courtesy of GeoSphere Austria.

In this section, the INP concentration measured at the two stations is compared with each other for the time period of the strong dust event in March 2022. The arrival of the dust plume to the SBO and the Helmos station was simulated with the WRF/Chem (Weather Research and Forecasting/Chemistry) model. The simulations in Figure 5.28 were generated by GeoSphere Austria with a horizontal resolution of 12km. The concentrations in the Figures do not show the dust load near the ground, but they are summed up over all height layers, which means that the total amount of Saharan dust in the atmosphere above each individual map point at the time under consideration is shown. The dust concentration at the two stations can therefore not be determined, but the model calculation can be used as an initial reference.

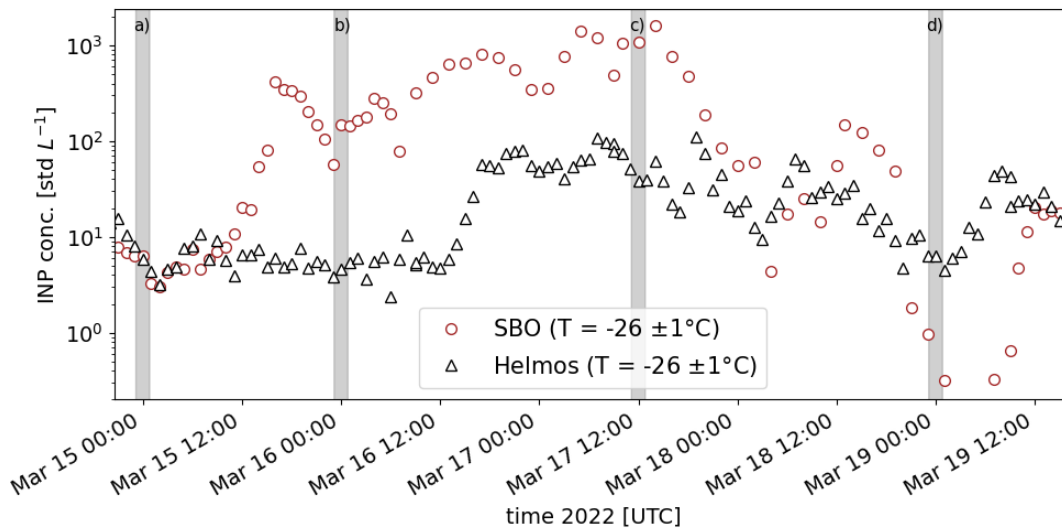


Figure 5.29.: INP concentrations measured at SBO (red circles) and the Helmos station (black triangles) in the time period from March 15-19, 2022. Both INP data were measured with PINE at a temperature of  $-26^{\circ}\text{C} \pm 1^{\circ}\text{C}$ . The gray shaded areas (a-d) indicate times for which the modeled dust load by the WRF/Chem model is shown in Figure 5.28.

Figure 5.29 shows the measured INP concentration at a temperature of  $-26^{\circ}\text{C} \pm 1^{\circ}\text{C}$  from the SBO (red circles) and the Helmos station (black triangles) in the time period from March 15 - 19, 2022. The gray shaded areas (a - d) indicate selected times for which the modeled dust load by the WRF/Chem model is shown in Figure 5.28. In Figure 5.29 example (a) (March 15, 00:00), the INP concentrations at both the SBO and the Helmos station are similarly low ( $\sim 6 \text{ std L}^{-1}$ ). At this time, the air masses at both stations were not yet influenced by dust (compare Figure 5.28a). About 24 hours later on March 16, 00:00 (b), the air masses at the SBO were already strongly influenced by dust (Figure 5.28b), which caused an increase of the INP concentration by more than one order of magnitude to  $\sim 148 \text{ std L}^{-1}$  compared to example (a). In comparison, the INP concentration at the Helmos station is still low ( $\sim 5 \text{ std L}^{-1}$ ) because the dust plume has not yet reached there (Figure 5.28b). On March 17, 12:00 (c), the dust plume also reached the Helmos station, while the location at the SBO is still strongly influenced by dust (Figure 5.28c). The same can also be seen in the INP concentration, which is now enhanced both at the SBO  $\sim 1076 \text{ std L}^{-1}$  and the Helmos station  $\sim 38 \text{ std L}^{-1}$ . On March 19, 00:00 (d), the air masses at the SBO are again influenced by less dust, while the dust load is now higher at the Helmos station. This can again be observed in the measured INP concentration (SBO:  $\sim 0.7 \text{ std L}^{-1}$ , Helmos:  $\sim 6 \text{ std L}^{-1}$ ). This example clearly shows that high dust concentrations can be transported to distant locations by long-range transport, and therefore have a significant influence on the INP concentration. In the future, this comparison could be analyzed in much more detail in a further analysis, for example by also considering the measurements of aerosol properties at the two stations.

## 5.6. Summary

Long-term INP measurements at the SBO in Austria (3106 m a.s.l.) were conducted as a part of this PhD thesis to investigate the diurnal and seasonal variation as well as shorter-term variations of the INP concentrations. Such long-term INP measurements in different environments provide a new basis to improve the formulation and prediction of primary ice formation in models (e.g., Burrows et al., 2022). The SBO site is a well-suited location, as it is located in the lower FT, and also receives air masses from the BL and is therefore influenced by regional aerosol and INP sources and long-range transported particles. INPs were measured in the temperature range from  $-5^{\circ}\text{C}$  to  $-25.5^{\circ}\text{C}$  (time resolution: 1/2 - 7 days) with the freezing experiment INSEKT. With continuous measurements from August 2019 to August 2022, this is the longest INP data set to date. In addition, a 14 month INP time series was obtained, starting in August 2021, with the PINE instrument, which measured in the temperature range from  $-15^{\circ}\text{C}$  to  $-30^{\circ}\text{C}$  (time resolution:  $\sim 6$  min).

The results show that the mean INP temperature spectra of the INSEKT data have a similar trend in spring and summer in the temperature range from  $-5^{\circ}\text{C}$  to  $-25.5^{\circ}\text{C}$ . The INP concentrations are significantly lower in autumn/winter, with the difference increasing with decreasing temperature. A recurring seasonal trend was observed in the INP concentration measured with INSEKT and PINE with the highest concentrations in spring/summer (e.g. at  $T = -14^{\circ}\text{C}$  up to  $0.98 \text{ std L}^{-1}$ ) and the lowest in December/January (e.g. at  $T = -14^{\circ}\text{C}$  up to  $0.0004 \text{ std L}^{-1}$ ). The measurements of the number concentration of the aerosol particles with a diameter larger than 90 nm and of the  $^{214}\text{Po}$  concentration both indicate, that the seasonal variability in the INP concentrations is caused by the influence of air masses from the BL as all three parameters show the same seasonal pattern of a sinusoidal function. The observations of the seasonal variability of the INP concentration at SBO are consistent with studies at other sites (e.g., Lacher et al., 2018a; Wex et al., 2019; Tobo et al., 2020; Schneider et al., 2021a; Brunner et al., 2022).

For the first time, a daily cycle in the INP concentrations was detected with PINE at  $T = -23^{\circ}\text{C} \pm 2^{\circ}\text{C}$ , but only from April to September, with a maximum around noon and a minimum at midnight. For example, in July 2022 the monthly averaged INP concentration varied between a minimum of  $2.4 \text{ std L}^{-1}$  and a maximum of  $9.8 \text{ std L}^{-1}$ . In contrast, from October 2021 to February 2022, the INP concentrations were consistently lower as compared to summer. A similar diurnal variation can be observed in the number concentration of aerosol particles with a diameter larger than 90 nm and  $^{214}\text{Po}$  concentration, which is likely also caused by the impact of enhanced BL mixing processes during the day.

A heat treatment of the sampled INP population before the INSEKT INP analysis in the temperature range from  $-5^{\circ}\text{C}$  to  $-25.5^{\circ}\text{C}$  shows reduced INP activity, indicating that biogenic compounds contribute to the INP abundance at SBO. This was most prominent at the higher temperatures (above  $-13^{\circ}\text{C}$ ) and was observed in all seasons. The INP concentrations measured during the winter months may represent the INP population in the lower FT, as both BL air mass origin tracers show low concentrations. Here, a significant contribution of heat-sensitive INPs was also observed at temperatures higher than

−21.5°C.

Strong peaks in the INP concentration (e.g. March 2022) were observed, which cannot be explained by the BL air influence but are likely caused by episodically occurring Saharan dust events (e.g., Liu et al., 2008). This can be concluded from a strong relation between the INP concentration and the particle mass concentration. The INP concentration measured with PINE during the dust event in March 2022 showed a reasonable agreement with the parameterization of DeMott et al. (2015). The temperature dependence of the measured data (slope) is well represented, and 98.5% of the data is within a factor of 10 around the parameterization line. The parameterizations for  $n_s$  by Niemand et al. (2012), Steinke et al. (2016), Ullrich et al. (2017) overestimate  $n_s$  of the measured data from the SBO by 2-3 orders of magnitude but the temperature dependence of the data is represented well. The deviation could be caused by an overestimation of the measured particle diameters, especially of the larger a-spherical dust particles. In contrast, the parameterizations for  $n_s$  by Boose et al. (2016b) for dust samples from different locations show a better agreement, and the temperature dependence is well predicted. This could be explained by the fact that Boose et al. (2016b) used transported dust for their parameterizations and a number of studies show that the ice activity of dust can be reduced by long transport distances in the atmosphere due to processes such as coating or aging (e.g., Kanji et al., 2013; Sullivan et al., 2010).

The INP measurements at SBO revealed that during clear-sky periods, a higher median INP concentration of 3.5 std L<sup>-1</sup> was observed compared to cloudy periods (1.9 std L<sup>-1</sup>) when considering the PINE data. This could be caused by processes such as wet-removal (Wang et al., 2014) or pre-activation (Stopelli et al., 2015) during cloud occurrence, and should be investigated in future studies in more detail.

Furthermore, the Spearman correlation coefficient between the measured INP concentration of both instruments and various aerosol properties, as well as meteorological parameters, was calculated to find further reasons for the variations of the INP concentration. Here, a relation between the INP concentration and the aerosol properties regarding concentration, size, and mass, especially at the colder nucleation temperatures, was found. In contrast, no relation between the INP concentration and the meteorological parameters (air temperature, air pressure, relative humidity, precipitation, wind direction, and wind speed) was found, which is in accordance with other studies at high-altitude mountain stations (e.g., Lacher et al., 2018b).

From this study, it can be concluded that the SBO is mainly influenced by different INP sources including free tropospheric aerosols, long-range transported dust, and local or regional aerosols transported from the BL to the station. In future studies, approaches should be made to identify the INPs, e.g. by investigating the chemical nature of the aerosol types or by performing ice residual measurements with a single particle mass spectrometer. Moreover, by using the INP data set from FT sampling periods, a new parameterization could be established for the INP concentration population in the lower FT. In general, this study demonstrated the value of long-term studies and INP measurements at high time resolution. Therefore, more long-term INP observations should be conducted, e.g. as part of the developing

research infrastructures ACTRIS, which aims to establish continuous INP concentration measurements at European observatories.



## 6. Summary and Outlook

This PhD thesis aimed at measuring ice-nucleating particles (INPs), which have a strong influence on the climate on Earth (e.g., Kanji et al., 2017; Burrows et al., 2022) and play important roles in the global water cycle (e.g., Mülmenstädt et al., 2015; Field and Heymsfield, 2015; Heymsfield et al., 2020). The measurements were carried out at the Sonnblick Observatory (SBO, 3106 m a.s.l.), with special emphasis on longer-term observation and high time resolution. The latter was only possible by using the newly developed instrument PINE (Portable Ice Nucleation Experiment, Möhler et al., 2021), which can autonomously monitor the INP concentration. In particular, for measurements in the free troposphere (FT), where the lack of INP data is largest so far (e.g., Lacher et al., 2018a), the new instrument PINEair (Portable Ice Nucleation Experiment airborne) was developed as part of this PhD thesis and used for the first time during an intensive test and observation period at SBO. Here, INP measurements were successfully performed at cirrus conditions, as studies at ambient air are sparse in this temperature range (e.g., Wolf et al., 2020). PINEair is also designed for aircraft-based measurements of INPs which are of importance for the formation of cirrus clouds. The aircraft version is currently under construction. The activities, results, and conclusions of the mentioned aspects (development of PINEair, INP measurements at cirrus conditions, and long-term INP measurements) are summarized in the following sections.

### **Development of a new aircraft-based INP instrument for measurements in the free troposphere:**

At present, little is known about the concentration and composition of INPs in the FT (Wolf et al., 2020), as INP measurements at high altitudes can only be performed at mountain stations (e.g., Brunner et al., 2022), with tethered balloons (e.g., Porter et al., 2020), with unmanned aerial vehicles (e.g., Bieber et al., 2020) or with aircraft (e.g., Grawe et al., 2023). However, more measurements are needed to investigate the spatial and temporal distribution of INPs in the FT and their influence on cirrus cloud formation and properties (e.g., Coluzza et al., 2017). Aircraft-based measurements, in particular, are needed to investigate INP concentrations at higher altitudes. To date, there is no aircraft-based instrument that can measure the INP concentration at temperatures lower than  $-40^{\circ}\text{C}$  and thus only at MPC (mixed-phase cloud) temperatures.

The new aircraft-based instrument PINEair was developed as part of this PhD thesis, which can measure the INP concentration in the temperature range between  $0^{\circ}\text{C}$  and  $-65^{\circ}\text{C}$  relevant for primary ice formation in both MPC and cirrus clouds. It is an expansion chamber (further development of PINE) and consists of three chambers with a volume of 3L, each connected to an optical particle counter (OPC).

Supersaturated conditions with respect to ice or water are established by rapidly reducing the pressure to cause cooling. Due to the alternating cycle between the three chambers, measurements with a time resolution of up to 2.5 – 5 min can be performed, to achieve a suitable spatial resolution in a fast-flying jet aircraft. The final version of PINEair is designed to measure INP concentrations onboard the German research aircraft HALO (High Altitude and Long Range) and is expected to be part of the measurement campaign “HALO-South” in New Zealand in September 2025. To already perform initial laboratory and field measurements and validate the new instrument, two PINEair prototypes were developed as part of this PhD thesis. First, prototype I which was built in the thermal housing of the AIDA (Aerosol Interaction and Dynamics in the Atmosphere, Möhler et al., 2003) chamber without its own cooling system, followed by prototype II, for mobile applications in the field due to its own cooling system.

Successful laboratory experiments for the differentiation of homogeneous and heterogeneous freezing at cirrus cloud conditions were performed with PINEair at the AIDA and APC (Aerosol Preparation and Characterization, Möhler et al., 2008) chamber, by measuring sulfuric acid aerosols for homogeneous nucleation and ATD (Arizona Test Dust) as INP at a temperature of approximately  $-45.5^{\circ}\text{C}$  to  $-49.3^{\circ}\text{C}$ . For the PINEair measurements, runs with step-wise expansions (immediate reduction of pressure) were performed with a buffer volume, thus the peak ice saturation ratio  $S_{ice,p}$  inside the chamber can be calculated by assuming an adiabatic temperature decrease. By systematically changing the pressure reduction by the buffer volume, different  $S_{ice,p}$  conditions can be achieved with doing a series of runs with step-wise expansions in the chamber. Above a certain threshold value for the pressure reduction,  $S_{ice,p}$  in the chamber is high enough that homogeneous freezing can occur. This was successfully detected in both the measurements in the laboratory and at ambient air conditions. Here, a transition area was observed where, for the same percentage pressure drop (*PPD*), sometimes only heterogeneous ice nucleation occurred, while at other times homogeneous freezing conditions were already achieved. This area shifts to different *PPDs* depending on the humidity of the sampled air. Therefore, regular relative humidity scans need to be performed by doing several runs with different *PPDs*, especially during longer operations.

Successful laboratory measurements were performed at aircraft-relevant conditions ( $p = 250\text{ mbar}$ ), where the formation of ice crystals by homogeneous and heterogeneous ice nucleation could be observed. Comparison experiments at MPC temperatures with other INP instruments such as AIDA and PINE demonstrated a good performance of PINEair, as the measured INP concentrations agreed within the temperature uncertainty for the different methods. In addition, the onset temperature of homogeneous freezing of supercooled water droplets was investigated using ammonium sulfate aerosols as cloud condensation nuclei for the supercooled droplets to form. The subsequent homogeneous freezing of the droplets was on average observed with an offset of about  $1.3^{\circ}\text{C}$  towards higher temperatures compared to the literature values, which may be caused by the temperature inhomogeneity inside the chamber. From the methodical experiments for performing the runs with step-wise expansion, it was found that for the waiting time, which is introduced before the start of the expansion to achieve a homogeneous temperature distribution within the chambers, a duration of 60 sec is optimal. Moreover, to ensure that

---

the formed ice crystals upon the step-wise expansion are transported to the OPC, and finally detected, the pump flow directly after the step-wise expansion  $flow_{exp}$  should be larger than  $0.7 \text{ L min}^{-1}$ .

In the future, more laboratory measurements should be performed to better quantify the determination and the uncertainties of  $S_{ice,p}$  inside the chamber. For this purpose, comparative measurements could be conducted with a Continuous Flow Diffusion Chamber (CFDC) both in the field and in the laboratory, as this instrument is known for its ability to determine  $S_{ice,p}$  with a higher accuracy. Furthermore, the influence of a longer operation of PINEair on the  $S_{ice,p}$  conditions inside the chamber will be investigated in more detail. This could cause a stable ice layer on the chamber walls, which could have an influence on  $S_{ice,p}$  inside the chamber during the step-wise expansion.

### **Measurements of the INP concentration at cirrus cloud conditions:**

Cirrus clouds have a significant influence on the Earth's radiative budget (Chen et al., 2000). However, the effect of INPs on cirrus clouds is highly uncertain (e.g., Kärcher, 2017; Krämer et al., 2020), as ice crystal formation in this temperature range is still not well understood, partly due to the lack of INP field data (DeMott et al., 2003b; Richardson et al., 2007; Kanji et al., 2017; Wolf et al., 2020). It is still unclear which fraction of the atmospheric aerosol particles can act as INP and at which different environmental conditions regarding  $S_{ice}$  and temperature (Beer et al., 2024). The current knowledge is based on laboratory measurements, e.g. by using the AIDA chamber (e.g., Wagner et al., 2021) or CFDCs (e.g., Mahrt et al., 2020). Only a few studies have been conducted in the field, all of them with a CFDC, namely at the mountain stations Storm Peak Laboratory in western Colorado (DeMott et al., 2003b; Richardson et al., 2007) and the Puy de Dôme Observatory in France (Wolf et al., 2020).

To measure the INP concentration in the cirrus temperature range, a campaign was conducted from May 8 - 22, 2023 at the Sonnblick Observatory (SBO, 3106 m a.s.l.) in Austria with the PINEair prototype II. The SBO site is located in the lower FT but is frequently also influenced by air mass injections from the boundary layer (BL). Consequently, the aerosols at the SBO may be influenced by both regional sources and long-range transport of mineral dust aerosols from the Sahara or other long-range transported aerosol particles.

In this campaign, PINEair measured almost continuously for several weeks and proved its suitability for longer-term operation. The measurement program during the SBO campaign included the following operations: During the night, continuous expansions were performed in the MPC temperature range at  $T = -22.7^\circ\text{C}$  and  $T = -27.5^\circ\text{C}$  with a time resolution of 2.5 min. During the day, PINEair measured, for the first time in the Alpine region, cirrus-relevant INP concentrations with a time resolution of 5 – 10 min. First measurements at a temperature of approximately  $-47.8^\circ\text{C}$  and  $S_{ice,p}$  in the range of 1.49 and 1.52 resulted in INP concentrations up to  $90.1 \text{ std L}^{-1}$ . For these measurements,  $S_{ice,p}$  was systematically varied by repeated runs with step-wise expansions inside the chamber. Generally higher

INP concentrations were measured at higher  $S_{ice,p}$  in the chamber. A case study revealed that during increased aerosol concentrations and particle mass concentrations, also increased INP concentrations are measured, with concentrations up to  $84 \text{ std L}^{-1}$  at  $T = -47.8^\circ\text{C}$  and  $S_{ice,p} = 1.52 - 1.55$ . However, no relation between the INP concentration and the aerosol parameters (concentration of all particles and particles with a diameter  $d$  larger than  $0.3 \mu\text{m}$ ,  $0.5 \mu\text{m}$ ,  $0.7 \mu\text{m}$ ,  $1.0 \mu\text{m}$  and the particle mass concentration), and the meteorological parameters (ambient temperature, relative humidity, pressure, wind speed), was found when analyzing the data of the whole time period, the Spearman correlation coefficient is  $\rho < 0.5$ . This is in agreement with the study by Wolf et al. (2020) at the Puy de Dôme Observatory in France. Remarkably, for the PINEair measurements in the MPC temperature range, a high positive correlation of  $\rho > 0.8$  was found between the measured INP concentration and the same aerosol parameters.

Based on the data obtained so far, it is not possible to identify the factors influencing the INP concentration at cirrus conditions, which makes it difficult to establish a parameterization specifically for this temperature range. More INP measurements at ambient air conditions at different locations are needed. In future studies, additional instruments such as single particle mass spectrometers could help to identify the ambient particles and could be coupled to PINEair to analyze the ice residuals. This combination of both instruments could contribute to get more information about the INP population active at cirrus temperatures.

### **Long-term measurements of the INP concentration at a high-altitude station:**

There are only a few long-term studies investigating INP concentrations, e.g. studies by Conen et al. (2015), Wex et al. (2019), Tobo et al. (2020), Schrod et al. (2020), Schneider et al. (2021a), Brunner et al. (2022). They were conducted at different locations around the globe, and all consistently observed that the highest INP concentrations are measured in spring and summer. However, except Brunner et al. (2022), the studies have a low time resolution from 24h to 2 weeks and thus provide no information on the diurnal variations of the INP concentration. Burrows et al. (2022) point out that, as the INP concentration can change significantly within short time periods, long-term measurements with a high time resolution could help to improve the implementation of INP predictions in models.

A long-term INP study in the MPC temperature range was conducted at the SBO site as part of this PhD thesis. INP measurements were performed in the temperature range from  $-5^\circ\text{C}$  to  $-25.5^\circ\text{C}$  (time resolution:  $1/2 - 7$  days) with the freezing experiment INSEKT (Ice Nucleation Spectrometer of the Karlsruhe Institute of Technology, Schneider et al., 2021a), in the period from August 2019 to August 2022 with a time resolution of one week. To date, this is the longest, continuous INP measurement series. In addition, a 14-month INP time series was conducted starting in August 2021 with the expansion chamber PINE, in the temperature range from  $-15^\circ\text{C}$  to  $-30^\circ\text{C}$  (time resolution:  $\sim 6$  min), making this the longest, continuous INP data set with such a high time resolution.

---

The results show that the INP temperature spectra in the temperature range from  $-5^{\circ}\text{C}$  to  $-25.5^{\circ}\text{C}$  show a similar temperature trend and similar concentrations at all temperatures in summer/spring, while the concentrations are significantly lower in fall/winter, with the difference increasing with decreasing temperature. The highest INP concentrations were generally measured in spring/summer (e.g.  $T = -14^{\circ}\text{C}$  up to  $0.98\text{std L}^{-1}$ ) and the lowest in December/January (e.g.  $T = -14^{\circ}\text{C}$  up to  $0.0004\text{std L}^{-1}$ ). The same was observed with PINE. This is likely caused by the influence of air masses from the BL, as the concentrations of the tracers (aerosol particles with a diameter larger than  $90\text{ nm}$  and  $^{214}\text{Polonium}$  concentration) show the same sinusoidal trend as the measured INP concentrations.

The impact from the air masses from the BL also likely caused a daily cycle in the INP concentrations at  $T = -23^{\circ}\text{C}$ , which was detected for the first time at a high-altitude station. However, this daily cycle is only occurring from April to September, with a maximum around noon and a minimum at midnight. For example, in July 2022, the monthly averaged INP concentration at  $T = -23^{\circ}\text{C}$  varied from  $2.4\text{std L}^{-1}$  (midnight) to  $9.8\text{std L}^{-1}$  (noon). In contrast, from October to February, no daily cycle was observed and the INP concentrations were consistently low (monthly averaged INP concentration at  $T = -23^{\circ}\text{C}$  ranges from  $0.2\text{std L}^{-1}$  to  $2.2\text{std L}^{-1}$ ). Therefore, the INP concentrations during the winter months may represent the INP population in the lower FT.

Furthermore, a contribution from biogenic compounds to the ice activity was derived from heat treatment of the aerosol suspensions before the analysis with INSEKT. This was especially observed at higher temperatures above  $-13^{\circ}\text{C}$ , and interestingly for all seasons.

The INP concentration at the SBO is also strongly influenced by episodically occurring Saharan dust events, which was observed by the strong relationship between the INP concentration and the particle mass concentration. The INP concentration measured with PINE during a dust event in March 2022 could thereby be well predicted by the parameterization of DeMott et al. (2015), which reproduces the temperature dependence of the measured INP concentration correctly, and 98.5% of the data within a factor of 10. The temperature dependence of the measured INP data from the dust event in March 2022 compares well with the parameterization for pure mineral dust aerosols derived from laboratory experiments (Niemand et al., 2012, Steinke et al., 2016, Ullrich et al., 2017), but in general the parameterizations overestimate the ice-active surface site density  $n_s$  by 2 to 3 orders of magnitude. This could be caused by an overestimation of the measured particle diameters, especially for the larger a-spherical dust particles. The difference to a parameterization from Boose et al. (2016b) is lower, which may be due to the fact that this parameterization is based on transported dust, which may have a reduced ice activity due to coating or aging processes during atmospheric transport (Kanji et al., 2013; Sullivan et al., 2010). When comparing the median INP concentration from the PINE measurements during cloudy and clear-sky periods at SBO, elevated concentrations were observed for the latter, respectively  $1.9\text{std L}^{-1}$  and  $3.5\text{std L}^{-1}$ . This may be caused by wet-removal (Wang et al., 2014) or pre-activation (Stopelli et al., 2015) processes during cloud occurrence.

To explain the short-term variations in the INP concentrations, the Spearman coefficient was calculated

for the correlation between the INP data set of INSEKT and PINE and various aerosol properties regarding concentration, size, and mass, and meteorological parameters (air temperature, air pressure, relative humidity, precipitation, wind direction, and wind speed). A correlation was found for aerosol properties, especially at lower nucleation temperatures, while no correlation was observed for meteorological parameters.

From this study, it can be concluded that the INP concentration at SBO is mainly influenced by different sources including free tropospheric aerosols, long-range transported dust, and local or regional aerosol sources transported from the BL to the station.

In a further analysis, the INP data set from the winter months could be used to establish a parameterization specifically for the INP concentration in the FT. Previous INP parameterizations were based on measurement data in the BL at ambient air conditions or laboratory studies. In general, more long-term INP measurements are needed, such as from developing research infrastructures ACTRIS (Aerosol, CLOUDS and Trace Gases Research Infrastructure), to better understand the abundance of INPs in the atmosphere and to better represent them in models.

In conclusion, new results were obtained as part of this PhD thesis which contribute to an improved understanding of INPs in the lower FT. The results showed, among other findings, a clear seasonal trend of the INP concentration at the SBO. The new instrument PINEair was developed and applied for the first time to measure INPs at MPC and cirrus conditions. The aircraft-based version of this instrument, which is currently under construction for use on the HALO research aircraft, will allow direct INP measurements in the FT and by that will provide new and unique data to better understand and predict the formation of MPC and cirrus clouds as well as their role in the climate system.



## A. List of Abbreviations and Symbols

Abbreviation	Description
ACTRIS	Aerosol, CLOUDS and Trace Gases Research Infrastructure
AIDA	Aerosol Interaction and Dynamics in the Atmosphere
APC	Aerosol Preparation and Characterization
APS	Aerodynamic Particle Sizer
ATD	Arizona test dust
BL	Boundary layer
CFDC	Continuous Flow Diffusion Chamber
CIS	Cloud In Situ
CPC	Condensation Particle Counter
CSU	Colorado State University
DLR	Deutsches Zentrum für Luft- und Raumfahrt
ECCINT	European Center for Cloud Ambient Intercomparison
FT	Free troposphere
GAW	Global Atmospheric Watch
HALO	High Altitude and Long Range
HERA	High-volume flow aEROSol particle filter sAmpler
HINC	Horizontal Ice Nucleation Chamber
INP	Ice-Nucleating Particle
INSEKT	Ice Nucleation Spectrometer of the Karlsruhe Institute of Technology
IPCC	Intergovernmental Panel on Climate Change
IS	Ice Spectrometer
JFJ	Jungfraujoch
KIT	Karlsruhe Institute of Technology
LOD	Limit of detection
MFC	Mass flow controller
MPC	Mixed-phase cloud
OPC	Optical particle counter
PINE	Portable Ice Nucleation Experiment
PINEair	Portable Ice Nucleation Experiment airborne
PINEc	commercial Portable Ice Nucleation Experiment
RBG	Rotating brush generator
SBO	Sonnblick Observatory

SDSA01	Soil Dust South Africa
SHARP	Synchronized Hybrid Ambient Real-time Particulate
SIP	Secondary ice production
SMPS	Scanning Mobility Particle Sizer
SOA	Secondary Organic Aerosols
SPIN	SPectrometer for Ice Nuclei
UAV	Unmanned Aerial Vehicles
welas	WEißLichtAerosolSpektrometer
WRF/Chem	Weather Research and Forecasting/Chemistry

Symbol	Description
$A$	Germ surface
$A_{tot}$	Available surface area concentration
$CH1$	Expansion chamber 1 of PINEair
$CH2$	Expansion chamber 2 of PINEair
$CH3$	Expansion chamber 3 of PINEair
$c_{INP,observed}$	Observed INP concentration
$c_{INP,predicted}$	Predicted INP concentration
$c_p$	Specific heat capacity of dry air
$d$	Particle diameter
$D_p$	Optical particle diameter
$\eta$	Dilution
$\Delta flow_{exp}$	Flow during an expansion
$\Delta G$	Gibbs free energy
$H_2SO_4$	Sulfuric acid
$k_B$	Boltzman constant
LW	Longwave irradiance measurements
$n_{d>0.5\mu m}$	aerosol particles with $d$ larger than $0.5 \mu m$
$n_{INP}$	INP concentration
$n_{INP,INSEKT}$	INP concentration measured with INSEKT
$n_s$	Ice-active surface site density
$N$	Number of molecules
$N^*$	Critical size of germ
$N_{all}$	Number of all samples
$N_{bgr}$	Number of background samples
$N_{f,bgr}$	Number of frozen samples
$\Delta N_{ice}$	Number of ice crystals per expansion

$N_u$	Number of unfrozen samples
$^{214}\text{Po}$	$^{214}$ Polonium
$p$	Pressure
$p_0$	Pressure at expansion start
$p_{AIDA}$	Start pressure in AIDA
$p_{ambient}$	Ambient pressure
$p_{balance}$	Balance pressure
$p_{buffer}$	Pressure in buffer volume
$p_{chamber}$	Pressure in expansion chamber
$p_{ice}(T_0)$	Saturation vapor pressure of ice at expansion start
$p_{ice}(T_{ad})$	Saturation vapor pressure as function of adiabatic temperature
$PPD$	Percentage pressure drop
$PPD_{threshold}$	Threshold of percentage pressure drop
$R_d$	Gas constant for dry air
$^{222}\text{Rn}$	$^{222}$ Radon
$\rho$	Spearman correlation coefficient
$S_{ice}$	Ice saturation ratio
$S_{ice,p}$	Peak ice saturation ratio
$\sigma$	Interface energy
$\Delta t_{exp}$	Duration of an expansion
$T$	Temperature
$T_0$	Temperature of lowest sensor at expansion start
$T_{ad}$	Adiabatic temperature
$T_{AIDA}$	Start temperature in AIDA
$T_{chiller}$	Temperature of the ethanol chiller
$T_{CH1}$	Gas temperature of PINEair chamber 1
$T_{CH2}$	Gas temperature of PINEair chamber 2
$T_{CH3}$	Gas temperature of PINEair chamber 3
$T_{DP}$	Dew point temperature
$T_f$	Freezing temperature
$T_{gas}$	Gas temperature
$T_{min}$	Minimum gas temperature
$T_{sky}$	Sky temperature
$T_{wall}$	Wall temperature
$V_{air}$	Volume of the sampled air
$V_{dwell}$	Volume of the suspension in one dwell
$\Delta V_{exp}$	Analyzed air volume per expansion
$V_{wash}$	Volume of wash water

## B. Bibliography

- Abdalmogith, S. S. and Harrison, R. M. (2005). The use of trajectory cluster analysis to examine the long-range transport of secondary inorganic aerosol in the uk. *Atmospheric Environment* 39: 6686–6695, doi:<https://doi.org/10.1016/j.atmosenv.2005.07.059>.
- Alpert, P., Aller, J. and Knopf, D. (2011). Ice nucleation from aqueous nacl droplets with and without marine diatoms. *Atmospheric Chemistry and Physics* 11, doi:10.5194/acp-11-5539-2011.
- Ansmann, A., Tesche, M., Althausen, D., Müller, D., Seifert, P., Freudenthaler, V., Heese, B., Wiegner, M., Pisani, G., Knippertz, P. and Dubovik, O. (2008). Influence of saharan dust on cloud glaciation in southern morocco during the saharan mineral dust experiment. *Journal of Geophysical Research: Atmospheres* 113, doi:<https://doi.org/10.1029/2007JD008785>.
- Archuleta, C. M., DeMott, P. J. and Kreidenweis, S. M. (2005). Ice nucleation by surrogates for atmospheric mineral dust and mineral dust/sulfate particles at cirrus temperatures. *Atmospheric Chemistry and Physics* 5: 2617–2634, doi:10.5194/acp-5-2617-2005.
- Atkinson, J., Murray, B., Woodhouse, M., Whale, T., Baustian, K., Carslaw, K., Dobbie, S., O’Sullivan, D. and Malkin, T. (2013). The importance of feldspar for ice nucleation by mineral dust in mixed-phase clouds. *Nature* 498, doi:10.1038/nature12278.
- Augustin, S., Wex, H., Niedermeier, D., Pummer, B., Grothe, H., Hartmann, S., Tomsche, L., Clauss, T., Voigtländer, J., Ignatius, K. and Stratmann, F. (2013). Immersion freezing of birch pollen washing water. *Atmospheric Chemistry and Physics* 13: 10989–11003, doi:10.5194/acp-13-10989-2013.
- Augustin-Bauditz, S., Wex, H., Denjean, C., Hartmann, S., Schneider, J., Schmidt, S., Ebert, M. and Stratmann, F. (2016). Laboratory-generated mixtures of mineral dust particles with biological substances: characterization of the particle mixing state and immersion freezing behavior. *Atmospheric Chemistry and Physics* 16: 5531–5543, doi:10.5194/acp-16-5531-2016.
- Barahona, D. and Nenes, A. (2009). Parameterizing the competition between homogeneous and heterogeneous freezing in ice cloud formation - polydisperse ice nuclei. *Atmospheric Chemistry and Physics Discussions* 9, doi:10.5194/acp-9-5933-2009.
- Barry, K. R., Hill, T. C. J., Levin, E. J. T., Twohy, C. H., Moore, K. A., Weller, Z. D., Toohey, D. W., Reeves, M., Campos, T., Geiss, R., Schill, G. P., Fischer, E. V., Kreidenweis, S. M. and DeMott,

- P. J. (2021). Observations of ice nucleating particles in the free troposphere from western us wildfires. *Journal of Geophysical Research: Atmospheres* 126, doi:<https://doi.org/10.1029/2020JD033752>.
- Bauer, P., Thorpe, A. and Brunet, G. (2015). The quiet revolution of numerical weather prediction. *Nature* 525: 47–55, doi:[10.1038/nature14956](https://doi.org/10.1038/nature14956).
- Baumann-Stanzer, K., Greilinger, M., Kasper-Giebl, A., Flandorfer, C., Hieden, A., Lotteraner, C., Ortner, M., Vergeiner, J., Schauer, G. and Piringer, M. (2018). Evaluation of wrf-chem model forecasts of a prolonged sahara dust episode over the eastern alps. *Aerosol and Air Quality Research* 19, doi:[10.4209/aaqr.2018.03.0116](https://doi.org/10.4209/aaqr.2018.03.0116).
- Beer, C. G., Hendricks, J. and Righi, M. (2024). Impacts of ice-nucleating particles on cirrus clouds and radiation derived from global model simulations with made3 in emac. *Atmospheric Chemistry and Physics* 24: 3217–3240, doi:[10.5194/acp-24-3217-2024](https://doi.org/10.5194/acp-24-3217-2024).
- Bellouin, N., Quaas, J., Gryspeerdt, E., Kinne, S., Stier, P., Watson-Parris, D., Boucher, O., Carslaw, K. S., Christensen, M., Daniau, A.-L., Dufresne, J.-L., Feingold, G., Fiedler, S., Forster, P., Gettelman, A., Haywood, J. M., Lohmann, U., Malavelle, F., Mauritsen, T., McCoy, D. T., Myhre, G., Müllmenstädt, J., Neubauer, D., Possner, A., Rugenstein, M., Sato, Y., Schulz, M., Schwartz, S. E., Sourdeval, O., Storelvmo, T., Toll, V., Winker, D. and Stevens, B. (2020). Bounding global aerosol radiative forcing of climate change. *Reviews of Geophysics* 58, doi:<https://doi.org/10.1029/2019RG000660>.
- Benz, S., Megahed, K., Möhler, O., Saathoff, H., Wagner, R. and Schurath, U. (2005). T-dependent rate measurements of homogeneous ice nucleation in cloud droplets using a large atmospheric simulation chamber. *Journal of Photochemistry and Photobiology A: Chemistry* 176: 208–217, doi:[10.1016/j.jphotochem.2005.08.026](https://doi.org/10.1016/j.jphotochem.2005.08.026).
- Bi, K., McMeeking, G. R., Ding, D. P., Levin, E. J. T., DeMott, P. J., Zhao, D. L., Wang, F., Liu, Q., Tian, P., Ma, X. C., Chen, Y. B., Huang, M. Y., Zhang, H. L., Gordon, T. D. and Chen, P. (2019). Measurements of ice nucleating particles in beijing, china. *Journal of Geophysical Research: Atmospheres* 124: 8065–8075, doi:<https://doi.org/10.1029/2019JD030609>.
- Bickel, M., Ponater, M., Bock, L., Burkhardt, U. and Reineke, S. (2020). Estimating the effective radiative forcing of contrail cirrus. *Journal of Climate* 33: 1991 – 2005, doi:[10.1175/JCLI-D-19-0467.1](https://doi.org/10.1175/JCLI-D-19-0467.1).
- Bieber, P., Seifried, T. M., Burkart, J., Gratzl, J., Kasper-Giebl, A., Schmale, D. and Grothe, H. (2020). A drone-based bioaerosol sampling system to monitor ice nucleation particles in the lower atmosphere. *Remote Sensing* 12: 552, doi:[10.3390/rs12030552](https://doi.org/10.3390/rs12030552).
- Bigg, E. K. (1967). Cross sections of ice nucleus concentrations at altitude over long paths. *Journal of Atmospheric Sciences* 24: 226 – 229, doi:[10.1175/1520-0469\(1967\)024<0226:CSOINC>2.0.CO;2](https://doi.org/10.1175/1520-0469(1967)024<0226:CSOINC>2.0.CO;2).

- Boer, G. de, Morrison, H., Shupe, M. D. and Hildner, R. (2011). Evidence of liquid dependent ice nucleation in high-latitude stratiform clouds from surface remote sensors. *Geophysical Research Letters* 38, doi:<https://doi.org/10.1029/2010GL046016>.
- Boose, Y., Sierau, B., García, M. I., Rodríguez, S., Alastuey, A., Linke, C., Schnaiter, M., Kupiszewski, P., Kanji, Z. A. and Lohmann, U. (2016a). Ice nucleating particles in the saharan air layer. *Atmospheric Chemistry and Physics* 16: 9067–9087, doi:10.5194/acp-16-9067-2016.
- Boose, Y., Welti, A., Atkinson, J., Ramelli, F., Niedorf, A., Bingemer, H., Plötze, M., Sierau, B., Kanji, Z. and Lohmann, U. (2016b). Heterogeneous ice nucleation on dust particles sourced from nine deserts worldwide – part 1: Immersion freezing. *Atmospheric Chemistry and Physics* 16: 15075–15095, doi:10.5194/acp-16-15075-2016.
- Boucher, O., Randall, D., Artaxo, P., Bretherton, C., Feingold, G., Forster, P., Kerminen, V.-M., Kondo, Y., Liao, H., Lohmann, U., Rasch, P., Satheesh, S. K., Sherwood, S., Stevens, B. and Zhang, X. Y. (2013). *Clouds and aerosols*. Cambridge, UK: Cambridge University Press. 571–657, doi:10.1017/CBO9781107415324.016.
- Boy, M., Kulmala, M., Ruuskanen, T. M., Pihlatie, M., Reissell, A., Aalto, P. P., Keronen, P., Dal Maso, M., Hellen, H., Hakola, H., Jansson, R., Hanke, M. and Arnold, F. (2005). Sulphuric acid closure and contribution to nucleation mode particle growth. *Atmospheric Chemistry and Physics* 5: 863–878, doi:10.5194/acp-5-863-2005.
- Bras, Y., Freney, E., Bouvier, L., Pichon, J.-M., Picard, D., Amato, P., Minguillón, M. and Sellegri, K. (2022). Seasonal variations, origin and parameterization of ice-nucleating particles at a mountain station in central france doi:10.1002/essoar.10511724.1.
- Brasseur, Z., Castarède, D., Thomson, E. S., Adams, M. P., Dusseldorp, S. Drossaart van, Heikkilä, P., Korhonen, K., Lampilahti, J., Paramonov, M., Schneider, J., Vogel, F., Wu, Y., Abbatt, J. P. D., Atanasova, N. S., Bamford, D. H., Bertozzi, B., Boyer, M., Brus, D., Daily, M. I., Fösig, R., Gute, E., Harrison, A. D., Hietala, P., Höhler, K., Kanji, Z. A., Keskinen, J., Lacher, L., Lampimäki, M., Levula, J., Manninen, A., Nadolny, J., Peltola, M., Porter, G. C. E., Poutanen, P., Proske, U., Schorr, T., Silas Umo, N., Stenszky, J., Virtanen, A., Moisseev, D., Kulmala, M., Murray, B. J., Petäjä, T., Möhler, O. and Duplissy, J. (2022). Measurement report: Introduction to the hyice-2018 campaign for measurements of ice-nucleating particles and instrument inter-comparison in the hyytiälä boreal forest. *Atmospheric Chemistry and Physics* 22: 5117–5145, doi:10.5194/acp-22-5117-2022.
- Brunner, C., Brem, B. T., Collaud Coen, M., Conen, F., Hervo, M., Henne, S., Steinbacher, M., Gysel-Beer, M. and Kanji, Z. A. (2021). The contribution of saharan dust to the ice-nucleating particle concentrations at the high altitude station jungfraujoeh (3580 m a.s.l.), switzerland. *Atmospheric Chemistry and Physics* 21: 18029–18053, doi:10.5194/acp-21-18029-2021.

- Brunner, C., Brem, B. T., Collaud Coen, M., Conen, F., Steinbacher, M., Gysel-Beer, M. and Kanji, Z. A. (2022). The diurnal and seasonal variability of ice-nucleating particles at the high altitude station jungfrauoch (3580 m a.s.l.), switzerland. *Atmospheric Chemistry and Physics* 22: 7557–7573, doi: 10.5194/acp-22-7557-2022.
- Brunner, C. and Kanji, Z. A. (2021). Continuous online monitoring of ice-nucleating particles: development of the automated horizontal ice nucleation chamber (hinc-auto). *Atmospheric Measurement Techniques* 14: 269–293, doi:10.5194/amt-14-269-2021.
- Burrows, S. M., Hoose, C., Pöschl, U. and Lawrence, M. G. (2013). Ice nuclei in marine air: biogenic particles or dust? *Atmospheric Chemistry and Physics* 13: 245–267, doi:10.5194/acp-13-245-2013.
- Burrows, S. M., McCluskey, C. S., Cornwell, G., Steinke, I., Zhang, K., Zhao, B., Zawadowicz, M., Raman, A., Kulkarni, G., China, S., Zelenyuk, A. and DeMott, P. J. (2022). Ice-nucleating particles that impact clouds and climate: Observational and modeling research needs. *Reviews of Geophysics* 60, doi:https://doi.org/10.1029/2021RG000745.
- Cantrell, W. and Heymsfield, A. (2005). Production of ice in tropospheric clouds: A review. *Bulletin of The American Meteorological Society - BULL AMER METEOROL SOC* 86, doi:10.1175/BAMS-86-6-795.
- Chen, T., Rossow, W. B. and Zhang, Y. (2000). Radiative effects of cloud-type variations. *Journal of Climate* 13: 264 – 286, doi:10.1175/1520-0442(2000)013<0264:REOCTV>2.0.CO;2.
- China, S., Alpert, P. A., Zhang, B., Schum, S., Dzepina, K., Wright, K., Owen, R. C., Fialho, P., Mazzoleni, L. R., Mazzoleni, C. and Knopf, D. A. (2017). Ice cloud formation potential by free tropospheric particles from long-range transport over the northern atlantic ocean. *Journal of Geophysical Research: Atmospheres* 122: 3065–3079, doi:https://doi.org/10.1002/2016JD025817.
- Chou, C., Stetzer, O., Weingartner, E., Jurányi, Z., Kanji, Z. A. and Lohmann, U. (2011). Ice nuclei properties within a saharan dust event at the jungfrauoch in the swiss alps. *Atmospheric Chemistry and Physics* 11: 4725–4738, doi:10.5194/acp-11-4725-2011.
- Coluzza, I., Creamean, J., Rossi, M. J., Wex, H., Alpert, P. A., Bianco, V., Boose, Y., Dellago, C., Felgitsch, L., Fröhlich-Nowoisky, J., Herrmann, H., Jungblut, S., Kanji, Z. A., Menzl, G., Moffett, B., Moritz, C., Mutzel, A., Pöschl, U., Schauerperl, M., Scheel, J., Stopelli, E., Stratmann, F., Grothe, H. and Schmale, D. G. (2017). Perspectives on the future of ice nucleation research: Research needs and unanswered questions identified from two international workshops. *Atmosphere* 8, doi:10.3390/atmos8080138.

- Conen, F., Morris, C. E., Leifeld, J., Yakutin, M. V. and Alewell, C. (2011). Biological residues define the ice nucleation properties of soil dust. *Atmospheric Chemistry and Physics* 11: 9643–9648, doi: 10.5194/acp-11-9643-2011.
- Conen, F., Rodríguez, S., Hueglin, C., Henne, S., Herrmann, E., Bukowiecki, N. and Alewell, C. (2015). Atmospheric ice nuclei at the high-altitude observatory Jungfraujoch, Switzerland. *Tellus B* 67, doi: 10.3402/tellusb.v67.25014.
- Connolly, P. J., Möhler, O., Field, P. R., Saathoff, H., Burgess, R., Choulaton, T. and Gallagher, M. (2009). Studies of heterogeneous freezing by three different desert dust samples. *Atmospheric Chemistry and Physics* 9: 2805–2824, doi:10.5194/acp-9-2805-2009.
- Creamean, J., Suski, K., Rosenfeld, D., Cazorla, A., DeMott, P., Sullivan, R., White, A., Ralph, F., Minnis, P., Comstock, J., Tomlinson, J. and Prather, K. (2013). Dust and biological aerosols from the Sahara and Asia influence precipitation in the western U.S. *Science (New York, N.Y.)* 339, doi:10.1126/science.1227279.
- Creamean, J. M., Primm, K. M., Tolbert, M. A., Hall, E. G., Wendell, J., Jordan, A., Sheridan, P. J., Smith, J. and Schnell, R. C. (2018). Hovercat: a novel aerial system for evaluation of aerosol–cloud interactions. *Atmospheric Measurement Techniques* 11: 3969–3985, doi:10.5194/amt-11-3969-2018.
- Cziczo, D., Stetzer, O., Worringer, A., Ebert, M., Weinbruch, S., Kamphus, M., Gallavardin, S., Curtius, J., Borrmann, S., Froyd, K., Mertes, S., Möhler, O. and Lohmann, U. (2009). Inadvertent climate modification due to anthropogenic lead. *Nature Geoscience*, v.2, 333–336 (2009) 2, doi:10.1038/ngeo499.
- Cziczo, D. J., Froyd, K. D., Hoose, C., Jensen, E. J., Diao, M., Zondlo, M. A., Smith, J. B., Twohy, C. H. and Murphy, D. M. (2013). Clarifying the dominant sources and mechanisms of cirrus cloud formation. *Science* 340: 1320–1324, doi:10.1126/science.1234145.
- Cziczo, D. J., Ladino, L., Boose, Y., Kanji, Z. A., Kupiszewski, P., Lance, S., Mertes, S. and Wex, H. (2017). Measurements of ice nucleating particles and ice residuals. *Meteorological Monographs* 58: 8.1 – 8.13, doi:10.1175/AMSMONOGRAPHS-D-16-0008.1.
- Cziczo, D. J., Murphy, D. M., Hudson, P. K. and Thomson, D. S. (2004). Single particle measurements of the chemical composition of cirrus ice residue during crystal-face. *Journal of Geophysical Research: Atmospheres* 109, doi:https://doi.org/10.1029/2003JD004032.
- David, R., Marcolli, C., Fahrni, J., Qiu, Y., Sirkin, Y., Molinero, V., Mahrt, F., Brühwiler, D., Lohmann, U. and Kanji, Z. (2019). Pore condensation and freezing is responsible for ice formation below water saturation for porous particles. *Proceedings of the National Academy of Sciences* 116: 201813647, doi:10.1073/pnas.1813647116.

- DeMott, P., Brooks, S., Prenni, A., Kreidenweis, S., Sassen, K., Poellot, M., Rogers, D. and Baumgardner, D. (2003a). African dust aerosols as atmospheric ice nuclei. *Geophys. Res. Lett.* 30, doi: 10.1029/2003GL017410.
- DeMott, P., Cziczo, D., Prenni, A., Murphy, D., Kreidenweis, S., Thomson, D., Borys, R. and Rogers, D. (2003b). Measurements of the concentration and composition of nuclei for cirrus formation. *Proceedings of the National Academy of Sciences of the United States of America* 100: 14655–60, doi: 10.1073/pnas.2532677100.
- DeMott, P., Hill, T., McCluskey, C., Prather, K., Collins, D., Sullivan, R., Ruppel, M., Mason, R., Irish, V., Lee, T., Hwang, C., Rhee, T., Snider, J., Mcmeeking, G., Dhaniyala, S., Lewis, E., Wentzell, J., Abbatt, J., Lee, C. and Franc, G. (2016). Sea spray aerosol as a unique source of ice nucleating particles. *Proceedings of the National Academy of Sciences of the United States of America* 113, doi: 10.1073/pnas.1514034112.
- DeMott, P., Möhler, O., Stetzer, O., Vali, G., Levin, Z., Petters, M., Murakami, M., Leisner, T., Bundke, U., Klein, H., Kanji, Z., Cotton, R., Jones, H., Benz, S., Brinkmann, M., Rzesanke, D., Saathoff, H., Nicolet, M., Saito, A. and Saunders, C. (2011). Resurgence in ice nuclei measurement research. *Bulletin of the American Meteorological Society* 92: 1623, doi:10.1175/2011BAMS3119.1.
- DeMott, P., Prenni, A., Liu, X., Kreidenweis, S., Petters, M., Twohy, C., Richardson, M., Eidhammer, T. and Rogers, D. (2010). Predicting global atmospheric ice nuclei distributions and their impact on climate. *Proceedings of the National Academy of Sciences of the United States of America* 107: 11217–22, doi:10.1073/pnas.0910818107.
- DeMott, P., Prenni, A., Mcmeeking, G., Sullivan, R., Petters, M., Tobo, Y., Niemand, M., Möhler, O., Snider, J., Wang, Z. and Kreidenweis, S. (2015). Integrating laboratory and field data to quantify the immersion freezing ice nucleation activity of mineral dust particles. *Atmospheric Chemistry and Physics* 15: 393–409, doi:10.5194/acp-15-393-2015.
- DeMott, P. J., Rogers, D. C. and Kreidenweis, S. M. (1997). The susceptibility of ice formation in upper tropospheric clouds to insoluble aerosol components. *Journal of Geophysical Research: Atmospheres* 102: 19575–19584, doi:https://doi.org/10.1029/97JD01138.
- Despres, V., Huffman, J., Burrows, S., Hoose, C., Safatov, A., Buryak, G., Fröhlich-Nowoisky, J., Elbert, W., Andreae, M., Schl, U. and Jaenicke, R. (2012). Primary biological particles in the atmosphere: A review. *Tellus B* 64, doi:10.3402/tellusb.v64i0.15598.
- Dufour, L. (1862). Ueber das gefrieren des wassers und über die bildung des hagels. *Annalen der Physik* 190: 530–554, doi:https://doi.org/10.1002/andp.18621901203.

- Durant, A., Bonadonna, C. and Horwell, C. (2010). Atmospheric and environmental impact of volcanic particulates. *Elements* 6, doi:10.2113/gselements.6.4.235.
- Eidhammer, T., DeMott, P., Prenni, A., Petters, M., Twohy, C., Rogers, D., Stith, J., Heymsfield, A., Wang, Z., Pratt, K., Prather, K., Murphy, S., Seinfeld, J. and Kreidenweis, S. (2010). Ice initiation by aerosol particles: Measured and predicted ice nuclei concentrations versus measured ice crystal concentrations in an orographic wave cloud. *Journal of the Atmospheric Sciences* 67, doi:10.1175/2010JAS3266.1.
- Eidhammer, T., DeMott, P. J. and Kreidenweis, S. M. (2009). A comparison of heterogeneous ice nucleation parameterizations using a parcel model framework. *Journal of Geophysical Research: Atmospheres* 114, doi:https://doi.org/10.1029/2008JD011095.
- Farah, A., Freney, E., Chauvigne, A., Baray, J., Rose, C., Picard, D., Colomb, A., Hadad, D., Abboud, M., Farah, W. and Sellegrì, K. (2018). Seasonal variation of aerosol size distribution data at the puy de dôme station with emphasis on the boundary layer/free troposphere segregation. *Atmosphere* 9: 244, doi:10.3390/atmos9070244.
- Field, P., Heymsfield, A., Shipway, B., DeMott, P., Pratt, K., Rogers, D., Stith, J. and Prather, K. (2012). Ice in clouds experiment-layer clouds. part ii: Testing characteristics of heterogeneous ice formation in lee wave clouds. *Journal of the Atmospheric Sciences* 69: 1066–1079, doi:10.1175/Jas-D-11-026.1.
- Field, P. R. and Heymsfield, A. J. (2015). Importance of snow to global precipitation. *Geophysical Research Letters* 42: 9512–9520, doi:https://doi.org/10.1002/2015GL065497.
- Field, P. R., Lawson, R. P., Brown, P. R. A., Lloyd, G., Westbrook, C., Moisseev, D., Miltenberger, A., Nenes, A., Blyth, A., Choulaton, T., Connolly, P., Buehl, J., Crosier, J., Cui, Z., Dearden, C., DeMott, P., Flossmann, A., Heymsfield, A., Huang, Y., Kalesse, H., Kanji, Z. A., Korolev, A., Kirchgassner, A., Lasher-Trapp, S., Leisner, T., McFarquhar, G., Phillips, V., Stith, J. and Sullivan, S. (2017). Secondary ice production: Current state of the science and recommendations for the future. *Meteorological Monographs* 58: 7.1 – 7.20, doi:10.1175/AMSMONOGRAPHS-D-16-0014.1.
- Flyger, H., Hansen, K., Megaw, W. J. and Cox, L. C. (1973). The Background Level of the Summer Tropospheric Aerosol Over Greenland and the North Atlantic Ocean. *Journal of Applied Meteorology* 12: 161–174, doi:10.1175/1520-0450(1973)012<0161:TBLOTS>2.0.CO;2.
- Forster, P., Storelvmo, T., Armour, K., Collins, W., Dufresne, J. L., Frame, D., Lunt, D. J., Mauritsen, T., Palmer, M. D., Watanabe, M., Wild, M., and Zhang, H. (2021). *The Earth's Energy Budget, Climate Feedbacks, and Climate Sensitivity*. Cambridge University Press.

- Freedman, M. (2015). Potential sites for ice nucleation on aluminosilicate clay minerals and related materials. *The Journal of Physical Chemistry Letters* 6: 150910160240008, doi:10.1021/acs.jpcllett.5b01326.
- Gachkivskiy, M. and Levin, I. (2022). User manual of the heidelberg radon monitor doi:10.18160/BWHB-KFAJ.
- Garimella, S., Kristensen, T. B., Ignatius, K., Welti, A., Voigtländer, J., Kulkarni, G. R., Sagan, F., Kok, G. L., Dorsey, J., Nichman, L., Rothenberg, D. A., Rösch, M., Kirchgäßner, A. C. R., Ladkin, R., Wex, H., Wilson, T. W., Ladino, L. A., Abbatt, J. P. D., Stetzer, O., Lohmann, U., Stratmann, F. and Cziczo, D. J. (2016). The spectrometer for ice nuclei (spin): an instrument to investigate ice nucleation. *Atmospheric Measurement Techniques* 9: 2781–2795, doi:10.5194/amt-9-2781-2016.
- Grawe, S., Jentsch, C., Schaefer, J., Wex, H. and Stratmann, F. (2023). Next-generation ice nucleating particle sampling on aircraft: Characterization of the high-volume flow aerosol particle filter sampler (hera) doi:10.5194/amt-2023-88.
- Greilinger, M., Schauer, G., Baumann-Stanzer, K., Skomorowski, P., Schöner, W. and Kasper-Giebl, A. (2018). Contribution of saharan dust to ion deposition loads of high alpine snow packs in austria (1987–2017). *Frontiers in Earth Science* 6: 126, doi:10.3389/feart.2018.00126.
- Griffiths, A. D., Conen, F., Weingartner, E., Zimmermann, L., Chambers, S. D., Williams, A. G. and Steinbacher, M. (2014). Surface-to-mountaintop transport characterised by radon observations at the jungfraujoch. *Atmospheric Chemistry and Physics* 14: 12763–12779, doi:10.5194/acp-14-12763-2014.
- Groß, S., Jurkat-Witschas, T., Li, Q., Wirth, M., Urbanek, B., Krämer, M., Weigel, R. and Voigt, C. (2023). Investigating an indirect aviation effect on mid-latitude cirrus clouds – linking lidar-derived optical properties to in situ measurements. *Atmospheric Chemistry and Physics* 23: 8369–8381, doi:10.5194/acp-23-8369-2023.
- Haag, W., Kärcher, B., Ström, J., Minikin, A., Lohmann, U., Ovarlez, J. and Stohl, A. (2003). Freezing thresholds and cirrus cloud formation mechanisms inferred from in situ measurements of relative humidity. *Atmospheric Chemistry and Physics* 3: 1791–1806, doi:10.5194/acp-3-1791-2003.
- Harrison, A., Whale, T., Carpenter, M., Holden, M., Neve, L., O’Sullivan, D., Vergara-Temprado, J. and Murray, B. (2016). Not all feldspars are equal: A survey of ice nucleating properties across the feldspar group of minerals. *Atmospheric Chemistry and Physics* 16: 10927–10940, doi:10.5194/acp-16-10927-2016.
- Herrmann, E., Weingartner, E., Henne, S., Vuilleumier, L., Bukowiecki, N., Steinbacher, M., Conen, F., Collaud Coen, M., Hammer, E., Jurányi, Z., Baltensperger, U. and Gysel, M. (2015). Analysis of long-

- term aerosol size distribution data from jungfraujoch with emphasis on free tropospheric conditions, cloud influence, and air mass transport. *Journal of Geophysical Research: Atmospheres* 120: 9459–9480, doi:<https://doi.org/10.1002/2015JD023660>.
- Heymsfield, A. J., Krämer, M., Luebke, A., Brown, P., Cziczo, D. J., Franklin, C., Lawson, P., Lohmann, U., McFarquhar, G., Ulanowski, Z. and Tricht, K. V. (2017). Cirrus clouds. *Meteorological Monographs* 58: 2.1 – 2.26, doi:10.1175/AMSMONOGRAPHS-D-16-0010.1.
- Heymsfield, A. J., Schmitt, C., Chen, C.-C.-J., Bansemer, A., Gettelman, A., Field, P. R. and Liu, C. (2020). Contributions of the liquid and ice phases to global surface precipitation: Observations and global climate modeling. *Journal of the Atmospheric Sciences* 77: 2629 – 2648, doi:10.1175/JAS-D-19-0352.1.
- Hill, T., Moffett, B., DeMott, P., Georgakopoulos, D., Stump, W. and Franc, G. (2013). Measurement of ice nucleation-active bacteria on plants and in precipitation by quantitative pcr. *Applied and environmental microbiology* 80, doi:10.1128/AEM.02967-13.
- Hill, T. C. J., DeMott, P. J., Tobo, Y., Fröhlich-Nowoisky, J., Moffett, B. F., Franc, G. D. and Kreidenweis, S. M. (2016). Sources of organic ice nucleating particles in soils. *Atmospheric Chemistry and Physics* 16: 7195–7211, doi:10.5194/acp-16-7195-2016.
- Hiranuma, N., Paukert, M., Steinke, I., Zhang, K., Kulkarni, G., Hoose, C., Schnaiter, M., Saathoff, H. and Möhler, O. (2014). A comprehensive parameterization of heterogeneous ice nucleation of dust surrogate: laboratory study with hematite particles and its application to atmospheric models. *Atmospheric Chemistry and Physics* 14, doi:10.5194/acp-14-13145-2014.
- Hiranuma, N., Vepuri, H., Lacher, L., Nadolny, J. and Möhler, O. (2020). Characterization of a new portable ice nucleation experiment chamber (pine) and first field deployment in the southern great plains doi:10.1002/essoar.10502526.1.
- Hobbs, P. V. and Rangno, A. L. (1998). Microstructures of low and middle-level clouds over the beaufort sea. *Quarterly Journal of the Royal Meteorological Society* 124: 2035–2071, doi:<https://doi.org/10.1002/qj.49712455012>.
- Holzinger, R., Kasper-Giebl, A., Staudinger, M., Schauer, G. and Röckmann, T. (2010). Analysis of the chemical composition of organic aerosol at the mt. sonnblick observatory using a novel high mass resolution thermal-desorption proton-transfer-reaction mass-spectrometer (hr-td-ptr-ms). *Atmospheric Chemistry and Physics* 10: 10111–10128, doi:10.5194/acp-10-10111-2010.
- Hoose, C., Kristjánsson, J. and Burrows, S. (2010). How important is biological ice nucleation in clouds on a global scale? *Environmental Research Letters*, v.5 (2010) 5, doi:10.1088/1748-9326/5/2/024009.

- Hoose, C. and Möhler, O. (2012). Heterogeneous ice nucleation on atmospheric aerosols: a review of results from laboratory experiments. *Atmospheric Chemistry and Physics* 12: 9817–9854, doi:10.5194/acp-12-9817-2012.
- Ignatius, K., Kristensen, T. B., Järvinen, E., Nichman, L., Fuchs, C., Gordon, H., Herenz, P., Hoyle, C. R., Duplissy, J., Garimella, S., Dias, A., Frege, C., Höppel, N., Tröstl, J., Wagner, R., Yan, C., Amorim, A., Baltensperger, U., Curtius, J., Donahue, N. M., Gallagher, M. W., Kirkby, J., Kulmala, M., Möhler, O., Saathoff, H., Schnaiter, M., Tomé, A., Virtanen, A., Worsnop, D. and Stratmann, F. (2016). Heterogeneous ice nucleation of viscous secondary organic aerosol produced from ozonolysis of  $\alpha$ -pinene. *Atmospheric Chemistry and Physics* 16: 6495–6509, doi:10.5194/acp-16-6495-2016.
- Isoni, K., Komabayasi, M., Takeda, T., Tanaka, T., Iwai, K. and Fujiwara, M. (1971). Concentration and nature of ice nuclei in rim of the north pacific ocean. *Tellus* 23: 40–59, doi:https://doi.org/10.1111/j.2153-3490.1971.tb00545.x.
- Jaenicke, R. (1982). Physical Aspects of the Atmospheric Aerosol. In Georgii, H. W. and Jaeschke, W. (eds), *Chemistry of the Unpolluted and Polluted Troposphere*. Dordrecht: Springer Netherlands, 341–373.
- Jimenez-Sanchez, C., Hanlon, R., Aho, K., Powers, C., Morris, C. and Schmale, D. (2018). Diversity and ice nucleation activity of microorganisms collected with a small unmanned aircraft system (suas) in france and the united states. *Frontiers in Microbiology* 9, doi:10.3389/fmicb.2018.01667.
- Järvinen, E., Vochezer, P., Möhler, O. and Schnaiter, M. (2014). Laboratory study of microphysical and scattering properties of corona-producing cirrus clouds. *Applied Optics* 53, doi:10.1364/AO.53.007566.
- Kalesse-Los, H., Boer, G., Solomon, A., Oue, M., Ahlgrimm, M., Zhang, D., Shupe, M., Luke, E. and Protat, A. (2016). Understanding rapid changes in phase partitioning between cloud liquid and ice in stratiform mixed-phase clouds: An arctic case study. *Monthly Weather Review* 144, doi:10.1175/MWR-D-16-0155.1.
- Kampe, H. J. aufm and Weickmann, H. K. (1951). The effectiveness of natural and artificial aerosols as freezing nuclei. *Journal of Atmospheric Sciences* 8: 283 – 288, doi:10.1175/1520-0469(1951)008<0283:TEONAA>2.0.CO;2.
- Kanji, Z. and Abbatt, J. (2009). Ice nucleation onto arizona test dust at cirrus temperatures: Effect of temperature and aerosol size on onset relative humidity. *The journal of physical chemistry. A* 114: 935–41, doi:10.1021/jp908661m.
- Kanji, Z., Ladino, L., Wex, H., Boose, Y., Burkert-Kohn, M., Cziczo, D. and Krämer, M. (2017). Ice formation and evolution in clouds and precipitation: Measurement and modeling challenges. chap-

- ter 1: Overview of ice nucleating particles. *Meteorological Monographs* 58: 1–25, doi:10.1175/AMSMONOGRAPHS-D-0006.1.
- Kanji, Z., Welti, A., Chou, C., Stetzer, O. and Lohmann, U. (2013). Laboratory studies of immersion and deposition mode ice nucleation of ozone aged mineral dust particles. *Atmospheric Chemistry and Physics Discussions* 13: 8701–8767, doi:10.5194/acpd-13-8701-2013.
- Kanji, Z. A., Welti, A., Corbin, J. C. and Mensah, A. A. (2020). Black carbon particles do not matter for immersion mode ice nucleation. *Geophysical Research Letters* 47: e2019GL086764, doi:https://doi.org/10.1029/2019GL086764.
- Karstens, U., Schwingshackl, C., Schmithüsen, D. and Levin, I. (2015). A process-based 222rn flux map for europe and its comparison to long-term observations. *Atmospheric Chemistry and Physics Discussions* 15: 17397–17448, doi:10.5194/acpd-15-17397-2015.
- Kiselev, A., Bachmann, F., Pedevilla, P., Cox, S., Michaelides, A., Gerthsen, D. and Leisner, T. (2016). Active sites in heterogeneous ice nucleation—the example of k-rich feldspars. *Science* 355, doi:10.1126/science.aai8034.
- Knippertz, P. and Stuut, J.-B. (2014). *Mineral Dust: A Key Player in the Earth System*. doi:10.1007/978-94-017-8978-3.
- Knopf, D. and Alpert, P. (2023). Atmospheric ice nucleation. *Nature Reviews Physics* 5, doi:10.1038/s42254-023-00570-7.
- Knopf, D., Alpert, P. and Wang, B. (2018). The role of organic aerosol in atmospheric ice nucleation – a review. *ACS Earth and Space Chemistry* 2, doi:10.1021/acsearthspacechem.7b00120.
- Knopf, D. A., Wang, P., Wong, B., Tomlin, J. M., Veghte, D. P., Lata, N. N., China, S., Laskin, A., Moffet, R. C., Aller, J. Y., Marcus, M. A. and Wang, J. (2023). Physicochemical characterization of free troposphere and marine boundary layer ice-nucleating particles collected by aircraft in the eastern north atlantic. *Atmospheric Chemistry and Physics* 23: 8659–8681, doi:10.5194/acp-23-8659-2023.
- Kok, J., Storelvmo, T., Karydis, V., Adebisi, A., Mahowald, N., Evan, A., He, C. and Leung, D. (2023). Mineral dust aerosol impacts on global climate and climate change. *Nature Reviews Earth Environment* 4, doi:10.1038/s43017-022-00379-5.
- Koop, T., Luo, B., Tsias, A. and Peter, T. (2000). Water activity as the determinant for homogeneous ice nucleation in aqueous solutions. *Nature* 406: 611–4, doi:10.1038/35020537.
- Korolev, A. (2007). Limitations of the wegener bergeron findeisen mechanism in the evolution of mixed-phase clouds. *Journal of The Atmospheric Sciences - J ATMOS SCI* 64, doi:10.1175/JAS4035.1.

- Korolev, A., DeMott, P. J., Heckman, I., Wolde, M., Williams, E., Smalley, D. J. and Donovan, M. F. (2022). Observation of secondary ice production in clouds at low temperatures. *Atmospheric Chemistry and Physics* 22: 13103–13113, doi:10.5194/acp-22-13103-2022.
- Korolev, A. and Field, P. (2008). The effect of dynamics on mixed-phase clouds: Theoretical considerations. *Journal of the Atmospheric Sciences* 65: 66–86, doi:10.1175/2007JAS2355.1.
- Korolev, A. and Leisner, T. (2020). Review of experimental studies of secondary ice production. *Atmospheric Chemistry and Physics* 20: 11767–11797, doi:10.5194/acp-20-11767-2020.
- Korolev, A., McFarquhar, G., Field, P. R., Franklin, C., Lawson, P., Wang, Z., Williams, E., Abel, S. J., Axisa, D., Borrmann, S., Crosier, J., Fugal, J., Krämer, M., Lohmann, U., Schlenczek, O., Schnaiter, M. and Wendisch, M. (2017). Mixed-phase clouds: Progress and challenges. *Meteorological Monographs* 58: 5.1 – 5.50, doi:10.1175/AMSMONOGRAPHS-D-17-0001.1.
- Krämer, M., Rolf, C., Spelten, N., Afchine, A., Fahey, D., Jensen, E., Khaykin, S., Kuhn, T., Lawson, P., Lykov, A., Pan, L. L., Riese, M., Rollins, A., Stroh, F., Thornberry, T., Wolf, V., Woods, S., Spichtinger, P., Quaas, J. and Sourdeval, O. (2020). A microphysics guide to cirrus – part 2: climatologies of clouds and humidity from observations. *Atmospheric Chemistry and Physics* 20: 12569–12608, doi:10.5194/acp-20-12569-2020.
- Krämer, M., C, S., A, A., R, B., I, G., Mangold, A., S, S., N, S., N, S., S, B., Reus, M. de and P, S. (2009). Ice supersaturations and cirrus cloud crystal numbers. *Atmospheric Chemistry and Physics* 8, doi:10.5194/acpd-8-21089-2008.
- Krämer, M., Rolf, C., Luebke, A., Afchine, A., Spelten, N., Costa, A., Meyer, J., Zöger, M., Smith, J., Herman, R. L., Buchholz, B., Ebert, V., Baumgardner, D., Borrmann, S., Klingebiel, M. and Avallone, L. (2016). A microphysics guide to cirrus clouds – part 1: Cirrus types. *Atmospheric Chemistry and Physics* 16: 3463–3483, doi:10.5194/acp-16-3463-2016.
- Kulmala, M. (2003). How particles nucleate and grow. *Science (New York, N.Y.)* 302: 1000–1, doi: 10.1126/science.1090848.
- Kärcher, B. (2017). Cirrus clouds and their response to anthropogenic activities. *Current Climate Change Reports* 3, doi:10.1007/s40641-017-0060-3.
- Kärcher, B. and Lohmann, U. (2003). A parameterization of cirrus cloud formation: Heterogeneous freezing. *Journal of Geophysical Research* 108: AAC2–1, doi:10.1029/2002JD003220.
- Kärcher, B. and Spichtinger, P. (2009). *Cloud-controlling Factors of Cirrus*, 2. 235–268, doi:10.7551/mitpress/9780262012874.003.0011.

- Lacher, L., Adams, M. P., Barry, K., Bertozzi, B., Bingemer, H., Boffo, C., Bras, Y., Büttner, N., Castarede, D., Cziczo, D. J., DeMott, P. J., Fösig, R., Goodell, M., Höhler, K., Hill, T. C. J., Jentsch, C., Ladino, L. A., Levin, E. J. T., Mertes, S., Möhler, O., Moore, K. A., Murray, B. J., Nadolny, J., Pfeuffer, T., Picard, D., Ramírez-Romero, C., Ribeiro, M., Richter, S., Schrod, J., Sellegri, K., Stratmann, F., Swanson, B. E., Thomson, E., Wex, H., Wolf, M. and Freney, E. (2024). The puy de dôme ice nucleation intercomparison campaign (picnic): Comparison between online and offline methods in ambient air. *EGUsphere* 2024: 1–37, doi:10.5194/egusphere-2023-1125.
- Lacher, L., Clemen, H.-C., Shen, X., Mertes, S., Gysel-Beer, M., Moallemi, A., Steinbacher, M., Henne, S., Saathoff, H., Möhler, O., Höhler, K., Schiebel, T., Weber, D., Schrod, J., Schneider, J. and Kanji, Z. A. (2021). Sources and nature of ice-nucleating particles in the free troposphere at jungfrauoch in winter 2017. *Atmospheric Chemistry and Physics* 21: 16925–16953, doi:10.5194/acp-21-16925-2021.
- Lacher, L., DeMott, P. J., Levin, E. J. T., Suski, K. J., Boose, Y., Zipori, A., Herrmann, E., Bukowiecki, N., Steinbacher, M., Gute, E., Abbatt, J. P. D., Lohmann, U. and Kanji, Z. A. (2018a). Background free-tropospheric ice nucleating particle concentrations at mixed-phase cloud conditions. *Journal of Geophysical Research: Atmospheres* 123: 10,506–10,525, doi:https://doi.org/10.1029/2018JD028338.
- Lacher, L., Lohmann, U., Boose, Y., Zipori, A., Herrmann, E., Bukowiecki, N., Steinbacher, M. and Kanji, Z. A. (2017). The horizontal ice nucleation chamber (hinc): in-p measurements at conditions relevant for mixed-phase clouds at the high altitude research station jungfrauoch. *Atmospheric Chemistry and Physics* 17: 15199–15224, doi:10.5194/acp-17-15199-2017.
- Lacher, L., Steinbacher, M., Bukowiecki, N., Herrmann, E., Zipori, A. and Kanji, Z. A. (2018b). Impact of air mass conditions and aerosol properties on ice nucleating particle concentrations at the high altitude research station jungfrauoch. *Atmosphere* 9, doi:10.3390/atmos9090363.
- Ladino, L., Yakobi-Hancock, J., Kilthau, W., Mason, R., Si, M., Li, J., Miller, L., Schiller, C., Huffman, J., Aller, J., Knopf, D., Bertram, A. and Abbatt, J. (2016). Addressing the ice nucleating abilities of marine aerosol: A combination of deposition mode laboratory and field measurements. *Atmospheric Environment* 132: 1–10, doi:10.1016/j.atmosenv.2016.02.028.
- Ladino, L., Zhou, S., Yakobi-Hancock, J., Aljawhary, D. and Abbatt, J. (2014). Factors controlling the ice nucleating abilities of -pinene soa particles. *Journal of Geophysical Research Atmospheres* 119, doi:10.1002/2014JD021578.
- Ladino Moreno, L. A., Stetzer, O. and Lohmann, U. (2013). Contact freezing: a review of experimental studies. *Atmospheric Chemistry and Physics* 13: 9745–9769, doi:10.5194/acp-13-9745-2013.

- Lau, W. and Wu, H.-T. (2003). Warm rain processes over tropical oceans and climate implications. *Geophysical Research Letters* 30: 2290–, doi:10.1029/2003GL018567.
- Levin, E. J., DeMott, P. J., Suski, K. J., Boose, Y., Hill, T. C., McCluskey, C. S., Schill, G. P., Rocci, K., Al-Mashat, H., Kristensen, L. J., Cornwell, G., Prather, K., Tomlinson, J., Mei, F., Hubbe, J., Pekour, M., Sullivan, R., Leung, L. R. and Kreidenweis, S. M. (2019). Characteristics of ice nucleating particles in and around california winter storms. *Journal of Geophysical Research: Atmospheres* 124: 11530–11551, doi:https://doi.org/10.1029/2019JD030831.
- Levin, I., Born, M., Cuntz, M., Langendörfer, U., Mantsch, S., Naegler, T., Schmidt, M., Varlagin, A., Verclas, S. and Wagenbach, D. (2002). Observations of atmospheric variability and soil exhalation rate of radon-222 at a russian forest site. technical approach and deployment for boundary layer studies. *Tellus B* 54, doi:10.3402/tellusb.v54i5.16681.
- Lighty, J., Veranth, J. and Sarofim, A. (2000). Combustion aerosols: Factors governing their size and composition and implications to human health. *Journal of the Air Waste Management Association* (1995) 50: 1565–618; discussion 1619, doi:10.1080/10473289.2000.10464197.
- Liu, D., Wang, Z., Liu, Z., Winker, D. and Trepte, C. (2008). A height resolved global view of dust aerosols from the first year calipso lidar measurements. *Journal of Geophysical Research: Atmospheres* 113, doi:https://doi.org/10.1029/2007JD009776.
- Lohmann, U. and Feichter, J. (2005). Global indirect aerosol effects: a review. *Atmospheric Chemistry and Physics* 5: 715–737, doi:10.5194/acp-5-715-2005.
- Lohmann, U. and Gasparini, B. (2017). A cirrus cloud climate dial? *Science* 357: 248–249, doi:10.1126/science.aan3325.
- Lohmann, U., Luond, F. and Mahrt, F. (2016). An introduction to clouds: From the microscale to climate .
- Lotteraner, C. and Piringer, M. (2016). Mixing-height time series from operational ceilometer aerosol-layer heights. *Boundary-Layer Meteorology* 161, doi:10.1007/s10546-016-0169-2.
- Mahrt, F., Kilchhofer, K., Marcolli, C., Grönquist, P., David, R. O., Rösch, M., Lohmann, U. and Kanji, Z. A. (2020). The impact of cloud processing on the ice nucleation abilities of soot particles at cirrus temperatures. *Journal of Geophysical Research: Atmospheres* 125: e2019JD030922, doi:https://doi.org/10.1029/2019JD030922, e2019JD030922 10.1029/2019JD030922.
- Mahrt, F., Marcolli, C., David, R. O., Grönquist, P., Barthazy Meier, E. J., Lohmann, U. and Kanji, Z. A. (2018). Ice nucleation abilities of soot particles determined with the horizontal ice nucleation chamber. *Atmospheric Chemistry and Physics* 18: 13363–13392, doi:10.5194/acp-18-13363-2018.

- Marcolli, C. (2014). Deposition nucleation viewed as homogeneous or immersion freezing in pores and cavities. *Atmospheric Chemistry and Physics* 14: 2071–2104, doi:10.5194/acp-14-2071-2014.
- Marcolli, C. (2020). Technical note: Fundamental aspects of ice nucleation via pore condensation and freezing including laplace pressure and growth into macroscopic ice. *Atmospheric Chemistry and Physics* 20: 3209–3230, doi:10.5194/acp-20-3209-2020.
- Mason, B. J. (1972). The physics of clouds. *Quarterly Journal of the Royal Meteorological Society* 98: 708–708, doi:https://doi.org/10.1002/qj.49709841723.
- Mason, R., Si, M., Chou, C., Irish, V., Dickie, R., Elizondo, P., Wong, R., Brintnell, M., Elsasser, M., Lassar, W., Pierce, K., Leaitch, W., Macdonald, A., Platt, A., Toom, D., Sarda-Estève, R., Schiller, C., Suski, K., Hill, T. and Bertram, A. (2016). Size-resolved measurements of ice-nucleating particles at six locations in north america and one in europe. *Atmospheric Chemistry and Physics* 16, doi: 10.5194/acp-16-1637-2016.
- Mason, R. H., Si, M., Li, J., Chou, C., Dickie, R., Toom-Sauntry, D., Pöhlker, C., Yakobi-Hancock, J. D., Ladino, L. A., Jones, K., Leaitch, W. R., Schiller, C. L., Abbatt, J. P. D., Huffman, J. A. and Bertram, A. K. (2015). Ice nucleating particles at a coastal marine boundary layer site: correlations with aerosol type and meteorological conditions. *Atmospheric Chemistry and Physics* 15: 12547–12566, doi:10.5194/acp-15-12547-2015.
- McCluskey, C. S., Hill, T. C. J., Humphries, R. S., Rauker, A. M., Moreau, S., Stratton, P. G., Chambers, S. D., Williams, A. G., McRobert, I., Ward, J., Keywood, M. D., Harnwell, J., Ponsonby, W., Loh, Z. M., Krummel, P. B., Protat, A., Kreidenweis, S. M. and DeMott, P. J. (2018). Observations of ice nucleating particles over southern ocean waters. *Geophysical Research Letters* 45: 11,989–11,997, doi:https://doi.org/10.1029/2018GL079981.
- McVay, R. C., Zhang, X., Aumont, B., Valorso, R., Camredon, M., La, Y. S., Wennberg, P. O. and Seinfeld, J. H. (2016). Soa formation from the photooxidation of  $\alpha$ -pinene: systematic exploration of the simulation of chamber data. *Atmospheric Chemistry and Physics* 16: 2785–2802, doi:10.5194/acp-16-2785-2016.
- Morris, C., Georgakopoulos, D. and Sands, D. (2004). Ice nucleation active bacteria and their potential role in precipitation. *Journal de Physique IV (Proceedings)* 121: 87–103, doi:10.1051/jp4:2004121004.
- Morrison, H., Boer, G., Feingold, G., Harrington, J., Shupe, M., Sulia, K. and Morrison, H. (2012). Resilience of persistent arctic mixed-phase clouds. *Nature Geoscience - NAT GEOSCI* 5: 11–17, doi: 10.1038/ngeo1332.

- Mossop, S. C. and Hallett, J. (1974). Ice crystal concentration in cumulus clouds: Influence of the drop spectrum. *Science* 186: 632–634, doi:10.1126/science.186.4164.632.
- Murphy, D. and Koop, T. (2005). Review of the vapour pressures of supercooled water for atmospheric applications. *Quarterly Journal of the Royal Meteorological Society* 131: 1539 – 1565, doi:10.1256/qj.04.94.
- Murray, B. J., Carslaw, K. S. and Field, P. R. (2021). Opinion: Cloud-phase climate feedback and the importance of ice-nucleating particles. *Atmospheric Chemistry and Physics* 21: 665–679, doi:10.5194/acp-21-665-2021.
- Murray, B. J. and Liu, X. (2022). Chapter 15 - ice-nucleating particles and their effects on clouds and radiation. In Carslaw, K. S. (ed.), *Aerosols and Climate*. Elsevier, 619–649, doi:https://doi.org/10.1016/B978-0-12-819766-0.00014-6.
- Murray, B. J., O’Sullivan, D., Atkinson, J. D. and Webb, M. E. (2012). Ice nucleation by particles immersed in supercooled cloud droplets. *Chem. Soc. Rev.* 41: 6519–6554, doi:10.1039/C2CS35200A.
- Murray, E. J. and Sivakumar, V. (2010). Unsaturated Soils: A fundamental interpretation of soil behaviour.
- Möhler, O., Adams, M., Lacher, L., Vogel, F., Nadolny, J., Ullrich, R., Boffo, C., Pfeuffer, T., Hobl, A., Weiß, M., Vepuri, H. S. K., Hiranuma, N. and Murray, B. J. (2021). The portable ice nucleation experiment (pine): a new online instrument for laboratory studies and automated long-term field observations of ice-nucleating particles. *Atmospheric Measurement Techniques* 14: 1143–1166, doi: 10.5194/amt-14-1143-2021.
- Möhler, O., Benz, S., Saathoff, H., Schnaiter, M., Wagner, R., Schneider, J., Walter, S., Ebert, V. and Wagner, S. (2008). The effect of organic coating on the heterogeneous ice nucleation efficiency of mineral dust aerosols. *Environmental Research Letters* 025007, doi:10.1088/1748-9326/3/2/025007.
- Möhler, O., Field, P., Connolly, P., Benz, S., Saathoff, H., Schnaiter, M., Wagner, R., Cotton, R., Krämer, M., Mangold, A. and Heymsfield, A. (2006). Efficiency of the deposition mode ice nucleation on mineral dust particles. *Atmospheric Chemistry and Physics Discussions* 6: 1539–1577, doi:10.5194/acpd-6-1539-2006.
- Möhler, O., Stetzer, O., Schaefers, S., Linke, C., Schnaiter, M., Tiede, R., Saathoff, H., Krämer, M., Mangold, A., Budz, P., Zink, P., Schreiner, J., Mauersberger, K., Haag, W., Kärcher, B. and Schurath, U. (2003). Experimental investigation of homogeneous freezing of sulphuric acid particles in the aerosol chamber aida. *Atmospheric Chemistry and Physics* 3: 211–223, doi:10.5194/acp-3-211-2003.

- Mülmenstädt, J. and Feingold, G. (2018). The radiative forcing of aerosol–cloud interactions in liquid clouds: Wrestling and embracing uncertainty. *Current Climate Change Reports* 4, doi:10.1007/s40641-018-0089-y.
- Mülmenstädt, J., Sourdeval, O., Delanoë, J. and Quaas, J. (2015). Frequency of occurrence of rain from liquid-, mixed-, and ice-phase clouds derived from a-train satellite retrievals. *Geophysical Research Letters* 42: 6502–6509, doi:https://doi.org/10.1002/2015GL064604.
- Nagare, B., Marcolli, C., Welti, A., Stetzer, O. and Lohmann, U. (2016). Comparing contact and immersion freezing from continuous flow diffusion chambers. *Atmospheric Chemistry and Physics* 16: 8899–8914, doi:10.5194/acp-16-8899-2016.
- Nazaroff, W. W. (1992). Radon transport from soil to air. *Reviews of Geophysics* 30: 137–160, doi:https://doi.org/10.1029/92RG00055.
- Niemand, M., Möhler, O., Vogel, B., Vogel, H., Hoose, C., Connolly, P., Klein, H., Bingemer, H., DeMott, P., Skrotzki, J. and Leisner, T. (2012). A particle-surface-area-based parameterization of immersion freezing on desert dust particles. *Journal of Atmospheric Sciences* 69: 3077–3092, doi:10.1175/JAS-D-11-0249.1.
- O’Sullivan, D., Adams, M., Tarn, M., Harrison, A., Vergara-Temprado, J., Porter, G., Holden, M., Sanchez-Marroquin, A., Carotenuto, F., Whale, T., McQuaid, J., Walshaw, R., Hedges, D., Burke, I., Cui, Z. and Murray, B. (2018). Contributions of biogenic material to the atmospheric ice-nucleating particle population in north western europe. *Scientific Reports* 8, doi:10.1038/s41598-018-31981-7.
- O’Sullivan, D., Marengo, F., Ryder, C. L., Pradhan, Y., Kipling, Z., Johnson, B., Benedetti, A., Brooks, M., McGill, M., Yorks, J. and Selmer, P. (2020). Models transport saharan dust too low in the atmosphere: a comparison of the metum and cams forecasts with observations. *Atmospheric Chemistry and Physics* 20: 12955–12982, doi:10.5194/acp-20-12955-2020.
- O’Sullivan, D., Murray, B. J., Malkin, T. L., Whale, T. F., Umo, N. S., Atkinson, J. D., Price, H. C., Baustian, K. J., Browse, J. and Webb, M. E. (2014). Ice nucleation by fertile soil dusts: relative importance of mineral and biogenic components. *Atmospheric Chemistry and Physics* 14: 1853–1867, doi:10.5194/acp-14-1853-2014.
- Pinsky, M., Khain, A. and Korolev, A. (2018). Theoretical analysis of liquid-ice interaction in unsaturated environment with application to the problem of homogeneous mixing. *Journal of the Atmospheric Sciences* 75: 1045–1062, doi:10.1175/JAS-D-17-0228.1.
- Ponsonby, J., King, L., Murray, B. and Stettler, M. (2023). Jet aircraft lubrication oil droplets as contrail ice-forming particles. *EGUsphere* 2023: 1–25, doi:10.5194/egusphere-2023-1264.

- Porter, G. C. E., Sikora, S. N. F., Adams, M. P., Proske, U., Harrison, A. D., Tarn, M. D., Brooks, I. M. and Murray, B. J. (2020). Resolving the size of ice-nucleating particles with a balloon deployable aerosol sampler: the shark. *Atmospheric Measurement Techniques* 13: 2905–2921, doi: 10.5194/amt-13-2905-2020.
- Pratt, K., DeMott, P., French, J., Wang, Z., Westphal, D., Heymsfield, A., Twohy, C., Prenni, A. and Prather, K. (2009). In situ detection of biological particles in cloud ice-crystals. *Nature Geoscience* 2: 398–401, doi:10.1038/NNGEO521.
- Prenni, A., Tobo, Y., Garcia, E., DeMott, P., Huffman, J., Mccluskey, C., Kreidenweis, S., Prenni, J., Pöhlker, C. and Pöschl, U. (2013). The impact of rain on ice nuclei populations at a forested site in colorado. *Geophysical Research Letters* 40: 227–231, doi:10.1029/2012GL053953.
- Prenni, A. J., Harrington, J. Y., Tjernström, M., DeMott, P. J., Avramov, A., Long, C. N., Kreidenweis, S. M., Olsson, P. Q. and Verlinde, J. (2007). Can ice-nucleating aerosols affect arctic seasonal climate? *Bulletin of the American Meteorological Society* 88: 541 – 550, doi:10.1175/BAMS-88-4-541.
- Price, H. C., Baustian, K. J., McQuaid, J. B., Blyth, A., Bower, K. N., Choularton, T., Cotton, R. J., Cui, Z., Field, P. R., Gallagher, M., Hawker, R., Merrington, A., Miltenberger, A., Neely III, R. R., Parker, S. T., Rosenberg, P. D., Taylor, J. W., Trembath, J., Vergara-Temprado, J., Whale, T. F., Wilson, T. W., Young, G. and Murray, B. J. (2018). Atmospheric ice-nucleating particles in the dusty tropical atlantic. *Journal of Geophysical Research: Atmospheres* 123: 2175–2193, doi:https://doi.org/10.1002/2017JD027560.
- Prospero, J. (1999). Long-range transport of mineral dust in the global atmosphere: Impact of african dust on the environment of the southeastern united states. *Proceedings of the National Academy of Sciences of the United States of America* 96: 3396–403, doi:10.1073/pnas.96.7.3396.
- Pruppacher, H. and Klett, J. (2010). *Microphysics of Clouds and Precipitation*, 18. doi:10.1007/978-0-306-48100-0.
- Pummer, B. G., Bauer, H., Bernardi, J., Bleicher, S. and Grothe, H. (2012). Suspendable macromolecules are responsible for ice nucleation activity of birch and conifer pollen. *Atmospheric Chemistry and Physics* 12: 2541–2550, doi:10.5194/acp-12-2541-2012.
- Richardson, M. S., DeMott, P. J., Kreidenweis, S. M., Cziczo, D. J., Dunlea, E. J., Jimenez, J. L., Thomson, D. S., Ashbaugh, L. L., Borys, R. D., Westphal, D. L., Casuccio, G. S. and Lersch, T. L. (2007). Measurements of heterogeneous ice nuclei in the western united states in springtime and their relation to aerosol characteristics. *Journal of Geophysical Research: Atmospheres* 112, doi:https://doi.org/10.1029/2006JD007500.
- Roedel, W. and Wagner, T. (2011). *Physik unserer Umwelt: die Atmosphäre*, 4.

- Rogers, D. C. (1988). Development of a continuous flow thermal gradient diffusion chamber for ice nucleation studies. *Atmospheric Research* 22: 149–181, doi:[https://doi.org/10.1016/0169-8095\(88\)90005-1](https://doi.org/10.1016/0169-8095(88)90005-1).
- Rogers, D. C. (1993). Measurements of natural ice nuclei with a continuous flow diffusion chamber. *Atmospheric Research* 29: 209–228, doi:[https://doi.org/10.1016/0169-8095\(93\)90004-8](https://doi.org/10.1016/0169-8095(93)90004-8).
- Rogers, D. C. (1994). Detecting ice nuclei with a continuous—flow diffusion chamber—some exploratory tests of instrument response. *Journal of Atmospheric and Oceanic Technology* 11: 1042 – 1047, doi: 10.1175/1520-0426(1994)011<1042:DINWAC>2.0.CO;2.
- Rogers, D. C., DeMott, P. J. and Kreidenweis, S. M. (2001a). Airborne measurements of tropospheric ice-nucleating aerosol particles in the arctic spring. *Journal of Geophysical Research: Atmospheres* 106: 15053–15063, doi:<https://doi.org/10.1029/2000JD900790>.
- Rogers, D. C., DeMott, P. J., Kreidenweis, S. M. and Chen, Y. (2001b). A continuous-flow diffusion chamber for airborne measurements of ice nuclei. *Journal of Atmospheric and Oceanic Technology* 18: 725 – 741, doi:10.1175/1520-0426(2001)018<0725:ACFDCF>2.0.CO;2.
- Rosinski, J., Nagamoto, C. T. and Zhou, M. Y. (1995). Ice-forming nuclei over the east china sea. *Atmospheric Research* 36: 95–105, doi:[https://doi.org/10.1016/0169-8095\(94\)00029-D](https://doi.org/10.1016/0169-8095(94)00029-D).
- Salby, M. L. (2012). *Physics of the Atmosphere and Climate*. Cambridge University Press, 2nd ed.
- Sanchez-Marroquin, A., Arnalds, O., Baustian-Dorsi, K. J., Browse, J., Dagsson-Waldhauserova, P., Harrison, A. D., Maters, E. C., Pringle, K. J., Vergara-Temprado, J., Burke, I. T., McQuaid, J. B., Carslaw, K. S. and Murray, B. J. (2020). Iceland is an episodic source of atmospheric ice-nucleating particles relevant for mixed-phase clouds. *Science Advances* 6: eaba8137, doi:10.1126/sciadv.aba8137.
- Sassen, K., Wang, Z. and Liu, D. (2008). Global distribution of cirrus clouds from cloudsat/cloud-aerosol lidar and infrared pathfinder satellite observations (calipso) measurements. *Journal of Geophysical Research: Atmospheres* 113, doi:<https://doi.org/10.1029/2008JD009972>.
- Schauer, G. (2015). Increased pm concentrations during a combined wildfire and saharan dust event observed at high-altitude sonnblick observatory, austria. *Aerosol and Air Quality Research* 16, doi: 10.4209/aaqr.2015.05.0337.
- Schiebel, T. (2017). Ice Nucleation Activity of Soil Dust Aerosols. Ph.d. thesis, Karlsruhe Institute of Technology.
- Schill, G., DeMott, P., Emerson, E., Rauker, A., Kodros, J., Suski, K., Hill, T., Levin, E., Pierce, J., Farmer, D. and Kreidenweis, S. (2020). The contribution of black carbon to global ice nucleating particle concentrations relevant to mixed-phase clouds. *Proceedings of the National Academy of Sciences* 117: 202001674, doi:10.1073/pnas.2001674117.

- Schill, G., Genareau, K. and Tolbert, M. (2015). Deposition and immersion-mode nucleation of ice by three distinct samples of volcanic ash. *Atmospheric Chemistry and Physics* 15: 7523–7536, doi: 10.5194/acp-15-7523-2015.
- Schmithüsen, D., Chambers, S., Fischer, B., Gilge, S., Hatakka, J., Kazan, V., Neubert, R., Paatero, J., Ramonet, M., Schlosser, C., Schmid, S., Vermeulen, A. and Levin, I. (2017). A european-wide <sup>222</sup>radon and <sup>222</sup>radon progeny comparison study. *Atmospheric Measurement Techniques* 10: 1299–1312, doi:10.5194/amt-10-1299-2017.
- Schneider, J., Höhler, K., Heikkilä, P., Keskinen, J., Bertozzi, B., Bogert, P., Schorr, T., Umo, N. S., Vogel, F., Brasseur, Z., Wu, Y., Hakala, S., Duplissy, J., Moisseev, D., Kulmala, M., Adams, M. P., Murray, B. J., Korhonen, K., Hao, L., Thomson, E. S., Castarède, D., Leisner, T., Petäjä, T. and Möhler, O. (2021a). The seasonal cycle of ice-nucleating particles linked to the abundance of biogenic aerosol in boreal forests. *Atmospheric Chemistry and Physics* 21: 3899–3918, doi:10.5194/acp-21-3899-2021.
- Schneider, J., Höhler, K., Wagner, R., Saathoff, H., Schnaiter, M., Schorr, T., Steinke, I., Benz, S., Baumgartner, M., Rolf, C., Krämer, M., Leisner, T. and Möhler, O. (2021b). High homogeneous freezing onsets of sulfuric acid aerosol at cirrus temperatures. *Atmospheric Chemistry and Physics* 21: 14403–14425, doi:10.5194/acp-21-14403-2021.
- Schrod, J., Thomson, E. S., Weber, D., Kossmann, J., Pöhlker, C., Saturno, J., Ditas, F., Artaxo, P., Clouard, V., Saurel, J.-M., Ebert, M., Curtius, J. and Bingemer, H. G. (2020). Long-term deposition and condensation ice-nucleating particle measurements from four stations across the globe. *Atmospheric Chemistry and Physics* 20: 15983–16006, doi:10.5194/acp-20-15983-2020.
- Schrod, J., Weber, D., Drücke, J., Keleshis, C., Pikridas, M., Ebert, M., Cvetkovic, B., Nickovic, S., Marinou, E., Baars, H., Ansmann, A., Vrekoussis, M., Mihalopoulos, N., Sciare, J., Curtius, J. and Bingemer, H. (2017). Ice nucleating particles over the eastern mediterranean measured by unmanned aircraft systems. *Atmospheric Chemistry and Physics* 17: 4817–4835, doi:10.5194/acp-17-4817-2017.
- Schulz, M., Gerrit, d. L. and Balkanski, Y. (2004). *Sea-salt aerosol source functions and emissions*. 333–359, doi:10.1007/978-1-4020-2167-1\_9.
- Seinfeld, J. H. and Pandis, S. N. (2012). *Atmospheric chemistry and physics: From air pollution to climate change*. Wiley 51: 88–90.
- Silva, R., West, J., Zhang, Y., Anenberg, S., Lamarque, J.-F., Shindell, D., Collins, W., Dalsøren, S., Faluvegi, G., Folberth, G., Horowitz, L., Nagashima, T., Naik, V., Rumbold, S., Skeie, R., Sudo, K., Takemura, T., Bergmann, D., Cameron-Smith, P. and Zeng, G. (2013). Global premature mortality due to anthropogenic outdoor air pollution and the contribution of past climate change. *Environmental Research Letters* 8: 034005, doi:10.1088/1748-9326/8/3/034005.

- Smith, S. J., Aardenne, J. van, Klimont, Z., Andres, R. J., Volke, A. and Delgado Arias, S. (2011). Anthropogenic sulfur dioxide emissions: 1850–2005. *Atmospheric Chemistry and Physics* 11: 1101–1116, doi:10.5194/acp-11-1101-2011.
- Spichtinger, P. and Cziczo, D. J. (2010). Impact of heterogeneous ice nuclei on homogeneous freezing events in cirrus clouds. *Journal of Geophysical Research: Atmospheres* 115, doi:https://doi.org/10.1029/2009JD012168.
- Steinke, I., Funk, R., Busse, J., Iturri, L., Kirchen, S., Leue, M., Möhler, O., Schwartz, T., Schnaiter, M., Sierau, B., Toprak, E., Ullrich, R., Ulrich, A., Hoose, C. and Leisner, T. (2016). Ice nucleation activity of agricultural soil dust aerosols from mongolia, argentina and germany. *Journal of Geophysical Research: Atmospheres* 121, doi:10.1002/2016JD025160.
- Stevens, B. and Bony, S. (2013). What are climate models missing? *Science* 340: 1053–1054, doi:10.1126/science.1237554.
- Stopelli, E., Conen, F., Morris, C., Herrmann, E., Bukowiecki, N. and Alewell, C. (2015). Ice nucleation active particles are efficiently removed by precipitating clouds. *Scientific Reports* 5: 16433, doi:10.1038/srep16433.
- Storelvmo, T. (2017). Aerosol effects on climate via mixed-phase and ice clouds. *Annual Review of Earth and Planetary Sciences* 45: 199–222, doi:10.1146/annurev-earth-060115-012240.
- Storelvmo, T., Hoose, C. and Eriksson, P. (2011). Global modeling of mixed-phase clouds: The albedo and lifetime effects of aerosols. *Journal of Geophysical Research* 116, doi:10.1029/2010JD014724.
- Storelvmo, T. and Tan, I. (2015). The wegener-bergeron-findeisen process - its discovery and vital importance for weather and climate. *Meteorologische Zeitschrift* 24: 455–461, doi:10.1127/metz/2015/0626.
- Storelvmo, T., Tan, I. and Korolev, A. (2015). Cloud phase changes induced by co2 warming—a powerful yet poorly constrained cloud-climate feedback. *Climatic Change* 1: 288–296, doi:10.1007/s40641-015-0026-2.
- Stull, R. (1988). *An Introduction to Boundary Layer Meteorology*.
- Sullivan, R., Petters, M., DeMott, P., Kreidenweis, S., Wex, H., Niedermeier, D., Hartmann, S., Clauß, T., Stratmann, F., Reitz, P., Schneider, J. and Sierau, B. (2010). Irreversible loss of ice nucleation active sites in mineral dust particles caused by sulphuric acid condensation. *Atmospheric Chemistry and Physics*, v.10, 11471-11487 (2010) 10, doi:10.5194/acp-10-11471-2010.
- Suski, K. J., Bell, D. M., Hiranuma, N., Möhler, O., Imre, D. and Zelenyuk, A. (2018). Activation of intact bacteria and bacterial fragments mixed with agar as cloud droplets and ice crystals in cloud chamber experiments. *Atmospheric Chemistry and Physics* 18: 17497–17513, doi:10.5194/acp-18-17497-2018.

- Tabazadeh, A., Toon, O. B. and Jensen, E. J. (1997). Formation and implications of ice particle nucleation in the stratosphere. *Geophysical Research Letters* 24: 2007–2010, doi:<https://doi.org/10.1029/97GL01883>.
- Tegen, I. and Schepanski, K. (2009). The global distribution of mineral dust. *IOP Conference Series: Earth and Environmental Science* 7: 012001, doi:[10.1088/1755-1307/7/1/012001](https://doi.org/10.1088/1755-1307/7/1/012001).
- Tobo, Y., DeMott, P., Hill, T., Prenni, A., Swoboda-Colberg, N., Franc, G. and Kreidenweis, S. (2014). Organic matter matters for ice nuclei of agricultural soil origin. *Atmospheric Chemistry and Physics* 14: 8521–8531, doi:[10.5194/acp-14-8521-2014](https://doi.org/10.5194/acp-14-8521-2014).
- Tobo, Y., Uetake, J., Matsui, H., Moteki, N., Uji, Y., Iwamoto, Y., Miura, K. and Misumi, R. (2020). Seasonal trends of atmospheric ice nucleating particles over tokyo. *Journal of Geophysical Research: Atmospheres* 125: e2020JD033658, doi:<https://doi.org/10.1029/2020JD033658>.
- Tomasi, C. and Lupi, A. (2017). *Primary and Secondary Sources of Atmospheric Aerosol*. John Wiley Sons, Ltd, chap. 1. 1–86, doi:<https://doi.org/10.1002/9783527336449.ch1>.
- Tsamalis, C., Chédin, A., Pelon, J. and Capelle, V. (2013). The seasonal vertical distribution of the saharan air layer and its modulation by the wind. *Atmospheric Chemistry and Physics* 13: 11235–11257, doi:[10.5194/acp-13-11235-2013](https://doi.org/10.5194/acp-13-11235-2013).
- Ullrich, R., Hoose, C., Möhler, O., Niemand, M., Wagner, R., Höhler, K., Hiranuma, N., Saathoff, H. and Leisner, T. (2017). A new ice nucleation active site parameterization for desert dust and soot. *Journal of the Atmospheric Sciences* 74: 699–717, doi:[10.1175/JAS-D-16-0074.1](https://doi.org/10.1175/JAS-D-16-0074.1).
- Umo, N. S., Ullrich, R., Maters, E. C., Steinke, I., Benker, N., Höhler, K., Wagner, R., Weidler, P. G., Hoshyaripour, G. A., Kiselev, A., Kueppers, U., Kandler, K., Dingwell, D. B., Leisner, T. and Möhler, O. (2021). The influence of chemical and mineral compositions on the parameterization of immersion freezing by volcanic ash particles. *Journal of Geophysical Research: Atmospheres* 126: e2020JD033356, doi:<https://doi.org/10.1029/2020JD033356>, e2020JD033356 2020JD033356.
- Vali, G. (1971). Quantitative evaluation of experimental results an the heterogeneous freezing nucleation of supercooled liquids. *Journal of Atmospheric Sciences* 28: 402–409, doi:[10.1175/1520-0469\(1971\)028<0402:QEOERA>2.0.CO;2](https://doi.org/10.1175/1520-0469(1971)028<0402:QEOERA>2.0.CO;2).
- Vali, G., DeMott, P. J., Möhler, O. and Whale, T. F. (2015). Technical note: A proposal for ice nucleation terminology. *Atmospheric Chemistry and Physics* 15: 10263–10270, doi:[10.5194/acp-15-10263-2015](https://doi.org/10.5194/acp-15-10263-2015).
- Varble, A. C., Nesbitt, S. W., Salio, P., Hardin, J. C., Bharadwaj, N., Borque, P., DeMott, P. J., Feng, Z., Hill, T. C. J., Marquis, J. N., Matthews, A., Mei, F., Öktem, R., Castro, V., Goldberger, L., Hunzinger,

- A., Barry, K. R., Kreidenweis, S. M., McFarquhar, G. M., McMurdie, L. A., Pekour, M., Powers, H., Romps, D. M., Saulo, C., Schmid, B., Tomlinson, J. M., Heever, S. C. van den, Zelenyuk, A., Zhang, Z. and Zipser, E. J. (2021). Utilizing a storm-generating hotspot to study convective cloud transitions: The cacti experiment. *Bulletin of the American Meteorological Society* 102: E1597 – E1620, doi: 10.1175/BAMS-D-20-0030.1.
- Vergara-Temprado, J., Holden, M. A., Orton, T. R., O’Sullivan, D., Umo, N. S., Browse, J., Reddington, C., Baeza-Romero, M. T., Jones, J. M., Lea-Langton, A., Williams, A., Carslaw, K. S. and Murray, B. J. (2018a). Is black carbon an unimportant ice-nucleating particle in mixed-phase clouds? *Journal of Geophysical Research: Atmospheres* 123: 4273–4283, doi:https://doi.org/10.1002/2017JD027831.
- Vergara-Temprado, J., Miltenberger, A., Furtado, K., Grosvenor, D., Shipway, B., Hill, A., Wilkinson, J., Field, P., Murray, B. and Carslaw, K. (2018b). Strong control of southern ocean cloud reflectivity by ice-nucleating particles. *Proceedings of the National Academy of Sciences* 115: 201721627, doi: 10.1073/pnas.1721627115.
- Vergara-Temprado, J., Murray, B. J., Wilson, T. W., O’Sullivan, D., Browse, J., Pringle, K. J., Ardon-Dryer, K., Bertram, A. K., Burrows, S. M., Ceburnis, D., DeMott, P. J., Mason, R. H., O’Dowd, C. D., Rinaldi, M. and Carslaw, K. S. (2017). Contribution of feldspar and marine organic aerosols to global ice nucleating particle concentrations. *Atmospheric Chemistry and Physics* 17: 3637–3658, doi:10.5194/acp-17-3637-2017.
- Vogel, F. (2022). Short-term Variation in Measurements of Atmospheric Ice-Nucleating Particle Concentrations. Ph.d. thesis, Karlsruhe Institute of Technology.
- Wagner, R., Benz, S., Möhler, O., Saathoff, H. and Schurath, H. (2006). Probing ice clouds by broadband mid-infrared extinction spectroscopy: Case studies from ice nucleation experiments in the aida aerosol and cloud chamber. *Atmospheric Chemistry and Physics* 6, doi:10.5194/acp-6-4775-2006.
- Wagner, R., Höhler, K., Huang, W., Kiselev, A., Möhler, O., Mohr, C., Pajunoja, A., Saathoff, H., Schiebel, T., Shen, X. and Virtanen, A. (2017). Heterogeneous ice nucleation of -pinene soa particles before and after ice cloud processing. *Journal of Geophysical Research: Atmospheres* 122: n/a–n/a, doi:10.1002/2016jd026401.
- Wagner, R., Ickes, L., Bertram, A. K., Els, N., Gorokhova, E., Möhler, O., Murray, B. J., Umo, N. S. and Salter, M. E. (2021). Heterogeneous ice nucleation ability of aerosol particles generated from arctic sea surface microlayer and surface seawater samples at cirrus temperatures. *Atmospheric Chemistry and Physics* 21: 13903–13930, doi:10.5194/acp-21-13903-2021.
- Wagner, R., Kiselev, A., Möhler, O., Saathoff, H. and Steinke, I. (2015). Pre-activation of ice nucleating particles by the pore condensation and freezing mechanism. *Atmospheric Chemistry and Physics Discussions* 15: 28999–29046, doi:10.5194/acpd-15-28999-2015.

- Wang, X., Zhang, L. and Moran, M. D. (2014). Development of a new semi-empirical parameterization for below-cloud scavenging of size-resolved aerosol particles by both rain and snow. *Geoscientific Model Development* 7: 799–819, doi:10.5194/gmd-7-799-2014.
- Welti, A., Lüönd, F., Stetzer, O. and Lohmann, U. (2009). Influence of particle size on the ice nucleating ability of mineral dusts. *Atmospheric Chemistry and Physics* 9: 6705–6715, doi:10.5194/acp-9-6705-2009.
- Wex, H., Augustin-Bauditz, S., Boose, Y., Budke, C., Curtius, J., Diehl, K., Dreyer, A., Frank, F., Hartmann, S., Hiranuma, N., Jantsch, E., Kanji, Z. A., Kiselev, A., Koop, T., Möhler, O., Niedermeier, D., Nillius, B., Rösch, M., Rose, D., Schmidt, C., Steinke, I. and Stratmann, F. (2015). Intercomparing different devices for the investigation of ice nucleating particles using snomax as test substance. *Atmospheric Chemistry and Physics* 15: 1463–1485, doi:10.5194/acp-15-1463-2015.
- Wex, H., Huang, L., Zhang, W., Hung, H., Traversi, R., Becagli, S., Sheesley, R. J., Moffett, C. E., Barrett, T. E., Bossi, R., Skov, H., Hünerbein, A., Lubitz, J., Löffler, M., Linke, O., Hartmann, M., Herenz, P. and Stratmann, F. (2019). Annual variability of ice-nucleating particle concentrations at different arctic locations. *Atmospheric Chemistry and Physics* 19: 5293–5311, doi:10.5194/acp-19-5293-2019.
- Whitby, K. T. (1978). The physical characteristics of sulfur aerosols. *Atmospheric Environment (1967)* 12: 135–159, doi:https://doi.org/10.1016/0004-6981(78)90196-8, proceedings of the International Symposium.
- Whytlaw-Gray, R., Speakman, J. B., Campbell, J. H. P. and Smithells, A. (1923). Smokes: Part i.—a study of their behaviour and a method of determining the number of particles they contain. *Proceedings of the Royal Society of London. Series A, Containing Papers of a Mathematical and Physical Character* 102: 600–615, doi:10.1098/rspa.1923.0018.
- Wieder, J., Mignani, C., Schär, M., Roth, L., Sprenger, M., Henneberger, J., Lohmann, U., Brunner, C. and Kanji, Z. A. (2022). Unveiling atmospheric transport and mixing mechanisms of ice-nucleating particles over the alps. *Atmospheric Chemistry and Physics* 22: 3111–3130, doi:10.5194/acp-22-3111-2022.
- Wilson, T., Ladino, L., Alpert, P., Breckels, M., Brooks, I., Browse, J., Burrows, S., Carslaw, K., Huffman, J., Judd, C., Kilthau, W., Mason, R., Mcfiggans, G., Miller, L., Nájera, J., Polishchuk, E., Rae, S., Schiller, C., Si, M. and Murray, B. (2015). A marine biogenic source of atmospheric ice-nucleating particles. *Nature* 525: 234, doi:10.1038/nature14986.
- Wolf, K., Bellouin, N. and Boucher, O. (2023). Sensitivity of cirrus and contrail radiative effect on cloud microphysical and environmental parameters. *Atmospheric Chemistry and Physics* 23: 14003–14037, doi:10.5194/acp-23-14003-2023.

- Wolf, M., Zhang, Y., Zawadowicz, M., Goodell, M., Froyd, K., Freney, E., Sellegri, K., Rösch, M., Cui, T., Winter, M., Lacher, L., Axisa, D., DeMott, P., Levin, E., Gute, E., Abbatt, J., Koss, A., Kroll, J., Surratt, J. and Cziczo, D. (2020). A biogenic secondary organic aerosol source of cirrus ice nucleating particles. *Nature Communications* 11, doi:10.1038/s41467-020-18424-6.
- Xue, H., Lu, Y., Geng, H., Dong, B., Wu, S., Fan, Q., Zhang, Z., Li, X., Zhou, X. and Wang, J. (2019). Hydroxyl groups on the graphene surfaces facilitate ice nucleation. *The Journal of Physical Chemistry Letters* 10, doi:10.1021/acs.jpcclett.9b01033.
- Yakobi-Hancock, J., Ladino, L. and Abbatt, J. (2013). Feldspar minerals as efficient deposition ice nuclei. *Atmospheric Chemistry and Physics* 13, doi:10.5194/acp-13-11175-2013.



## C. List of Figures

1.1	Schematic representation of different nucleation modes (adapted from Hoose and Möhler (2012)). . . . .	2
1.2	Schematic of different INP instruments. . . . .	3
2.1	Schematic of the particle number, surface and mass size distribution for different modes .	8
2.2	Total aerosol effective radiative forcing . . . . .	9
2.3	Classification of clouds containing ice in the atmosphere . . . . .	10
2.4	Schematic of the Gibbs free energy . . . . .	11
2.5	Two different cirrus clouds formed by homogeneously or heterogeneously ice formation	13
2.6	Distribution of liquid and ice phase of two different mixed-phase clouds . . . . .	14
2.7	Overview of different INP field studies (adapted from Kanji et al. (2017) ) . . . . .	15
2.8	Overview of different aerosol types (adapted from DeMott et al. (2010) with changes) . .	17
3.1	Photo and schematic drawing of PINE . . . . .	22
3.2	Measurement cycle of a run with PINE . . . . .	24
3.3	Example time series with PINE . . . . .	25
3.4	Schematic drawing of the setup of INSEKT . . . . .	26
3.5	Schematic drawing of AIDA . . . . .	28
4.1	Schematic drawing of the setup of PINEair . . . . .	36
4.2	Simplified schematic drawing of PINEair . . . . .	37
4.3	Example of a complete run cycle with PINEair . . . . .	38
4.4	Pressure profile for a (continuous) expansion and a step-wise expansion . . . . .	40
4.5	Example for a step-wise expansion in PINEair . . . . .	41
4.6	Timeline about the construction of different PINEair versions . . . . .	42
4.7	Pictures of the different PINEair versions . . . . .	44
4.8	Results about the onset temperature of homogeneous freezing experiments . . . . .	46
4.9	Results about the distinction between homogeneous and heterogeneous freezing . . . . .	47
4.10	Ice saturation ratio as a function of adiabatic temperature for homogeneous and hetero- geneous freezing experiments . . . . .	48
4.11	Example for a measurement with PINEair at a reduced start pressure . . . . .	49
4.12	Comparison between PINEair and other INP instruments . . . . .	50

4.13	Temperature measurements in PINEair during the waiting time . . . . .	51
4.14	Influence of the waiting time on the start of homogeneous freezing . . . . .	52
4.15	Comparison of the measured temperature and calculated adiabatic temperature during a step-wise expansion . . . . .	53
4.16	Measurements to find optimal settings for the flow after the step-wise expansion . . . . .	54
4.17	Particle concentration as function of time for different pump flow settings after the step- wise expansion . . . . .	56
4.18	Measurements to find settings for the duration of the expansion . . . . .	57
4.19	Pressure profile in PINEair during a step-wise expansion . . . . .	58
4.20	Standard deviation for the calculation of the pressure balance . . . . .	59
4.21	Example of a relative humidity scan in PINEair . . . . .	59
4.22	Laboratory experiments with PINEair for the distinction between homogeneous and het- erogeneous freezing . . . . .	60
4.23	Comparison of peak ice saturation ratio in PINEair between the experiments at APC and AIDA chamber . . . . .	62
4.24	Particle concentration for different runs with step-wise expansions as function of <i>PPD</i> for laboratory experiments . . . . .	63
4.25	Particle concentration for different runs with step-wise expansions as function of the <i>PPD</i> for experiments at ambient air conditions . . . . .	64
4.26	Comparison of two measurement series with PINEair at different dew point temperatures	65
4.27	Dew point temperature as function of the threshold for <i>PPD</i> during step-wise expansions	66
4.28	Picture of the mountain Hoher Sonnblick in Austria . . . . .	67
4.29	Schematic of the inlet setup of the SBO campaign . . . . .	68
4.30	Example time series with PINEair at cirrus conditions performed at SBO . . . . .	69
4.31	Time series of INP concentration measured with PINEair in comparison to aerosol pa- rameters . . . . .	71
4.32	Comparison between PINEair and INSEKT data . . . . .	73
4.33	ice crystal concentration as function of peak ice saturation ratio for homogeneous and heterogeneous freezing . . . . .	75
4.34	INP concentration as function of peak ice saturation ratio for heterogeneous freezing . . .	76
4.35	Trajectories of air masses reached SBO on May 18, 2023 and May 22, 2023 . . . . .	76
4.36	Comparison between two days: INP concentration as function of ice saturation ratio . . .	77
4.37	Peak ice saturation ratio as function of adiabatic temperature for SBO data . . . . .	78
4.38	Time series of INP concentration measured with PINEair in comparison to aerosol pa- rameters at cirrus conditions . . . . .	79
4.39	Time series of two days: INP concentration measured with PINEair at cirrus conditions and other aerosol parameters . . . . .	81

4.40	Total aerosol and INP concentrations as function of time from Puy de Dôme observatory (Figure adapted from Wolf et al. (2020)) . . . . .	83
4.41	Comparison of INP concentration performed at Campus North and SBO . . . . .	84
4.42	Comparison of peak ice saturation ratio as function of adiabatic temperature, measurements performed at Campus North and SBO . . . . .	85
5.1	Location of the SBO in Austria . . . . .	91
5.2	Photo of SBO in summer and winter . . . . .	92
5.3	Photo of the aerosol inlet at SBO . . . . .	92
5.4	Timeline of the INP measurements performed at SBO . . . . .	93
5.5	Example of a time series of PINE measurements at SBO . . . . .	94
5.6	Schematic setup of the INP and aerosol measurements at SBO . . . . .	95
5.7	INP temperature spectra of INSEKT and PINE . . . . .	98
5.8	Mean INP temperature spectra of INSEKT . . . . .	99
5.9	Time series of INP concentration measured with INSEKT and PINE . . . . .	99
5.10	Monthly averaged diurnal variation of INP concentration . . . . .	101
5.11	INP temperature spectra of untreated and heated samples for INSEKT . . . . .	102
5.12	Mean INP temperature spectra of untreated and heated samples for INSEKT . . . . .	103
5.13	Time series of untreated and heated samples for INSEKT . . . . .	103
5.14	Time series of INP, <sup>214</sup> Polonium, and aerosol particles with a diameter larger than 90 nm concentration . . . . .	105
5.15	Monthly averaged diurnal variation of the number concentration of aerosol particles with diameters larger than 90 nm . . . . .	106
5.16	Monthly averaged diurnal variation of <sup>214</sup> Polonium concentration . . . . .	106
5.17	Time series for INP and particle mass concentration . . . . .	108
5.18	Comparison between dust and no dust influence: INP, aerosol particles with $d > 90$ nm, <sup>214</sup> Polonium, and particle mass concentration . . . . .	109
5.19	Time series of INP concentration split into cloudy and clear-sky periods . . . . .	110
5.20	Spearman correlation coefficient between INP data (INSEKT and PINE) and meteorological parameters . . . . .	111
5.21	Spearman correlation coefficient between INP data (INSEKT and PINE) and aerosol parameters . . . . .	113
5.22	Comparison between INSEKT and PINE data . . . . .	114
5.23	INP temperature spectra for INSEKT and PINE data . . . . .	115
5.24	Time series of particle concentration with different diameters . . . . .	115
5.25	Time series of INP and particle mass concentration during dust event in March 2022 . . . . .	117
5.26	Comparison between observed and predicted INP concentration . . . . .	118

5.27 Comparison between observed and predicted ice-active surface site density . . . . . 120

5.28 Simulations of the dust load with the WRF/Chem model . . . . . 121

5.29 INP concentrations at SBO and the Helmos station during the dust event in March 2022 . 122

## D. List of Tables

3.1	Overview of aerosols for test measurements with PINEair . . . . .	30
4.1	Overview of AIDA experiments to test PINEair prototype I . . . . .	45
4.2	Spearman correlation coefficient between INP concentration measured with PINEair and other aerosol parameters at MPC conditions . . . . .	72
4.3	Spearman correlation coefficient between INP concentration measured with PINEair and aerosol and meteorological parameters at cirrus conditions . . . . .	80
5.1	Overview of instruments for meteorological data at SBO . . . . .	96
5.2	Times for minima and maxima of INP, <sup>214</sup> Polonium, and aerosol particles with d >90 nm concentration . . . . .	107
5.3	Equations for INP parameterization of DeMott et al. (2010) and DeMott et al. (2015) . . . . .	118
5.4	Equations for the parameterization of ice-active surface site density . . . . .	119



## Acknowledgments

At this point, I would like to thank all the people who have supported and accompanied me during my PhD time. I am very grateful for the nice journey, during which I experienced a lot of new things.

First, I would like to thank Prof. Dr. Thomas Leisner and Prof. Dr. Joachim Curtius for being my referee and co-referee and for the helpful discussions we had during the last years.

I am especially thankful to my supervisors, Dr. Ottmar Möhler and Dr. Larissa Lacher, who supported me throughout my PhD. Without your ideas and suggestions for all the major milestones of this work, such as the first measurements with PINEair or the evaluation and interpretation of the data, the work would never have been so successful. Your enthusiasm for all projects and new ideas always created a very positive working atmosphere, and I always enjoyed working with you.

All the people from AAF have also contributed to the very nice working atmosphere, and for this, I want to say thank you. Thanks, especially to the technical team, Rainer Buschbacher, Tomasz Chudy, Olga Dombrowski, Jens Nadolny, Georg Scheurig, and Steffen Vogt for all the support with lab experiments at the AIDA and the APC chamber and the help with setting up new test experiments. I particularly want to thank Olga Dombrowski and the INSEKT student assistants who analyzed the majority of the INSEKT filters. A special thank you goes to Jens Nadolny and Steffen Vogt. Without your help in setting up the PINEair prototype, the instrument would never have been ready in time. I always had a lot of fun working with you in the workshop and during AIDA experiments. Many thanks to Susanne Bolz for her help with all organizational questions and Frank Schwarz for the IT support. Thanks to Nicole Büttner and Dr. Romy Fösig for the development of the Python analysis tool for PINE and the adaptation of the program for PINEair.

The development for PINEair is in collaboration with the Goethe University Frankfurt (Joachim Curtius, Jann Schrod, Beke Tietjen, Laurin Merkel), Bilfinger Nuclear & Energy Transition GmbH (Alexander Vatagin, Achim Hobel) and enviscope GmbH (Rolf Maser, Jannik Völker). I would like to take this opportunity to thank all the people mentioned for the good cooperation and the interesting meetings. Special thanks to Beke Tietjen, who was involved in the first AIDA test campaign for PINEair. A big thank you to Jann Schrod, who also enthusiastically supported the first laboratory campaign with PINEair

in Karlsruhe, as well as the first field campaign at the Sonnblick Observatory in Austria.

During my PhD time, I had the opportunity to bring my instruments to the Sonnblick Observatory several times, for which I would like to thank Elke Ludewig and the whole Sonnblick team. My stays on-site were one of the highlights of my PhD and I always enjoyed my time at the mountain a lot. Many thanks to all the technicians who were always very helpful in transporting the instruments to the top floor of the laboratory and who regularly changed the filters on-site. Thanks to Johannes Graf, who supported me during one intensive campaign on-site as part of his bachelor's thesis and who evaluated some of the filters for INSEKT.

I want to thank all my friends in and outside of Karlsruhe for having a great time together in the last few years. Through numerous bouldering sessions, walks, game nights, and phone calls, you have always helped me reset my mind from work.

Finally, I would like to thank my parents and my two brothers from the bottom of my heart for always supporting me throughout my PhD and always being there for me.